
Search for very-high-energy gamma-ray emission from astrophysical transients with VERITAS

Dissertation zur Erlangung des akademischen Grades

DOCTOR RERUM NATURALIUM

(Dr. rer. nat.)

im Fach Physik

eingereicht an der

Mathematisch-Naturwissenschaftlichen Fakultät

der

Humboldt-Universität zu Berlin

von

M.Sc. Maria Kherlakian

Präsidentin der Humboldt-Universität zu Berlin:

Prof. Dr. Julia von Blumenthal

Dekanin der Mathematisch-Naturwissenschaftlichen Fakultät:

Prof. Dr. Caren Tischendorf

Gutachter/innen:

1. Prof. Dr. David Berge
2. Prof. Dr. Marek Kowalski
3. Prof. Dr. Jörn Wilms

Tag der mündlichen Prüfung: 19.02.2025

Abstract

Wide-field of view, high-cadence optical surveys have led to the discovery of several new sources in the transient sky each year. Certain transient classes, such as Tidal disruption events (TDEs) and Fast blue optical transients (FBOTs), are presumed to be powered by shock interactions. These shocks could accelerate cosmic rays to petaelectronvolt (PeV) energies, potentially leading to a detectable very-high-energy; $100 \text{ GeV} < E < 100 \text{ TeV}$ (VHE) gamma-ray component. Nonetheless, the complexity of these events, combined with scarce follow-ups by Imaging atmospheric Cherenkov telescopes (IACTs), limits our understanding of the non-thermal picture in these systems. In addition, the potential VHE gamma-ray emission is presumed to be significantly attenuated by lower-energy ambient photons. This thesis focuses on the search for VHE gamma rays from transient events with the Very Energetic Radiation Imaging Telescope Array System (VERITAS), a ground-based gamma-ray observatory in Arizona. VERITAS is composed by four IACTs and is sensitive to gamma rays in the range of 80 GeV to 40 TeV.

I present the application of the Optimised Next Neighbor (ONN) method for image cleaning to the VERITAS event reconstruction. Images from Cherenkov telescopes contain noise signals induced by the night sky background (NSB) and electronic noise. Image cleaning methods must be employed to remove the pixels in the camera which are exclusively contaminated by this noise. With the ONN cleaning method, dynamic threshold cuts are set on both the pixel signal and on the limited time duration of the Cherenkov pulses. This method has increased effective areas by a factor of $\gtrsim 3$ below 100 GeV, reducing the energy threshold by 20% for specific Monte Carlo configurations. Overall, an increase by a factor of ~ 2.5 in reconstructed events below 100 GeV for an extensive Crab Nebula dataset is achieved.

As part of this doctoral project, I established the first Target of opportunity (ToO) proposal for TDE follow-up with VERITAS, leading to the observing campaigns on TDEs AT2022dbl, AT2022dsb and AT2023clx. No gamma-ray emission was detected by either VERITAS or the Large Area Telescope of the Fermi Gamma-ray Space Telescope (Fermi-LAT), and I derive flux upper limits (ULs). The extent of gamma-ray attenuation is estimated by assuming annihilation with the optical and UV components of each TDE. I show that for AT2022dbl and AT2022dsb, most gamma rays in the VERITAS sensitivity range would be attenuated up to 150 days after the peak of the UV light curve if the size of the radiation zone is between $5 \cdot 10^{14} \text{ cm}$ and $1 \cdot 10^{16} \text{ cm}$.

Additionally, I established the ToO proposal for FBOT follow-up with VERITAS, including trigger criteria for observing nearby, dimmer core-collapse supernovae and distant, brighter ones. I present the follow-up campaign for FBOT AT2023ufx, with analysis results from VERITAS and from Fermi-LAT yielding no detection and leading to the estimation of flux ULs.

Finally, the outburst of GRB 221009A prompted a major follow-up campaign across the electromagnetic spectrum. The first three hours of VERITAS observations, conducted ~ 37 hours post the initial Gamma-ray Burst Monitor of the Fermi Gamma-ray Space Telescope (Fermi-GBM) trigger, were performed with an ultra violet filter (UVF) to protect the photomultiplier tubes of the camera due to the high moonlight levels. I present a correction for event reconstruction in the UVF observing mode and its validation with a Crab Nebula dataset. This corrected analysis chain was used to analyse GRB 221009A, yielding flux ULs.

In conclusion, I present an alternative image cleaning method for VERITAS, which is employed in the analysis of most sources presented in this thesis. Following, I discuss the follow-up program of different classes of transient phenomena and present the VERITAS analysis results for triggered events. Although no VHE emission was detected for GRB 221009 and for the TDEs and FBOTs discussed in this thesis, the establishment of flux ULs and the development of comprehensive analysis techniques have provided a foundation for future transient research with VERITAS.

Kurzzusammenfassung

Optische Vermessungen mit großem Sichtfeld und hoher Kadenz haben jährlich zur Entdeckung zahlreicher neuer Quellen am transienter Himmelsereignisse geführt. Es wird vermutet, dass bestimmte transiente Klassen, wie TDEs und FBOTs, durch Schockwechselwirkungen angetrieben werden. Diese Schocks könnten kosmische Strahlung auf PeV-Energien beschleunigen, was möglicherweise zu einer nachweisbaren VHE-Komponente führt. Dennoch schränkt die Komplexität dieser Ereignisse in Verbindung mit den spärlichen Nachuntersuchungen durch IACTs unser Verständnis des nichtthermischen Anteils in diesen Systemen ein. Außerdem dürfte die potenzielle Gammastrahlenemission im GeV- und TeV-Bereich durch niederenergetische Photonen aus der Umgebung erheblich abgeschwächt werden. Diese Arbeit konzentriert sich auf die Suche nach VHE-Strahlung aus transienten Ereignissen mit dem VERITAS, ein bodengebundenes Gammastrahlenobservatorium in Arizona. VERITAS besteht aus vier IACTs und ist empfindlich für Gammastrahlen im Bereich von 80 GeV bis 40 TeV.

Ich stelle die Anwendung der ONN-Methode zur Bildbereinigung auf das VERITAS-Observatoriums vor. Bilder von Cherenkov-Teleskopen enthalten Rauschsignale, die durch das NSB und elektronisches Rauschen verursacht werden. Um die ausschließlich durch dieses Rauschen kontaminierten Kamerapixel zu entfernen, werden Bildreinigungsmethoden angewandt. Bei der ONN-Reinigungsmethode werden dynamische Schwellenwerte sowohl für das Pixelsignal als auch für die begrenzte Zeitdauer der Cherenkov-Pulse festgelegt. Diese Methode hat die effektiven Flächen unterhalb von 100 GeV um den Faktor $\gtrsim 3$ erhöht und die Energieschwelle für bestimmte Monte-Carlo-Konfigurationen um 20% verbessert. Insgesamt wurde eine Steigerung um den Faktor $\sim 2,5$ bei den rekonstruierten Ereignissen unterhalb von 100 GeV für einen umfangreichen Krebsnebel Datensatz erreicht.

Im Rahmen dieses Promotionsprojekts wurde das erste ToO-Programm für die Nachverfolgung von TDE mit VERITAS erstellt, der zu den Beobertungskampagnen auf TDEs AT2022dbl, AT2022dsb und AT2023clx führten. Es wurde keine Gammastrahlenemission entdeckt, und ich habe den Flussobergrenze abgeleitet. Das Ausmaß der Gammastrahlungattenuation wird durch die Abschätzung der Auslöschung mit den optischen und UV-Komponenten jeder TDE geschätzt. Ich zeige, dass für AT2022dbl und AT2022dsb die meisten Gammastrahlen im VERITAS-Empfindlichkeitsbereich bis zu 150 Tage nach Erreichen des Maximums der UV-Lichtkurve abgeschwächt werden, wenn die Größe der Strahlungszone zwischen $5 \cdot 10^{14}$ cm und $1 \cdot 10^{16}$ cm liegt.

Darüber hinaus diskutiere ich einen ToO-Programm für die Nachverfolgung von FBOTs mit VERITAS, einschließlich Triggerkriterien für die Beobachtung von nahen, schwächeren Kernkollaps-Supernovae und entfernten, helleren Supernovae. Ich stelle die Kampagne für FBOT AT2023ufx vor, wobei die Analyseergebnisse von VERITAS und Fermi-LAT keine Entdeckung erbrachten und zur Schätzung des Flussobergrenze führten.

Schließlich, führt der Ausbruch von GRB 221009A zum einem umfangreichen Nachfolgekampagne im gesamten elektromagnetischen Spektrum. Die ersten drei Stunden der VERITAS-Beobachtungen, die ~ 37 Stunden nach dem ersten Fermi-GBM-Trigger durchgeführt wurden, wurden mit einem UVF durchgeführt, um die Photomultiplier-Röhren der Kamera aufgrund des hohen Mondlichts zu schützen. Ich präsentiere eine Korrektur für die Ereignisrekonstruktion im UVF-Beobachtungsmodus und ihre Validierung mit einem Krebsnebel Datensatz. Diese neue Analyseketten wurde für die Analyse von GRB 221009A verwendet und es wurden neuen Flussobergrenze ermittelt.

Abschließend präsentiere ich eine alternative Bildbereinigungsmethode für VERITAS, die bei der Analyse der meisten in dieser Arbeit vorgestellten Quellen eingesetzt wird. Im Anschluss bespreche ich das Folgeprogramm verschiedener Klassen von transienten Phänomenen und präsentiere die VERITAS-Analyseergebnisse für ausgelöste Ereignisse. Obwohl keine VHE-Emission für GRB 221009 und für die in dieser Arbeit diskutierten TDEs und FBOTs nachgewiesen wurde, haben die Etablierung von Fluss-Obergrenzen und die Entwicklung umfassender Analysetechniken eine Grundlage für zukünftige Forschung zu transienten Ereignissen mit VERITAS geschaffen.

Contents

List of Figures	vi
List of Tables	xii
1 Introduction	1
2 Very High Energy Gamma Rays	5
2.1 Mechanisms of production and absorption of gamma rays	7
2.2 Absorption mechanisms of gamma rays	11
2.3 Acceleration mechanisms of cosmic rays	13
2.3.1 The diffusive shock acceleration mechanism	13
2.4 The Imaging atmospheric Cherenkov technique	17
2.5 Shock powered transients	20
2.5.1 Tidal disruption events	21
2.5.2 Gamma ray Bursts	30
2.5.3 Fast Blue Optical Transients	33
2.5.4 The generic shock powered transient scenario	35
2.5.5 Future prospects	36
3 The Very Energetic Radiation Imaging Telescope Array System	39
3.1 The Very Energetic Radiation Imaging Telescope Array System	40
3.1.1 Fundamentals of the data acquisition and trigger systems	40
3.1.2 Calibrations of the telescope optical response	42
3.1.3 The throughput correction of the VERITAS array	44
3.1.4 The Night Sky Background	45
3.2 Event reconstruction	49
3.2.1 Charge integration and image cleaning	49
3.2.2 Image parametrisation	51
3.3 Stereoscopic reconstruction of events	52
3.3.1 Direction reconstruction	53
3.3.2 Energy reconstruction	54
3.3.3 Gamma/hadron separation	54
3.3.4 Background estimation	57
3.4 Flux estimation and inference of model parameters	59

3.4.1	Instrument response functions	59
3.4.2	Flux estimation	60
4	Implementation of the Optimised Next Neighbour image cleaning method for the VERITAS array	65
4.1	Conventional image cleaning methods for IACTs	66
4.2	The Optimised Next Neighbour image cleaning method	68
4.3	Results on simulations and instrument response functions	75
4.4	Results on test sources	78
4.4.1	Crab Nebula	78
4.4.2	Monte Carlo data comparison	81
4.4.3	PKS 1424+240	84
4.4.4	PG 1553+113	86
4.4.5	M87	86
4.5	The optimised next neighbour image cleaning for runs of short duration	88
4.6	The optimised next neighbour image cleaning for data taken with Reduced High Voltage	89
4.7	Chapter conclusions	95
5	Observations of tidal disruption events with VERITAS	99
5.1	Target of Opportunity observations of tidal disruption events	101
5.1.1	AT2022dbl	104
5.1.2	AT2022dsb	105
5.1.3	AT2023clx	106
5.2	VERITAS and Fermi-LAT results	107
5.3	Modelling the internal gamma-ray attenuation for AT2022dbl and AT2022dsb	112
5.3.1	Results of the blackbody characterisation of the OUV components for AT2022dbl and AT2022dsb	113
5.3.2	Optical depth from $\gamma\gamma$ attenuation	114
5.3.3	Time evolution of the optical depth	116
5.3.4	Broadband gamma-ray flux ULs for AT2022dbl and AT2022dsb	118
5.3.5	Upper limits on the proton luminosity	118
5.4	Updating the VERITAS results on Swift J1644	121
5.5	Chapter conclusions and final remarks	123
6	VERITAS Observations of GRB 221009A	125
6.1	UVF observations with the VERITAS array	126
6.2	Corrections for UV Filter Observations with EventDisplay	127
6.3	The VERITAS GRB follow-up program	131
6.4	GRB 221009A in very high energies	132
6.4.1	VERITAS Observations of GRB 221009A	133
6.5	Chapter conclusions	136

7	Observations of fast blue optical transients with VERITAS	138
7.1	Target of opportunity observations of fast blue optical transients with VERITAS	138
7.2	AT2023ufx	140
7.2.1	VERITAS results for AT2023ufx	141
7.3	Conclusions and future prospects	141
8	Summary and outlook	143
Appendices		
A	Supplementary material for Chapter 3	148
B	Multiwavelength analysis methods for tidal disruption events	194
B.0.1	Optical and UV instruments	194
B.0.2	X-ray and radio	195
B.0.3	Gamma rays	196
B.1	Methods for bolometric light curve calculation	200
B.2	Photometry tables	201
	Bibliography	210
	Acronyms	237
	Acknowledgements	240
	Selbständigkeitserklärung	241

List of Figures

1.1	The spectrum of cosmic-rays.	1
2.1	The sky map of the diffuse gamma-ray emission constructed with 12 years of observations from Fermi-LAT.	5
2.2	The sky-map of VHE sources according to the TeV Catalog.	6
2.3	Klein–Nishina cross-section.	10
2.4	The optical depth for gamma-ray attenuation with the EBL.	12
2.5	Schematic view of a shock wave in its reference frame. In this particular representation, the plasma flow and magnetic fields are perpendicular to the shock plane. Figure from: [Wilhelm, 2021].	15
2.6	Extensive air showers produced by a primary gamma ray.	17
2.7	Extensive air showers produced by a primary hadronic particle (protons and nuclei).	18
2.8	Longitudinal and XY projection for gamma ray and proton induced showers, both with a primary particle energy of 100 GeV.	19
2.9	Schematic view of the Cherenkov emission triggered by secondary particles produced in the development of an EAS.	20
2.10	Artistic illustration of a Tidal Disruption Event.	22
2.11	Integrated OUV luminosity for different TDEs as a function of time elapsed since either the peak.	23
2.12	The X-ray light curves of Swift J1644+57 and Swift J2058.4+0516.	25
2.13	The radio light curve of Swift J1644+57.	25
2.14	Radio light curves of several TDEs.	26
2.15	The TDE unified model.	28
2.16	The global picture of acceleration regions in a TDE.	29
2.17	Differential neutrino and gamma ray luminosities for the wind model of TDEs.	29
2.18	Artistic view of a GRB.	31
2.19	Distribution of GRBs according to their BAT fluence of XRT flux.	33
2.20	Parameter space of the peak of the r-band absolute magnitude (or pseudo bolometric luminosity on the right axis) by the rise time for different SNe.	34
2.21	The FBOT AT2018cow and host galaxy.	35
2.22	The luminosity of transient events given in the parameter space of wind mass-loss rate against the velocity of the shock.	38
3.1	The Very Energetic Radiation Imaging Telescope Array System.	39

3.2	The Davies-Cotton mirror design and the VERITAS telescope.	41
3.3	The camera of the VERITAS array.	41
3.4	Example of a bias curves used to measure the rate of L3 and L2 triggers.	43
3.5	The throughput calibration factors per VERITAS telescope and per observing season.	45
3.6	Brightness of some component of the NSB.	47
3.7	Distribution of pedestals in two different channels (200 in red and 300 in blue) during the same observing run.	48
3.8	Dependence of simulated pedestal variances with noise rates.	49
3.9	Method for FADC trace integration for a particle shower and a pedestal event.	50
3.10	The time gradient of pixels after image cleaning.	51
3.11	Average pedestal in the camera, camera image composed of Cherenkov light and noise and final image after the full application of the double-pass method.	51
3.12	Hillas parameters of an image from a particle shower.	52
3.13	Illustration of the geometrical method for direction reconstruction.	54
3.14	Lookup-table consisting of $E_{MC,1}$ and $\sigma_{EMC,i}$	56
3.15	Lookup-tables for $w_{MC,1}$ and $\sigma_{MC,1}^w$	56
3.16	Examples of the distributions of MSCW and MSCL parameters for simulated gamma rays plus cosmic rays and only cosmic-ray events.	57
3.17	Ring and reflected regions background methods.	58
3.18	Typical significance distributions expected for background and source events.	59
3.19	Effective areas and energy threshold for VERITAS.	60
3.20	The integral sensitivity of the VERITAS array.	61
3.21	Differential flux sensitivity of several gamma-ray instruments. IACTs: VERITAS, H.E.S.S., MAGIC and CTA (North and South). Additionally, the figure also presents HAWC and Fermi-LAT sensitivities.	62
3.22	The Rolke method to find upper limits.	64
4.1	Raw image, image after conventional cleaning and final image after the application of the double-pass method.	67
4.2	The Next Neighbour software implemented for the image cleaning of the MAGIC array.	68
4.3	The Optimised Next Neighbour image cleaning method applied to simulated events of the CTAO.	69
4.4	Noise rates per VERITAS telescope in the range from 100 MHz to 500 MHz.	70
4.5	Illustration of the same event reconstruction assuming different values for the maximum probability of false group detection.	72
4.6	Distribution of energy, MSCW and MSCL for reconstructed Monte Carlo events assuming different values for the fake image probability.	73
4.7	Dynamical cuts in the $\Delta T - Q$ plane for each telescope in the VERITAS array.	73
4.8	Dynamical cuts in the $\Delta T - Q$ plane for data runs taken at different NSB levels.	74
4.9	Schematic workflow of the ONN cleaning on a triggered event.	75
4.10	Number of reconstructed simulated events with the ONN and AP methods.	76

4.11	Comparison of IRFs for the ONN and afterpulsing cleaning methods.	77
4.12	Counts spectrum and reconstructed flux for a Crab Nebula dataset after the application of the ONN and afterpulsing image cleaning methods.	79
4.13	Validation of the ONN cleaning based on the distribution of the MSCW stereo parameter considering data and simulated events.	82
4.14	Validation of the ONN cleaning based on the distribution of the MSCL stereo parameter considering data and simulated events.	83
4.15	Data/Monte Carlo validation of the ONN cleaning based on the distribution of the stereo parameters for a single telescope.	84
4.16	Counts spectrum and reconstructed flux for a PKS 1424+240 dataset after the application of the ONN and afterpulsing image cleaning methods.	85
4.17	Counts spectrum and reconstructed flux for a PG 1553+113 dataset after the application of the ONN and afterpulsing image cleaning methods.	87
4.18	Counts spectrum and reconstructed flux for a M87 dataset after the application of the ONN and afterpulsing image cleaning methods.	87
4.19	Noise rates and dynamical contours for short-duration runs.	88
4.20	Counts spectrum and reconstructed flux for a RedHV Crab Nebula dataset after the application of the ONN and afterpulsing image cleaning methods.	90
4.21	Validation of the ONN cleaning based on the distribution of the stereo parameter MSCW based on RedHV data and simulated events.	91
4.22	Validation of the ONN cleaning based on the distribution of the stereo parameter MSCWL based on RedHV data and simulated events.	92
4.23	Average of <i>pedvars</i> in pixels composing a telescope image for a run taken under dark conditions and under bright moonlight.	93
4.24	Differential noise rate calculated in time intervals of 180 seconds per telescope in the VERITAS array.	94
4.25	Dynamical cuts calculated based on the IPR curves in time intervals of 180 seconds.	94
4.26	Differential noise rate per pixel for each telescope in the VERITAS array.	95
5.1	Optical images of host galaxies for AT2022dbl, AT2022dsb and AT2023clx.	103
5.2	Significance map, excess events map and significances distributions for AT2022dbl as obtained by VERITAS for the first night of observations.	109
5.3	Multi-wavelength light curve for AT2022dbl.	109
5.4	Significance map, excess events map and significances distributions for AT2022dsb as obtained by VERITAS for the first night of observations.	110
5.5	Multi-wavelength light curve for AT2022dsb.	110
5.6	Significance map, excess events map and significances distributions for AT2023clx as obtained by VERITAS for the first night of observations.	111
5.7	Multi-wavelength light curve for AT2023clx.	111
5.8	Bolometric luminosity estimation for AT2022dbl and AT2022dsb.	114
5.9	Optical depth for AT2022dbl between $R_0 = 5.0 \cdot 10^{14}$ cm and $R_3 = 1.0 \cdot 10^{16}$ cm.	115

5.10	Optical depth for AT2022dsb between $R_0 = 5.0 \cdot 10^{14}$ cm and $R_3 = 1.0 \cdot 10^{16}$ cm.	116
5.11	Time evolution of the optical depth for AT2022dbl assuming different radii.	117
5.12	Time evolution of the optical depth for AT2022dsb assuming different radii.	118
5.13	Broadband gamma-ray flux ULs for AT2022dbl.	119
5.14	Broadband gamma-ray flux ULs for AT2022dsb.	119
5.15	VERITAS flux ULs and Swift-XRT count rates for Swift J1644.	122
6.1	UVF plate and filter transmission compared to Cherenkov emission and solar spectrum at ground level.	126
6.2	Comparison effective areas for the nominal, RedHV and UVF observing modes and Crab Nebula spectrum reconstructed under each mode.	127
6.3	Fit of the Crab Nebula UVF dataset assuming different values of the correction factor.	130
6.4	Comparison of previously published UVF effective area with the one with additional correction factor.	131
6.5	Distribution of GRBs followed up by VERITAS based on triggers by Swift and LAT.	132
6.6	Light curve and significance map of GRB 221009A as obtained by LHAASO-KM2A.	133
6.7	For Night 1: Significance map, excess events map and significances distributions for GRB 221009A as obtained by VERITAS for the first night of observations.	134
6.8	For the entire dataset: Significance map, excess events map and significances distributions for GRB 221009A as obtained by VERITAS for the first night of observations.	135
6.9	VERITAS flux upper limits for GRB 221009A during the first night and total dataset.	136
7.1	Light curve for AT2023ufx.	140
7.2	Significance map, excess events map and significances distributions for AT2023ufx as obtained by VERITAS for the first night of observations.	141
7.3	AT2023ufx gamma ray SED.	142
A.1	Spectrum of source events from the Crab Nebula with boxcuts and BDT cuts.	152
A.2	Stereo parameters for the ONN AP methods for the Crab Nebula dataset.	153
A.3	Counts spectrum and reconstructed flux for the Crab Nebula - $30^\circ - 40^\circ$	154
A.4	Counts spectrum and reconstructed flux for the Crab Nebula - $40^\circ - 50^\circ$	155
A.5	Counts spectrum and reconstructed flux for the Crab Nebula - $50^\circ - 90^\circ$	156
A.6	Counts spectrum and reconstructed flux for the Crab Nebula - 100 MHz - 200 MHz.	157
A.7	Counts spectrum and reconstructed flux for the Crab Nebula - 200 MHz - 300 MHz.	158
A.8	Counts spectrum and reconstructed flux for the Crab Nebula - 300 MHz - 400 MHz.	159
A.9	Counts spectrum and reconstructed flux for the Crab Nebula - 400 MHz - 500 MHz.	160
A.10	Counts spectrum and reconstructed flux for the Crab Nebula - 2012 - 2013.	161
A.11	Counts spectrum and reconstructed flux for the Crab Nebula - 2013 - 2014.	162
A.12	Counts spectrum and reconstructed flux for the Crab Nebula - 2014 - 2015.	163
A.13	Counts spectrum and reconstructed flux for the Crab Nebula - 2015 - 2016.	164
A.14	Counts spectrum and reconstructed flux for the Crab Nebula - 2016 - 2017.	165
A.15	Counts spectrum and reconstructed flux for the Crab Nebula - 2017 - 2018.	166

A.16	Counts spectrum and reconstructed flux for 1ES 1118+424 after the application of the ONN and afterpulsing image cleaning methods.	167
A.17	Counts spectrum and reconstructed flux for Markarian 501 after the application of the ONN and afterpulsing image cleaning methods.	168
A.18	Comparison of IRFs at zenith = 40° and noise level = 75 MHz - 2012 - 2013 season.	169
A.19	Comparison of IRFs at zenith = 40° and noise level = 400 MHz - 2012 - 2013 season.	170
A.20	Comparison of IRFs at zenith = 55° and noise level = 75 MHz - 2012 - 2013 season.	171
A.21	Comparison of IRFs at zenith = 55° and noise level = 200 MHz - 2012 - 2013 season.	172
A.22	Comparison of IRFs at zenith = 55° and noise level = 400 MHz - 2012 - 2013 season.	173
A.23	Comparison of IRFs at zenith = 40° and noise level = 400 MHz - 2017 - 2018 season.	174
A.24	Comparison of IRFs at zenith = 55° and noise level = 200 MHz - 2017 - 2018 season.	175
A.25	Comparison of RedHV IRFs at zenith = 45° and noise level = 450 MHz - 2012 - 2013 season.	176
A.26	Data/Monte Carlo validation of the ONN cleaning based on the distribution of the MSCW stereo parameter - 2017 - 2018.	177
A.27	Data/Monte Carlo validation of the ONN cleaning based on the distribution of the MSCL stereo parameter - 2017 - 2018.	178
A.28	Data/Monte Carlo validation of the afterpulsing cleaning based on the distribution of the MSCW stereo parameter - 2012 - 2013.	179
A.29	Data/Monte Carlo validation of the afterpulsing cleaning based on the distribution of the MSCL stereo parameter - 2012 - 2013.	180
A.30	Data/Monte Carlo RedHV validation of the afterpulsing cleaning based on the distribution of the MSCW stereo parameter - 2012 - 2013.	181
A.31	Data/Monte Carlo RedHV validation of the afterpulsing cleaning based on the distribution of the MSCW stereo parameter - 2012 - 2013.	182
A.32	Data/Monte Carlo validation of the ONN cleaning based on the distribution of the stereo parameters for a single telescope (2).	183
A.33	Data/Monte Carlo validation of the ONN cleaning based on the distribution of the stereo parameters for a single telescope (3).	184
A.34	Data/Monte Carlo validation of the ONN cleaning based on the distribution of the stereo parameters for a single telescope (4).	185
A.35	Data/Monte Carlo validation of the afterpulsing cleaning based on the distribution of the stereo parameters for a single telescope (1).	186
A.36	Data/Monte Carlo validation of the afterpulsing cleaning based on the distribution of the stereo parameters for a single telescope (2).	187
A.37	Data/Monte Carlo validation of the afterpulsing cleaning based on the distribution of the stereo parameters for a single telescope (3).	188
A.38	Data/Monte Carlo validation of the afterpulsing cleaning based on the distribution of the stereo parameters for a single telescope (4).	189
A.39	Data/Monte Carlo RedHV validation of the ONN cleaning based on the distribution of the stereo parameters for a single telescope (1). Image cleaning method: ONN.	190

A.40	Data/Monte Carlo RedHV validation of the ONN cleaning based on the distribution of the stereo parameters for a single telescope (2). Image cleaning method: ONN.	191
A.41	Data/Monte Carlo RedHV validation of the ONN cleaning based on the distribution of the stereo parameters for a single telescope (3). Image cleaning method: ONN.	192
A.42	Data/Monte Carlo RedHV validation of the ONN cleaning based on the distribution of the stereo parameters for a single telescope (4). Image cleaning method: ONN.	193
B.1	Swift-UVOT image of AT2023clx.	196
B.2	Time evolution of the significance for each event dataset.	200
B.3	Interpolated light curves for AT2022dbl and AT2022dsb.	200

List of Tables

3.1	Observing conditions, HV, CFD settings and typical currents for all observing modes of the VERITAS array.	46
5.1	Summary of the trigger criteria for the Target of Opportunity observations of TDEs within the VERITAS Collaboration.	103
5.2	Summary of AT2022dbl, AT2022dsb and AT2023clx.	104
5.3	Summary of VERITAS observations of TDE candidates	107
5.4	Results for the VERITAS analysis of TDEs AT2022dbl, AT2022dsb, and AT2023clx.	108
5.5	Time periods for the derivation of Fermi-LAT upper limits.	108
5.6	Results of the estimation of the bolometric light curve for AT2022dbl and AT2022dsb.	114
5.7	Upper limits on the proton luminosity,	120
5.8	Results for VERITAS analysis of Swift J1644.	122
6.1	Parameters of the power-law fit of the Crab Nebula UVF dataset.	128
6.2	Summary of VERITAS observations of GRB 221009A.	134
6.3	Summary of VERITAS flux ULs for GRB 221009A.	135
7.1	Trigger criteria for FBOTs ToO	139
7.2	List of FBOT alerts.	139
A.1	Results of source analysis with the application of ONN and AP cleaning methods.	149
A.2	Results of test configuration analysis with the application of ONN and AP cleaning methods.	151
B.1	Filters used in the multiwavelength analysis of TDEs.	197
B.2	AT2022dbl - OUV photometry.	204
B.3	AT2022dsb - OUV photometry.	205
B.4	AT2023clx - OUV photometry.	209

Introduction

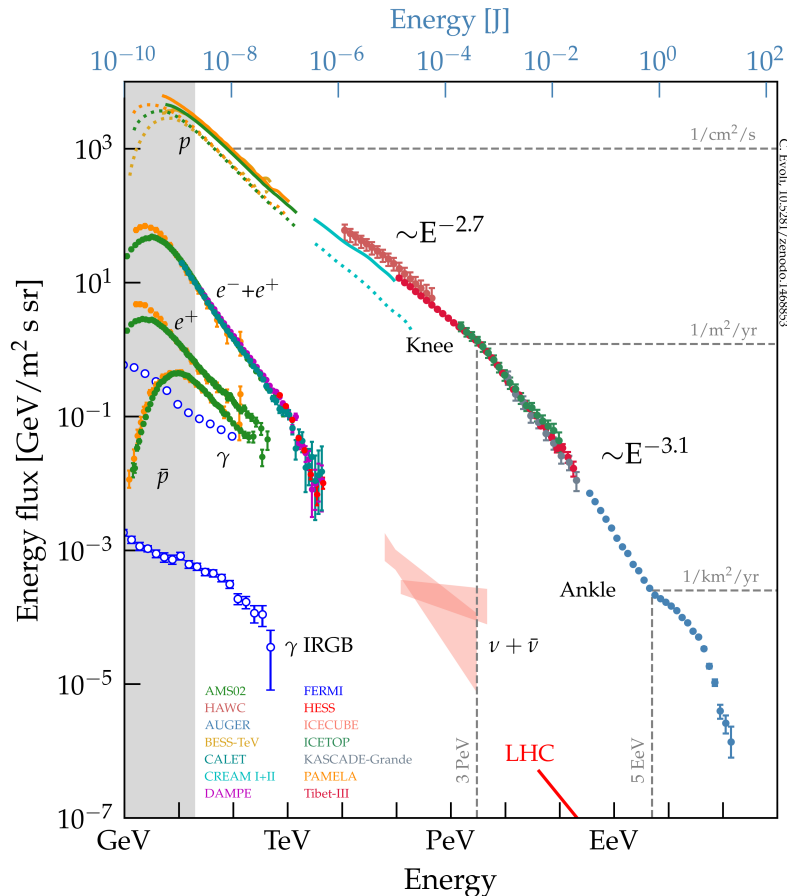


Figure 1.1: The spectrum of cosmic-rays. Figure from: [Evoli, 2020]

In 1912, Victor Franz Hess discovered cosmic rays during a series of balloon flights. Cosmic rays are composed of highly energetic charged particles, with protons being the primary component. In addition, they also consist of smaller amounts of heavier atomic nuclei and leptonic particles, namely electrons and positrons. Unlike photons, these charged particles do not trace back to their point of origin because they are deflected in magnetic fields. As a result, they reach Earth from various directions. The cosmic-ray spectrum up to ~ 3 petaelectronvolt (PeV) steadily decreases as a power-law with an index of 2.7. Particles up to this energy are of galactic origin and are presumed to be accelerated by supernova remnants (SNRs). Above ~ 3 PeV, there is a softening of the spectrum to an index of 3.1, a feature commonly referred to as the *knee* [Gaisser, 2006]. This marks the transition of the spectrum towards heavier nuclei, which gain more energy given the

same acceleration conditions. Another feature (the *ankle*) is observed above $\gtrsim 5 \cdot 10^{18}$ eV, generally marking the transition to cosmic rays of extra-galactic origin - although other interpretations are also explored (see e.g. discussions in [Gabici et al., 2019; Parizot, 2014]).

While the spectrum of cosmic rays has been extensively measured over 10 decades of energy (Figure 1.1), many questions in the field remain open. For example, the origin of ultra-high-energy cosmic rays; $E > 10^{17}$ eV (UHECRs) is still not completely clear. It is known, however, that these particles have extra-galactic origin since they could not be produced and confined within the Milky Way. A cut-off of the spectrum at $\sim 5 \cdot 10^{19}$ eV is observed, e.g., by the Pierre Auger Observatory [Abraham et al., 2008]. Above this energy, the Greisen–Zatsepin–Kuzmin (GZK) [Greisen, 1966; Zatsepin and Kuzmin, 1966] effect becomes significant, as these very energetic protons lose energy when they interact with photons of the cosmic microwave background (CMB) [Dicke et al., 1965; Durrer, 2015; Penzias and Wilson, 1965], producing pions ($p + \gamma_{\text{CMB}} \rightarrow \Delta^+ \rightarrow \pi^0 + p$ or $p + \gamma_{\text{CMB}} \rightarrow n + \pi^+$). The GZK effect imposes a limit not on the maximum energy acquired by protons during acceleration processes, but on the observable energy of protons that travel through cosmological distances ($z \gg 1$) and lose energy through repeated interactions with the CMB.

Although significant progress has been made in the field, the mechanisms responsible for accelerating cosmic rays to PeV energies are still not fully understood. In one of the proposed scenarios, known as diffusive shock acceleration (DSA), particles are accelerated in the fast winds or ejecta released during catastrophic astrophysical events. Another viable mechanism that could take particles to these energies is magnetic reconnection. The question that still remains is where can these processes occur in the Universe. It is believed that some astrophysical sources capable of producing PeVatrons (cosmic rays with PeV energies) could either be galactic, such as pulsars, pulsar wind nebulae (PWNe), such as the Crab Nebula, and the already mentioned SNRs. Otherwise, they could also be extragalactic, such as several types of active galactic nuclei (AGNi) [Aharonian, 2004]. As particles gain relativistic energies, they interact in such manner (e.g., via collisions with other protons or via interactions with photon-fields) that detectable signals of neutrinos and **gamma-ray radiation** (> 100 keV) could be produced.

Over the past few decades, significant advancements in multimessenger surveys have provided a unique perspective on the diverse astrophysical processes occurring in our Universe. Coordinated efforts from multiwavelength and neutrino observatories (e.g., the IceCube experiment [Halzen and Klein, 2010]), as well as cosmic-rays and gravitational wave detectors (e.g., the Laser Interferometer Gravitational-wave Observatory (LIGO) [Cahillane and Mansell, 2022]) have provided a broader picture in the field of time-domain astronomy. In particular, the establishment of ground-based gamma-ray observatories, starting with the Whipple telescope over 50 years ago [Kildea et al., 2007], has led to the identification of hundreds of new astrophysical sources in the very-high-energy; $100 \text{ GeV} < E < 100 \text{ TeV}$ (VHE) regime [Bose et al., 2022]. In addition, the Large Area Telescope of the Fermi Gamma-ray Space Telescope (Fermi-LAT) [Ajello et al., 2021] has played a crucial role in identifying thousands of new gamma-ray sources in the range of ~ 20 MeV to > 300 GeV [Abdollahi et al., 2020]. The confirmation of the VHE emission scenario for several source classes that were previously identified at lower frequencies constitute significant discoveries

of modern astrophysics. Notable examples include the discovery of TeV gamma-ray emission from gamma-ray bursts (GRBs) [H. Abdalla et al., 2021; H. E. Abdalla et al., 2019; Acciari et al., 2019] and the recurrent nova RS Ophiuchi [Acciari et al., 2022; Aharonian et al., 2022] by the third generation of imaging atmospheric Cherenkov telescopes (IACTs). These detections provided a better understanding of the mechanisms of particle acceleration and allowed for further exploration of the non-thermal processes that produce photons of the highest energies.

With the growing sensitivity of wide-Field of View (FoV) high-cadence optical surveys, such as the Zwicky Transient Facility (ZTF) [Bellm et al., 2018], hundreds of new sources are discovered each year in the optical transient sky. Astrophysical transients are distinguished by their variable luminosities while operating in time-scales ranging from seconds to years. They are often associated with extreme astrophysical events, such as the disruption or the collapse of massive stars. This is the case, for example, of tidal disruption events (TDEs) (e.g., review in [Gezari, 2021]) and the extreme instances of bright and rapidly evolving core-collapse supernovae, such as fast blue optical transients (FBOTs) [Lyutikov, 2022]. Although their detection in the optical - and occasionally X-ray bands - has been long established, it is still unknown if they could produce a detectable gamma-ray emission. It is expected, however, that the fast ejecta released during their disruption or outburst could lead to the ideal conditions for shock acceleration as the material interacts with its surrounding environment. In the case of TDEs, the picture is even more complex, with potential jet formation and self-shock interactions of the stellar debris that remains bound to the black hole. This hypothesis has gained even more attention with the first claims of TDE associations with astrophysical neutrinos detected by the IceCube experiment [Reusch et al., 2022; Stein et al., 2021].

It was only until the development of this thesis that dedicated target of opportunity (ToO) follow-up programs were established to systematically observe TDEs and FBOTs with the Very Energetic Radiation Imaging Telescope Array System (VERITAS) [Holder et al., 2006]. The scarce literature on the topic and the minimal VHE dataset available until now highlight the urgency of prioritising the search for VHE components from these transient classes. Nevertheless, one challenge often anticipated for sources exhibiting bright optical and ultraviolet radiation fields (e.g., from disc outflows, accretion flows or shock cooling) within a confined radiation zone is the suppression of a substantial fraction of GeV and TeV photons from internal attenuation by pair-production ($\gamma + \gamma' \rightarrow e^+ + e^-$). For this reason, achieving the highest possible sensitivities with existing instruments is a crucial point in the search for transient gamma ray emission with the current generation of IACTs.

This doctorate project is focused on the search for VHE gamma-ray emission from the transient sky with the VERITAS array. In parallel, I have also contributed to the implementation of novel analysis methods for the VERITAS Collaboration. This thesis is organised as follows: In Chapter 2 I introduce the field of VHE gamma-ray astronomy, including fundamentals of ground-based gamma-ray detection. I also outline the most recent results from multimessenger observations of TDEs, GRBs, and FBOTs. In Chapter 3, I describe the analysis chain and performance of VERITAS. Next, I introduce in Chapter 4 the application of the Optimised Next Neighbour technique [Shayduk, 2013] for cleaning images from extensive air showers (EAS) collected by

VERITAS. During the recording of an event, also known as an array trigger, IACTs collect not only the Cherenkov light triggered by secondary particles created in the showers but also an undesirable amount of electronic noise and photons from the Night sky background (NSB). Image cleaning techniques are applied to remove camera pixels that are exclusively contaminated with this noise. Traditionally, cleaning methods have required the application of high charge thresholds to effectively eliminate the noise-induced pixels. However, this approach often leads to the suppression of gamma-ray events in the GeV range. With this novel technique, charge cuts can be lowered by implementing temporal coincidence thresholds among neighbouring pixels. In this way, the suppression of low-energy events is prevented. In addition, cleaning thresholds can also be tailored for each observation by calculating noise rates derived from pedestal events. Chapter 4 details the development, performance, and validation of the Optimised Next Neighbor (ONN) image cleaning technique through a comprehensive dataset of test sources and Monte Carlo (MC) simulations. In subsequent chapters, the ONN image cleaning is applied to the analysis chain of transients in order to provide better constraints in the GeV range.

In Chapter 5, I describe the new ToO proposal for the observation of TDEs with the VERITAS array, for which I have been the principal investigator since the observing season of 2021 - 2022. I present results on the follow-up of three TDEs and apply a simplified model to estimate the gamma-ray attenuation in source. I find that when the observed optical and ultra-violet photon fields act as targets for two-photon annihilation, virtually all gamma rays would be suppressed above the GeV range. In Chapter 6, I introduce the additional throughput correction for ultra violet filter (UVF) observations with VERITAS. Due to the high level of moon illumination during the outburst of GRB221009A, the first hours of VERITAS observations on the GRB were taken with a protective camera filter. Flux upper limits on GRB221009A are presented based on the corrected analysis. In Chapter 7, the new ToO proposal for the follow-up of FBOTs with VERITAS is presented. I discuss the trigger criteria and candidates that were discarded because they do not satisfy the minimum brightness and light curve features necessary for a trigger. Within the scope of the proposal, AT2023ufx has triggered observations. Flux ULs are presented for this event. Finally, conclusions of this thesis and future prospects are presented in Chapter 8.

Very High Energy Gamma Rays

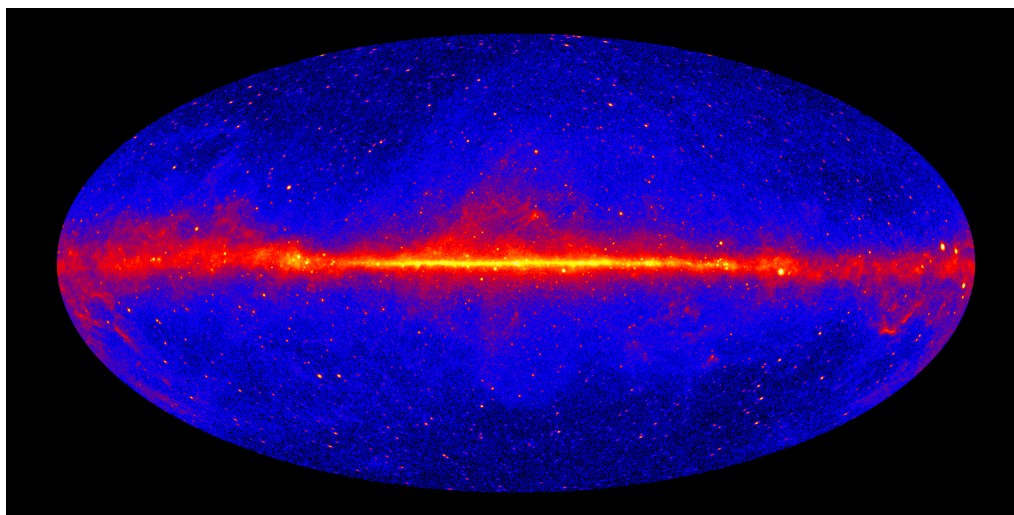


Figure 2.1: The sky map of the diffuse gamma-ray emission constructed with 12 years of observations from Fermi-LAT. The map features gamma-ray events with energies > 1 GeV. The Milky Way appears brighter due to the diffuse gamma-ray emission produced in interactions of cosmic rays with the interstellar medium. Image credit: NASA/EGRET Team and NASA/DOE/Fermi-LAT Collaboration.

Much of the radiation incident on Earth is thermal emission originating from astrophysical sources such as stars and galaxies. Under extreme conditions, these photons can extend into the keV range. Although thermal processes can often describe the emission from various astrophysical sources, only extreme relativistic mechanisms can account for the production of electromagnetic radiation above ~ 100 keV. Because gamma-ray photons hardly ever penetrate the Earth's atmosphere without interacting with atomic nuclei, a wide set of techniques must be employed for their detection. Space-borne observatories, such as the Energetic Gamma Ray Experiment Telescope (EGRET) [Thompson, 2008] and the Fermi-LAT, specifically target the detection of gamma rays up to a few hundred GeV. These instruments are equipped with calorimeters that measure the particle's energy as it induces an electromagnetic cascade through their scintillator material [Schönfelder, 2004]. The Fermi-LAT observatory has been crucial for the development of gamma-ray astronomy in the past decade. Due to its coverage of $\sim 20\%$ of the sky at any given time and since it scans the entire sky every three hours, any astrophysical object detected in lower wavebands can be monitored at high cadence. The gamma-ray sky as measured by the Fermi-LAT in over 10 years of observations is shown in Figure 2.1.

As energy increases, detecting these gamma rays with space-based instruments becomes impractical due to their limited size and collection area, which is in the order of 1 m^2 [Ajello et al., 2021]. To detect the flux of VHE gamma rays, ground-based observatories with significantly larger areas, in the order of $100 - 1000 \text{ m}^2$ [Funk, 2015], are employed. On the ground, gamma rays are detected indirectly, with telescopes measuring the Cherenkov light triggered by interactions of secondary particles from EAS with the atmosphere [Holder, 2015; Lemoine-Goumard, 2015].

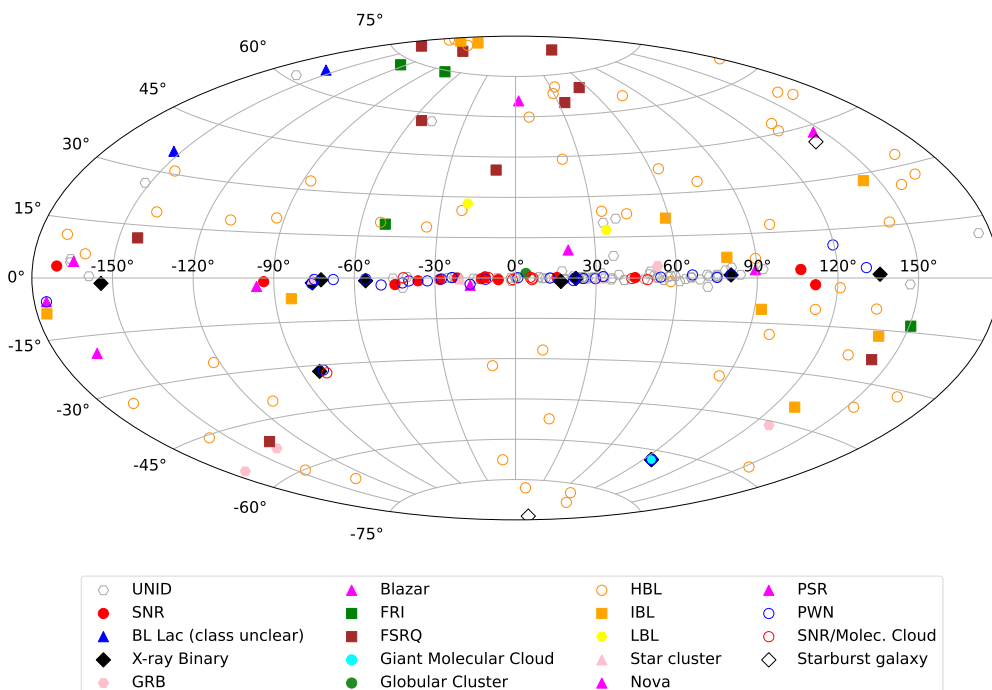


Figure 2.2: The sky-map of VHE sources according to the TeV Catalog (TeVCat)¹: SNRs, BL Lacs, X-ray binaries, GRBs, Blazars, Fanaroff and Riley radio galaxies I (FRI), Flat Spectrum Radio Quasar (FSQR), giant molecular clouds, globular clusters, High Frequency BL Lacs (HBLs), Intermediate Frequency BL Lacs (IBL), Low Frequency BL Lacs (LFB), star clusters, novae, pulsating sources of radio (PSR), pulsar wind nebulae (PWNe), starburst galaxies and unidentified sources (UNID).

The field of ground-based gamma-ray astronomy has undergone substantial advances in the past decades, particularly with the introduction of the imaging atmospheric Cherenkov technique [Hillas, 2013]. The development of stereoscopic observations by the High-Energy-Gamma-Ray Astronomy (HEGRA) array [The HEGRA Collaboration, 1997] and the implementation of fine-grained cameras by the Cherenkov Array at Themis (CAT) [Barrau et al., 1998] have contributed to more than a tenfold increase in sensitivity. Advanced analysis techniques that were introduced

¹<http://tevcat.uchicago.edu/>

by the third generation of Cherenkov telescopes in the 2000s have improved the cosmic-ray background rejection and enhanced angular and energy resolution. These developments marked a major evolution in the field since the discovery of the first VHE gamma-ray source by the Whipple telescope. The third generation of IACTs comprises the High Energy Stereoscopic System (H.E.S.S.) in Namibia [Hinton, 2004], the Major Atmospheric Gamma Imaging Cherenkov Telescopes (MAGIC) on La Palma [Garczarczyk, 2011], and VERITAS in Arizona, USA [Holder et al., 2006]. These facilities are equipped with large reflective mirrors and high quantum efficiency cameras, which significantly boost their sensitivity (ranging from a few tens of GeV to a few tens of TeV) to VHE gamma rays.

The identification of new non-thermal source classes remains a challenging task that requires further exploration. Figure 2.2 presents the 275 VHE sources reported by the TeV Catalog until March of 2024. Several sites within the Milky Way and outside of it have been identified as VHE emitters. Additionally, several other classes of astrophysical objects are presumed to produce VHE gamma rays, but no confirmed detection has been made yet.

In this chapter, I discuss different mechanisms of gamma-ray production and absorption in Sections 2.1 and 2.2, the imaging atmospheric Cherenkov technique in Section 2.4 and the current status of multimessenger searches of selected transient sources in Section 2.5.

2.1 Mechanisms of production and absorption of gamma rays

A blackbody spectrum is characterised by a distinct peak that reflects the system’s temperature. For astrophysical objects operating at exceedingly high temperatures, $> O(10^6)$ K, such as accretion disks [Liu and Qiao, 2022], thermal emission can extend into the **X-ray spectrum (100 eV < E < 100 keV)**. However, these energies are substantially lower than those that characterise high-energy; $100 \text{ MeV} < E < 100 \text{ GeV}$ (HE) and VHE gamma rays, which are exclusively produced by non-thermal processes involving distinct interactions between radiation fields and matter ².

Non-thermal mechanisms can be categorised into leptonic, such as Bremsstrahlung emission, synchrotron radiation and Inverse Compton (IC) scattering, and hadronic processes, which involve interactions with relativistic hadrons. A review of the production and absorption mechanisms of gamma rays discussed in this Chapter can be found in Refs. [Aharonian, 2004] and [Longair, 2011]. Below, I focus on summarising each of these processes.

Synchrotron emission: charged particles (Ze) moving relative to magnetic fields (\mathbf{B}) emit radiation due to the acceleration from magnetic forces $-Ze(\mathbf{v} \times \mathbf{B})$. This motion affects the component of the particle’s velocity that is perpendicular to the magnetic field, resulting in the subsequent emission of synchrotron radiation. It can be shown that the energy loss rate of an electron by synchrotron radiation is given by the following equation in the relativistic limit ($\beta \rightarrow 1$) [Longair, 2011]:

²Some particular physical processes beyond the Standard Model, such as weakly interacting massive particle (WIMP) annihilation, are also presumed to produce a gamma-ray signal that could be probed by IACTs [Funk, 2014].

$$-\left(\frac{dE}{dt}\right)_{\text{syn}} = \frac{4}{3}\sigma_T c U_B \beta^2 \gamma^2, \quad (2.1)$$

where σ_T represents the Thomson scattering cross-section, U_B the energy density of the magnetic field and $\gamma = (1-\beta^2)^{-1/2}$ the electron's Lorentz factor. This equation is obtained by averaging over an isotropic distribution of the electron's pitch angle, ρ , which is subtended by the electron's velocity vector and by the direction of the magnetic field. In the ultra-relativistic scenario and considering the laboratory frame, the synchrotron emission assumes the form of a cone with an opening angle of $\theta = 1/\gamma$ and is strongly beamed forward. For an electron with 1 TeV, an opening angle of $\theta \sim 0.1$ arcsec is expected. Because the synchrotron radiation power is inversely proportional to the fourth power of the mass of the particle in question, this process is more significant for electrons in comparison to heavier charged particles – for protons, the radiation power would be lower by a factor $(m_e/m_p)^4 \sim 10^{-13}$.

From about the critical emission frequency onward, given below in the limit $\beta \rightarrow 1$ [Longair, 2011]:

$$\nu_c = \frac{3}{2}\gamma^2 \nu_g \sin\rho, \quad (2.2)$$

the spectrum starts to rapidly decay. For a 1 GeV electron travelling in a magnetic field in the order of 10^{-6} G, the peak emission ($\sim 0.29\nu_c$) happens in the radio regime: this is the typical scenario of the Milky Way. Higher magnetic field strengths and a higher particle energy will shift this peak to higher frequencies, e.g., to the gamma-ray regime near the surface of neutron stars [Diehl, 2001].

The synchrotron cooling time scale for relativistic electrons is given by:

$$t_{\text{cool}} = \frac{E_e}{-dE_e/dt} = \frac{3m_e c^2}{4\sigma_T c U_B \beta^2 \gamma}. \quad (2.3)$$

For an electron with a few tens of TeV gyrating in a magnetic field of strength 10^{-4} G (as is estimated for the Crab Nebula [The LHAASO Collaboration, 2021]), $t_{\text{cool}} \sim 10$ years.

For an electron population following continuous injection with a power-law distribution, $dN/dE \propto E^{-\alpha}$, the synchrotron spectrum follows a power-law with index $(\alpha + 1)/2$ [Funk, 2015]. Due to energy losses, the initial electron distribution is modified so that the steady state spectrum has a break and a new index of $(\alpha + 1)$ [Funk, 2015]. This break happens at an energy corresponding to where the cooling time scales become comparable to the age of the system.

Bremsstrahlung: gamma rays can be produced due to the change in acceleration of charged particles deflected by the electric fields of atomic nuclei. The total intensity emitted in relativistic Bremsstrahlung is given by [Bethe and Heitler, 1934]:

$$-\left(\frac{dE}{dt}\right)_{\text{brems}} \propto \frac{Z(Z+1.3)e^6 n E_e}{m_e^2} \cdot \left[\ln\left(\frac{183}{Z^{1/3}}\right) + \frac{1}{8} \right]. \quad (2.4)$$

In the above equation, Z is the atomic number of the nucleus, e the electron charge and n the density of nuclei. Because dE/dt is proportional to the electron energy, the radiation loss will be

exponential. The radiation length X_0 at which the electron loses a fraction of $(1 - 1/e)$ of its energy is defined by the total stopping power $-(dE/d\zeta) = E/\zeta_0$, with $\zeta_0 = \rho X_0$ representing the mass per distance squared that is traversed by the particle [Longair, 2011]. In the air, the typical value of the Bremsstrahlung's radiation length is equivalent to $X_0 = 280$ m ($\zeta_0 = 365$ km m⁻²) [Longair, 2011]. The probability per unit frequency of the emission of a photon via bremsstrahlung emission drops sharply to zero above the electron's initial kinetic energy, corresponding to the frequency at which this energy is completely transferred to one photon.

Inverse Compton (IC) scattering: When relativistic electrons or positrons up-scatter lower energy ambient photons, gamma rays are produced. This process occurs, for example, when relativistic electrons that compose cosmic rays scatter the light of the CMB.

In the Thomson regime, i.e., when the photon energy in the electron's frame of reference is lower than the rest energy of the electron ($h\nu \ll m_e c^2$), the energy-loss via IC is given by

$$-\left(\frac{dE}{dt}\right)_{IC} = \frac{4}{3}\sigma_T c \rho_{\text{rad}} \beta^2 \gamma^2, \quad (2.5)$$

where ρ_{rad} is the energy density of the radiation. Conversely, the Klein–Nishina (KN) regime applies when the electron is travelling at ultra-relativistic energies ($h\nu \gtrsim 0.5$ MeV). In this regime, the electron scattering cross-section reduces to the following expression (KN formula, right side of Figure 2.3) [Aharonian, 2004]:

$$\sigma_{\text{KN}} = \frac{3\sigma_T}{8} \frac{1}{x} (\ln 2x + 0.5), \quad (2.6)$$

with $x = h\nu/m_e c^2$, where ν represents the frequency of the incident photon. The main effect observed in the KN regime is the reduction of the cross-section with increasing photon energy (at $x \gg 1$ the cross-section is \ll few percent of σ_T). Given the similarity of equations 2.5 and 2.3, one can expect a similar shape for the emission spectrum of synchrotron and IC scattering, but that this shape will be characteristic in different energies. For an electron population following continuous injection with a power-law distribution $dN/dE \propto E^{-\alpha}$, the IC spectrum yields a slope of index $(\alpha + 1)/2$ in the Thomson regime. In the KN regime, this results in a steeper index of $(\alpha + 1)$, after the break energy.

In the Synchrotron self-Compton (SSC) scenario, photons produced via the synchrotron emission of electrons in a magnetised medium can be up-scattered to higher energies by the same electron population.

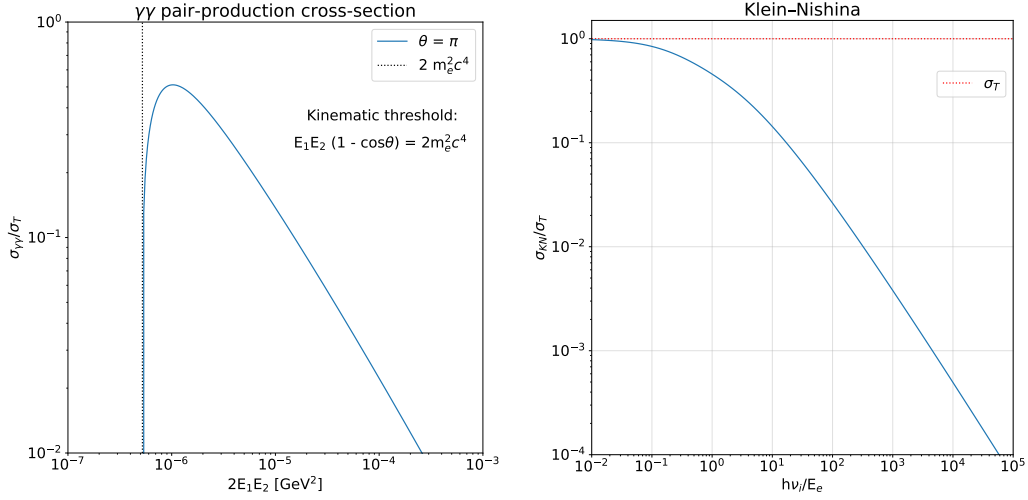
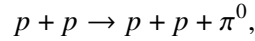
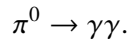


Figure 2.3: **Left:** Cross-section of two-photon absorption. The plot assumes a head-on collision ($\theta = \pi$). **Right:** Klein–Nishina compared to Thomson cross-section as a function of the incident photon energy by the electron rest energy.

Hadronic processes: secondary neutral and charged pions (π^0 , π^\pm) are created when relativistic cosmic rays, composed mainly of protons, collide with ambient matter:

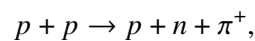


Neutral pions have a mean lifetime of $\sim 8.4 \times 10^{-17}$ s and when they are produced in these collisions, they decay almost immediately into two gamma-ray photons (with a branching ratio of 98.8%):



The π^0 decay is the main channel for the conversion of the kinetic energy of protons into high energy photons. In order for the production of π^0 to take place (given its mass $m_\pi = 134.97$ MeV c^{-2}), the parent protons energy should exceed the threshold of $2m_\pi c^2(1 + m_\pi/4m_p) \approx 280$ MeV [Aharonian, 2004]. Independent of the energy of the neutral pion, and consequently from the parent protons, the decay spectrum of the π^0 shows a maximum at $(m_\pi c^2)/2 \approx 67.5$ MeV. The decay spectrum of monoenergetic neutral pions (with energy E_π and velocity v_π) is constant ($= c/(v_\pi E_\pi)$) in the energy range between $0.5E_\pi(1 - v_\pi/c)$ and $0.5E_\pi(1 + v_\pi/c)$ [Aharonian, 2004; Stecker, 1971]. Therefore, the final decay spectrum is given by the superposition of a series of constant spectra for which the point $m_\pi c^2/2$ is always present.

At high energies, the production of all the three types of pions (π^0 , π^\pm) happen with comparable probabilities. The charged pions decay (via muons) into electrons and positrons, also producing a neutrino signature:



$$p + p \rightarrow p + p + \pi^+ + \pi^-.$$

$$\pi^- \rightarrow \mu^- + \bar{\nu}_\mu \quad ; \quad \mu^- \rightarrow e^- + \bar{\nu}_e + \nu_\mu$$

$$\pi^+ \rightarrow \mu^+ + \nu_\mu \quad ; \quad \mu^+ \rightarrow e^+ + \nu_e + \bar{\nu}_\mu.$$

The energy distribution of the produced photons closely follows the spectrum of the parent protons above 1 GeV. Therefore, detecting VHE gamma rays resulting from hadronic processes provides direct information about the acceleration spectrum of the progenitor particles. In a multimessenger approach, hadronic processes can be investigated by detecting both neutrinos and gamma-ray signals from a given source, e.g. the case of the blazar TXS 0506+056 [Gao et al., 2018]. However, neutrino signals can be obscured in environments with very dense radiation fields, as charged pions may interact with nucleons or photons before decaying. Another mechanisms of VHE gamma-ray production happens via photo-meson production involving photohadronic interactions of relativistic protons with photons in the optical, ultra-violet (UV) and X-ray ranges: $p + \gamma \rightarrow p + \pi^0$. In these cases, neutrinos should also be expected via the charged pion channel: $p + \gamma \rightarrow n + \pi^+$. Knowing that this interaction has a inelasticity of ~ 0.2 [Aharonian, 2004] (the fraction of proton energy transferred to secondary particles), the collision of protons of energy E with ambient low energy photons results in gamma rays of mean energy $\sim 0.1E$ and neutrinos of mean energy $\sim 0.05E$ [Kelner and Aharonian, 2008].

2.2 Absorption mechanisms of gamma rays

Absorption mechanisms of gamma rays prevent their escape from compact astrophysical sources or from objects containing bright radiation fields. Photon-photon ($\gamma\gamma$) pair production ($\gamma\gamma \rightarrow e^+e^-$) is one of the most relevant processes of gamma-ray absorption due to the large cross-sections involved in these interactions. Since this process is just the inverse of pair annihilation, the cross-section (left side of Figure 2.3) can be approximated to the following analytical form [Aharonian, 2004]:

$$\sigma_{\gamma\gamma}(\beta) = \frac{3\sigma_T}{16}(1 - \beta^2) \left[2\beta(\beta^2 - 2) + (3 - \beta^4) \ln \left(\frac{1 + \beta}{1 - \beta} \right) \right], \quad (2.7)$$

where β is the ratio of the electron velocity by the speed of light and σ_T is the Thompson cross-section. This process has a strict kinematic threshold, defined by the collision angle θ as follows:

$$E_1 E_2 (1 - \cos\theta) = 2m_e^2 c^4, \quad (2.8)$$

where E_1 and E_2 represent the energy of the gamma ray and of the target photon, respectively. gamma rays with energies in the TeV range interact most efficiently with infrared photons.

The optical depth characterizes the level of gamma ray absorption in an isotropically emitting source with radius R [Aharonian, 2004]:

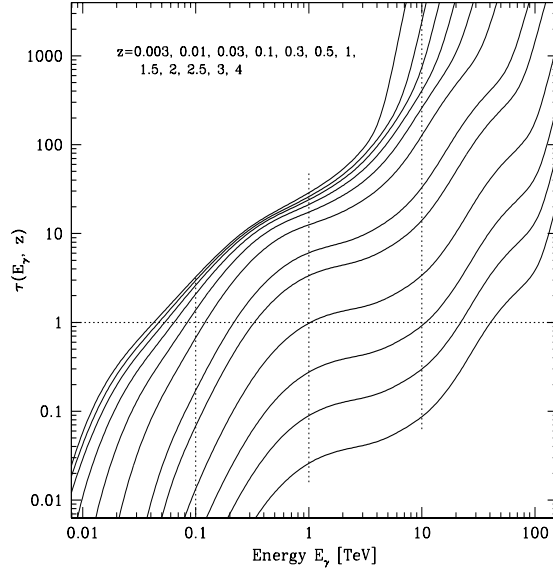


Figure 2.4: The optical depth for gamma-ray attenuation with the EBL. Redshift values increase from bottom to top. Figure from: [Franceschini and Rodighiero, 2017].

$$\tau_{\gamma\gamma}(E_1) = \int_0^R dr \int_{\frac{1}{4\pi}} d\Omega (1 - \cos \theta) \int_{\frac{2m_e^2 c^4}{E_1(1-\cos \theta)}}^{\infty} dE_2 n_{\text{ph}}(\epsilon_2, \Omega, r) \sigma_{\gamma\gamma}(E_1, E_2, \cos \theta), \quad (2.9)$$

where n_γ represents the spatial (r, Ω) and energy distribution of the target photon field, which could be, for example, a blackbody spectrum. The differential number density distribution, n_γ (in units of $\text{eV}^{-1}\text{cm}^{-3}$), of a blackbody with radius R and temperature T is described as follows:

$$n_\gamma = \frac{8\pi}{h^3 c^3} \cdot \frac{E^2}{e^{\frac{E}{k_B T}} - 1}. \quad (2.10)$$

Here, h and k_B are the Planck's and Boltzmann's constants, respectively. The thermal luminosity of the blackbody radiation is proportional to the integral of the photon energy density:

$$L = 4\pi R^2 c \int E_\gamma n_\gamma dE_\gamma. \quad (2.11)$$

The process of $\gamma\gamma$ pair-production becomes particularly important when observing sources at large cosmological distances ($z > 1$, Figure 2.4), as their flux is severely suppressed by interactions with the extragalactic background light (EBL) [Acciari et al., 2019; Cooray, 2016; Franceschini and Rodighiero, 2017]. The EBL is a diffuse radiation field that permeates the Universe. It covers nearly the entire range of the electromagnetic spectrum, with the exception of the microwave band, which is mainly dominated by the CMB. The EBL has been extensively studied and measured through observations of the Fermi-LAT observatory and other gamma-ray instruments [Acciari et al., 2019].

Gamma-ray absorption can also occur through interactions with hadronic particles. However, these interactions are sub-dominant in environments where radiation fields are much denser than

ambient matter. In addition, the cross-section of the hadronic absorption processes are very small compared to $\gamma\gamma$ pair production. For instance, interactions of gamma rays with ambient photons have a cross-section that exceeds by three orders of magnitude the one expected for photo-meson production [Aharonian, 2004]. The hadronic mechanisms of gamma-ray absorption can be summarised in the following interactions:

- **IC scattering of protons:** $p + \gamma \rightarrow p + \gamma$,
- **Electron-positron pair production:** $p + \gamma \rightarrow p + e^+ + e^-$,
- **Photodisintegration of nuclei:** $A + \gamma \rightarrow A + kN$,
- **Photo-meson production:** $p + \gamma \rightarrow p + \pi^0$ or $p + \gamma \rightarrow n + \pi^+$.

2.3 Acceleration mechanisms of cosmic rays

As discussed in the last section, interactions among relativistic particles can lead to the production of a VHE gamma-ray signal. In this section, I summarise the mechanisms that can accelerate particles to relativistic energies. One of these mechanisms, which can be highly effective under certain conditions, is through shock interactions [Bell, 1978; R. D. Blandford and Ostriker, 1978; Fermi, 1949]. The second order Fermi acceleration mechanism, proposed in 1949 [Fermi, 1949], provides a stochastic model for the acceleration of particles via collisions with interstellar clouds. In this scenario, charged particles reflect off magnetic mirrors caused by irregularities in the galactic magnetic field. These mirrors are thought to move randomly in different directions, with an average typical velocity U . The energy of the reflected particles increases during head-on collisions but decreases during overtaking ones. After multiple reflections, the average energy gain per unit time is given by $8U^2E/lv$, where E is the particle's initial energy, l is the mean free path and v is the particle's velocity. For interstellar clouds within the Milky Way, U is in the order of $U/c \ll 10^{-4}$. Given that l is comparable to the scale of magnetic inhomogeneities in the interstellar medium (~ 0.1 parsec [Aharonian, 2004]) the time scales of collisions would be in the order of $\sim 10^7$ seconds. As a result, the frequency of collisions would be of only a few per year, making this mechanism extremely slow and inefficient. This process is referred to as the second order Fermi acceleration due to its the dependence of the acquired energy on U^2 .

2.3.1 The diffusive shock acceleration mechanism

The first order Fermi acceleration, also known as the diffusive shock acceleration process, provides a higher acceleration efficiency by considering either particles moving between two mutually approaching clouds or via supersonic shocks propagating through a diffuse medium. This thesis focuses on the acceleration processes induced by shock waves that originate from the explosion or ejection from astrophysical sources.

Shock waves are formed when a perturbation of pressure and matter density travels in a medium at a velocity higher than the speed of sound and also greater than the Alfvén speed of the medium.

As the shock waves propagate through a plasma, they act as transition layers, altering the state of the medium. Due to the perturbed state, magnetic fields in the regions behind and ahead of the shock are non-uniform and contain variations which lead to the particle being scattered back and forth multiple times across the shock.

In the rest frame of the shock front, the "undisturbed" region (Figure 2.5) of density ρ_1 , known as the upstream medium, approaches the discontinuity at a speed u_1 . When the gas passes through the shock front, it travels away from the discontinuity at a speed u_2 . This region behind the shock front is known as the downstream region.

Regarding the passage of gas between the upstream (velocity u_1 , temperature T_1 , density ρ_1 and pressure P_1) and downstream (index 2) regions, the conservation laws of energy, momentum and mass fluxes must be valid. First, the mass per unit time and area is conserved in the passage of the gas. Therefore,

$$\rho_2 u_2 = \rho_1 u_1. \quad (2.12)$$

Second, the energy flux should also be conserved (considering the case where the passage of material happens perpendicularly to the shock plane):

$$\rho_1 u_1 \left(\frac{1}{2} u_1^2 + \epsilon_1 + \frac{P_1}{\rho_1} \right) = \rho_1 u_2 \left(\frac{1}{2} u_2^2 + \epsilon_2 + \frac{P_2}{\rho_2} \right). \quad (2.13)$$

In the equation above, ϵ_i represents the internal energy per unit mass of each medium.

Lastly, the momentum flux through the plane given by the shock wave should also be continuous:

$$P_2 + \rho_2 u_2^2 = P_1 + \rho_1 u_1^2. \quad (2.14)$$

For simplicity, studies of DSA are often done for perfect gases with a specific heat capacity, γ , and a specific volume, V . In this particular scenario, the following comparisons can be derived for the upstream and downstream regions in the limit of very strong shocks:

$$\frac{p_2}{p_1} = \frac{2\gamma M_1^2}{(\gamma + 1)}, \quad \frac{\rho_2}{\rho_1} = \frac{(\gamma + 1)}{(\gamma - 1)}, \quad \frac{T_2}{T_1} = \frac{2\gamma(\gamma - 1)M_1^2}{(\gamma + 1)^2}. \quad (2.15)$$

In the equations above, M_1 represents the Mach number of the shock wave, defined as $M_1 = u_1/c_1$, where c_1 is the velocity of sound in the undisturbed medium. Strong shocks are those with $M_1 \gg 1$.

In the limit of $M_1 \gg 1$, the pressure and temperature in the downstream region become arbitrarily large, while particular relations are attained for the density and velocity ratios. In the case of a mono-atomic gas ($\gamma = 5/3$), $\rho_1/\rho_2 = u_2/u_1 = 1/4$. When the undisturbed gas crosses the shock front, it gets heated and accelerated. Eventually, the thin layer of shocked gas will cool down. These processes happen in the order of a few mean free paths of the gas [Longair, 2011].

To understand the energy gain of particles via shock interactions, we must look at the change of reference frames between the upstream and downstream regions. Viewing from the upstream frame of reference, the shock front is approaching at a velocity u_1 while the downstream is also

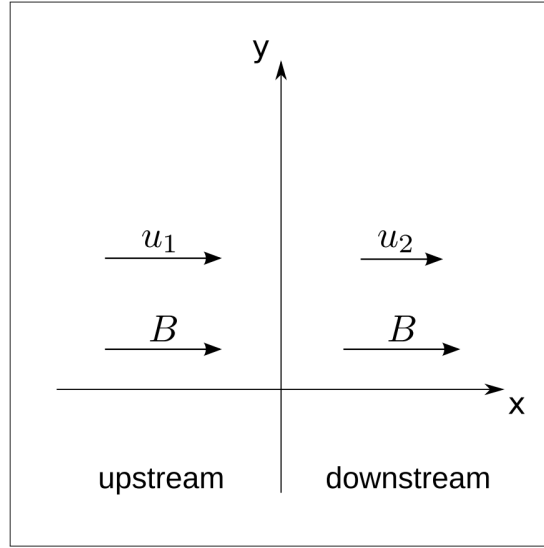


Figure 2.5: Schematic view of a shock wave in its reference frame. In this particular representation, the plasma flow and magnetic fields are perpendicular to the shock plane. Figure from: [Wilhelm, 2021].

approaching, but at a velocity $u_1 - u_2$. In the frame where the downstream region is static, the shock front is departing at a velocity u_1 while the upstream is approaching at a velocity $u_2 - u_1$. A particle in both reference frames encounters an approaching magnetised cloud. When the particles cross the shock front, they can be quickly scattered ($p'_x \rightarrow -p'_x$) back into the primary region. It can be shown that for a round trip in an ideal gas, the particle gains an amount of energy equivalent to $\Delta E/E \sim u_1/c$, with half being acquired in each crossing [Longair, 2011]. Charged particles continue to deflect off these magnetic irregularities, crossing back and forth through the shock front and suffering a slight acceleration in every passage. Unlike the second order process, the time scales of acceleration are much shorter, and depending on the shock wave velocity, the particles can gain energy equivalent to $\sim \Delta E \sim 10^{-3} - 10^{-2} E$ every time they are scattered. This process continues until the particle escapes the shock region.

2.3.1.1 Maximum particle energy gained via DSA

After k crossings, the particle will have an energy equivalent to

$$E_k = (1 + \zeta)^k E, \quad \zeta = \frac{u}{c}. \quad (2.16)$$

If particles have a probability, P_{esc} , to escape the accelerating region, after k scatterings the number of particles remaining is

$$N = N_0 \cdot P_{\text{esc}}^k. \quad (2.17)$$

We can then find that the spectrum of particles accelerated via the diffusive shock acceleration mechanism follows a power-law function:

$$NdE \propto E^{-1+\frac{\ln(P_{\text{esc}})}{\ln(1+\zeta)}} dE. \quad (2.18)$$

An index of E^{-2} is found considering the argumentation presented in Ref. [Longair, 2011]. Although the DSA describes a physical acceleration process that could explain the power-law emission observed for several sources, it does not directly reproduce the measured cosmic-ray spectrum index (see Chapter 1). This difference arises from a series of complex factors that interplay in the acceleration process, such as different acceleration mechanisms, the energy-dependent transport and diffusion of cosmic rays and interactions in the interstellar medium (ISM).

By studying the back and forth diffusion of particles across the shock wave, Ref. [Lagage and Cesarsky, 1983] finds the following limit for the maximum energy of the accelerated particles:

$$E_{\text{max}}(t_{\text{acc}}) \propto (Ze)u^2 B t_{\text{acc}}, \quad (2.19)$$

where B is the magnetic field, Ze is the electric charge of the particle and t_{diff} represents the diffusion time. Considering $u = 10^4$ km/s, $B = 100$ μ G and a free expansion time of 1000 years, which is a typical value for SNRs, a maximum proton energy of about 1 PeV is achieved.

The relativistic particles participate in inelastic collisions with ambient ions after they escape the upstream region, or when they are advected into the downstream cooling shell. In these interactions, charged and neutral pions and the corresponding gamma rays and neutrinos are produced. Given a maximum proton energy of 10^{16} eV, gamma rays up to the PeV range could plausibly be produced. In principle, the accelerated particles could also escape the shock region before pion production. For shock velocities greater than 10^3 km/s, the bulk of the shock kinetic power is emitted in the X-ray range and can be reprocessed into optical light due to the high opacity of the external medium [Fang et al., 2020].

The physical mechanisms discussed here should be adapted for the case of relativistic shocks. In such scenario, it can be shown that in the first crossing, the particles gain an energy proportional to the shock's Lorentz factor squared ($\Gamma_{\text{sh}} \sim 10^2 - 10^3$), while further crossings are not so efficient in terms of energy gain [Achterberg et al., 2001; Gallant and Achterberg, 1999]. The resulting energy spectrum for particles accelerated in relativistic shocks also follows a power-law function, but with a steeper index of 2.2 - 2.3. In addition, non-linear effects introduced by the accelerated particles greatly enhance the level of turbulence of the system and, therefore, also increase the maximum acceleration energy [Bell, 1987]. These effects become significant when the pressure of accelerated particles approaches that of the shocked fluid, influencing the turbulence level. The quantification of this effect is understood via numerical simulations [Blasi, 2002].

On top of DSA, magnetic reconnection has also been suggested as a viable acceleration mechanism in a diverse range of astrophysical phenomena, e.g., the solar flares (review in [Biskamp, 1996]). Reconnection happens due to the shear of magnetic field lines oppositely directed, e.g. due to highly conducting plasma with opposite magnetic flux regions brought into contact. These lines break and rejoin, allowing the conversion of electromagnetic energy into kinetic, thermal and particle acceleration energy. For instance, in the case of solar flares, when these field lines encounter, a flow of particles is propelled away and towards the Sun.

2.4 The Imaging atmospheric Cherenkov technique

IACTs detect the Cherenkov light produced when the atmosphere that has been polarised by charged particles returns to its ground state. These charged particles, mainly electrons and positrons, are produced in EAS triggered by gamma rays and cosmic rays arriving at Earth. The typical conical shape of the emission is produced as charged particles travel through a dielectric at speeds greater than the velocity of light in that medium [Cherenkov, 1934]. The Cherenkov photons are characterised by a wavelength in the range of about 200 nm up to 700 nm, with a peak emission on the ground at roughly 300 - 350 nm [Aharonian, 2004].

As seen in Figures 2.6 and 2.7, particle cascades initiated by gamma rays differ significantly from those triggered by protons or nuclei from cosmic rays [Hillas, 1996]. When the primary particle is a gamma ray, it first interacts with the atmosphere via pair production, generating an electron/positron pair after traversing on average an interaction length of $\chi_{\text{pair}} \sim 47 \text{ g cm}^{-2}$ for photons above $\sim 1 \text{ GeV}$ [Grieder, 2010]. These secondary particles further travel in the atmosphere and undergo the process of Bremsstrahlung emission in the presence of the Coulomb fields from atmospheric atomic nuclei, with the following relation for the Bremsstrahlung interaction length: $\chi_r = 7\chi_{\text{pair}}/9$. The electromagnetic cascades develop until a critical electron energy of $\sim 84 \text{ MeV}$ is achieved [Grieder, 2010]. Above this energy, ionisation losses dominate over bremsstrahlung and the shower reaches the point of peak particle density. The characteristic grammage at which this happens is referred to as the depth of maximum development, χ_{max} . This grammage then relates with the height above ground as $h_{\text{max}} \propto \ln(\chi_0/\chi_{\text{max}})$, where $\chi_0 \sim 1000 \text{ g cm}^{-2}$ at the sea level. Although EAS triggered by electrons and positrons result in the same underlying processes, their point of first interaction is slightly higher compared to gamma rays.

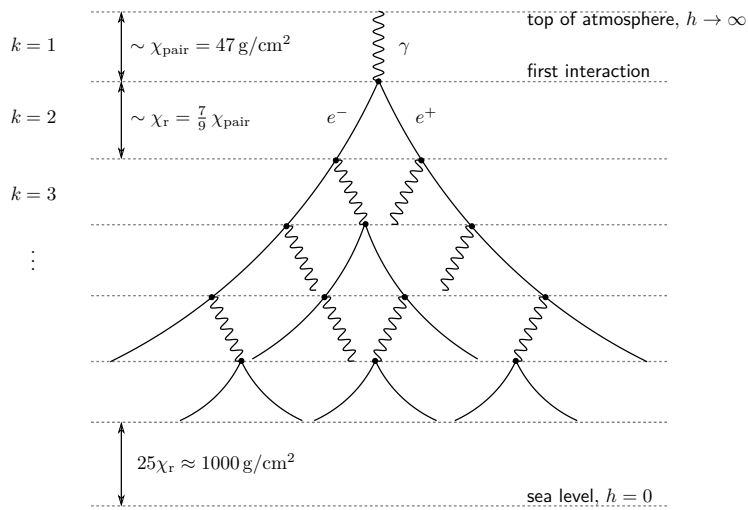


Figure 2.6: Representation of an electromagnetic shower induced by a primary gamma ray. χ_{pair} and χ_r represent, respectively, the average interaction length of pair-production and Bremsstrahlung. Figure from: [Hütten, 2017].

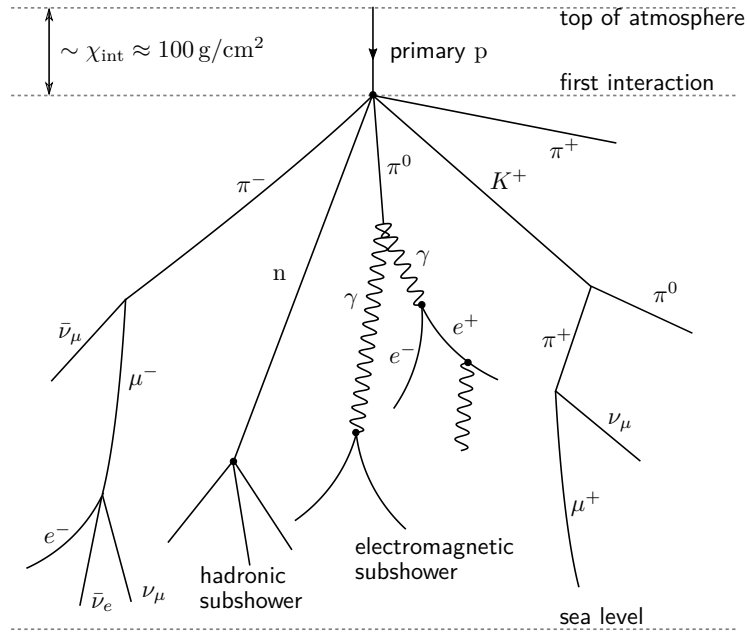


Figure 2.7: Hadronic shower triggered by primary protons or nuclei. The proton induced shower presents electromagnetic, muonic and hadronic components. This happens since the proton interacts via the strong force. Figure from: [Hütten, 2017].

Conversely, when cosmic-ray protons and nuclei reach the Earth, they participate in interactions through the strong force with the nuclei of air molecules, resulting in the formation of a hadronic shower, which comprises a central hadronic core, a muonic component, and electromagnetic sub-showers. The fraction of the energy transferred to the electromagnetic showers depend on the energy of the primary particle. Above roughly 200 GeV, this fraction is $\gtrsim 60\%$ [Leroy and Rancoita, 2016].

Hadrons typically penetrate deeper into the atmosphere due to the larger nuclear interaction length compared to the radiation length. Additionally, images of hadronic showers show greater shape fluctuations due to the complexity of the cascades, which consist of various particle types. The interaction of the primary proton results in the production of charged and neutral pions, as well as other types of mesons. The π^0 decays producing electromagnetic sub-showers. In the hadronic shower development, secondary particles have greater lateral displacement due to inelastic scattering and decay processes of the hadronic particles. This is depicted in Figure 2.8, which shows the lateral and longitudinal development of showers initiated by a gamma ray and a proton of the same energy. For instance, energetic muons produced in hadronic showers also produce Cherenkov light. However, their characteristic images are seen as rings in the camera, due to the symmetry of the emission around the axis of the muon trajectory and given that they interact later in the atmosphere.

In the plane crossing the longitudinal development of the shower and containing the shower axis, the cascades assume an elliptical shape, starting at an altitude of about ~ 20 km [Aharonian, 2004]. Relativistic electrons move along the shower axis, exhibiting varying levels of lateral displacement in the perpendicular plane.

Cherenkov light is emitted at a characteristic angle (θ_c) that depends on the refractive index

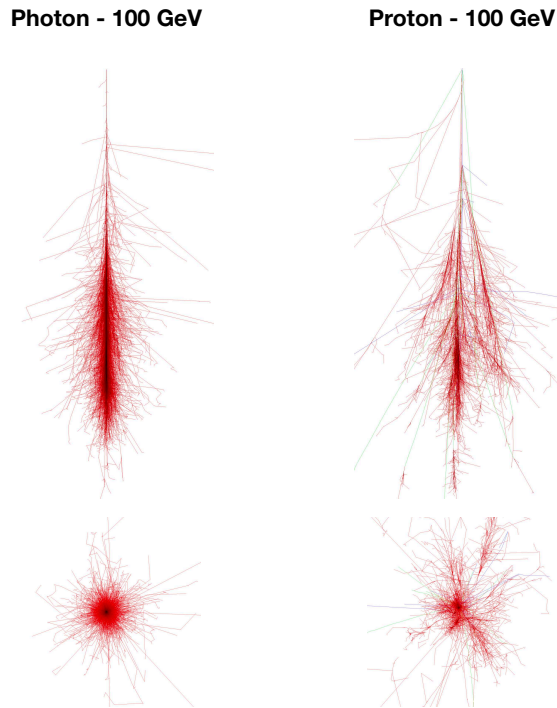


Figure 2.8: Longitudinal and shower projection for a gamma ray and a proton induced shower, both with a primary particle energy of 100 GeV. Figures are available at <https://www-zeuthen.desy.de/jknapp/fs/showerimages.html>.

(n) of the atmosphere:

$$\cos\theta_c = \frac{1}{\beta n}, \quad (2.20)$$

where $\beta = v/c$ corresponds to the velocity of the travelling particle. From the same equation, it is straightforward to derive that the minimum particle energy required for Cherenkov emission is $mc^2/\sqrt{1-n^{-2}}$. For electrons at sea level, this energy is of about 21 MeV. The resulting Cherenkov cone lasts for a few nanoseconds and produces a pool of light on the ground with a radius of $\sim 80 - 120$ m and a faint photon density of ~ 100 photons m^{-2} (for a 1 TeV gamma ray, depending on the altitude level) [Aharonian, 2004]. This is due to the fact that the refractive index of the atmosphere is a function of the altitude. Figure 2.9 shows the schematic diagram of Cherenkov emission and a depiction of its arrival on the observatory. At the ground level, the refractive index of $n \simeq 1.0003$ results in a maximum opening angle of $\sim 1.4^\circ$.

Because the Cherenkov light from the cascades is very faint and brief, ground-based telescopes need large reflective areas and cameras sensitive to blue light with rapid time gates. The typical time-scales for electromagnetic cascades are 2 - 5 ns, while for hadronic cascades, they range from 10 - 15 ns. In the later case, the time-scales are longer due to the larger transverse momentum and electromagnetic subshowers [Grieder, 2010].

The field of ground-based gamma ray detection was revolutionised by multi-telescope arrays, which employ stereoscopic reconstruction methods for better background rejection and improved

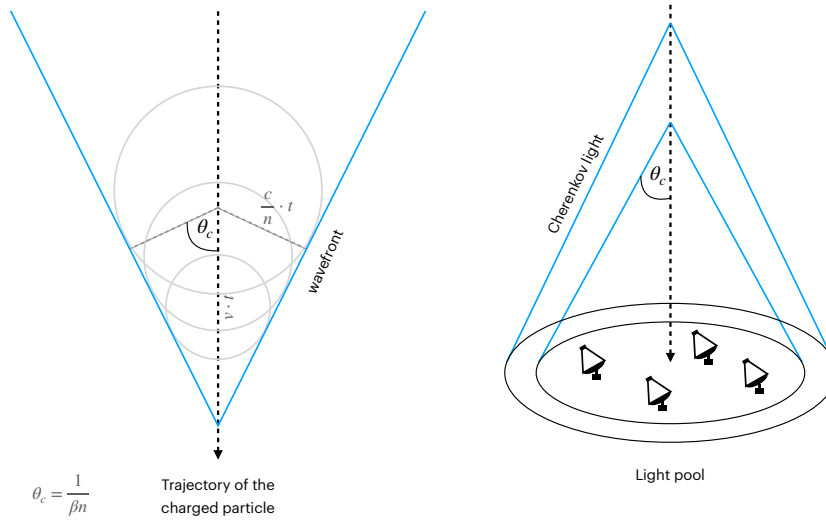


Figure 2.9: **Left:** Schematic view of the Cherenkov emission triggered by secondary particles produced in the development of EAS. **Right:** Schematic view of the Cherenkov light producing the light pool on the ground, where an observatory is located.

event reconstruction. The concept of stereo reconstruction is based on the analysis of the shower with at least two simultaneous telescope projections. In multi-telescope arrays, telescopes are spaced at distances similar to the effective radius of the Cherenkov light pool. The stereo reconstruction allows the unambiguous reconstruction of shower parameters. Due to limitations imposed by the moonlight, these instruments have a duty cycle of $\sim 10\%$, which accounts for approximately 1000 hours of observing time per year.

2.5 Shock powered transients

Some of the most energetic ($L \gtrsim 10^{40} \text{ erg s}^{-1}$) astrophysical sources exhibit a transient nature which can be characterised by either a permanent but variable emission or by a sudden energy release, lasting from a few minutes up to years. They could be one-time events, involving the extreme transformation of astrophysical sources, but they also englobe permanent sources that exhibit high variability in the flux, e.g., via the presence of flares. The underlying mechanisms that drive these extreme energy outputs and their rapid variability are not completely understood. Although some transient sources seen by X-ray instruments have not been detected in the VHE range, the extreme conditions associated with these events suggest their potential to emit gamma rays.

Optical transients which are commonly detected by wide-field optical surveys, such as extreme supernovae (SNe), classical novae and TDEs, reach very high peak luminosities that are inconsistent with purely radioactive decay or thermal emission. One way to enhance the energy output of these sources is through shock interactions between their ejected material and the external medium.

One of the most important evidence of shock interactions in transients was observed through the detection of the time-correlated optical and gamma-ray emission (0.1 - 10 GeV by Fermi-LAT) from classical novae, such as ASASSN-16ma [K.-L. Li et al., 2017] and V906 Car [Aydi et al.,

2020]. These observations imply that their spectrum is directly associated with diffuse acceleration processes at shocks driven by the ejected material³. In principle, the gamma-ray emission from novae could also be generated by Bremsstrahlung or via IC scattering of relativistic electrons. However, the hadronic mechanism is favoured because the intense magnetic fields required to confine the accelerated progenitor particles to energies above 10 GeV cause relativistic electrons to lose energy through lower-frequency synchrotron radiation, thereby disfavoured the leptonic mechanism [Aydi et al., 2020; Fang et al., 2020; Vurm and Metzger, 2018]. The thermal origin of the optical emission is discarded since it happens simultaneously with the detection of the HE component (with a lag of 5.3 ± 2.7 h). The high gas densities in the nova ejecta could lead to the reprocessing of X-ray photons into optical radiation with near-total efficiency. Evidence for shock interactions were also suggested for the emission of the recurrent nova RS Ophiuchi by Fermi-LAT, H.E.S.S. and MAGIC [Acciari et al., 2022; Aharonian et al., 2022; Cheung et al., 2022]. The observed VHE component had a similar temporal profile to the emission detected in the lower-energy GeV range, which favours the hadronic emission scenario over the leptonic alternative.

Although gamma-ray emission has not been identified for several transient classes, there is compelling evidence to support their ongoing pursuit with IACTs. In this section, I summarise some of the main transient classes for which VHE searches are conducted with the VERITAS array.

2.5.1 Tidal disruption events

Tidal disruption events happen when stars passing within the Roche limit of super-massive black holes (SMBHs) are torn apart by tidal forces [Frank and Rees, 1976]. The Roche radius characterises the distance at which the self-gravitation of a star (or planet) becomes comparable to the tidal forces from a second body. Depending on how closely the star approaches the massive ($> 10^6$) SMBH at the centre of a galaxy, the tidal pull can be powerful enough to overcome the star's self-gravity at its core [Rees, 1988]. About half of the resulting debris from the star falls-back towards the SMBH and is accreted, creating a luminous burst of electromagnetic radiation. The other half escapes on hyperbolic orbits and is free to collide with the circumnuclear medium (CNM) (ejecta velocities are typically $\lesssim 10^3 - 10^4$ km s⁻¹ [Matsumoto and Piran, 2021]). The tidal radius involving the system of a star (M_*, r_*) and a black hole of mass M_{BH} can be described as

$$r_t \approx 7 \times 10^{12} \left(\frac{M_{\text{BH}}}{10^6 M_\odot} \right)^{\frac{1}{3}} \left(\frac{M_*}{M_\odot} \right)^{-\frac{1}{3}} \frac{r_*}{r_\odot} \text{ cm.} \quad (2.21)$$

³The envelope of classical novae is ejected at velocities of 500 – 5000 km s⁻¹ [Aydi et al., 2020].



Figure 2.10: Artistic illustration of a Tidal Disruption Event. The figure shows the star approaching the black hole and elongating in its line of trajectory. The star is disrupted as it passes the tidal radius. A fraction of the mass ($\sim 50\%$) remains bound to the black hole while the other part scatters off. Figure credit: NASA/CXC/M.Weiss.

2.5.1.1 Multiwavelength searches of Tidal Disruption Events

Initial analytical studies indicate that TDE light curves should exhibit a $t^{-5/3}$ power-law decay [Rees, 1988], which is a characteristic result of the analytical calculation of the fall-back rate of the circularised bound debris. This model allowed the initial discovery of TDEs in the 1990s by X-ray observatories, such as the ROSAT all-sky survey [Komossa and Bade, 1999; Truemper, 1982]. Subsequent studies have shown that viscous accretion delays can influence the luminosity decay, leading to variations in the expected behaviour of the light curves [Auchettl et al., 2017].

Today, TDEs are typically discovered through systematic multiwavelength searches. They are identified by employing a combination of their expected photometric behaviour with known spectroscopic features. Optical surveys such as the ZTF and the All Sky Automated Survey for SuperNovae (ASAS-SN) [Kochanek et al., 2017; Shappee et al., 2014] have played a crucial role in drastically increasing the identification rate of TDEs. Over the course of its first three years of operations, more than 30 new flares were reported by ZTF [Hammerstein et al., 2022]. The identification of a wider population of transient events by optical surveys enabled the differentiation of TDE light curves from certain types of nuclear transients, such as variable AGNi and SNe happening close to the centre of galaxies. For instance, unlike other transient classes, TDE light curves exhibit a rise time in the order of weeks, a hot blue continuum and a smooth power-law decay over the course of several months. In addition, the extensive follow-up of new events has enabled the identification of spectroscopic features, such as very broad Hydrogen and (or) Helium emission lines in the order of 5000 to 15000 km s^{-1} .

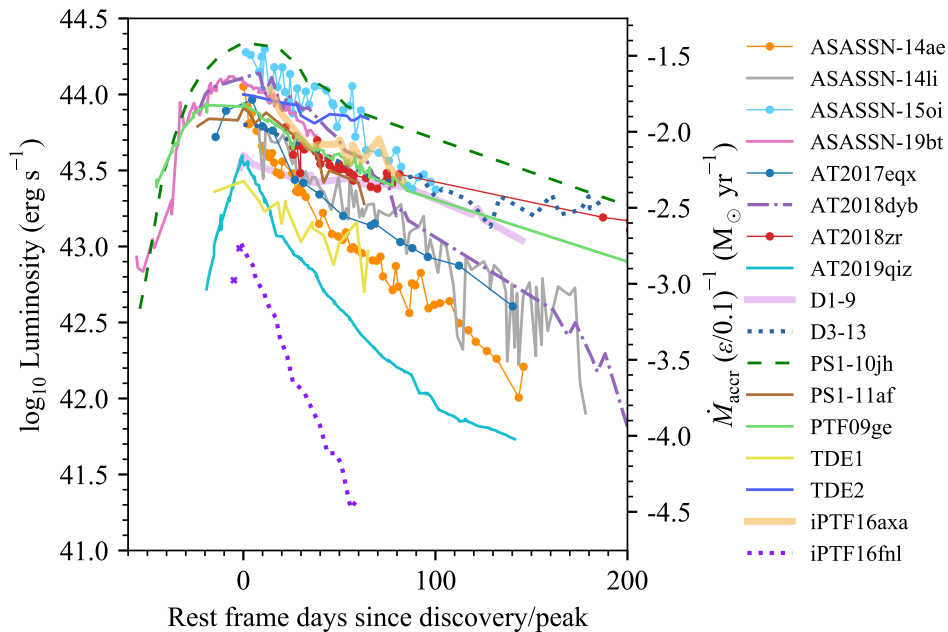


Figure 2.11: Integrated OUV luminosity inferred from the fit of the spectral energy distribution for different TDEs as a function of time elapsed since either the peak of the light curve or since discovery. On the right side of the y-axis, the accretion rate is found as $L/(\eta c^2)$, with $\eta = 0.1$. The parameter η refers to the efficiency of mass accretion. Figure from: [van Velzen, Gezari, et al., 2021].

TDEs identified by optical and ultra-violet (OUV) surveys are typically well described by a thermal blackbody spectrum and often show no signs of non-thermal emission. The X-ray follow-up of these events also frequently yields in no detection or aligns with thermal blackbody predictions at keV energies [van Velzen, Gezari, et al., 2021]. Figure 2.11 presents several light curves of optically discovered TDEs. Over the last few decades, the Swift X-ray telescope (Swift-XRT) (0.2 - 10 keV) [Burrows et al., 2005] has played a crucial role in providing timely follow-ups and offering precise constraints on the luminosity evolution. For instance, it has been argued that the detection of OUV discovered TDEs in X-ray bands is typically consistent with a significantly hotter and smaller blackbody radius than that inferred from the OUV observations. These results align with expectations that the X-ray emission originates from the inner accretion disk [R. Saxton et al., 2021]. A comprehensive overview of the radiative mechanisms powering TDEs and their expected emission across different bands is detailed in Table 1 from Ref. [Roth et al., 2020].

2.5.1.2 Relativistic Tidal Disruption Events

Some astrophysical sources are seen to emit collimated beams composed of plasma, dense magnetic fields and extremely energetic particles. These jets are emitted by compact objects, often in the central region of galaxies. This is the case, e.g., of the different classes of AGNi [R. Blandford et al., 2019]. AGNi are galaxies that host a region of very bright emission associated with the accretion of matter by the black hole in the galaxy core. The intense luminosities, reaching up to

$\sim 10^{47}$ erg s⁻¹, can be detected in a wide range of the electromagnetic spectrum (from radio waves to gamma rays).

The discovery of Swift J164449.3+573451 (from now on referred to as Swift J1644+57) [Socrates, 2012] has shed light on a new and rare class of TDEs that are associated with relativistic jets. Initially identified by the Swift Burst Alert Telescope (Swift-BAT) (15 - 150 keV) [Evans et al., 2010] as a long GRB, this event was later reclassified as a TDE event featuring relativistic outflows and jet collimation [Bloom et al., 2011]. Considering that the observed radiation is emitted in isotropic mode, the average X-ray luminosity of Swift J1644+57 can be estimated at 10^{47} erg s⁻¹, whereas the emission over about three weeks after discovery amounts to approximately 10^{53} erg [Burrows et al., 2011]. Although these energetics are comparable to those observed for long GRBs, they were detected in much longer timescales (for ultra-long GRBs, a comparable emission is seen in the order of $\lesssim 10^4$ s [Levan et al., 2013; Pescalli et al., 2015]).

During the first two weeks after the initial trigger, the X-ray light curve of Swift J1644+57 (Figure 2.12) showed several flares with luminosities ranging from $\sim 10^{45}$ - 10^{48} erg s⁻¹ over time scales of 100 s [Burrows et al., 2011]. This initial phase is credited to a possible violent rearrangement, or wobbling, of the jet [Tchekhovskoy et al., 2014]. The prolonged light curve of Swift J1644+57 showed other distinct features. For example, after about 10 days, the light curve dropped approximately as a power law with an index of -5/3 [De Colle and Lu, 2020] (an index of -1.5 is also suggested [Mangano et al., 2016]). Up to ~ 100 days after the initial trigger, the light curve still shows flares and then it enters a plateau phase for about a year. The emission flares were interpreted as originating from the effect of jet's precession, causing the collimated beams to briefly and partially leave our line of sight and later stabilise [C. J. Saxton et al., 2012]. Other studies, such as in Ref. [Tchekhovskoy et al., 2014], suggest that the flares are actually caused by the accumulation of magnetic fluxes near the central black hole, causing the accretion flow of the stellar debris to become magnetically-arrested.

About 500 days after the initial trigger, the X-ray flux drops dramatically and can barely be detected, apparently indicating the jet has switched off. Around the same time, the accretion rate drops to about a fraction of the Eddington accretion rate [Zauderer et al., 2013]. In Ref. [Tchekhovskoy et al., 2014], it is suggested that at this moment the disc has become geometrically thin (low optical depth) and that the state of accretion becomes thermally dominant, thus not producing powerful jets [Russell et al., 2011]. These conclusions likely indicate a relationship between super-Eddington accretion and jet ejection.

Unlike the X-ray emission, the radio flux from Swift J1644+57 (Figure 2.13) continues to rise up to about 100 days before it declines. The total radio afterglow is inferred to be in the order of 10^{53} erg [De Colle and Lu, 2020]. The very distinct behaviours of the X-ray and radio light curve and the lack of strong radio variability suggest that these two emission components likely have different origins.

Since the discovery of Swift J1644+57 in 2011, only three other relativistic TDEs have been identified (Swift J2058.4+0516 [Bradley Cenko et al., 2012], Swift J1112.28238 [Brown et al., 2015] and AT2022cmc [Pasham et al., 2022]) [De Colle and Lu, 2020; Yao et al., 2024]. Both Swift

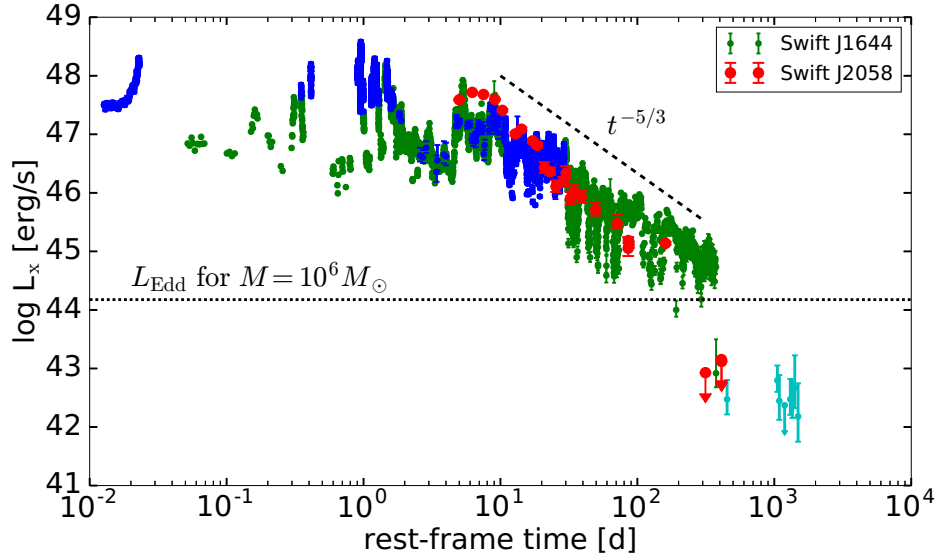


Figure 2.12: The light curves of Swift J1644+57 and Swift J2058.4+0516. Blue, green and cyan dots represent, respectively, datapoints taken with Swift-XRT photo counting mode, windowed timing mode and from the Chandra X-ray observatory [Weisskopf, 2012], respectively. The light curve of Swift J2058 is given as the red dots. Figure from: [De Colle and Lu, 2020]

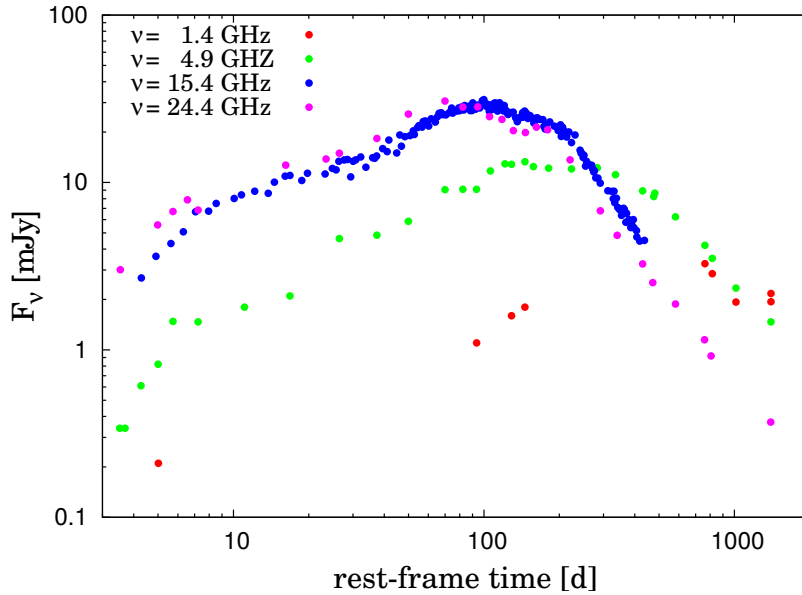


Figure 2.13: The radio light curve of Swift J1644+57 by the Very Large Array [Lacy et al., 2020; Zauderer et al., 2011]. The emission continues to rise up to 100 days before declining. Figure from: [De Colle and Lu, 2020]

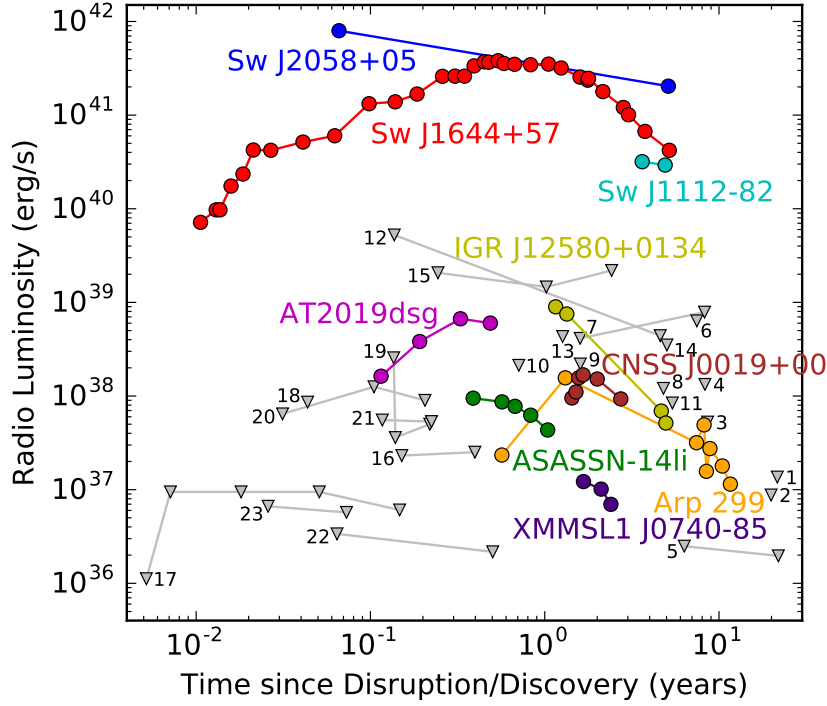


Figure 2.14: Radio light curves of TDEs. Grey triangles represent upper-limits (3σ) from several other events. Figure from: [Alexander et al., 2020]

J2058.4+0516 and Swift J1112.28238 presented similar light curve features as Swift J1644+57. For instance, they show long lasting X-ray and radio emissions and a power-law decay of the X-ray flux. As seen in Figure 2.12, Swift J2058.4+0516 also presented a sudden drop in luminosity after a few hundred days post discovery, and also roughly coinciding with the transition from super- to sub-Eddington accretion rates.

In most cases, the radio flux detected for different TDEs is interpreted as synchrotron emission from the interaction of fast outflows (relativistic or sub-relativistic) interacting with the CNM. As shock waves travel through this medium, the free electrons are accelerated. In some cases, the synchrotron emission might result from internal shocks within a jet.

While the jet luminosity can be Doppler boosted by a factor of several thousands for nearly on-axis observations, off-axis jets may be beamed away from the observer and only become visible once the jet decelerates. This is the case of TDE Arp 299-B AT1, whose radio emission is consistent to an off-axis jet constrained to an observing angle of $25^\circ - 35^\circ$ [Mattila et al., 2018].

Some events, such as ASASSN-14li [Alexander et al., 2016], ($z = 0.0206$) had their radio emission associated with synchrotron radiation emerging from external shocks between non-relativistic wind outflows and the CNM or from interactions between the unbound debris and the CNM [Krolik et al., 2016]. Alternatively, simulations suggest that these outflows could also be launched from interactions of self-intersecting bound debris flows [Lu and Bonnerot, 2020]. The non-relativistic radio emission detected for TDEs such as ASASSN-14li indicates that jet launching is likely not a

universal occurrence in all events [De Colle and Lu, 2020]. Most thermal TDEs are either radio-quiet ($< 10^{40}$ erg s^{-1}), generating less intense jets or non-relativistic or mildly-relativistic outflows, or they do not emit detectable radio waves at all. In addition, radio follow-up observations are also completely absent for some events, or they may be too sparse or too shallow to uncover low-luminosity outflows.

The rate of detected on-axis jetted TDEs is already expected to be constrained due to an observational bias since not always will the jet be pointed in our direction. A volumetric rate of $\sim 10^{-4}$ - 10^{-3} is inferred in respect to the overall rate of TDEs, which is expected to be $\sim 10^2$ - 10^3 Gpc $^{-3}$ yr $^{-1}$, or about one event every 10^4 - 10^5 years per galaxy [Donley et al., 2002; Gezari et al., 2008; Magorrian and Tremaine, 1999; Teboul and Metzger, 2023]. TDEs with off-axis jets, which should be more frequent over on-axis events, should then be much fainter in hard X-rays and gamma-ray wavelengths [De Colle and Lu, 2020]. To date, the exact conditions that favour the formation of relativistic jets over non-relativistic outflows remain uncertain. The low number of observed events remains as a major limitation in understanding the mechanisms powering jetted TDEs.

2.5.1.3 The TDE unified model and multimessenger searches

TDE observations are often interpreted in light of the TDE unified model (Figure 2.15; [L. Dai et al., 2018]). The emission spectrum is heavily influenced by the observer's viewing angle in relation to the orientation of the disk. It has been observed that the ratio of optical to X-ray flux increases with the observer's viewing angle. Near the disk's mid-plane, intrinsic X-ray emission is absorbed and re-emitted as near-UV/optical radiation due to the photoionisation by a dense, slow-moving outflow or disk. From higher viewing angles, where the outflow travels at a fraction of the speed of light, the gas is optically thin, and adiabatic expansion is the main cooling effect of the system. The inner disk's intense, beamed X-ray emission can only be observed directly into the funnel region. The presence or absence of a jet does not alter the dependence of the optical to X-ray flux ratio with the viewing angle.

The investigation of TDEs in a multimessenger approach has provided strong evidence for hadronic mechanisms. Associations of astrophysical neutrinos from IceCube with TDEs AT2019dsg, AT2019fdr and AT2019aal have been reported in the past years [Reusch et al., 2022; Stein et al., 2021; van Velzen et al., 2024]. A stacked search constrained the total contribution of TDEs to $\lesssim 30\%$ of the diffuse neutrino flux measured by IceCube [Stein and IceCube Collaboration, 2019]. Jetted TDEs have also been proposed as sources of UHECR [Biehl et al., 2018; Guépin et al., 2018].

In principle, neutrino emission from TDEs could arise either from pp or $p\gamma$ interactions. However, studies suggest that the rate of pp interactions could be subdominant in comparison to $p\gamma$ [Winter and Lunardini, 2023; Yuan and Winter, 2023]. In any case, an efficient acceleration region should be present in order to raise the proton energies to the PeV range (to explain the ~ 100 TeV neutrinos). Figure 2.16 presents the different possible acceleration regions for a black hole of mass $10^7 M_{\odot}$ (corresponding to a gravitational radius of $R_S \simeq 3 \cdot 10^{12}$ cm). Namely, these regions are the X-ray photosphere and hot corona, spanning from 2 - 30 R_S , the OUV photosphere or inner

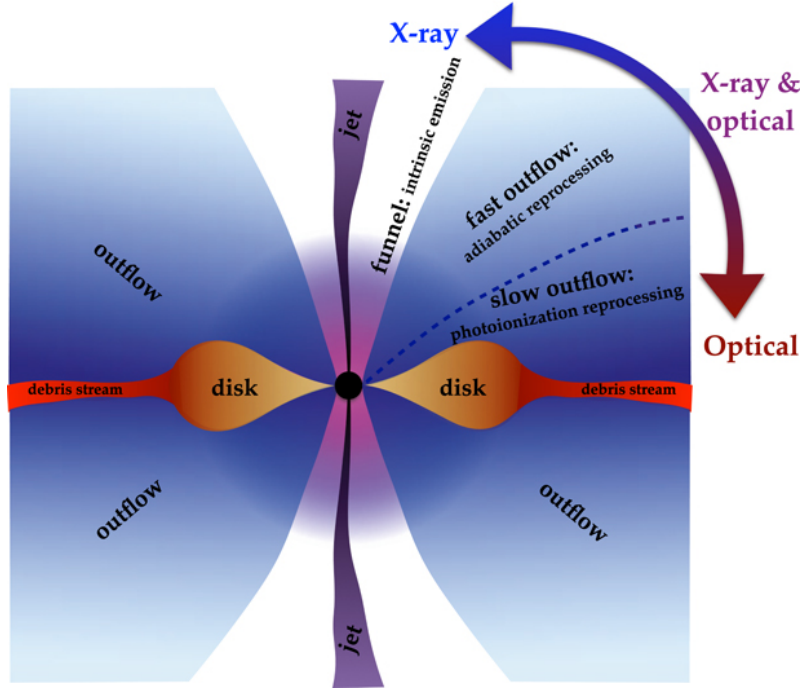


Figure 2.15: The unified model for TDEs describes how the viewing angle of the observer affects the observed radiation. Figure from: [L. Dai et al., 2018]

jet structure, at about $10^3 R_S$, or also acceleration in outflows or stream-stream collisions ($R_S \approx 10^{16} - 10^{17}$ cm). Because protons of energy E_p should be magnetically confined in order for the acceleration to be efficient ($R_{\text{acc}} < R_L$), a simple estimation that provides an upper limit on the acceleration region is given by the Larmor radius (or gyroradius), R_L , of protons in a region of magnetic field of strength B :

$$R_L \approx 3 \cdot 10^{12} \text{ cm} \left(\frac{E_p}{\text{PeV}} \right) \left(\frac{B}{\text{G}} \right)^{-1}. \quad (2.22)$$

2.5.1.4 The literature of TDEs on high and very high energies

As no detection of TDEs at high and very high energies has been identified, the literature on the subject is fairly scarce. It has been suggested that collisions between the unbound debris stream and dense molecular clouds surrounding the black hole could produce gamma ray emission in the 0.1 - 10^5 GeV range [X. Chen et al., 2016]. However, the study specifies that not only the shock-acceleration time-scale is in the order of 10 - 100 years but also that this emission would only be relevant up to about 10 Mpc due to the extremely long observation time required for detection at larger distances (>1000 hours with the Cherenkov Telescope Array Observatory (CTAO)). Gamma rays have also been proposed to be produced in collisions between the TDE outflows and pre-existing dust tori from AGN hosts. This has also been suggested to happen years after the disruption [Mou and Wang, 2021].

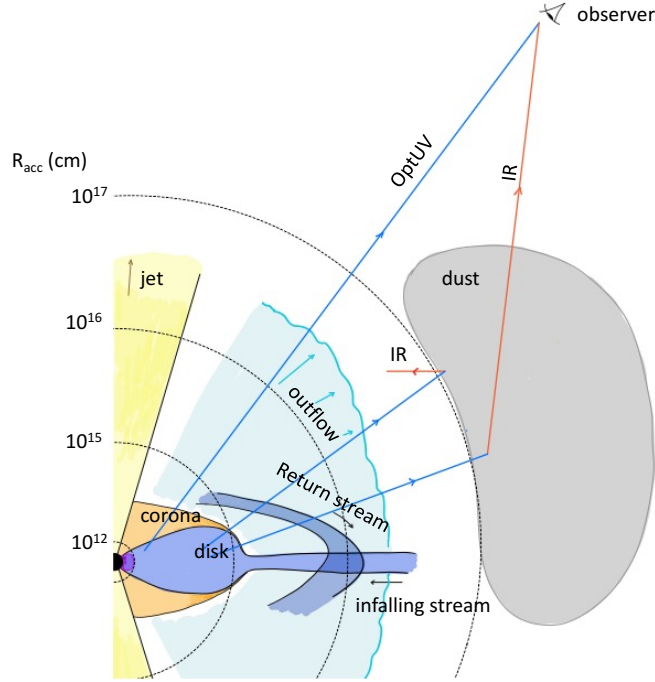


Figure 2.16: The global picture of acceleration regions in a TDE. The figure shows the inner X-ray photosphere and hot disk corona, the OUV photosphere and inner jet region and the outflow and stream-stream collision region. A black hole of mass $10^7 M_{\odot}$ is assumed. A dust torus is also represented in the figure, but it is not found to be present in every TDE scenario. Figure from: [Winter and Lunardini, 2023]

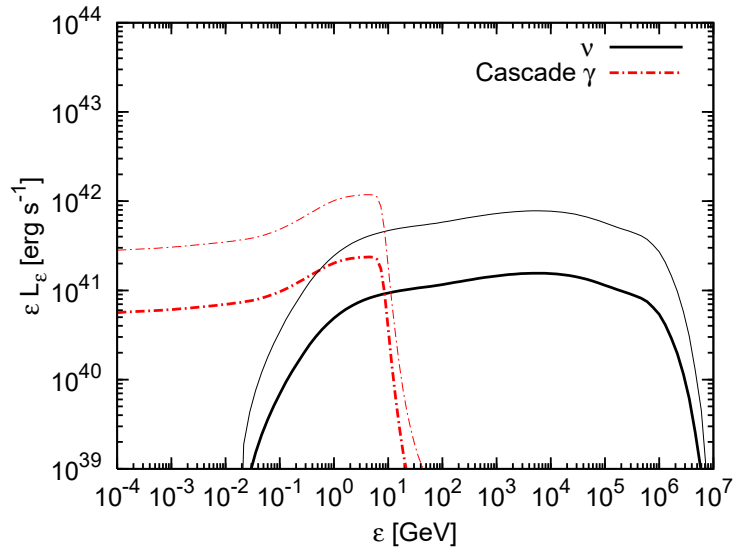


Figure 2.17: Differential neutrino (black lines) and gamma ray (red lines) luminosities calculated for the wind model of TDEs. The thin curves represent a cosmic ray loading parameter $L_{CR}/L_{OUV} = 1$, while the thick curves assume $L_{CR}/L_{OUV} = 0.2$. Figure from: [Murase et al., 2020].

In addition to the above, Ref. [Murase et al., 2020] explores possible gamma-ray and neutrino emission scenarios from non-jetted TDE components. Among the several different core regions considered, none are found to produce a gamma ray emission above ~ 100 MeV. It is argued that this is mainly due to the high level of attenuation of gamma rays occurring with disk and coronal photons. The attenuation of a possible GeV and TeV photons up to 90 days after disruption is also supported in the scenario of shock interactions between the unbound debris stream and the CNM [Fang et al., 2020]. The only emission scenario with a significant emission in the GeV regime ($\lesssim 100$ GeV) was given by the wind model (Figure 2.17) [Murase et al., 2020]. Here, cosmic rays are assumed to be accelerated by high-speed winds originating from super-Eddington accretion rates or, possibly, by shocks induced from the collisions among the bound debris stream.

Although a high attenuation level is expected because of the dense radiation fields, high and very high energy observations of TDEs still impose important constraints for future non-thermal emission models. A discovery would naturally result in exciting discussions regarding the role of shock mechanisms in these events.

2.5.2 Gamma ray Bursts

Gamma-ray bursts are among the most energetic astrophysical phenomena observed in the universe. Due to the extreme luminosities ($10^{49} - 10^{55}$ erg s^{-1} in gamma rays; [Miceli and Nava, 2022]) and the rapid variability of the emission, these events are associated with catastrophic events which lead to the formation of compact objects, such as accreting black holes and rapidly spinning massive neutron stars. Constraints on the Lorentz factor of GRB outflows (with typical values in the order of 100 - 1000 [Racusin et al., 2011]), indicate that their jets are among the most relativistic ones. The GRBs transient radiation exhibits a distinct pattern, starting with a prompt emission, followed by an afterglow radiation (Figure 2.18). Although both emission phases are linked to the release of relativistic jets, they are expected to take place at different distances from the central engine ($R \sim 10^{13} - 10^{14}$ cm and $R \sim 10^{15} - 10^{20}$ cm, respectively) [Miceli and Nava, 2022].

2.5.2.1 The Prompt and Afterglow Emissions

The observed rapid variability of the prompt emission suggests it has an internal origin [Sari and Piran, 1997], i.e., the emission is triggered by dissipation mechanisms within the internal structure of the ejecta. The most accepted scenario to describe the prompt phase, known as the *fireball* model [Piran, 1999], suggests that a central engine is responsible for producing relativistic flows composed of plasma shells, or *fireballs*. These shells should have a diverse range of Lorentz factors (due to the ejection of irregular outflows at different velocities) and collide among each other [Kobayashi et al., 1997; Rees and Meszaros, 1994]. In these collisions, internal relativistic shocks are created and particles can be accelerated. The duration of the prompt emission can vary from a few seconds up to several minutes and is dominated by photons in the keV to the MeV energy range [Z. Dai et al., 2017]. The typical spectrum shape of the prompt emission is given by a broken power-law (Band function) in the MeV range. There are also discussions in the literature

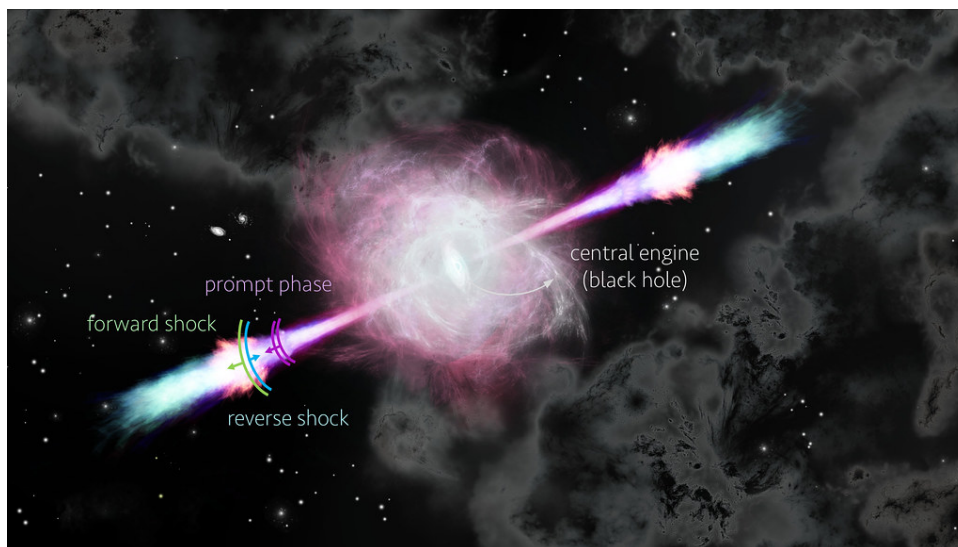


Figure 2.18: Artistic view of a GRB jet, indicating the regions responsible for the prompt and afterglow emissions. Credit: Nuria Jordana-Mitjans.

considering effects of a dissipative photosphere [Beloborodov and Mészáros, 2017] or magnetic reconnection [Drenkhahn and Spruit, 2002; Spruit et al., 2001].

A bimodal pattern is observed for the duration distribution of the prompt emission [Kouveliotou et al., 1993]. This pattern is usually employed to categorise GRBs into long (lasting for $> 2 - 10^3$ seconds) and short events (< 2 seconds). In addition, features in the spectrum (fitted by a smoothly broken power-law in the so called Band-function) are also observed: the break energy of long GRBs spans from tens of keV to 0.1 - 0.8 MeV, while for short GRBs it is around $\gtrsim 0.5 - 0.8$ MeV. Due to the observed energetics and time scales, long GRBs are often associated with the formation of collimated jets triggered by the accretion of the surrounding disk developed from the collapse of massive stars into black holes [Woosley, 1993]. In addition, several long GRBs have been detected in spatial and time coincidence with type Ic SNe, corroborating their association with the death of massive stars [Klose et al., 2019]. Alternative models also consider that rapidly rotating neutron stars, known as millisecond magnetars, could be the progenitors of at least a fraction of long GRBs [Beniamini et al., 2017; Usov, 1992]. On the other hand, short GRBs are now associated with mergers of neutron stars (or also likely neutron stars and black holes), as it is recently suggested from the association of GRB 170817A with the gravitational wave GW170817, detected by the LIGO and Virgo observatories [Abbott et al., 2017]. In more recent studies, the classification of GRBs based solely on their emission duration is considered a simplistic description of the known population. The detection of several events with distinct characteristics, e.g., long GRBs with no supernova counterpart, challenges the bimodal classification and suggest that more complex models are necessary to explain all scenarios in which GRBs can originate.

The long-lasting and weaker afterglow emission, observed from radio to X-ray or gamma-ray frequencies, is likely associated with the external deceleration of the ejecta by collisions with the ambient medium [Meszaros and Rees, 1993; Meszaros and Rees, 1997]. These interactions

trigger the development of a reverse shock (caused by the ram pressure applied by the external compressed material) travelling into the ejecta and a forward shock travelling towards the external medium. These shocks promote particle acceleration and the deceleration of the outflow down to non-relativistic velocities. The first afterglow emission signature is mainly identified as the synchrotron cooling from the electrons accelerated in the forward shock [Sari et al., 1998] (this is the primary mechanism for photons with energies \ll GeV. This same electron population up-scatter the synchrotron photons, resulting in a SSC component. The afterglow emission is seen to decay smoothly with a power-law over the course of weeks to a few months, while the typical frequency shifts from X-rays to radio waves (due to the lower Lorentz factor achieved from deceleration) [Miceli and Nava, 2022].

Similarly to TDEs, the Swift experiment has been crucial in identifying a variety of both short and long GRBs. While the Swift-BAT instrument promptly locates new events, Swift-XRT and the Swift UltraViolet/Optical Telescope (Swift-UVOT) [Roming et al., 2005] search for X-ray and UV counterparts (the slewing time after a BAT trigger is of approximately 100 seconds). Among some of the most interesting discoveries by the Swift experiment are the detection of the most distant events, namely GRB 090423 [Lin et al., 2010] and GRB 090429B [Cucchiara et al., 2011], located at $z = 8.2$ and $z = 9.4$, respectively. Reports containing triggering coordinates and other candidate characteristics are sent to subscribed astronomers via the Gamma-ray Coordination Network (GCN) ⁴. The typical observed rate of GRBs is about $10^{-5} - 10^{-6}$ per galaxy per year.

2.5.2.2 Very High Energy Observations of GRBs

Through an observing campaign in place since its commission, H.E.S.S. observes GRBs automatically (no need for human input) by monitoring alerts from the GCN system. Triggering decisions are essentially made based on the source significance obtained with the Gamma-ray Burst Monitor of the Fermi Gamma-ray Space Telescope (Fermi-GBM) and also based on the event's distance. The number of GRBs observed by H.E.S.S. is in the order of 100. Similarly, the MAGIC telescopes also implement a filter system with predefined criteria for the observations. About 100 GRBs have also been observed by MAGIC. Particularly for VERITAS, triggering decisions are made onsite after a GCN alert is received.

In 2019, the first GRB detections in the TeV band ($\sim 0.1 - 3$ TeV) were reported by the H.E.S.S. and MAGIC Collaborations [H. Abdalla et al., 2021; H. E. Abdalla et al., 2019; Acciari et al., 2019] (Figure 2.19). The derived flux of the total emission in TeV energies represents a sizeable fraction of 20% up to 50% of the total energy emission in the afterglow phase. The Fermi-GBM and Fermi-LAT have been crucial in the identification of the afterglow from several GRBs. About 4% of the total events detected by GBM are also detected by LAT.

By analysing the balance between acceleration and cooling within the accelerator, there is a limit on the maximum electron energy acquired in shocks. In specific conditions of the flow, this limit is known as the synchrotron burn-off limit - $E_{\text{syn}}^{\text{max}} \sim 100\Gamma$ MeV [de Jager et al., 1996]. An SSC component by the same population of electrons that produced the synchrotron emission

⁴<https://gcn.gsfc.nasa.gov/>

could explain the TeV component [Derishev and Piran, 2019; Veres et al., 2019; Wang et al., 2019]. Alternatively, for GRB 190829A [H. Abdalla et al., 2021], it has been shown that not only the VHE emission matches an extrapolation of the X-ray spectrum, but also they faded in time coincidence, indicating they likely were originated by the same mechanism. The modelling of the spectral energy distribution (SED) indicated a preference for a pure synchrotron mechanism when not applying a limit on the electron energy. This result suggests the need for a different and highly efficient process that is able to accelerate electrons above the synchrotron burn-off energy. It has been suggested that a two-zone emission model [Khangulyan et al., 2023], composed of a radiation and acceleration zone with magnetic fields of different intensities, could provide an explanation for the VHE component.

With only a handful of events detected above 100 GeV, the production mechanisms of HE and VHE emissions are still under debate. The improved characterisation of the VHE spectrum of GRBs by IACTs is expected to further constrain the full multiwavelength picture. Although searches for associations with IceCube neutrinos in a population of 807 GRBs have been conducted, no association has been confirmed [Aartsen et al., 2016].

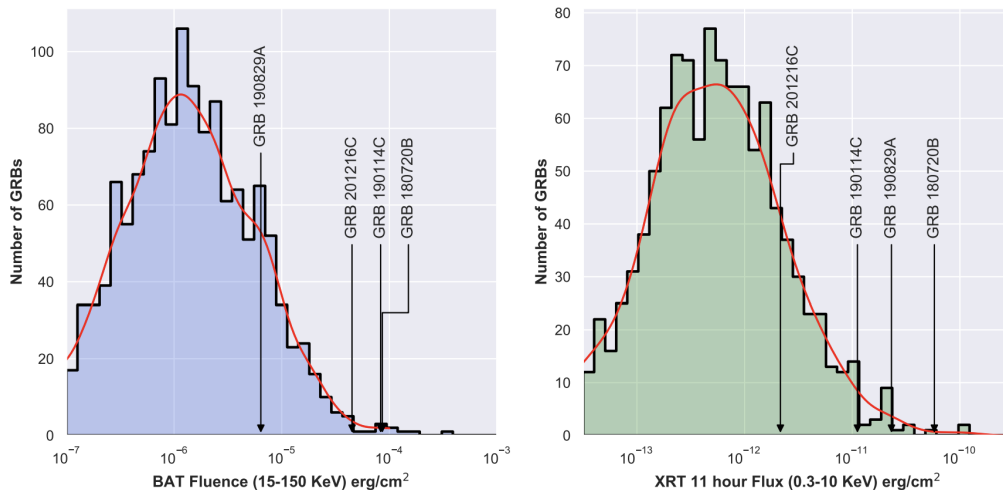


Figure 2.19: Left: distributions of BAT fluences for VHE GRBs. The GRBs detected in VHE up to December of 2021 are outlined (GRB 180720B, GRB 190114C, GRB 190829A, GRB 201216C). Right: same as the left panel, but for the XRT 11 hour flux. The red line gives the probability density of each distribution. GRBs detected in the (sub-)TeV regime were relatively bright in the keV range, with at least 3 of them being in the top 1% of all VHE GRB fluences. Figure from: [Noda and Parsons, 2022].

2.5.3 Fast Blue Optical Transients

The ejected material from SNe drives a strong shock as it travels into the shell of circumstellar medium (CSM) pre-ejected by massive stars when they become unstable in the months (or years) prior to the explosion [N. Smith, 2017]. The higher the gas density of the progenitor stellar wind, the more efficiently the kinetic energy of the shock is converted into particle acceleration. In such

cases, the output of secondary gamma rays should also proceed very efficiently.

The efficient nature of shock interactions in specific SNe systems is reinforced by the identification of FBOTs via optical surveys [Ho et al., 2023]. FBOTs represent the most extreme instances of interaction-powered SNe, comprising events which exhibit the highest luminosities and faster timescales [Inserra, 2019; Yu et al., 2015]. This becomes clear from Figure 2.20, which shows that FBOTs exhibit significantly higher luminosities and a very short rise period in comparison to thermonuclear and typical core-collapse SNe. Compared to Superluminous supernova (SLSN), the luminosities are similar but the timescales are still faster.

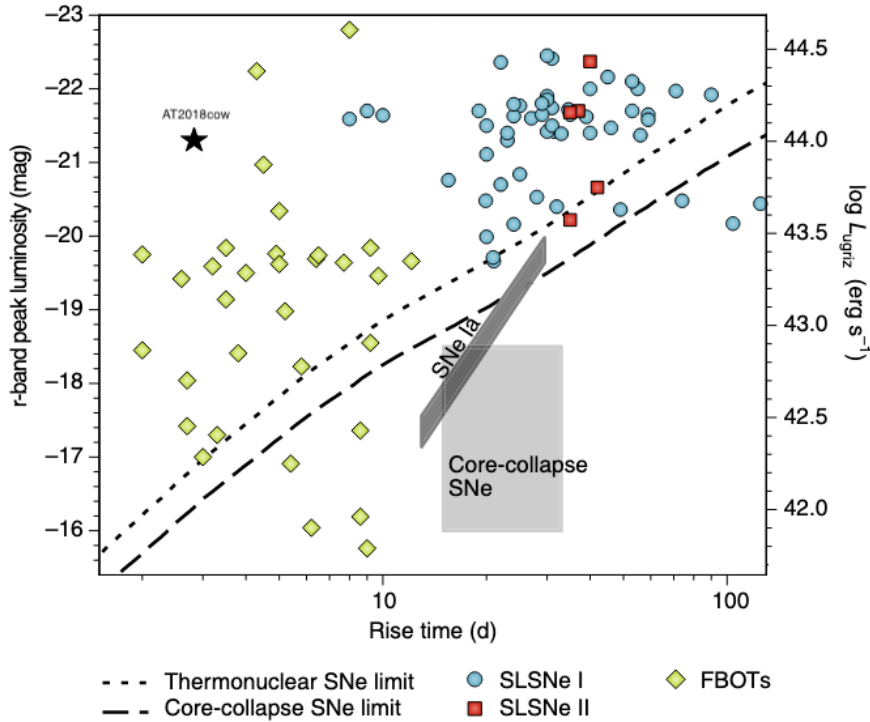


Figure 2.20: Parameter space composed by the peak of the r-band absolute magnitude (or pseudo bolometric luminosity on the right axis) and by the rise time. The dotted and dashed lines represent, respectively, the maximum luminosity for thermonuclear and core-collapse SNe. FBOTs operate at similar or brighter luminosities in comparison to SLSN type I and II, but on much shorter timescales. The highlighted position of AT2018cow indicates it is one of the most powerful and fast FBOTs ever recorded. Figure adapted from: [Inserra, 2019].

FBOTs are categorised by their blue color ($-0.3 < g - r < -0.2$), rapidly rising and declining light curves and high bolometric luminosities ($L_{\text{bol}} \gtrsim 10^{43}$ erg/s) [C. Chen and Shen, 2022]. These characteristic features are very hard to be explained with typical radiative emission models of stellar explosion, e.g., from radioactive decay mechanisms from SN Type Ia [Lyutikov, 2022]. Instead, they are better understood in light of hydrodynamic processes requiring mechanisms of particle interaction. For the particular case of FBOTs, it is believed that the optical emission is produced when the SN ejecta hits the slow and dense confined shell of CSM that was released during stellar pre-outbursts [Strotjohann et al., 2021]. In practice, the denser and the lighter and thinner the shell

of pre-ejected material ($\lesssim 10\% M_{\odot}$), the faster are the shock interactions, resulting also in faster and brighter optical transients [Ho et al., 2020].

To date, the most extreme FBOT observed was AT2018cow [Fox and Smith, 2019; Mohan et al., 2020; Xiang et al., 2021] (Figure 2.21), which showed a peak luminosity of 10^{44} erg/s and an outstanding rise time-scale of $t_{1/2} < 1.7$ days ($t_{1/2}$ represents the time to rise above half-maximum). This event was located at ~ 60 Mpc and triggered an extensive multiwavelength follow-up campaign from radio to gamma-ray waves. The inferred densities of the CSM, $n_H = 10^9 - 10^{11} \text{ cm}^{-3}$, suggest that the system acts as a cosmic ray calorimeter, with most (or at least a major fraction) of the energy from accelerated particles being transferred into π^0 decay [Yaron et al., 2017]. This scenario is very similar to the observed high ejecta speed and densities derived from the recent detection of RS Ophiuchi. In summary, FBOTs have emerged as a unique group of potential sites for cosmic-ray acceleration, and in particular of PeVatrons, due to the right conditions provided by the high-density winds of the progenitor stars [Bell and Lucek, 2001; Cristofari, 2021; Schure and Bell, 2013]. Their probe by IACTs could further constrain the environment in which they develop.

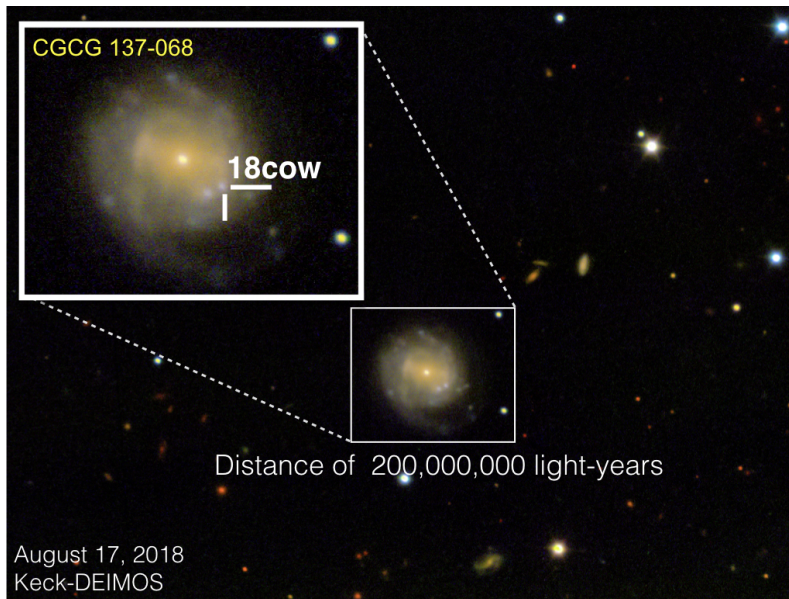


Figure 2.21: W. M. Keck Observatory’s image of AT2018cow and its host galaxy. Credit: R. Margutti/W. M. Keck Observatory

2.5.4 The generic shock powered transient scenario

As previously mentioned, the nova V906 Car displayed a correlated detection of its optical and high-energy gamma ray emissions, suggesting that both components originate from the same mechanism [Aydi et al., 2020]. The proposed scenario considers that in the early stages of the eruption, a dense and slowly expanding torus composed of a very complex density profile is ejected with an expansion velocity of $\lesssim 600 \text{ km s}^{-1}$ from the orbital plane of the binary. This ejection is then followed by fast winds (travelling at speeds of $\lesssim 1000 - 3000 \text{ km s}^{-1}$) that collide with the pre-existing

torus. These non-relativistic shocks lead to the production of the observed GeV gamma-ray radiation. As has been noted in several other different novae, no detection of X-rays has been observed in coincidence with the optical and gamma ray emission. It is proposed that most of the luminosity of V906 Car is radiated as X-rays from shock dissipation, but that this emission is strongly reprocessed and emerges in the optical regime. The kinetic power of V906 Car's shocks is estimated at $\gtrsim 10^{38}$ erg s $^{-1}$, which is of the same order of magnitude as the inferred bolometric luminosity ($\sim 10^{38}$ erg s $^{-1}$). These results suggest that in the classical novae scenario, a substantial fraction of the luminosity derived from energetic shocks can emerge as optical light due to intense absorption effects.

A generic calorimetric technique has been proposed to infer upper limits on the gamma-ray and neutrino fluences in a generic shock powered transient scenario [Fang et al., 2020]. This model has shown great success in explaining the observed SED of V906 Car. An explosion ejecta (e.g., the unbound stellar debris stream from TDEs or the explosion ejecta from SNe) collides with the dense external medium, covering a fractional solid angle of $f_{\Omega} < 1$. As the gas heats, the bulk of the shock kinetic energy is converted into thermal emission with a given energy of $kT_{\text{sh}} \propto v_{\text{sh}}^2$ keV. For typical shock velocities greater than 10^3 km s $^{-1}$, most of this radiated energy would be emitted in the X-ray range. Due to the high photoelectric opacity expected to take place during the time of the optical peak, most of the thermal emission would be absorbed and reprocessed into the optical band. In order for the shocks to be radiative, i.e., for the bulk of their kinetic energy to be converted into electromagnetic radiation instead of lost via adiabatic shock expansion, it is necessary that both thermal and relativistic particles have enough time to cool in comparison to the dynamical time of the shock, $t_{\text{cool}} < t_{\text{dyn}}$.

A small fraction of the shock power is converted into non-thermal particle acceleration, resulting in a total luminosity L_p placed in protons. From this fraction of non-thermal power, a second fraction is then irradiated in gamma rays, producing the following luminosity [Fang et al., 2020] (Eq. 21)

$$L_{\gamma} \approx f_{\gamma} f_{\pi} L_p. \quad (2.23)$$

In the above equation, $f_{\pi} = 1 - e^{-\tau}$ represents the pion production efficiency from either photo-meson interactions or from pp collisions. The factor f_{γ} is introduced to account for the energy transfer of protons to the secondary gamma rays, with approximately half of channels in pion production leading to π^0 [Hümmer et al., 2010]. Provided that $\tau_{\gamma\gamma}$ and $\tau_{p\gamma}$ (or τ_{pp}) are known at a given energy and time, the unabsorbed gamma-ray luminosity (correcting for both internal and EBL attenuation) can be used to constrain L_p in a specific energy band.

2.5.5 Future prospects

Astrophysical transient events operate at a wide scope of time-scales, ranging from fractions of a second to weeks or even years. They can be observed within our own Milky Way and at high redshift cosmological distances. In addition, they are often characterised by their extreme nature, involving the total or partial explosion or disruption of an astrophysical source. For this reason, their transient

emission can be comprehended by a wide range of wavelengths, both in electromagnetic radiation and gravitational waves. In the past few years, observations by the Fermi-LAT and optical surveys suggest that some specific classes of transients provide the ideal conditions for the formation of shock interactions and could produce HE or VHE gamma-ray emission [Fang et al., 2020]. Figure 2.22 presents the shock luminosity and time of peak brightness for several classes of transient events.

The study of astrophysical transient phenomena with the current generation of IACTs is still partly understood. This is mainly due to the low statistics of observed events, which must follow strict triggering criteria and compete with the pre-allocated observing program of each array. Because the VHE emission from transient sources can be obscured in the presence of very dense photon and matter fields, the search of these events with IACTs highly benefit from improved analysis techniques.

The CTAO is the next generation ground-based observatory of VHE gamma rays. It will provide an improvement in sensitive of up to an order of magnitude compared to current instruments. Additionally, it will be the largest gamma-ray observatory, composed of a total of 64 telescopes within two sites, one in the northern hemisphere (at the island of La Palma) and the second in the southern hemisphere (near Paranal, Chile)⁵. By employing telescopes of different sizes (small, medium and large), the array will be able to investigate gamma rays ranging from 20 GeV to 300 TeV [Hofmann and Zanin, 2024].

The CTA observatory is expected to boost the probe of short time-scales at the highest energies. With its dedicated transient program, it will play a crucial role in the era of multi-messenger astrophysics. Follow-up observations will be conducted for a wide range of multi-wavelength and multi-messenger alerts. For instance, the new observatory will be able to provide the first high-statistics measurements of GRBs above ~ 10 GeV [Schussler, 2019].

⁵<https://www.ctao.org/emission-to-discovery/array-sites/>

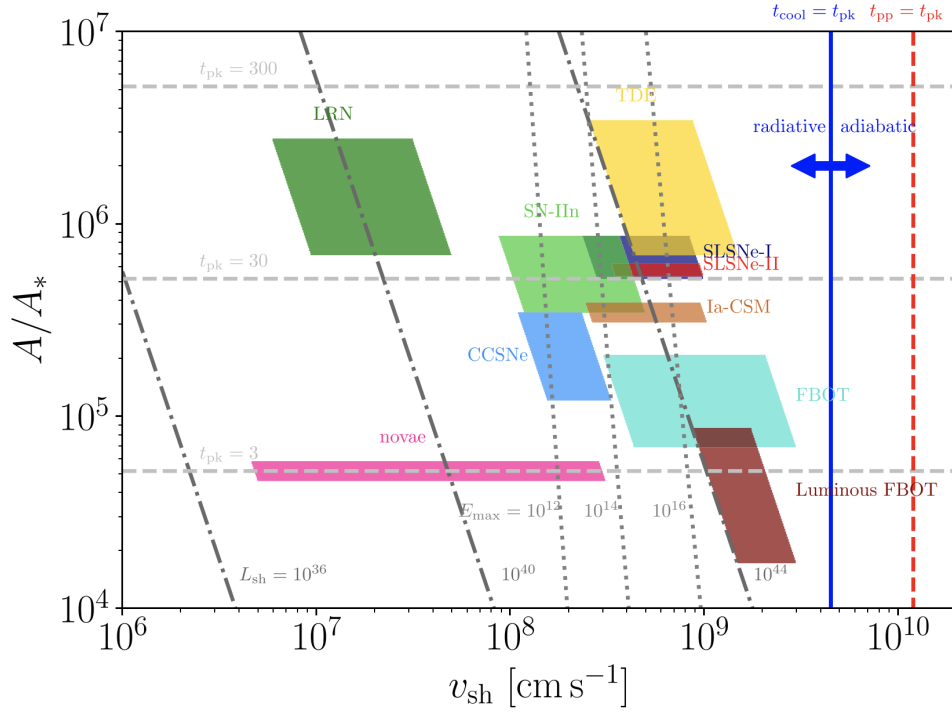


Figure 2.22: The luminosity of transient events given in the parameter space of wind mass-loss rate (A) against the velocity of the shock (v_{sh}). To produce this figure, the authors assume that a spherically expanding homologous ejecta travelling at a velocity v_w collides with an stationary external medium. The wind mass-loss rate parameter is defined as $A \equiv \dot{M}/(4\pi f v_w)$, where \dot{M} represents the steady wind of mass-loss rate, f the a fractional solid angle at which the external medium is concentrated and v_w the velocity of the wind. Typical values of $\dot{M} \sim 10^{-4} - 10 M_{\odot}$ are inferred for SNe. The parameter A is normalised to a fiducial value of $A_* = 5 \cdot 10^{11} \text{ g/cm}$. The contours represent the shock luminosity L_{sh} , peak time t_{pk} and maximum proton energy E_{max} . The vertical lines represents t_{pp} , the time scale of relativistic ions undergoing inelastic collisions with ambient ions, and t_{cool} , the cooling time of the shocked gas. Colored boxes represent the parameter space derived for several different classes of transients. More details on the calculation are available in Ref. [Fang et al., 2020]. Figure from: [Fang et al., 2020].

The Very Energetic Radiation Imaging Telescope Array System



Figure 3.1: The Very Energetic Radiation Imaging Telescope Array System. The array consists of four telescopes, which are numbered in the image (T1, ..., T4). Credit: Center for Astrophysics - Harvard and Smithsonian (Adapted)

The Very Energetic Radiation Imaging Telescope Array System [Holder et al., 2006] is a ground-based gamma-ray observatory located at the Fred Lawrence Whipple Observatory in southern Arizona, USA. A layout of the array is presented in Figure 3.1. VERITAS features four IACTs and has been operational since 2007 [Holder et al., 2008]. The final configuration of the array was completed after two major telescope upgrades. The initial upgrade, carried out in 2009, involved repositioning one of the telescopes to increase the array's symmetry, resulting in a sensitivity boost of about 30% [Perkins and Maier, 2010]. The second upgrade was carried out in 2012 and involved replacing the camera's photomultiplier tubes (PMTs) with high-quantum-efficiency devices. The new PMTs increased the photon-detection efficiency by an average of 50%. Moreover, the trigger

system was refined to account for the timing discrepancies in the pulse arrival time across different pixels [Kieda, 2013; Otte et al., 2011]. This update enabled the implementation of a narrower time coincidence window for the trigger system at the telescope level, boosting the signal-to-noise ratio by rejecting NSB-induced triggers. These improvements have collectively lowered the energy threshold of the array by approximately 15%. All data used in this thesis were gathered post these instrumental upgrades ¹.

In this chapter, I summarise the optical and mechanical structure of the VERITAS array followed by an overview of the fundamentals of data acquisition and trigger systems in Section 3.1. The analysis process, including image cleaning, and parameterisation, is described in Sections 3.2 and 3.3. Finally, a summary of the inference analysis methods for flux estimation is given in Section 4.3.

3.1 The Very Energetic Radiation Imaging Telescope Array System

The VERITAS array consists of four Davies-Cotton optical design [Davies and Cotton, 1957] telescopes (Figure 3.2), each having a focal length of 12 meters. In this particular design, the telescopes feature a spherical mirror surface, on which individual mirror facets are mounted and arranged to focus the Cherenkov light collected by the dish onto the focal point. The reflector dish of each telescope is built with 345 identical hexagonal mirror facets [Roache et al., 2008]. Each facet achieves a peak reflectivity of 92% at 320 nm, which falls within the wavelength range of Cherenkov light.

At the focal point of each telescope, there is a camera equipped with 499 high-quantum-efficiency PMTs. Each PMT contributes with a FoV of 0.15° , resulting in a total camera FoV of 3.5 degrees [Holder et al., 2006; Nagai et al., 2007] (Figure 3.3). To enhance the camera performance, each PMT is fitted with a Winston cone [Nagai et al., 2007; Winston, 1974], which serves to fill the spaces between the PMTs and to narrow the acceptance angle, thus minimising the contamination of scattered background light. After the optical alignment of the entire system, the telescopes exhibit an on-axis point spread function (PSF) ² diameter of approximately $0.10 - 0.12$ degrees, with 80% of the light being concentrated within a single camera pixel [McCann et al., 2010]. The PSF is regularly checked and shows variations under 0.02° over time and elevation angles. Moreover, the PSF progressively worsens for off-axis observations, i.e., when the source position is not at the centre of the FoV. Comparing to on-axis observations, the PSF degradation is observed to be $\lesssim 0.02^\circ$ for offset angles up to 0.6 degrees. For even larger offsets, the PSF can be up to ~ 0.2 degrees poorer [Adams et al., 2022].

3.1.1 Fundamentals of the data acquisition and trigger systems

The PMTs of the camera operate at a nominal gain of approximately $2 \cdot 10^5$ [Holder et al., 2006]. Each PMT is also coupled with high-speed pre-amplifiers, which enhance the signal by a factor

¹The period comprising the start of first observations (01.09.2007) to the first upgrade (31.08.2009) is referred to as V4. Similarly, the period between the first and second upgrade (01.09.2012) is referred to as V5, while the period after the second upgrade is referred to as V6.

²The PSF defines the area within which the telescope focuses 68% of light from a point source at infinity.

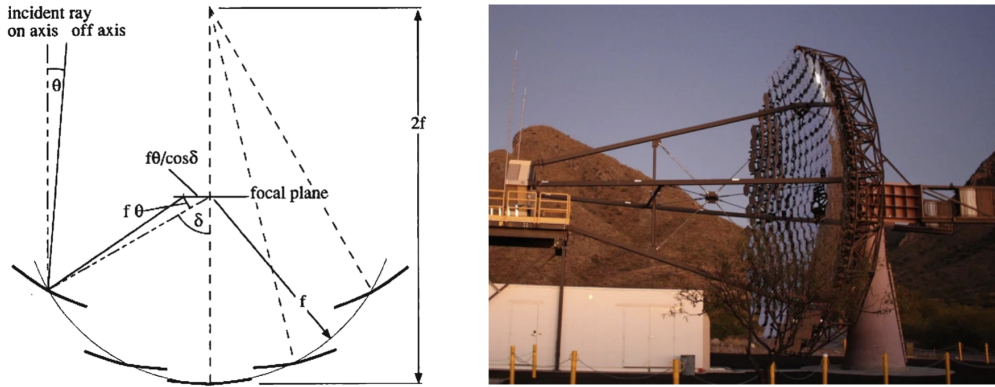


Figure 3.2: **Left:** Illustration of the Davies-Cotton mirror design, in which several mirror facets compose the reflective dish. This production is significantly more cost effective. Each mirror facet has the same focal length f (and thus a radial curvature of $2f$) as the spherical profile of the dish in which they are arranged. The telescope camera is mounted at the focal point. An on-axis gamma-ray is incident on the same direction as the pointing of the telescopes. On the other hand, off-axis gamma-rays are at an angle from the pointing position. Figure from: [Actis et al., 2011]. **Right:** The dish of one of the telescopes that compose the array. Figure from: [Hanna and Mukherjee, 2024].

of 6.6 prior to its arrival at the data acquisition system (DAQ) [Hays, 2007]. This amplification allows the camera to operate with lower high voltage (HV) settings (typically 10^3 V), thus enabling observations during partial moonlight while maintaining PMT safety against damage from high currents. The preamplifiers also feature a direct DC output for anode current monitoring, enabling the automatic shutdown of PMTs when high currents occur due to intense light sources such as bright stars or incidental illumination sources near the observatory. [Nagai et al., 2007].



Figure 3.3: **Left:** The camera of the VERITAS array. Each telescope camera contains 499 pixels. **Right:** Winston cones mounted on each pixel. Figure from: [Hanna and Mukherjee, 2024].

The PMT signals are converted to digital form by flash analog-to-digital converters (FADCs),

which capture 500 million samples per second of the PMT output [Hays, 2007]. This high-frequency digitization translates the signal into a series of digital counts across 2 ns intervals, and the data is temporarily stored in memory buffers with a capacity of 64 μ s (one digital count is equivalent to ~ 5.3 photoelectrons). This buffer size is sufficient to retain several relevant signal segments until they are processed and logged.

The VERITAS array is designed to record the Cherenkov light from EAS while effectively filtering out fluctuations from the NSB. To achieve this, the array employs a three-tiered trigger mechanism [Weinstein, 2007; Zitzer, 2013]. Upon the final trigger, the DAQ system initiates the buffer read-out of a data segment consisting of 16 samples (32 ns). During this process, the array does not respond to any triggers, a period known as dead-time. VERITAS has a typical dead-time of about 15% for a data acquisition rate of 300 Hz.

The trigger system of the VERITAS array covers the following steps:

1. *First Level Trigger (L1 - PMT Level)*: Each PMT is equipped with a constant fraction discriminator (CFD) that triggers when the signal surpasses a typical threshold of 5-6 photoelectrons.
2. *Second Level Trigger (L2 - Telescope level)*: This trigger level requires at least three adjacent pixels in a single telescope to have an L1 trigger within a time coincidence window of 5 ns. This step successfully eliminates L1 triggers caused by the NSB or by PMT fluctuations.
3. *Third Level Trigger (L3 - Array level)*: The final trigger happens at the array level. It requires that at least two telescopes register an L2 trigger within a 50 ns coincidence window, after adjusting for the propagation time of the shower front across the array.

The exact CFD thresholds are optimised for each particular set of observation conditions, as described in Table 3.1. The thresholds are calibrated by exposing the telescopes to the NSB and then selecting the threshold that maintains L3 trigger rates at a few hundred Hz, while minimising data losses due to the dead-time. Figure 3.4 shows the rate of L3 and L2 triggers under dark conditions after applying different values for the CFD threshold. The optimal CFD threshold is determined by locating the inflection point where the L3 rate induced by cosmic rays meets the rate induced by noise. An example of this calculation is shown in Figure 3.4. After a valid L3 trigger, the corresponding PMT charge over time for the event is recorded in a specialised VERITAS data format. Moreover, additional event information such as weather conditions, trigger settings and the target source are stored to a database. These final products are available for the offline data analysis.

3.1.2 Calibrations of the telescope optical response

Over time, external factors lead to the deterioration of the mechanical and electronic components of telescopes. This degradation directly affects the efficiency with which telescopes transmit light, known as the optical throughput [Adams et al., 2022]. Several factors influence this efficiency,

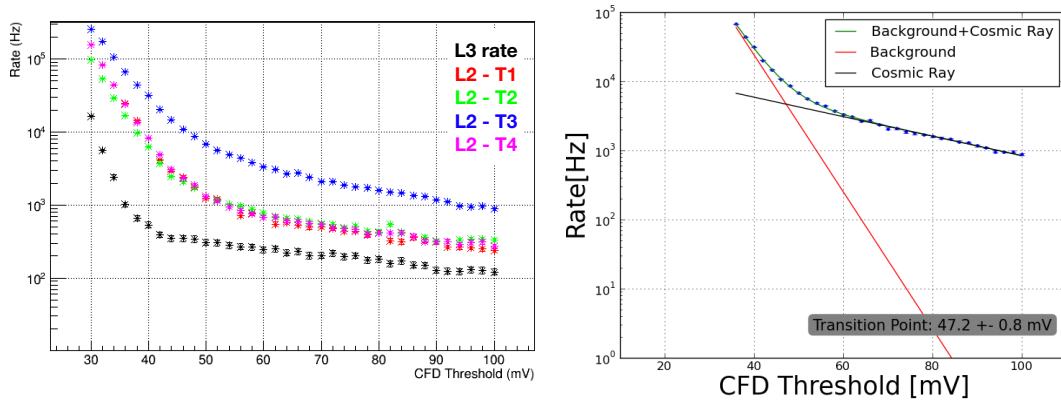


Figure 3.4: Left: Example of a bias curve which measures the rate of L3 triggers (black) and the individual rate of L2 triggers per telescopes: T1 (red), T2 (green), T3 (blue) and T4 (pink). Right: Rate of L2 triggers for telescope 4. The inflection point is calculated by the intersection between the fit of the curve expected to be generated by the noise and the fit expected by cosmic ray triggers.

including the reflectivity of the dish and Winston cones, as well as changes in the gains and quantum efficiencies of the PMTs.

To maintain the throughput performance, it is crucial to monitor these changes and implement the necessary calibrations and adjustments. Calibrations can be made through nightly measures of the relative gain of PMTs. Alternatively, absolute gains can be monitored over observing seasons³ and corrected in the simulations of the telescopes instrument response function (IRF), which establish the relationship between the recorded shower signal and the actual shower energy. The optical throughput of the telescopes should be calibrated for the following factors:

PMT gains: PMTs age and degrade due to charge accumulation. Additionally, PMTs also experience fluctuations in their relative gains due to temperature changes. To measure the relative gain of PMTs, LED flashers are used to uniformly illuminate the camera on a nightly basis [Hanna et al., 2010]. The resulting gain distributions are used to perform the flat-fielding of the camera, ensuring a uniform response across all channels. This calibration is done within the data analysis framework. If the quadratic mean of the relative gain exceeds 10%, the high voltage in the channels is adjusted. This process is usually performed twice every observing season.

On the other hand, the absolute gains of the PMTs are determined by detecting the signal from a single photo-electron [Hanna et al., 2010]. This is achieved by placing a specific camera cover that reduces the light transmission. This cover contains small holes aligned with each channel and allows less than 2% of the LED flasher light to reach the PMTs. When using this cover, the observed signal distribution is given by a histogram with distinct peaks that indicate the distribution of signals given by an integer number of photo-electrons. The measure of the single photo-electron signal is performed every month.

³An observing season for the VERITAS telescopes is defined as the period in between summer monsoons in Arizona, which occur approximately from June until August. During the monsoon period, the telescope shutdown is conducted to avoid further degrading because of the heavy rains. Therefore, an observing season lasts roughly from September until the beginning of June of the following year.

Dish reflectivity: The reflective dish of the telescopes is exposed to distinct weather conditions, including snow, sand, temperature fluctuations and the monsoon season in Arizona, which lasts for approximately three months every summer. These conditions lead to the mechanical and chemical degradation of the mirror facets. As a result, the dish can scatter light in random directions, affecting the quality of light focused into the camera and degrading the PSF. Although periodic cleaning and re-coating of the mirrors and Winston cones help regain some reflectivity, they introduce additional variability in the telescopes optical throughput [McCann et al., 2010]. Winston cones are usually protected from direct exposure to the weather conditions when the telescopes are stowed, due to a cover that protects the camera. As a result, their reflectivity remains relatively stable over time.

The calculation of the reflectivity for each VERITAS telescope is measured with a wide-field digital CCD camera device equipped with a blue filter, reproducing the PMT's spectral response to Cherenkov light. The camera is mounted at the focal plane of the reflective dish and measures the intensity of bright stars. By comparing the intensity measured by the CCD camera with that measured by the PMTs, the whole-dish reflectivity is calculated. Additionally, the same CCD method is employed to make corrections in pointing and tracking accuracy. Variations between the measured and known position of the stars allow the periodic realignment of the mirror facets [McCann et al., 2010]. The accuracy of the mechanical pointing of the VERITAS array is typically lower than 0.01° [Holder et al., 2006].

3.1.3 The throughput correction of the VERITAS array

To compensate for long-term changes in optical throughput, a correction factor per telescope, i , denoted as t_i , is implemented at the level of the simulations of the IRFs [Adams et al., 2022]. This is necessary because the simulated IRFs become increasingly inaccurate over time due to telescope degradation. One effect of the degradation is that images are seen to have a lower size than they should. The throughput factor is used to adjust the signal of the simulated gamma-ray events before the integration of the PMT trace is conducted. Therefore, we have separate sets of IRFs for each observing season. To account for seasonal changes in the atmosphere, the IRFs are also specifically categorised in summer and winter.

This throughput correction method assumes that adjustments to the simulated PMT traces can be effectively corrected with two main factors: one for camera gain adjustments and another for dish reflectivity corrections. The throughput calibration factor for each telescope, i , is given by the product of the following components $t_i = g_i \times r_i$:

Gain factor - g_i : After the PMT upgrade in 2012, an average value for the absolute PMT gain, $G_{MC,i}$, was established for each telescope, i , by using Monte Carlo simulations of the telescope design. By measuring the absolute gains, G_i , for each telescope and comparing them with the gains derived via Monte Carlo simulations, a gain correction factor per telescope, $g_i = G_i/G_{MC,i}$, is calculated.

Reflectivity factor - r_i : the term r_i focuses on the reflectivity of the telescope dish. It is given by $r_i = R_i/R_{MC,i}$, where R_i is the reflectivity measured with the CCD cameras and $R_{MC,i}$ is the

Monte Carlo simulated reflectivity after the PMT upgrade in 2012.

In this way, t_i is normalised against reference values (the reference is the 2012 PMT upgrade) based on simulations of the telescopes optical design. The evolution of t_i over different observing seasons is presented in Figure 3.5. A more detailed description of the methods for optical throughput corrections can be found in [Adams et al., 2022].

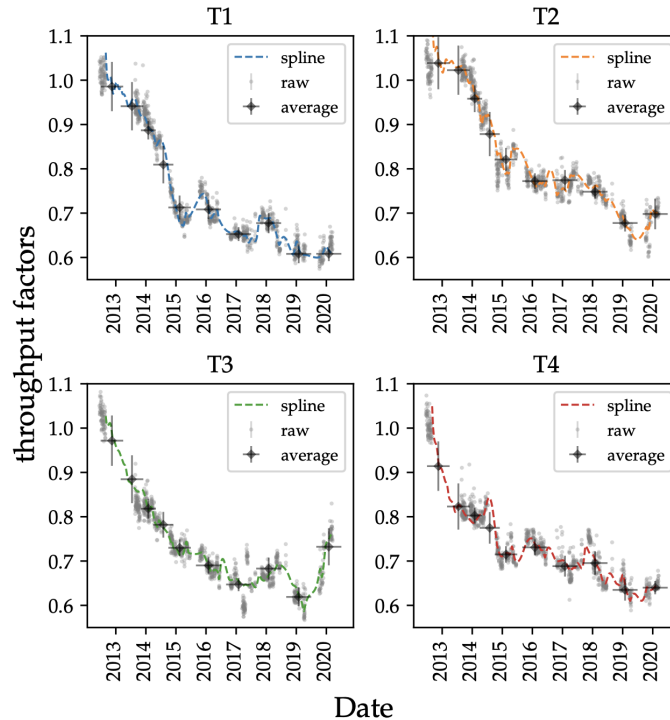


Figure 3.5: The throughput calibration factors (grey dots) per VERITAS telescope and per observing season. Black dots represent the average of the calibration factors in each observing season. A spline interpolation of t_i is given as the dashed line. Figure from: [Adams et al., 2022].

3.1.4 The Night Sky Background

High voltage and CFD settings for VERITAS observations are adapted to the intensity of the NSB in order to protect the PMTs from high currents. A safety threshold of $15 \mu\text{A}$ is generally enforced to ensure the safe operation of the camera. Observations during dark time occur when both the Sun and Moon are below the horizon, or when the Moon's illumination is less than 35%. In such conditions, the average current in the cameras depends mostly on whether the FoV is composed mainly of galactic or extragalactic fields, with galactic fields being brighter due to diffuse gamma-ray emission in the Milky Way.

For moderate moonlight conditions (Moon illumination $< 35\%$), an increased CFD threshold is applied to mitigate the accidental rate from the NSB. In this mode, typical currents are observed in the range of $10 \mu\text{A}$ to $15 \mu\text{A}$. Under bright moonlight (35% to 65% illumination), the high voltage in the PMTs is reduced to maintain the current levels between $5 \mu\text{A}$ and $15 \mu\text{A}$. When the moonlight is very bright (Moon illumination $> 65\%$), it is necessary to use a UV filter cover on

the camera [Archambault et al., 2017]. This cover significantly reduces ($> 90\%$) the transmission of moonlight while still allowing a reasonable amount of Cherenkov light to reach the PMTs. This operational mode, referred to as UVF, is further discussed in Chapter 6. The observation settings are summarised in Table 3.1.

Observing conditions	Settings	Typical currents (μA)
Dark conditions	Nominal voltage / ~ 50 mV CFD	4 - 7
Moonlight $\lesssim 35\%$	Nominal voltage / ~ 50 mV CFD	$\lesssim 10$
$35\% \lesssim$ Moonlight $\lesssim 65\%$	85% Nominal voltage / ~ 60 mV CFD	5 - 15
Moonlight $\gtrsim 65\%$	UV filter	2 - 10
Full moon	No observations	-

Table 3.1: Observing conditions, HV, CFD settings and typical currents for all observing modes of the VERITAS array.

In this section, I summarise the different factors which contribute to the variability of the NSB:

- **Astrophysical Light Sources:** The light from stars within the FoV of the camera is one of the main components of the NSB. Very bright stars can cause high currents in specific camera pixels, leading to their shutdown. The intensity of starlight varies with the observed sky section. In particular, when taking calibration runs, it is important to point the telescope to dark patches of the sky in order to decrease the contribution of the starlight.
- **Galactic vs. Extragalactic Fields:** The variability of the NSB is influenced by whether the FoV is primarily composed of galactic or extragalactic fields. Galactic fields are notably brighter due to the diffuse gamma-ray emission from proton interactions with interstellar dust. The EBL contribution to the background is negligible.
- **Airglow:** During the day, the atmosphere absorbs UV radiation from the Sun. This leads to the airglow effect at night, which is emitted by the excited atoms and molecules of the atmosphere. The airglow features different atmospheric emission lines, which are influenced by processes such as photo-ionisation and dissociation. The intensity of the airglow can change in timescales from minutes to years, depending on the atmospheric conditions and solar activity. In addition, the airglow is also highly dependent on the zenith angle, with higher angles suffering with a brighter intensity.
- **Light Pollution:** Light from cities, vehicles, and aircraft near the observatory affects the NSB. This effect is especially seen at the VERITAS site when the telescopes point at low elevations towards urban areas, like the nearby city of Tucson. The artificial light sources can significantly impact the currents in the PMT. This is also often seen when private vehicles drive on the public road near the observatory. In such cases, the observations have to be interrupted.

- **Moonlight:** As the major NSB source, the moonlight introduces special operational adjustments based on its phase and illumination. The effects of moonlight are exacerbated by clouds, which scatter the light. Ideally, observations would be conducted in the darkest conditions, i.e., during new Moon or when the Moon is below the horizon. However, this would significantly reduce the available observation time. One strategy to mitigate the impact of the moonlight on PMT currents is pointing the telescope 90 degrees away from the Moon. As will be further discussed in Chapter 6, the spectrum of the Moon and Cherenkov light look remarkably different (Figure 6.1). For this reason, much of the moonlight is also not expected to affect the telescope cameras.
- **Zodiacal Light:** The difusive sunlight can also add a new component to the NSB when it is scattered by interplanetary dust, known as the zodiacal light. Although this light is very faint compared, for example, to the moonlight or the light pollution, it can still affect the PMTs.

Figure 3.6 presents the different intensities in the contribution of each noise source to the NSB. Due to their random and independent nature, the distribution of the NSB signal should be consistent with a Poissonian distribution.

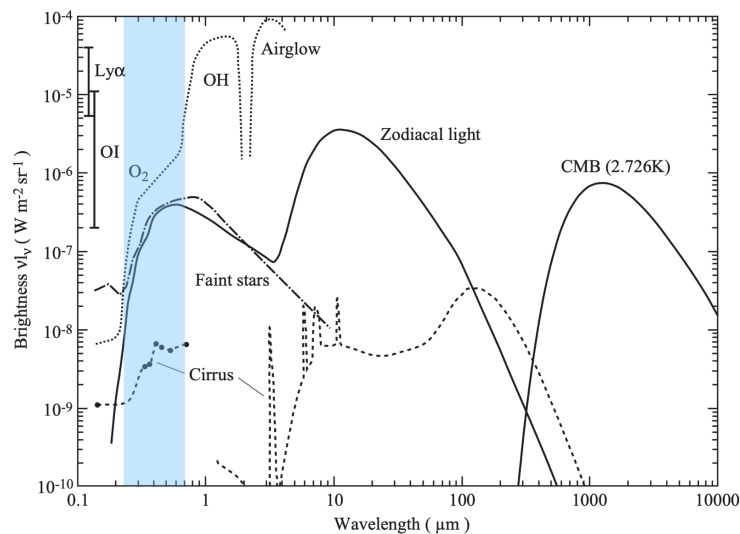


Figure 3.6: The brightness of some components of the NSB. The range of Cherenkov light is highlighted in blue. Figure adapted from: [Leinert et al., 1998].

Besides the NSB, telescopes are also subjected to electronic noise originating from spontaneous fluctuations of currents and voltages. Disturbances originate, e.g., from the thermal noise of the electronic components and fluctuations of the read-out and digitisation devices. Each of these components contributes to the overall noise floor and affects the sensitivity and accuracy of the telescopes. In order to measure the baseline intensity of the variable noise, artificial triggers of the telescope, known as **pedestal events** [Daniel, 2007], are taken at a rate of 1 Hz. These events are being recorded in the absence of any L3 triggers to specifically capture the noise intensity without the contamination of the Cherenkov light from particle showers. In 30 minutes of observations,

approximately 1500 independent pedestal events will be recorded from each pixel (taking into account that a data acquisition rate of ~ 300 Hz has a dead-time of $\sim 15\%$). Since the NSB may fluctuate during data collection, the pedestals are averaged in time intervals of 3 minutes. This is particularly important in scenarios like moderate moonlight conditions, where the Moon's elevation changes throughout the run. Pedestals can have drastically different distributions depending on the random noise sources acting on each pixel. Figure 3.7 shows the pedestal size for two different channels in the same observing run.

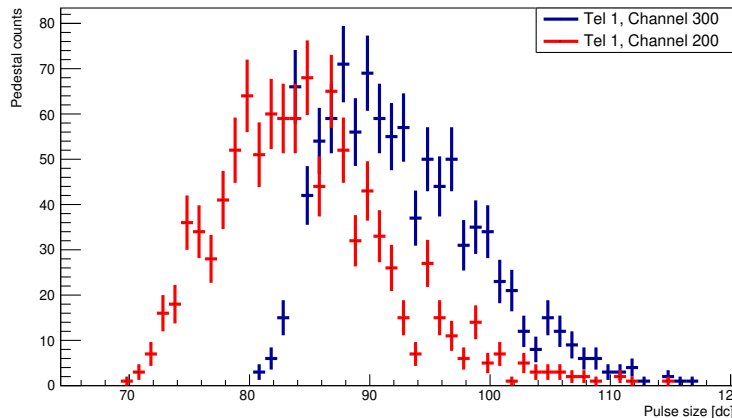


Figure 3.7: Distribution of pedestals in two different channels (200 in red and 300 in blue) during the same observing run.

Subtracting the pedestal level from the complete PMT signal is crucial to identify the true Cherenkov signal. Under dark sky conditions, the typical NSB rate is observed to be a few hundred MHz per pixel, but it can increase up to 1000 MHz under bright moonlight, while L3 trigger rates can be twice as high. Figure 3.8 shows the dependence of the NSB rate with the variance of the pedestal levels⁴ for Monte Carlo simulations of the VERITAS array. The NSB is typically described as the frequency (in MHz) at which the pixels of a camera will experience a charge of a certain value. This frequency can be translated as an integrated noise flux by convolving with the camera's collection area and the mirror's area and reflectivity. For instance, an NSB rate of 200 MHz corresponds to an NSB integrated flux of $2.8 \cdot 10^{12}$ photons/m²/s/sr [Maier, 2005].

To achieve a reliable reconstruction of the shower signals, it is crucial to effectively eliminate the noise-induced image pixels. The higher the NSB level, the more stringent should be the charge cuts for this elimination. A poor image cleaning can lead to distortions in the assessment of the true energy and incoming direction of the primary particles.

⁴From now on the variance of the pedestals is also referred to as *pedvar*.

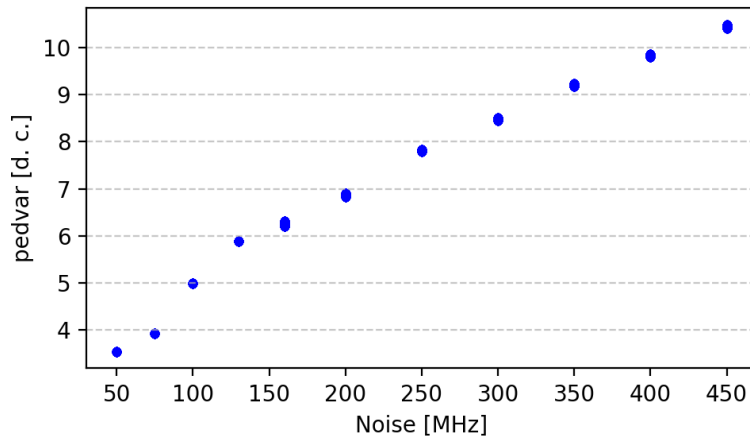


Figure 3.8: Dependence of simulated pedestal variances with noise rates.

3.2 Event reconstruction

The steps regarding event reconstruction and inference analysis presented in this thesis are implemented within the *EventDisplay* framework [Maier and Holder, 2017], an analysis and reconstruction package for IACTs. An additional analysis pipeline is also provided within the *VEGAS* framework [Cogan, 2007]. Since variations in the analysis procedure can be observed within the two pipelines, we focus on the methods implemented by *EventDisplay*.

3.2.1 Charge integration and image cleaning

Figure 3.9 presents a typical FADC trace for a camera pixel, demonstrating examples both with and without Cherenkov light. The typical pulse shape containing Cherenkov light is characterised by a rapid rise from the pedestal level to the peak charge, followed by a slower decline back to the baseline level. Conversely, pixels containing only noise are characterised by fluctuations around the pedestal level. An initial estimation of the pulse arrival time, T_0 , is given as the midpoint of the signal's maximum height.

The conventional procedure for cleaning and calibrating VERITAS data is known as the double-pass method [Holder, 2005]. The charge in each pixel is first measured using a wide integration window of 16 ns (which is equivalent to 8 samples of 2 ns), and then the pedestal is subtracted.

The final image is composed in two groups: core pixels and boundary pixels [Bond et al., 2003; Daniel, 2007]. Core pixels undergo a strict threshold cut, while boundary pixels are selected based on a less strict charge cut, provided they are adjacent to core pixels.

The conventional image cleaning process can be described in three main steps:

1. The potential core pixels of the image are selected by finding the pixels with a signal strength that is at least 5 standard deviations (σ) higher than the pedestal variance, which provides the baseline noise level.

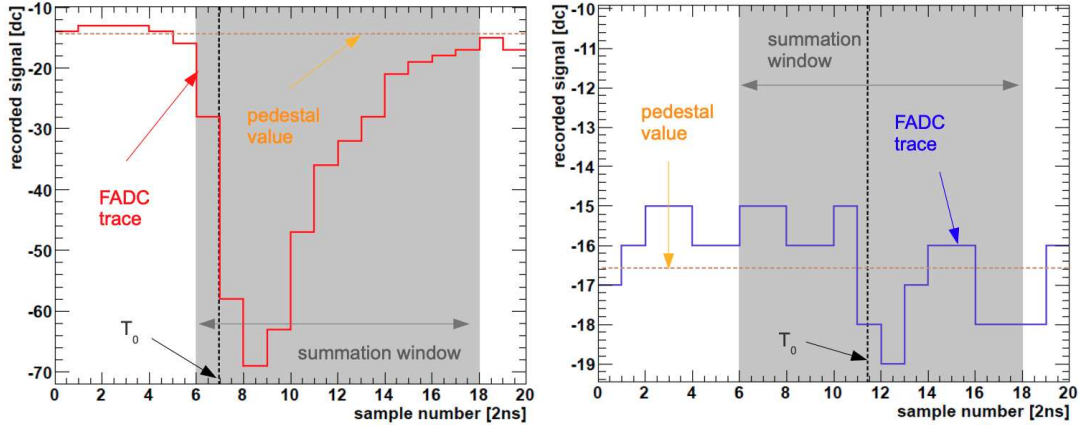


Figure 3.9: The method for pixel charge integration. The FADC digitises the analogue current of the PMT in samples of 2 ns. Left: Typical pulse of a pixel containing Cherenkov light and NSB. The pedestal level is shown as the orange line, while the digitised pulse is shown in red. The initial estimate of the arrival time of the pulse in the pixel, T_0 , is given by the sample at half-maximum. The integration is first performed on a wide window of 12 ns. After the image is cleaned and the time gradient has been determined, a narrower integration window of 6 samples is used. Right: The typical FADC trace of a pixel with no Cherenkov light fluctuates around the pedestal level. Figure from: [Prokoph, 2013]

2. The criterion for selecting boundary pixels is based on their direct adjacency to core pixels and their charge level being at least 2.5σ above the pedvar.
3. Core pixels with no neighbours meeting the boundary threshold (2.5σ) are discarded. This topological condition guarantees that upward noise fluctuations are removed.

With the applied threshold cuts ($5\sigma/2.5\sigma$), the majority of pixels contaminated by noise will be eliminated but also some pixels containing the shower signal might be inadvertently removed.

The morphology and distribution of arrival times obtained from the elliptical images captured by the camera are directly correlated to the longitudinal development of the shower and the variations in the path lengths of the Cherenkov photons to each PMT. As a result, a time gradient, $T_{\text{grad},x}$ is observed along the major axis of the images, as seen in Figure 3.10. This gradient is used to determine the starting position of a narrower integration window (12 ns), which is chosen because it maximises the signal-to-noise ratio. This second measure of the PMT charge with this narrower window is then used to re-parametrise the image and is employed in the subsequent steps of the analysis. The typical time resolution achieved by VERITAS in the double-pass method is in the order of 0.2 ns [Holder, 2005]. Figure 3.11 shows the average pedestal in the camera, along with the raw image, containing the pedestal and Cherenkov light, and the final image constructed with the double-pass method.

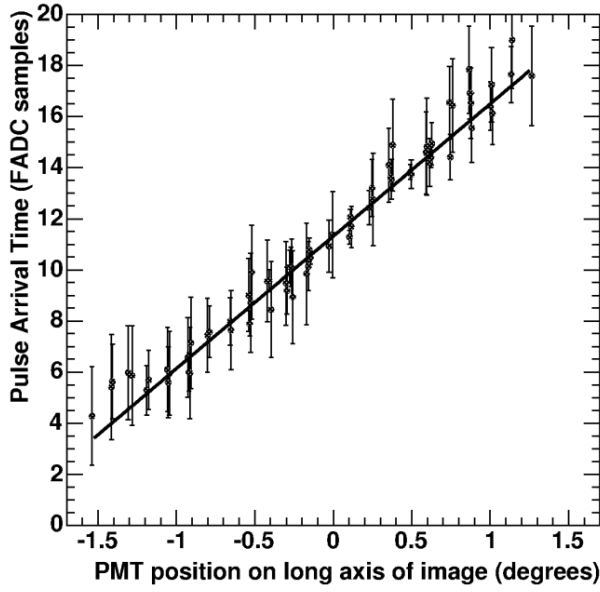


Figure 3.10: The time gradient of pixels after image cleaning. The gradient is given by the distribution of T_0 by the PMT position along the major axis of the image. This gradient is used to place a second narrower integration window. Figure from: [Holder, 2005].

Improvements in the threshold cleaning were achieved by eliminating outlier pixels which contain signal from afterpulsing effects. Afterpulsing refers to the secondary pulses triggered by ions generated during the PMT amplification process [Otte et al., 2011]. They originate from the collisions of the electrons with the PMT dynodes. Because they are positively charged, the ions can travel back to the photocathode and the collision with the material can release secondary electrons. This new pulse arrives nano- to microseconds after the initial one and appears in the camera as high signal-isolated pixels. It was observed that removing these outliers significantly improved the sensitivity of the telescope since they are typically bright and appear randomly in various locations of the camera, thereby distorting the Hillas parameterisation of the image, which is discussed in the next section.

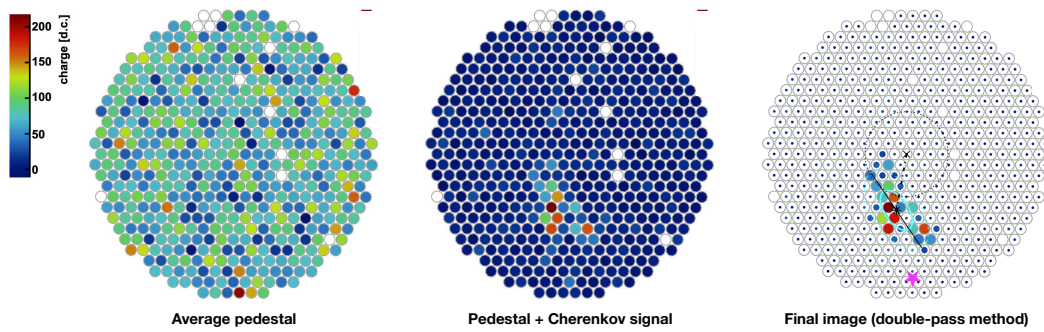


Figure 3.11: Right: Average pedestal in the telescope camera. Middle: Event composed of noise and Cherenkov light. Right: Final image, composed after the full application of the double-pass method. Blank pixels are either dead or disabled due to high currents.

3.2.2 Image parametrisation

The two-dimensional projection of the intersection of the Cherenkov light from particle showers with telescope cameras produces elliptically shaped images. This shape is a result of a combination

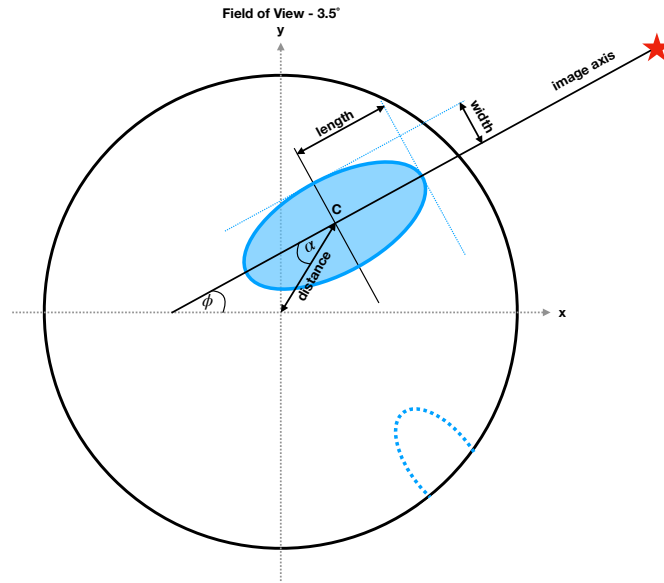


Figure 3.12: Hillas parameters of an image from a particle shower: width (w), length (l), centroid of the image (C) and distance. A truncated image is also represented with the dashed line. The major axis of the image points to the shower arrival direction, marked as the red star.

of the Cherenkov emission angle, the distribution of particles within the shower and the pointing of the telescope. The size and dimensions of the images are determined by various factors, including the type, energy, and angle of the primary particle, as well as the telescope's viewing angle. In order to derive the properties of the incoming particle, the image is parametrised according to the method from *Hillas, 1985* [de Naurois, 2006; Hillas, 1985]. The following parameters are calculated:

- **Size (s):** the total charge of the image, obtained by the sum of the FADC trace integrations over all image pixels, after the application of the double-pass method;
- **Width (w):** the root mean square of the minor axis of the image;
- **Length (l):** the root mean square of the major axis of the image;
- **Centroid (C):** the coordinates of the centre-of-gravity of the image;
- **Distance (R):** the distance from the image centroid to the center of the FoV of the camera;
- **Loss:** the fraction of the size on the edge of the camera from truncated images.

Figure 3.12 illustrates the Hillas parameters described above.

3.3 Stereoscopic reconstruction of events

The stereoscopic reconstruction of events recorded by IACTs involves using the images from two or more telescopes to derive properties of the primary particle that initiated the shower, such as

incoming direction and energy. An initial quality assessment of the camera images is performed. Images that do not pass the following criteria are discarded from the subsequent analysis steps:

- Angle between image axes > 10 degrees,
- Number of pixels in image > 5 ,
- Image size > 100 digital counts,
- Image loss (only for truncated images) $< 20\%$,
- Image width $> 0.02^\circ$.

The stereoscopic reconstruction methods rely on simulations of gamma-ray showers and detector response. Simulations of atmospheric showers are conducted using the CORSIKA⁵ program [Alameddine, 2023], assuming that gamma-rays arrive at particular values of zenith angle (ranging from 0° to 65°) and within the full range of azimuth angles (0° - 360°), to account for the different effects of the geomagnetic field deflections. The simulated showers cover the energy range from 30 GeV to 200 TeV, following a E^{-2} power-law spectrum. In these simulations, telescopes are assumed to be fiducial spheres at the telescope position. Any shower that intersects this sphere is recorded.

The CARE⁶ and GrOptics⁷ packages provides the simulated response of the array. This includes a design model of the telescope's optical and trigger systems, as well as other attributes, such as mirror reflectivity and atmosphere conditions. In addition, noise from the NSB is simulated and incorporated into the analysis.

3.3.1 Direction reconstruction

Since the major axis of each image represents the shower axis, the direction of the shower is determined by combining the images from different cameras onto a single plane [Hofmann et al., 1999]. The direction of the shower is given by the size-weighted intersection of the major image axes. Similarly, the core position (or impact parameter) can be calculated by projecting the intersection point of the image axes on a plane perpendicular to the pointing position of the telescopes. With this information, we find the distance, R , from the shower core to the telescopes.

Showers with impact parameters further away from the telescopes tend to produce images with parallel axes, reducing the angular resolution. The angular resolution of an instrument represents the angular distance from the true source position that contains 68% of the reconstructed gamma-ray events. The best accuracy in direction reconstruction happens when the angle between two image axes is close to 90 degrees. Conversely, smaller angles between the axes reduce the effectiveness of the method. The limitations of this method can be overcome with machine learning

⁵www.iap.kit.edu/corsika/

⁶<https://github.com/nepomukotte/CARE>

⁷<https://github.com/groptics/GrOptics>

techniques, which use boosted decision trees (BDTs) trained with simulated image parameters. The geometrical method for direction reconstruction is shown in Figure 3.13.

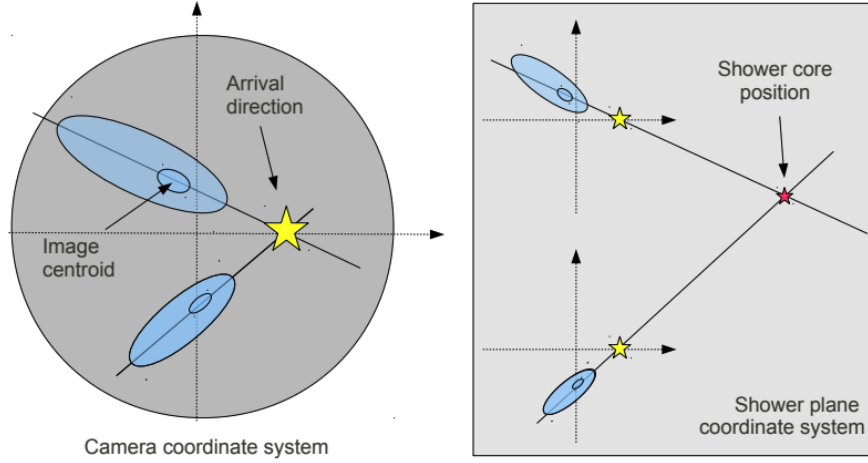


Figure 3.13: Illustration of the geometrical method for direction reconstruction. Left: The images from the triggered telescopes are superimposed into a single camera coordinate system. The direction is found by calculating the intersection of the major axis of the images and calculating the size-weighted point of intersection. Right: The shower plane is given by the intersection of the images major axis. Figure from: [Prokoph, 2013]

3.3.2 Energy reconstruction

To reconstruct the total energy of the primary particles, lookup-tables consisting of simulated image sizes and impact parameter distances (R) are produced. Figure 3.14 presents one example of a lookup-table for simulated showers arriving at a zenith angle of 20 degrees. The energy of a shower for an event with N triggered telescopes is given by:

$$E = \frac{\sum_{i=1}^N \frac{E_{MC,i}(R,s)}{\sigma_E^2(R,s)}}{\sum_i \frac{1}{\sigma_E^2(R,s)}}, \quad (3.1)$$

where $E_{MC,i}$ is the median energy of the distribution of simulated shower energies (for telescope i) given the measured shower parameters: s and R . The factor σ_E represents the 90% containment range of this distribution.

3.3.3 Gamma/hadron separation

In an ideal scenario without background contamination, the number of reconstructed events would follow a Poisson distribution with a variable given by the number of source counts. However, hadronic cosmic rays, which are typically about 1000 times more prevalent than the gamma-ray signals, dominate these events [Maier and Knapp, 2007]. Due to the distinct nature of cosmic-ray showers compared to the electromagnetic cascades initiated by gamma-rays, the resulting images

exhibit different density distributions. For this reason, the Hillas parametrisation can be employed to discriminate between gamma-ray signals and background noise [Fegan, 1997; Krawczynski et al., 2006]. The two main parameters observed to have very distinct distributions for gamma-rays and cosmic-rays are the mean scaled width (MSCW) [Krawczynski et al., 2006]:

$$\text{MSCW} = \frac{1}{N} \sum_i^N \left(\frac{\text{width} - w_{MC,i}(R, S)}{\sigma_{MC,i}^w(R, S)} \right), \quad (3.2)$$

and the mean scaled length (MSCL):

$$\text{MSCL} = \frac{1}{N} \sum_i^N \left(\frac{\text{length} - l_{MC,i}(R, S)}{\sigma_{MC,i}^l(R, S)} \right), \quad (3.3)$$

where $w_{MC,i}$ ($l_{MC,i}$) is the median width (length) of the distribution of simulated shower widths (lengths) given the shower parameters s and R . In addition, $\sigma_{MC,i}^w$ ($\sigma_{MC,i}^l$) represent the 90% deviation of this distribution. The values of $w_{MC,i}$ ($l_{MC,i}$) and $\sigma_{MC,i}^w$ ($\sigma_{MC,i}^l$) are also determined with lookup-tables composed of the impact parameter distance and size from simulated showers, such as in Figure 3.15.

An example of the distributions of these parameters is presented in Figure 3.16. The gamma-ray distribution follow a Gaussian profile centred around zero. In contrast, background events exhibit distributions with extended tails, and mean values shifted towards larger numbers, indicating their image profiles are much broader than for gamma-rays. Additional parameters for the gamma/hadron separation also include the emission height [Aharonian et al., 1997], which is the altitude at which the shower achieves maximum density, and the offset of the event's reconstructed direction to the source position. Events with significantly high offsets are less likely to originate from the gamma-ray source.

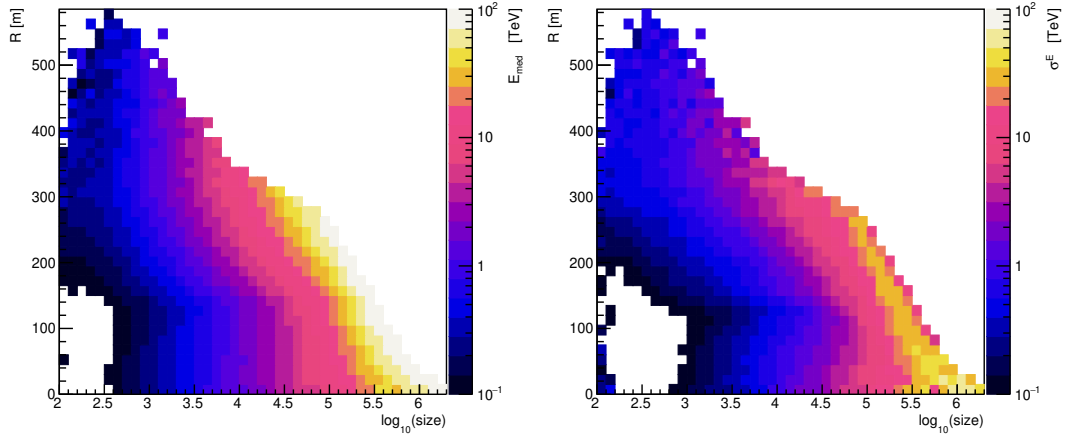


Figure 3.14: Lookup-table consisting of the median energy of the distribution of simulated shower energies, $E_{MC,1}$, (left) and 90% containment range of the energy distribution, $\sigma_{E_{MC,i}}$, (right) per image size and impact parameter distance (R). One lookup-table is produced per telescope. Simulated events were produced for a zenith of 60 degrees, with a noise rate of 200 MHz and assuming a FoV offset of 0.5° from the source position. The process of the lookup-table consists in finding the size and impact parameter distance of the real (recorded) shower image and then finding which is their likely energy and width deviation based on Monte Carlo simulations that have the same values of R and s .

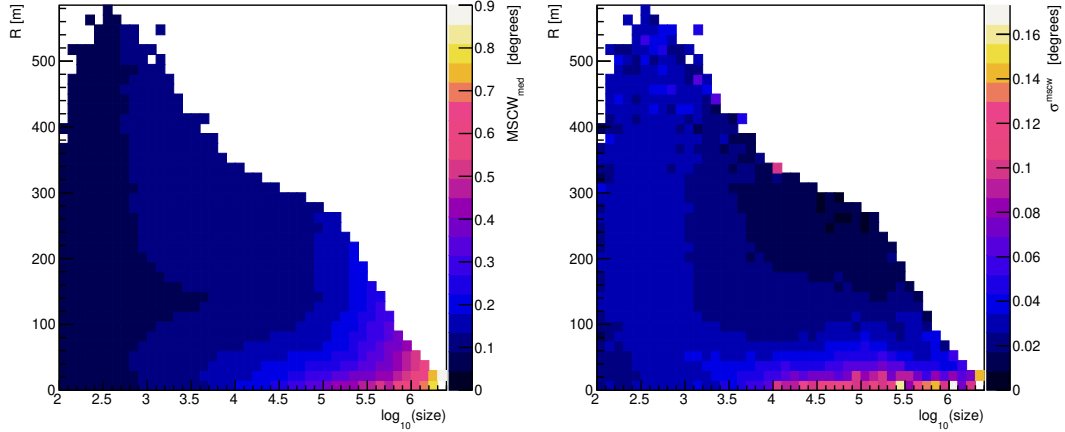


Figure 3.15: Lookup-tables for $w_{MC,1}$ and $\sigma_{MC,1}^w$. One lookup-table is produced per telescope. Simulated events were generated for a zenith of 60 degrees, with a noise rate of 200 MHz and assuming a FoV offset of 0.5° from the source position. Simulated events exhibit a distribution of widths depending on their impact parameter distance and image size. The idea of the lookup-table consists in finding the size and impact parameter distance of the true (measured) shower image and then finding which is their likely width based on Monte Carlo simulations that have the same values of R and s .

The best set of cuts for the gamma/hadron separation can be found with methods such as the grid-search (box cuts), which are derived from the optimisation of the significance on a control

dataset, or through machine learning techniques, such as BDTs [Krause et al., 2017]. The latter has the advantage of identifying non-linear correlations between parameters used for the training and also identifying those which have no discrimination power. Gamma/hadron separation cuts are optimised for source spectra following a power-law with varying spectrum indices, Γ , into the categories hard ($\Gamma < 2$), moderate ($\Gamma = 2$), soft ($\Gamma = 3$), and super-soft ($\Gamma \geq 3$). Additionally, optimisations are also made based on the energy threshold of the observation, with super-soft cuts being less stringent on the offset cut, allowing a greater reconstruction of gamma-rays at the cost of increased background noise.

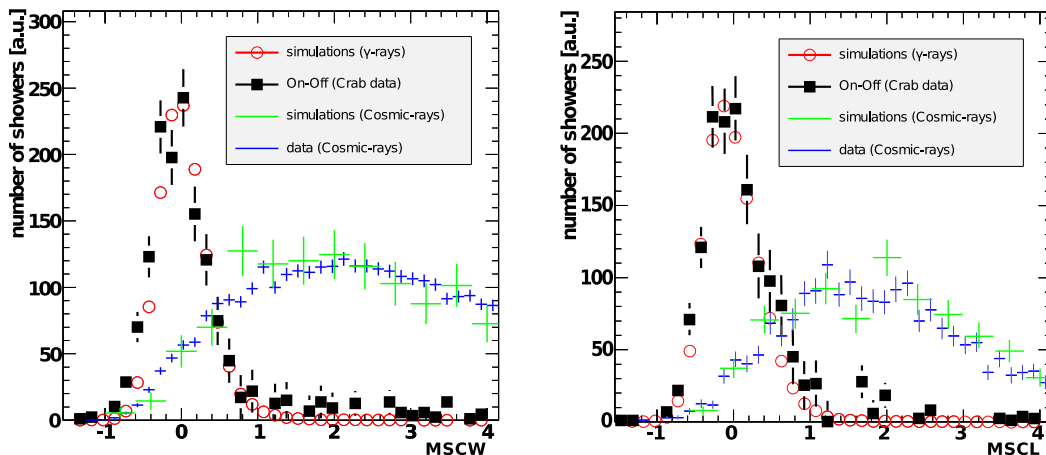


Figure 3.16: Examples of the distributions of MSCW (left) and MSCL (right). Distributions are presented for simulated gamma rays (red circles) and cosmic rays (yellow crosses). In addition, excess events from a Crab Nebula dataset (black squares) and background events (blue crosses) are also shown. Figure from: [Skole, 2016].

3.3.4 Background estimation

The final set of events obtained after the stereo reconstruction consists of a combination of gamma rays and background events, which is composed mostly of protons from cosmic-rays. To determine the excess counts within the collected data, we need to estimate the remaining background. We consider the scenario where the background counts are estimated from a region containing no source events. For this purpose, we define a Region of Interest (RoI), also known as ON region, and one or more background regions, also referred to as OFF regions [Berge et al., 2007]. Each provide respectively the number of counts N_{ON} , containing the background and events from the source, and N_{OFF} , which should contain only background events.

The selection of OFF regions is conducted on a per-run basis, either through the reflected-regions or ring background methods [Berge et al., 2007], illustrated in Figure 3.17. They are presented for the usual case of wobble observations, where the FoV centre is placed on a small offset from the source position – typically 0.5° to 2.0° . In the reflected regions method, OFF regions are given by a certain number of circular areas with the same angular size and offset from the FoV centre as the ON region. In contrast, the ring background method designates a single OFF

annular area concentric with the ON region. For both methods, regions containing particularly bright stars should be avoided or removed.

To account for differences in area and acceptance from each method, a normalisation factor is introduced [Berge et al., 2007]:

$$\alpha = \frac{\int_{\text{ON}} A(x, t) dx dt}{\int_{\text{OFF}} A(x, t) dx dt}, \quad (3.4)$$

where $A(x, t)$ denotes the camera acceptance on a particular ON or OFF region. The acceptance depends on the exposure time (t) and on the distance (x) of this region to the FoV centre. In general, the acceptance is assumed to be symmetric within the camera.

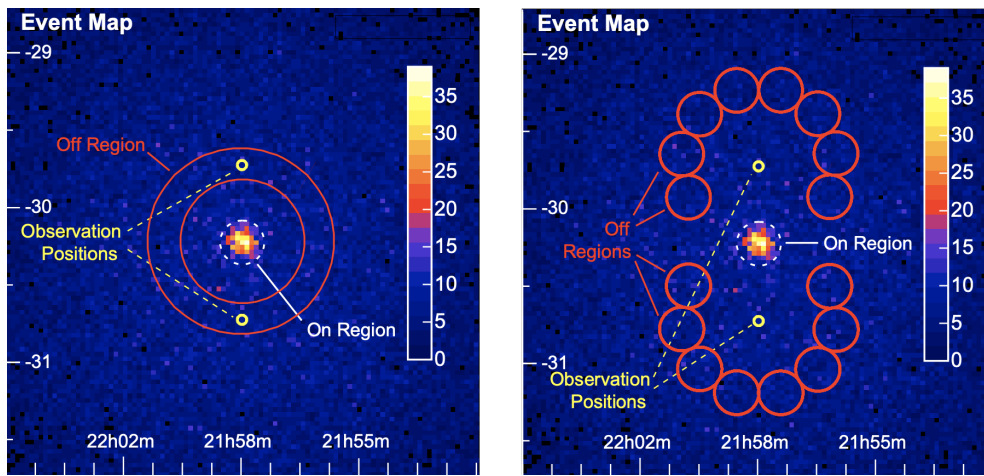


Figure 3.17: **Left:** Ring background, given as an annular region concentric to the ON region. **Right:** Reflected -regions background method, given as a certain number of circular regions with the same angular size and offset from the FoV centre as the ON region. Figure from: [Berge et al., 2007]

For the reflected regions case, the OFF and ON regions have the same acceptance due to their identical offset from the FoV center. The normalisation of the background in this method is calculated as the inverse of the number of OFF regions. Hence, if there are N reflected regions, N_{OFF} is adjusted by a factor $\alpha = 1/N$. The number of excess events is given by $N_s = N_{\text{ON}} - \alpha \cdot N_{\text{OFF}}$.

With the known number of excess and background events, the significance of the observation is given by the Li and Ma formula:

$$S = \pm \sqrt{2} \left[N_{\text{on}} \log \left(\frac{(1 + \alpha) N_{\text{on}}}{\alpha N_{\text{on}} + N_{\text{off}}} \right) + N_{\text{off}} \log \left(\frac{(\alpha + 1) N_{\text{off}}}{N_{\text{on}} + N_{\text{off}}} \right) \right]^{1/2}, \quad (3.5)$$

which is derived from statistical hypothesis methods [T. P. Li and Ma, 1983]. The positive sign of S is chosen when the number of excess events is also positive, and vice-versa. A detection is conventionally claimed for $S \geq 5\sigma$, which is equivalent to a probability of $> 99.9999\%$ that the observed excess was not caused by statistical fluctuations of the background. In the absence of a source signal, the significance follows a normal distribution with mean $\mu = 0$ and standard deviation $\sigma = 1$, as seen in Figure 3.18.

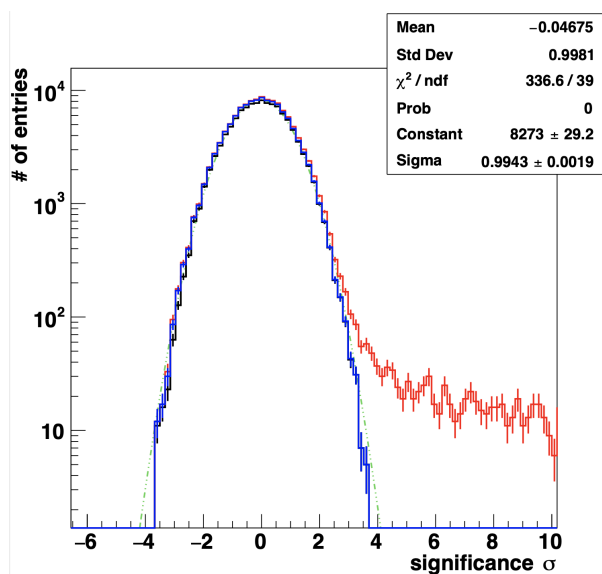


Figure 3.18: Significance distributions for source and background events. The distribution for the dataset with the ON region is shown in red, while the distribution without the ON and exclusion regions is shown in blue. The significance distribution of the latter should follow a Gaussian profile with mean ~ 0 and standard deviation ~ 1 (given as the fit by the green line).

3.4 Flux estimation and inference of model parameters

3.4.1 Instrument response functions

The outcome of the statistical analysis inference is the differential gamma ray flux, Φ , which is used to infer model parameters of the source emission. In order to derive Φ , the number of excess events must be convolved with the IRFs, which are derived from Monte Carlo simulations.

The IRFs of the VERITAS array comprise the following:

Effective Areas (A_{eff}): this parameter represents the total detection area of the telescope for gamma-rays at a certain energy. The effective area is calculated with showers simulated up to a radius in the order of $R_{\text{eff}} \sim 10^2 - 10^3$ m from the telescopes (depending on the zenith angle). The effective area reflects the quantity of simulated events that are successfully processed by the VERITAS analysis pipeline and meet the final gamma/hadron selection criteria, N_{γ}^{sel} , in comparison to the total number of simulated events, N_{γ}^{MC} :

$$A_{\text{eff}}(E) = \pi R_{\text{eff}}^2 \cdot \frac{N_{\gamma}^{\text{sel}}(E, \theta_w, \phi_z, \phi_{az})}{N_{\gamma}^{\text{MC}}(E, \theta, \phi_z, \phi_{az})}. \quad (3.6)$$

This is naturally a quantity that depends on the wobble offset, θ_w and on the energy, zenith, ϕ_z , and azimuth, ϕ_{az} , of the simulated event. Figure 3.19 shows effective areas by assuming a constant noise level with varying zenith angles. As expected, the effective area is lower at smaller elevation angles because gamma-ray showers have to pass through a higher portion of the atmosphere, leading to a loss of lower energy events before they can reach the detector.

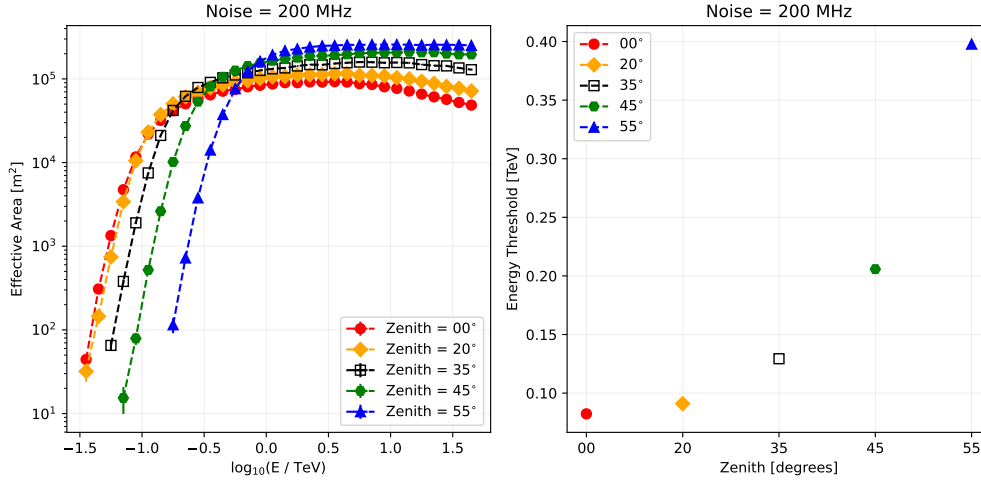


Figure 3.19: **Left:** Effective areas derived from Monte Carlo simulations by assuming a constant noise level of 200 MHz and varying the zenith angle. **Right:** Energy threshold for each respective effective area. The energy threshold is defined as the energy at which the effective area reaches 10% of its maximum.

Energy threshold: for simulated events, it is defined by the energy at which the effective area is 10% of its maximum value. It represents the lowest energy level at which a gamma rays can be detected by the telescope, under a given set of observational conditions. The energy threshold is shown on the right side of Figure 3.19. As expected, it is worse at low elevations.

Energy bias: it is defined as $(E_{\text{true}} - E_{\text{MC}})/E_{\text{MC}}$, where E_{true} refers to the true energy of the simulated gamma-ray and E_{MC} , to the reconstructed energy in the simulations. Ideally, the energy bias should be near zero across all energies, indicating a perfect reconstruction. However, in reality, the energy bias tends to fluctuate around zero. This happens, e.g., due to low-energy events being suppressed at low elevation angles or by the high cleaning thresholds, as well as due to the quality cuts, which might filter out events with small image sizes or pixel count.

Energy and angular resolution: the energy (angular) resolution is defined as the standard deviation of the energy distribution (angular distance from the source) which contains 68% of all reconstructed gamma rays simulated at a specific position.

IRFs are interpolated according to the true pointing position and noise level of the observation.

3.4.2 Flux estimation

The differential gamma ray flux, Φ , corresponds to the number of source photons per unit energy, E , time, T , and area, A :

$$\frac{dN}{dE dT dA}(E) = \frac{N_s(E)}{A_{\text{eff}}(E) T dE}, \quad (3.7)$$

where T represents the exposure corrected for the dead-time. When N observations are performed, they can be combined as:

$$\frac{dN}{dE dT dA}(E) = \sum_{i=0}^N \frac{N_s^i(E)}{A_{\text{eff}}^i(E) T^i dE}. \quad (3.8)$$

A systematic uncertainty of 25% is expected to affect the reconstructed gamma-ray energies and fluxes [Adams et al., 2022]. Systematic errors are mainly based on calibration measurements and limitations of the Monte Carlo simulations.

The minimum gamma-ray flux required for detection (5σ) in a certain amount of exposure time provides the flux sensitivity of the instrument. The sensitivity of the VERITAS array is shown in Figure 3.20. A source with 1% of the Crab Nebula strength can be detected in ~ 24 hours. Figure 3.21 shows the differential sensitivity of the VERITAS array and other gamma-ray instruments for 50 hours of observation time. The CTAO is expected to have a highly improved sensitivity in the energy range of ~ 20 GeV to 300 TeV [Caraveo, 2020].

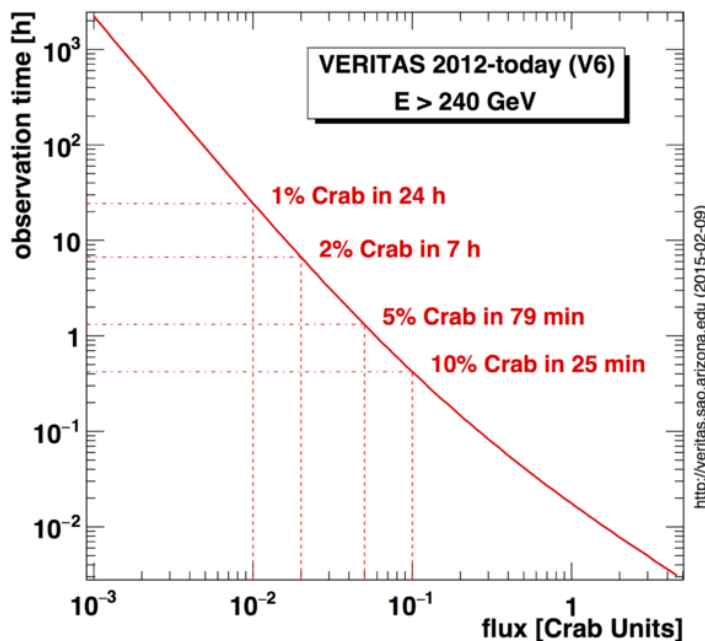


Figure 3.20: The integral sensitivity of the VERITAS array gives the necessary observing time to detect of a source of a given strength (integrated flux). A source with 1% of the Crab Nebula strength can be detected in about 24 hours. Figure available at: <https://veritas.sao.arizona.edu/>.

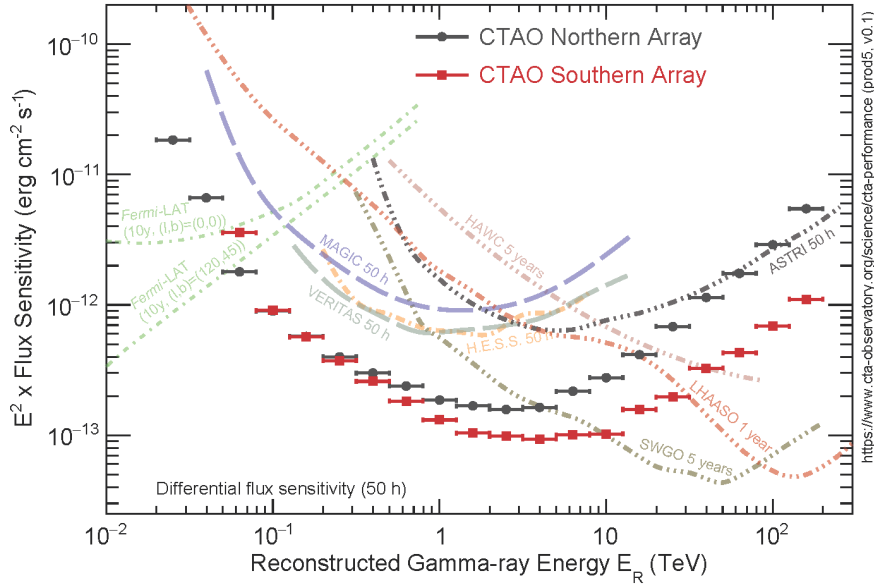


Figure 3.21: Differential flux sensitivity of several gamma-ray instruments. IACTs (50 hours): VERITAS, H.E.S.S., MAGIC and CTA (North and South). Additionally, the HAWC sensitivity is given for 1 and 5 years, while for the Fermi-LAT, for 10 years of operations. Figure from: [Pierro, 2023].

3.4.2.1 The Rolke method for the estimation of flux upper limits

Throughout this thesis, when no detection ($< 5\sigma$) is found for a given dataset, flux ULs are inferred using the *Rolke* method [Rolke and Lopez, 2001]. Some of the advantages of this method include the extrapolation to small signals and the generalisation when including additional errors on the noise estimation. For this reason, Rolke ULs are widely used in high-energy physics.

In a given observation, an experiment provides the number x and y of events recorded in the signal and background regions, respectively. The parameter τ describes the ratio between the size of the background and signal regions. In principle, τ could refer to the ratio of live-times instead of a typical area. Given the random and independent nature of every recorded photon, the probability model of the data can be described as

$$f(x, y | \mu, b) = \frac{(\mu + b)^x}{x!} e^{-(\mu+b)} \cdot \frac{(\tau b)^y}{y!} e^{-\tau b}, \quad (3.9)$$

where μ and b correspond to the expected signal and background rates, respectively. Here, b is a nuisance parameter. Confidence intervals are found using the standard technique of likelihood ratio. A null hypothesis which constrains the model parameter to a specific subset of values ($\mu = \mu_0$) is tested against the complement of the set $\mu \setminus \mu_0$, known as the alternative hypothesis. In our problem, the null hypothesis represents the absence of signal, i.e., $\mu_0 = 0$.

The likelihood ratio test statistic is denoted as

$$\lambda(\pi_0 | X) = \frac{\sup\{L(\mu_0, b | x, y); \}}{\sup\{L(\mu, b | x, y); \mu, b\}}, \quad (3.10)$$

with $L(\mu, b|x, y) = f(\mu, b|x, y)$ in this particular case. This test statistic approximates to a χ^2 distribution with one degree of freedom (2 observables minus one model parameter). Maximising $L(\mu, b|x, y)$ for b at a fixed μ yields

$$\hat{b}(\mu) = \frac{x + y - (1 + \tau)\mu + \sqrt{(x + y - (1 + \tau)\mu)^2 + 4(1 + \tau)y\mu}}{2(1 + \tau)}. \quad (3.11)$$

Figure 3.22 presents $2 \cdot \log(\lambda)$ for $x = 8$, $y = 15$ and $\tau = 5$. To determine the confidence interval corresponding to a certain Confidence Level (C. L.), two critical points are identified on either side of the function's minimum, corresponding to the maximum likelihood estimator. These points are selected such that the increase in the test statistic from the maximum likelihood estimator equals the p -th percentile of the χ^2 distribution. For example, for a confidence level of 90%, the confidence interval corresponds to the the points which show an increase of ~ 2.706 from the minimum (blue dashed line). In the case of the figure, the lower and upper bounds of the confidence interval are 0.27 and 12.01, respectively.

In the case of small (or null) signals, i.e., $x < y$, the loglikelihood function becomes approximately linear and a positive ($\mu > 0$) minimum can't be found (see e.g. the grey line in Figure 3.22). In such cases, the same method is applied, but the lower bound is then set to zero (negative rates do not have physical meaning). For the low signal curve represented in Figure 3.22 ($x = 2$, $y = 15$), an upper limit of 3.35 is found, while the lower bound is negative. In some extreme scenarios, the full confidence interval results in negative values for μ . In such cases, the first positive upper limit is found by monotonically increasing x .

In our scenario, $x = N_{\text{ON}}$, $y = N_{\text{OFF}}$ and $\tau = \alpha^{-1}$. We are interested in finding confidence intervals in the case of small signals. Once the upper bound of the lower limit has been found, $\mu = N_e^{\text{UL}}$, and assuming that the source spectrum follows a power-law function given by

$$\frac{dN}{dE} = N_0 \left(\frac{E}{E_0} \right)^{-\Gamma}, \quad (3.12)$$

the normalisation N_0 is found as

$$N_0 = \frac{N_e^{\text{UL}}}{\langle A_{\text{eff}} \rangle T}, \quad (3.13)$$

where $\langle A_{\text{eff}} \rangle$ represents the averaged effective area considering the entire energy range and weighted by the assumed power-law energy spectrum. In this equation, T represents the live-time corrected for dead-time. Integral upper limits in the range $(E_{\text{min}}, E_{\text{max}})$ can be found as

$$\begin{aligned} \Phi^{\text{UL}} &= \int_{E_{\text{min}}}^{E_{\text{max}}} \frac{dN}{dE} dE \\ &= \int_{E_{\text{min}}}^{E_{\text{max}}} N_0 \left(\frac{E}{E_0} \right)^{-\Gamma} dE \\ &= N_0 \cdot \frac{1}{1 - \Gamma} \cdot \frac{1}{E_0^{-\Gamma}} \cdot \left(E_{\text{max}}^{-\Gamma+1} - E_{\text{min}}^{-\Gamma+1} \right) \\ &= \frac{N_e^{\text{UL}}}{\langle A_{\text{eff}} \rangle \cdot T} \cdot \frac{1}{1 - \Gamma} \cdot \frac{1}{E_0^{-\Gamma}} \cdot \left(E_{\text{max}}^{-\Gamma+1} - E_{\text{min}}^{-\Gamma+1} \right). \end{aligned} \quad (3.14)$$

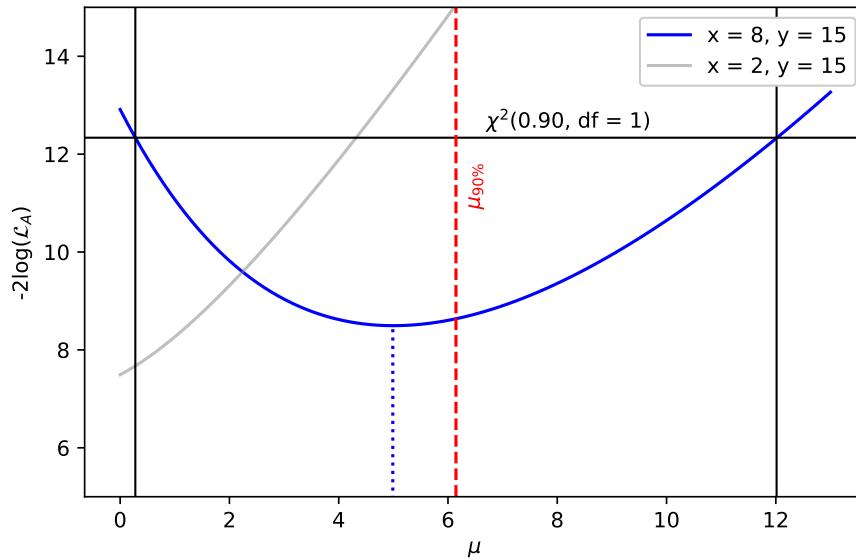


Figure 3.22: The Rolke method to find upper limits. The blue curve represents the likelihood ratio test statistic assuming $x = 8$, $y = 15$ and $\tau = 5$. The maximum likelihood estimator is represented as the blue dashed line. The confidence bounds for a confidence level of 95% are shown as the black lines. The upper limit (red dashed curve) is defined as the mean of the lower and higher bounds of the confidence interval. For comparison, the case of $x = 2$, $y = 15$ and $\tau = 5$ is also shown. When obtaining very low signals, the likelihood ratio function is approximately linear and the lower bound is negative, which does not really have a physical meaning.

Implementation of the Optimised Next Neighbour image cleaning method for the VERITAS array

During the data acquisition process of IACTs, the read-out window captures a significant amount of background noise along with the Cherenkov light from the showers. The source of noise for IACTs is composed of the NSB ¹ and electronic noise, which stem, e.g., from the afterpulsing effect. In addition, there may be occasional uncontrollable sources of light that illuminate the camera, such as aircraft and vehicles in the observatory's vicinity. The rate of these undesired noise signals can reach up to 1000 MHz per camera pixel during moonlight observations. If not properly removed, they might introduce strong bias effects during image parametrisation. For this reason, cleaning methods must be employed in order to reduce the impact of the noise on the event images.

The conventional method to avert image contamination caused by upward noise fluctuations is through the application of high signal thresholds (as discussed in Chapter 3). However, one major disadvantage of this method is the inadvertent suppression of GeV gamma rays (in the first tail of the sensitivity curve of the telescope), which form low-signal-level images that cannot meet the charge cut requirements. Although lower thresholds could in principle be applied, this would result in the susceptibility to an increased NSB contamination, which is not desired.

In this chapter, I present the application of the Optimised Next Neighbour image cleaning [Shayduk, 2013] for the VERITAS array. With this novel technique, pixels are selected based on both their signal and on the time structure of particle showers. One of main advantage of this method is that lower charge threshold cuts can be applied, leading to a decrease in the suppression of low-energy events. Preliminary results presented here were already published in Ref. [Kherlakian, 2023].

This Chapter is organised as follows: in sections 4.1 and 4.2 I review different image cleaning techniques for IACTs and introduce the Optimised Next Neighbour method and its application to simulations of the CTAO. Results of the implementation of the ONN to the VERITAS array are given by comparing IRFs with traditional cleaning methods in section 4.3 and with a set of test sources in section 4.4. I present the validation of the cleaning based on comparisons of Monte Carlo simulations with a Crab Nebula dataset. Moreover, in sections 4.5 and 4.6, I discuss the performance of the cleaning for short observations and on data collected under bright moonlight, respectively.

¹A summary of the different components of the NSB is given in Chapter 3 - Section 3.1.4.

4.1 Conventional image cleaning methods for IACTs

VERITAS employs the double-pass method to reconstruct pixel charges and eliminate noise. The first step involves integrating the FADC trace in each pixel over a wide integration window, equivalent to 8 samples of 2 ns (16 ns). The corresponding pedestal baseline is then subtracted from the measured charge. Additionally, a first estimation of the pulse arrival time, denoted as T_0 , is determined as the midpoint of the signal's maximum height.

Afterwards, a cleaning process is conducted to eliminate noise-induced pixels. The cleaned image is composed of pixels categorised into core or boundary classes. Core pixels are identified by applying a strict threshold criteria, indicating a high likelihood of true Cherenkov signal being present. In contrast, boundary pixels are selected using a less stringent threshold, but only if they are direct neighbours of core pixels.

The image cleaning process can be summarised in the following steps:

1. Core pixels are identified by an integrated size of at least 5σ above the variance of the pedestal level (*pedvar*).
2. Boundary pixels must have a charge of at least 2.5σ above the *pedvar*, as long as they are adjacent to core pixels.
3. Pixels that meet the core criteria but do not have any neighbours meeting the 2.5σ threshold are discarded. This topological condition effectively removes upward noise fluctuations.

After completing the image cleaning process, a second pass in the estimation of the pulse arrival time is performed by calculating the gradient, $T_{\text{grad},x}$, of the distribution of T_0 observed along the major axis of the image. The origin of this gradient is directly correlated to the longitudinal development of the shower and to the variations in the path lengths of the Cherenkov photons to each PMT (Figure 3.10). Finally, $T_{\text{grad},x}$ is used to relocate a narrower summation window of 12 ns, which is used to perform a second and final integration of the FADC trace.

As mentioned before, this process was improved by eliminating outlier pixels which contain signals from afterpulsing effects. Figure 4.1 shows a recorded event in different stages: A) the raw image, containing noise and Cherenkov light, B) the image after the $5\sigma/2.5\sigma$ threshold cleaning and C) the final image constructed after the application of the complete double-pass method. A more detailed description of the method is provided in Chapter 3 - Section 3.2.1.

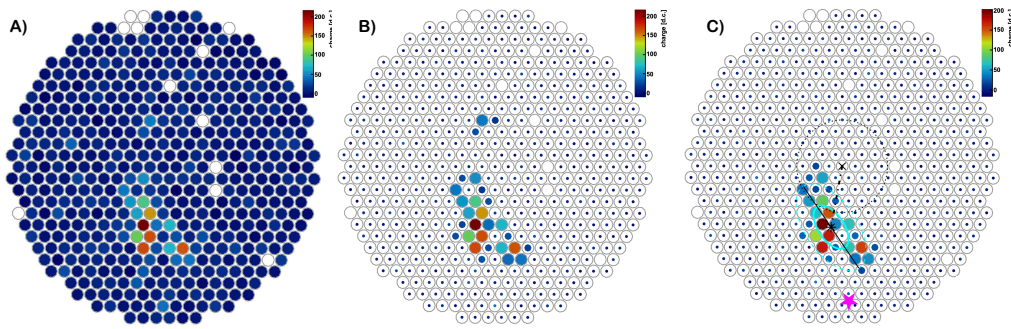


Figure 4.1: (A) Pixel charges in a raw image, composed of noise and Cherenkov light. (B) Pixel charges after the application of the cleaning thresholds ($5\sigma/2.5\sigma$). (C) Final image after the application of the complete double-pass method.

The traditional threshold cleaning method has been widely established as an effective technique for IACTs analysis [Chantell et al., 1995; The HEGRA Collaboration, 1997]. For instance, the H.E.S.S. array has used a similar approach, where core pixels are chosen if their charge exceeds 10 photoelectrons (p.e.), and boundary neighbouring pixels are selected if their charge is at least 5 p.e. [Aharonian et al., 2005]. In more recent analysis developments, H.E.S.S. makes use of the Image Pixelwise fit for Atmospheric Cherenkov Telescopes (ImPACT) [Parsons et al., 2015] for event reconstruction. The algorithm performs the likelihood fit of the pixel amplitudes to a library of image templates generated with Monte Carlo simulations. This technique has shown significant improvements in event reconstruction, particularly at low energies.

Even though the conventional threshold cleaning is already effective at removing the noise, selecting pixels based on the time development of the shower’s light would be a natural improvement. The typical duration of a Cherenkov pulse depends on the specific characteristics of the event and the design of the IACT camera, but it generally falls within the 2 to 10 ns range [Aharonian, 2004]. Therefore, pixels that contain the light from the showers will exhibit strong temporal correlation. For this reason, threshold cuts may be reduced by allowing short time-differences in the arrival time of the pulse within neighbouring pixels. This is only possible due to the random nature of the noise, which makes it very unlikely that two or more bright noise fluctuations will be originated in a short time interval within neighbouring pixels.

A simplified approach in which the time structure information is taken into account was implemented for the analysis of the MAGIC array of telescopes [Shayduk et al., 2005]. To minimise the noise contribution in the signal read-out, the integration window for signal extraction can be shortened and performed near the shower peak. However, when dealing with low energy showers, the reduction of the integration window has the risk of selecting high NSB fluctuations instead of the true signal. This effect is observed on the left panel of Figure 4.2, which shows the cumulative probability of selecting noise-induced groups based on the true (simulated) event size given different values of the integration window.

To address this issue, the MAGIC Collaboration has introduced a new trigger and cleaning approach, referred to as the Next Neighbour software [Shayduk et al., 2005]. This method requires

groups of n pixels (denominated here n -multiplicity) to meet both a minimum charge threshold and a maximum difference in pulse arrival times. Figure 4.2 presents the new cumulative probability for NSB selection. The values for the maximum arrival time difference are fixed and chosen to optimise the signal-to-noise ratio. In the figure, the black curve represents the cumulative probability given by the traditional cleaning (solely charge based) method (in this case, the maximum arrival time difference is the size of the read-out window). The new implementation effectively reduces the level of NSB selection. According to Ref. [Shayduk et al., 2005], the Next Neighbour software leads to a 21% increase in the number of reconstructed events below 100 GeV. Additionally, it is claimed that the minimum pixel charge required to form an image is nearly half of that in the traditional cleaning method.

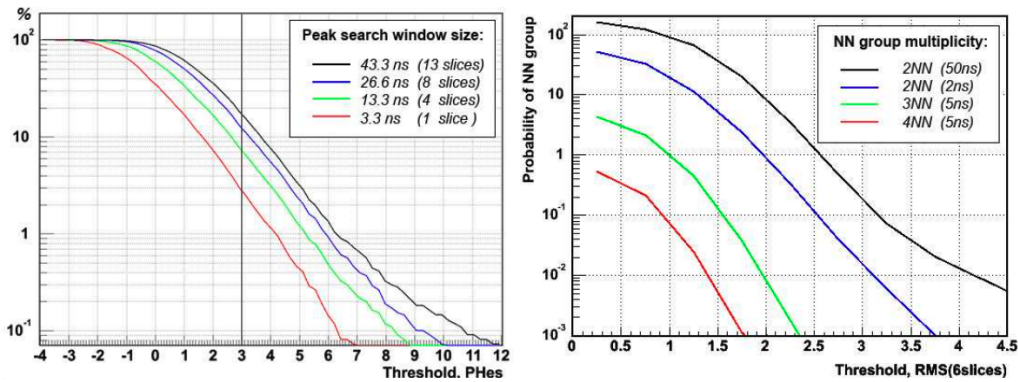


Figure 4.2: Left: Cumulative probability for NSB based on the true shower signal. Curves are given assuming different peak search windows. The event size is given in number of photoelectrons. As the integrated charge decreases, NSB fluctuations are often mistaken for the true shower signal. In addition, for larger integration windows, the NSB is more frequently selected over the true signal. Right: Probability that a group of multiplicities $n = 2, 3$ and 4 ($2nn, 3nn$ and $4nn$) are found assuming a time-window. The threshold is given in units of pedestal standard deviations, integrated over 6 samples of 3.3 ns. Results are given for different peak search windows. The cumulative distribution considering the threshold cleaning is shown as the black curve. Figure from: [Shayduk et al., 2005].

4.2 The Optimised Next Neighbour image cleaning method

In Ref. [Shayduk, 2013], the author introduces the Optimised Next Neighbour image cleaning, a new methodology for the application of the time information on image cleaning. This method has been applied to the Monte Carlo simulations of the CTAO, and it shows significant improvements in terms of event reconstruction. Figure 4.3 shows the reconstructed spectrum for simulated gamma-ray showers for the Large-sized telescope of the CTAO (LST) for a 2013 array configuration. A remarkable gain of at least double the events below ~ 300 GeV is observed.

In contrast to the time-dependent approach implemented by MAGIC, with the Optimised Next

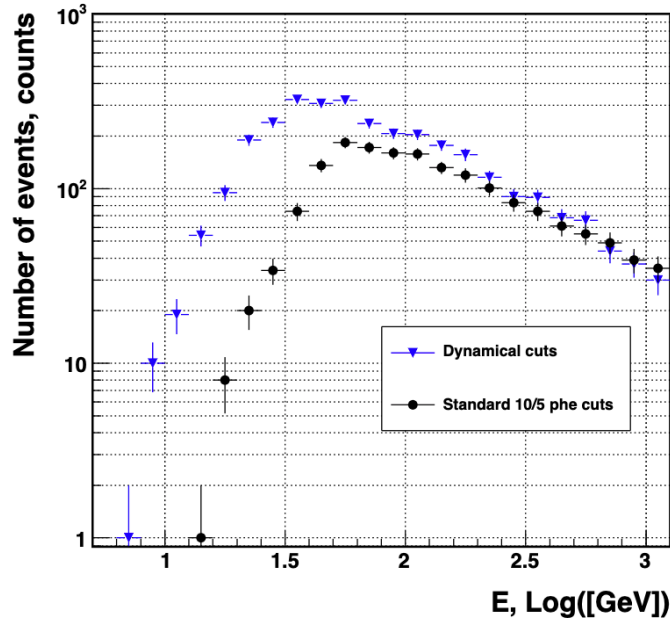


Figure 4.3: Number of well-reconstructed Monte Carlo gamma-ray events for the LST. The events were simulated assuming a power-spectrum with index $E^{-\Gamma}$, $\Gamma = 2$. The results for the conventional image cleaning with thresholds of 10 p.e for core pixels and 5 p.e. for boundary pixels is shown as the black circles. Results with the ONN cleaning are shown as the blue triangles. Figure from: [Shayduk, 2013].

Neighbour technique, threshold values are given as dynamical cuts in the parameter space composed of the group charge (Q) and the difference in pulse arrival time (ΔT) in a group of pixels. By estimating the noise in the camera, a minimum pixel charge and maximum time difference are determined to ensure that the group has a fixed probability of being associated with the noise. Supposing we have a group of p pixels with charges Q_1, Q_2, \dots, Q_p , the value of Q used to define the cuts is given by the lowest charge in the group: $Q = \min(Q_i)$, with $i \in 1, 2, \dots, p$. In a similar manner, supposing the arrival time ($T_{\text{grad},x}$) of the pulse in each of these pixels are T_1, T_2, \dots, T_p , the value of ΔT is given by the maximum time difference between a pair of pixels in the group: $\Delta T = \max(T_i - T_j)$, where $i, j \in 1, 2, \dots, p$, with $i \neq j$. Allowing ΔT values that are too high increases the probability that noise-induced neighbouring pixels will compose the final image. This happens because in a larger time interval, it is more likely that two adjacent pixels would contain a certain charge value caused by two uncorrelated random noise sources. Therefore, a maximum ΔT depending on the minimum group charge must be imposed. As discussed earlier, groups with very short ΔT values are more likely to have originated from Cherenkov light instead of noise. The maximum allowed ΔT will depend on the pixel charges forming the group. Since the noise has a Gaussian distribution with a mean of a few digital counts, it is much less likely that these random fluctuations will generate very-high-signal pixels. For this reason, it is reasonable to understand that a higher ΔT for pixel charges of dozens of digital counts will not significantly increase the probability of noise selection. This is true for a group of n pixels in case we know that all pixels

in the group have a charge above a certain threshold. We find the minimum possible charge required to keep the probability of accepting noise-induced pixels at a reasonable value. Further in the section, the true concept of this probability and its desired level will be better discussed.

The implementation of the Optimised Next Neighbour image cleaning method for the VERITAS array was done within the *EventDisplay* [Maier and Holder, 2017] framework. Results presented below are done based on either simulations or data collected by VERITAS.

The typical noise rate in the telescopes, $I(Q)$, represent the frequency (in Hz) at which pixels have a charge equal to or lower than Q . This quantity is referred to as individual pixel rate (IPR) in Ref. [Shayduk, 2013]. We also adopt this nomenclature in this chapter. Figure 4.4 presents typical IPRs averaged over the pixels of each camera. The IPR in each data acquisition depends on the various noise sources contained in the FoV. It can largely vary depending, for example, if the data acquisition was taken under dark conditions or if the FoV is composed of galactic or extragalactic fields. As expected, higher average noise levels lead to more frequent occurrences of pixels with high charges. One advantage of the ONN is that it detects fine variations in the noise, allowing for the determination of the optimal set of cuts in the $\Delta T - Q$ plane for each observation. This ensures that stricter thresholds will be implemented if the noise levels are higher, and vice versa.

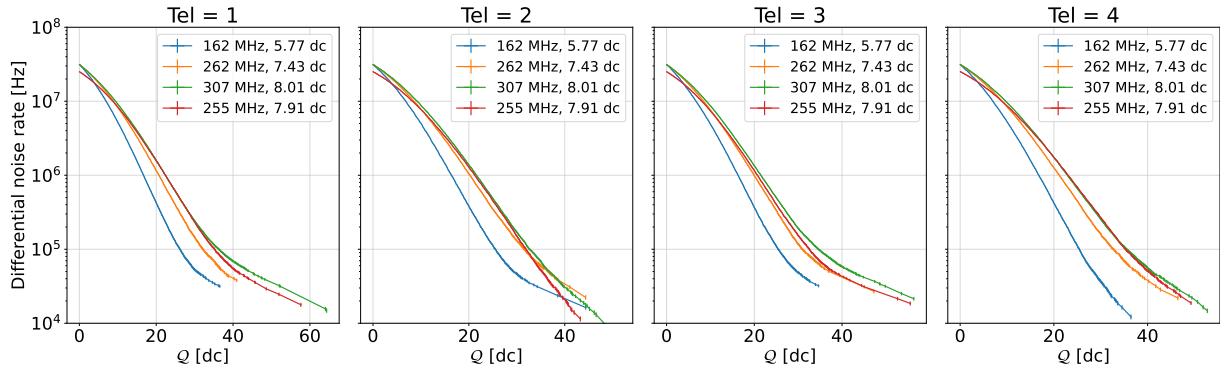


Figure 4.4: Noise rate, $I(Q)$, per telescope in the VERITAS array as a function of pixel charge in digital counts (dc). The rate is given as the average over all cameras pixels. The different colors represent the IPR in different noise levels.

To obtain $I(Q)$, the following steps are performed:

1. First, we estimate the noise rate by calculating the charge in the pixels from the pedestal events. This involves integrating the charge over a 12 ns time-window using the sliding-window technique. This method ensures the maximal integrated charge is found by changing the starting position of the window within the read-out of the event.
2. Next, we construct a frequency histogram (H_Q) representing the distribution of the integrated charges. To guarantee enough statistics, we remove any charge values that do not contain at least 5 entries in this histogram.

3. To determine the frequency, N_Q , at which pixels exhibit a charge less than or equal to a specific threshold Q , we integrate the histogram H_Q from zero up to Q : $N_Q = \int_0^Q H_Q(Q') dQ'$.
4. Finally, to convert the observed frequency of counts into a noise rate, $I(Q)$, we divide N_Q by the total duration of the integration window.

When considering a group of only two pixels, i.e. a group of multiplicity $n = 2$, the rate at which both pixels will contain a signal Q induced by the noise within a given time interval ΔT is referred to as the accidental rate of false detection, \mathcal{R}_{acc} . At this point, we need to remember that the IPR represents how often pixels have a charge up to a given threshold value - Q . Therefore, \mathcal{R}_{acc} represents the rate at which noise is inducing pixel signals up to a threshold Q in a fixed amount of time ΔT . For a single pixel, naturally we have $\mathcal{R}_{acc} = I$.

Since the noise rate is averaged over the entire camera in order to increase statistics, every pixel has the same IPR. Therefore, the rate \mathcal{R}_{acc} of noise-induced charge in two neighbouring pixels within a time interval ΔT is simply given by:

$$\mathcal{R}_{acc}(Q, \Delta T) = I^2(Q) \cdot \Delta T. \quad (4.1)$$

Similarly, considering three pixels ($n = 3$):

$$\mathcal{R}_{acc}(Q, \Delta T) = (I^2(Q) \cdot \Delta T) \times (I(Q) \cdot \Delta T) = I^3(Q) \cdot \Delta T^2. \quad (4.2)$$

When we extend our analysis to any level of multiplicity, we find:

$$\mathcal{R}_{acc}(n, Q, \Delta T) = I^n(Q) \cdot \Delta T^{n-1}. \quad (4.3)$$

To account for the different arrangements of a group of n pixels in the camera, we need to factor in C_n , which represents all the possible combinations of n adjacent pixels given the topology of the camera:

$$\mathcal{R}_{acc}(n, Q, \Delta T) = C_n I^n(Q) \Delta T^{n-1}. \quad (4.4)$$

For a constant value of the accidental rate of false detection, $\overline{\mathcal{R}_{acc}}$, we obtain contours in the $(Q - \Delta T)$ plane:

$$\Delta T(n, Q, \mathcal{R}_{acc}) = \exp \left[\frac{1}{n-1} \ln \left(\frac{\overline{\mathcal{R}_{acc}}}{C_n I^n(Q)} \right) \right]. \quad (4.5)$$

Thresholds are established as dynamic contours in a two-parameter space, diverging from the static linear thresholds such as the ones used in the Next Neighbour software currently employed by MAGIC or the conventional cleaning employed by the VERITAS array. This approach enables the fine-tuning of $\overline{\mathcal{R}_{acc}}$ to any desired level. In practice, we define a maximum probability of false group detection, f , with the maximum accidental rate of false detection, $\overline{\mathcal{R}_{acc}}$, being defined as the ratio of f by the length of the integration window. This allows the discrimination between pixel groups based on whether their likelihood of noise induced formation is higher or lower than f . As

a result, we can effectively filter out groups with a higher probability of being noise-induced. A false group detection probability of f means that in every 100 images, $100 \cdot f$ of them will contain a *fake* (noise induced) pixel group. Naturally, we want this number to be as low as possible, without compromising the cleaning performance. A typical trigger rate in the order of 10^2 Hz is generally expected for Crab Nebula observations. A choice of $f = 5 \cdot 10^{-2}$ means that at the stage of image cleaning, there are about 5 images contaminated by a fake group in every second of data (or 5000 images out of $\sim 10^5$ recorded in a 30 minutes run) - ignoring quality cuts.

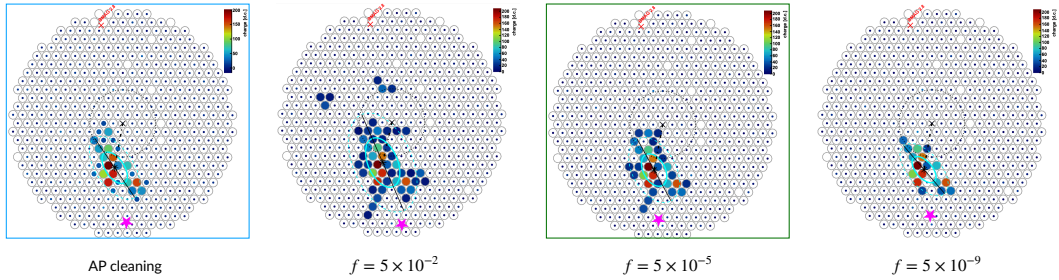


Figure 4.5: Reconstruction of the same event with the conventional cleaning method (AP) and with the ONN cleaning assuming the following values for the maximum probability of false group detection: $f = 5 \cdot 10^{-2}$, $f = 5 \cdot 10^{-5}$ and $f = 5 \cdot 10^{-9}$.

Figure 4.5 shows the same event reconstruction assuming different values of f . A probability of $f \lesssim 5 \cdot 10^{-3}$ results in the identification of isolated islands of noise-induced pixels, whereas higher thresholds of $f \gtrsim 5 \cdot 10^{-6}$ lead to the suppression of events containing the true Cherenkov light. We empirically find that optimal values of the maximum probability are within the range $5 \cdot 10^{-4} < f < 5 \cdot 10^{-6}$, since it provides a reasonable balance between noise subtraction and accurate event reconstruction. This is better understood in Figure 4.6, which shows the number of reconstructed Monte Carlo events and the distribution of image parameters for different values of f . For $f \gtrsim 5 \cdot 10^{-3}$, images are highly distorted due to the presence of the fake groups. For $f \lesssim 5 \cdot 10^{-7}$, the method is too strict in terms of pixel rejection, leading to a lower number of reconstructed events in comparison with the traditional afterpulsing cleaning (conventional method plus correction for afterpulsing affect, from now referred to as only "afterpulsing"). For results presented in this chapter, we assume $f = 5 \cdot 10^{-4}$. This choice results in about 50 fake groups in a run of 30 minutes, i.e., about 0.05% of images will be contaminated.

Figure 4.7 shows the dynamical contours in the $Q - \Delta T$ parameter space for an observation with a mean noise rate of 307 MHz, considering group multiplicities of $n = 2$ (2nn), 3 (3nn), and 4 (4nn). The noise rate for this particular observation has been shown in Figure 4.4 (noise = 307 MHz). Slight variations in the contours can be observed across the telescopes due to the subtle discrepancies in the measured noise rate by each telescope, as seen in Figure 4.4. These variations can be attributed to the slight differences in the telescope's response to light. Moreover, we find that a maximum group multiplicity of $n = 4$ is sufficient to reconstruct most pixels containing the Cherenkov light. Considering higher multiplicities not only does not significantly contribute to

the cleaning process but also significantly increases the computational time. The differences in contours for observations taken at different noise levels can be seen in Figure 4.8. As expected, higher noise levels produce stricter thresholds.

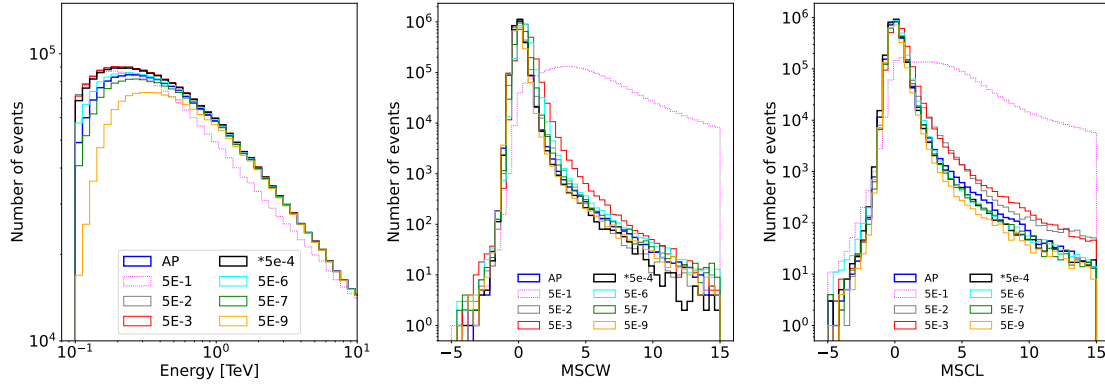


Figure 4.6: Left panel: Reconstruction of Monte Carlo events with the afterpulsing cleaning method and with the ONN cleaning, assuming different values for the maximum probability of false group detection: $f = 5 \cdot 10^{-1}$, $5 \cdot 10^{-2}$, $5 \cdot 10^{-3}$, $5 \cdot 10^{-4}$, $5 \cdot 10^{-6}$, $5 \cdot 10^{-7}$ and $5 \cdot 10^{-9}$. The final choice is $f = 5 \cdot 10^{-5}$. Middle panel: same as left panel, but showing the distribution of MSCW from reconstructed images. Right panel: same as left panel, but showing the distribution of MSCL from reconstructed images.

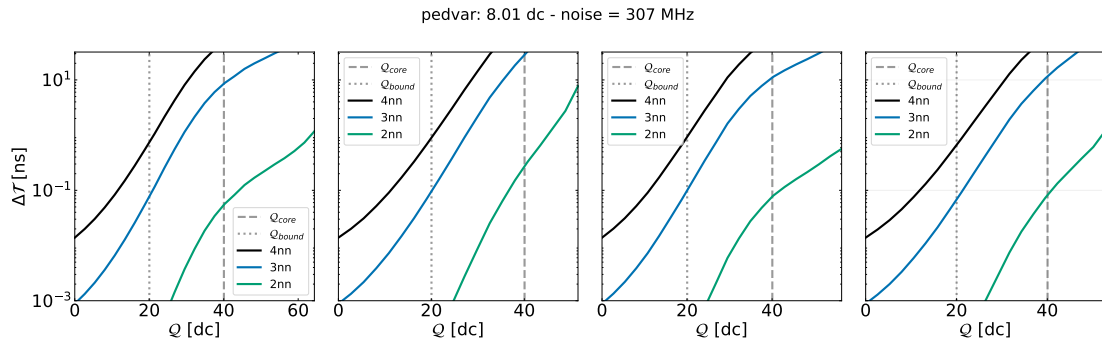


Figure 4.7: Dynamical cuts in the maximum difference in pulse arrival time, ΔT , per minimum group charge, Q , for each telescope in the VERITAS array. The contours are shown for multiplicities $n = 2$ (2nn - black), 3 (3nn - blue) and 4 (4nn - green). The allowed times for ΔT span from 0 up to the size of the read-out window (32 ns). The conventional cleaning thresholds are shown as the grey curves for core (dashed line) and boundary (dotted line) pixels.

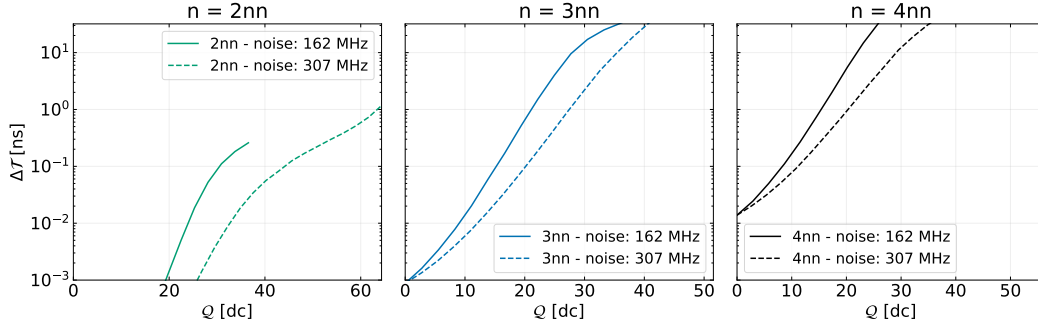


Figure 4.8: Dynamical cuts for runs taken at different noise levels: 162 MHz (solid line) and 307 MHz (dashed line), for the same telescope. The contours are shown for multiplicities $n = 2$ (2nn - black), 3 (3nn - blue) and 4 (4nn - green).

Figure 4.9 shows a schematic view of the ONN cleaning workflow on a real recorded event:

1. **Initial filtering:** In the first step, a pre-cut of a few digital counts on the charge is applied.
2. **2nn search:** adjacent pairs of pixels with a minimum charge and difference in arrival time below the defined 2nn contour are included in the image.
3. **3nn search:** A search is conducted within the neighbours of the previously selected 2nn pairs to discover third pixels that potentially meet the 3nn contour. This is possible since the 2nn condition is less strict than the 3nn condition.
4. **4nn search:** Finally, this process is extended by searching for potential fourth pixels that satisfy the 4nn condition within the neighbours of the selected 3nn sets.
5. **Boundary search:** a boundary pixel search is also conducted within all neighbours of pixels selected via the 2nn, 3nn and 4nn searches. Boundary pixels are included in the final image if they pass a looser condition, given by:

$$\mathcal{R}_{acc}(Q, \Delta T) = C' I^2(Q) \times \Delta T,$$

where $C' = 1$, i.e., just a combination between the boundary and the pre-selected image pixel.

While optimising the removal of pixels in an image containing noise signals, cleaning methods should also guarantee that the maximal number of pixels containing the shower signal are kept for the reconstruction. In practice, however, it is observed that the sensitivity of the telescope reaches a plateau in relation to the number of pixels in the image and that at a certain point, a greater number of pixels containing the true signal will not necessarily provide a better performance. This happens because the pixels that are more distant to the image core contain a lower Cherenkov signal and they do not significantly contribute to the parametrisation and total size of the image.

The ONN method offers several advancements compared to the threshold cleaning:

- Pedestal events, and therefore the IPR, account for all sources of NSB fluctuations. In this manner, the identification of the most effective cleaning thresholds for each specific observation are found. For a similar reason, it is also possible to account for slight differences in each individual telescope. In this way, the best set of cuts for each telescope is provided.
- Changes in the throughput of the telescope, such as increased electronic noise due to after-pulsing or loss in mirror reflectivity and PMT gain, are constantly being assessed.

In conclusion, the ONN cleaning method dynamically adapts to noise variations, resulting in optimal cutoffs for each observation and telescope.

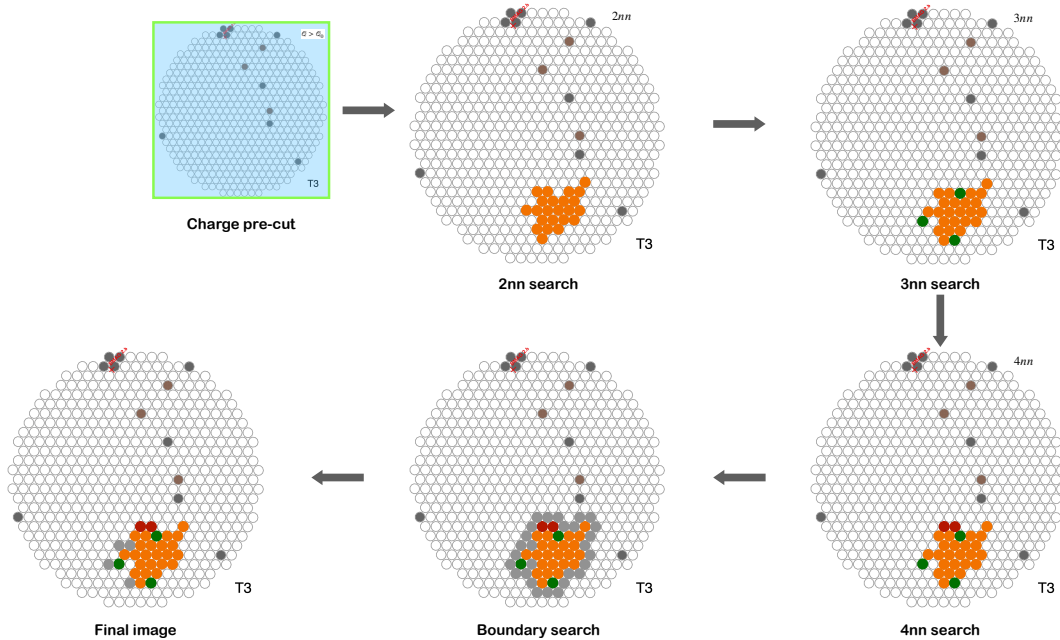


Figure 4.9: Schematic workflow of the ONN cleaning on a triggered event. Initially, a low charge threshold is applied to discard all pixels with less than just a few digital counts. Next, the algorithm searches for groups of multiplicity $n = 2$ that fulfil the 2nn contour. The selected pixels are shown in orange. A search is performed on adjacent pixels of the 2nn pairs to find those that meet the 3nn contour. The pixels that pass the 3nn selection are shown in green. Finally, a 4nn search is conducted on pixels neighbouring the ones discovered by the 3nn condition. Pixels that are part of a 4nn group are shown in red. A last search is also performed on the boundary pixels, depicted in grey. The final image is then composed. Dead pixels are shown in brown.

4.3 Results on simulations and instrument response functions

Monte Carlo simulations of gamma-ray showers were used to evaluate the performance of the ONN image cleaning for the VERITAS array. The events were simulated with the CORSIKA shower simulator program [Alameddine, 2023] for gamma rays arriving at a zenith angle of 40 degrees. The simulations include an average noise level of 200 MHz and a telescope pointing offset of 0.5° .

Figure 4.7 showed that the ONN method allows lower-signal-simulated events for the CTAO to pass the image cleaning criteria. As a result, we anticipate an increase in the number of reconstructed events in the GeV range for VERITAS simulations. These events have a significant impact on the IRFs of the array.

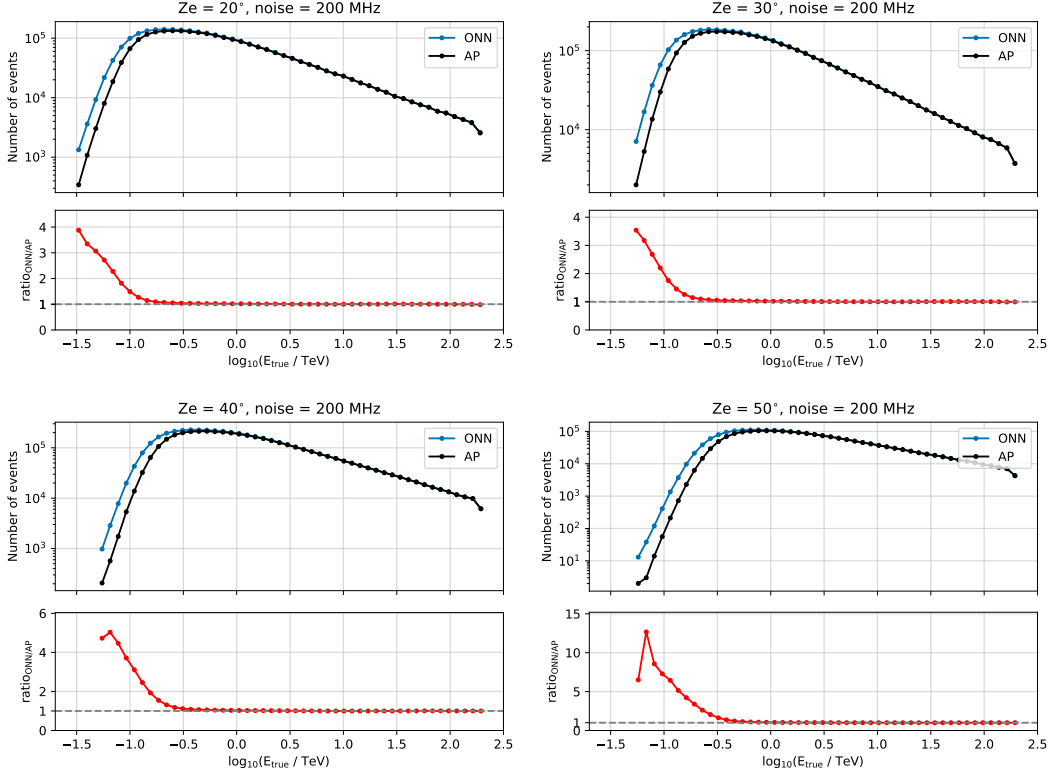


Figure 4.10: Top panels: Number of reconstructed simulated events with the ONN (blue) and afterpulsing cleaning (black) for a set of Monte Carlo events generated at zenith 20°, 30°, 40° and 50° and noise level of 200 MHz. Bottom panels: ratio of events reconstructed by the ONN and afterpulsing cleaning methods.

The number of simulated reconstructed events with the ONN and afterpulsing cleaning is presented in Figure 4.10. Below 300 GeV (500 GeV), the ONN cleaning reconstructs at least 22% (17%) more events. Figure 4.11 shows the effective area, energy bias, energy resolution and angular resolution achieved with the ONN cleaning. We also show the same set of IRFs generated with the afterpulsing (AP) cleaning for comparison. From the upper left panel of Figure 4.11, a higher effective area is achieved (by a factor of $\lesssim 3$) compared to the afterpulsing cleaning below $\lesssim 100$ GeV. This is due to the reduced suppression of low amplitude events. We also observe a decrease in the energy bias in the same energy range, with a difference between ONN and afterpulsing of $\lesssim 10\%$. Since we anticipate the reconstruction of more low-energy events, the energy bias below < 1 TeV is not as largely dominated by high signal events.

Concerning the angular resolution, we observe a difference of $\lesssim 10\%$ at low energies. It is expected that with a larger number of reconstructed events, there will be a minor difference in the

standard deviation of the angular distribution. A similar conclusion can be drawn for the energy resolution.

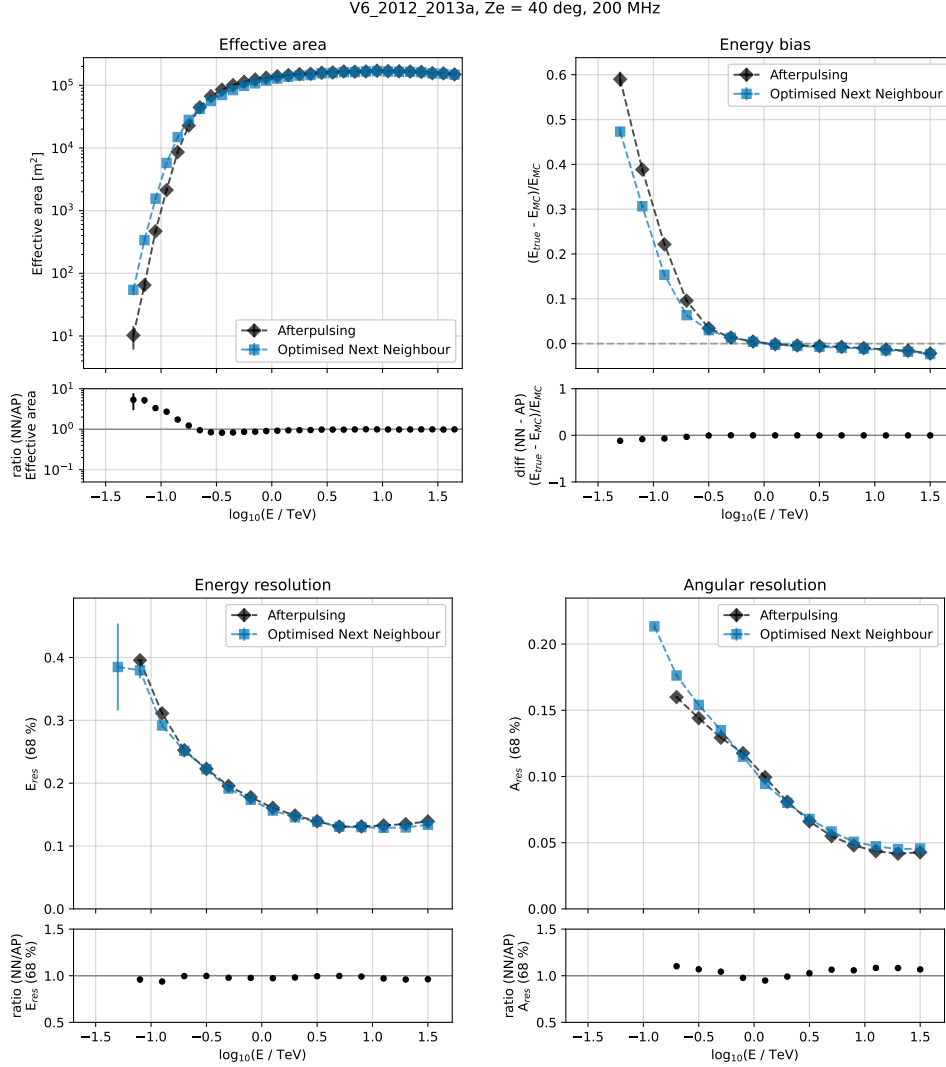


Figure 4.11: Set of IRFs for the 2012-2013 observing season at zenith = 40° and noise level = 200 MHz for the ONN (blue squares) and afterpulsing (black diamonds). Upper left: effective area, upper right: energy bias, lower left: energy resolution and lower right: angular resolution. The lower panels show the ratio between the two methods.

An increased number of simulated events is observed across all the discrete range of simulated zenith angles, noise levels and observing seasons. We refer the reader to the Supplementary Figures A.18 - A.24 in Appendix A, where we present IRFs for different subsets of Monte Carlo simulations in the following configurations:

- noise levels: 75 MHz, 200 MHz and 400 MHz,
- elevation angles: 40 and 55 degrees,
- observing seasons: 2012-2013 and 2017-2018.

To summarise, the implementation of the ONN cleaning results in increased effective areas and reduced energy bias at low-energies ($\lesssim 200$ GeV). With the ONN, we can also achieve a lower energy threshold of 145 GeV with ONN in comparison to 175 GeV with AP, for the particular case of Figure 4.11. This reduction significantly impacts the reconstruction of the spectrum of soft and faint gamma-ray sources.

4.4 Results on test sources

Our analysis results primarily focus on the Crab Nebula, which is the remnant of a core-collapse supernova at a distance of approximately 2 kpc. Due to its well-measured SED, the Crab Nebula is widely used as a standard candle in VHE astrophysics, making it the ideal source for the study of astrophysical processes and method performance. Appendix A includes a more comprehensive analysis of the performance of the ONN cleaning by investigating analysis results for various testing configurations, including elevation angles, noise levels, observing seasons and gamma-hadron separation cuts in the same Crab Nebula dataset.

We expect the ONN to be particularly useful in the study of sources with soft spectral indices ($\Gamma > 3$), as well as fainter sources, which require long exposures (> 100 hours) for detection. To test the ONN in these particular scenarios, we analyse in this Chapter five known TeV-sources with varying spectral indices and flux strength: PKS1424+240, PG1553+114, Markarian 501, Messier 87 (M87), and 1ES1118+424.

We assume *super-soft* box cuts, which provide the lowest possible energy threshold and are optimised for sources with spectral index $\Gamma > 3$:

- $-1.2 < \text{MSCW} < 0.3$,
- $-1.2 < \text{MSCL} < 0.5$,
- Emission height > 6 km,
- Squared offset from source position (θ^2) < 0.012 degrees².

We estimate the background using the reflected regions method [Berge et al., 2007]. A summary of the test sources results and Crab Nebula configurations are presented in Tables A.1 and A.2 in Appendix A.

4.4.1 Crab Nebula

Figure 4.12 shows the number of reconstructed excess events for the Crab Nebula dataset with the ONN and afterpulsing cleaning methods. The dataset comprises 303 hours of live-time, taken with a pointing offset of 0.5° from the Crab Nebula's position. The data was collected in a wide range of observing seasons, spanning from 2012 to 2021, and elevation angles, with an average of 63.5° .

From Figure 4.12, we notice that the ONN method can reconstruct more events than the afterpulsing cleaning by a factor of at least ~ 2.5 below $\lesssim 100$ GeV. The ratio plot highlights the bins

where ONN reconstructs events which are completely absent in the traditional cleaning method (indicated by the upper black arrows, only shown for $E < 1$ TeV). These bins are centred at energies of ~ 65 GeV and ~ 75 GeV.

We notice an increase in the gamma-ray rate per minute from 10.89 ± 0.03 to 13.00 ± 0.03 , along with an increase in the background rate from 2.612 ± 0.005 to 6.29 ± 0.01 events per minute. These results suggest an overall efficacy in reconstructing more events, either from gamma-rays or from the background of cosmic rays. This is expected, since the cleaning is done before the gamma/hadron separation. Because of the high increase in the background rate, the significance drops from approximately 557σ with AP to around 499σ with ONN. One way to deal with a lower significance is to provide gamma/hadron separation cuts generated with machine learning algorithms, such as in Ref. [Krause et al., 2017]. We present in Figure A.1, a comparison of *super-soft* box cuts and *super-soft* cuts derived with BDT methods. With this new set of cuts, a significance of 648.6σ is achieved at the expense of a lower gamma-ray rate, which is still higher in comparison to AP. A significance of 628.3σ is obtained with AP and BDT cuts optimised with simulation run with the AP cleaning. Therefore, an improvement of $\sim 20\sigma$ is obtained with ONN when considering BDT cuts for both methods. In order to show a fair comparison between the cleaning methods, I continue showing results with box gamma/hadron cuts (same cuts for both ONN and AP) throughout this thesis.

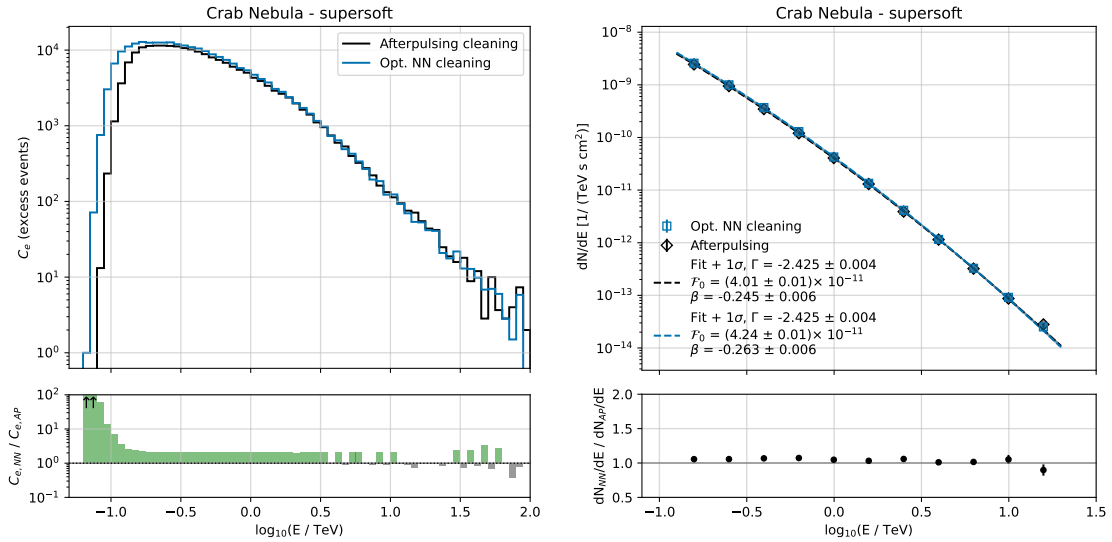


Figure 4.12: Left panel: spectrum of reconstructed source events from the Crab Nebula with the ONN (blue) and afterpulsing (black) cleaning methods. The lower left plot shows the ratio of the number of reconstructed events by ONN and AP. Bins for which ONN reconstruct more events than AP are given in green and the opposite in grey. Bins at energies < 1 TeV for which there are no reconstructed events for AP but ONN reconstructs at least one source event are marked with the upper black arrows. Right panel: spectrum of the Crab Nebula and fit ($+ 1\sigma$) of the data points with a log-parabola function for ONN (blue) and AP (black). \mathcal{F}_0 is given in units of $\text{cm}^{-2} \text{s}^{-1} \text{TeV}^{-1}$. The lower right panel shows the ratio of the reconstructed spectra.

The VERITAS Collaboration (2015) [Meagher, 2015], find that the best fit of the Crab Nebula in the VHE regime is given by a log-parabola function

$$\frac{dN}{dE} = \mathcal{F}_0 \cdot \left(\frac{E}{\text{TeV}} \right)^{-\Gamma + \beta \cdot \log_{10}(E)}, \quad (4.6)$$

in the energy range from 115 GeV to 42 TeV, with parameters $\Gamma = 2.467 \pm 0.006$ and $\beta = -0.16 \pm 0.01$. A log-parabola description is also supported by observations from H.E.S.S. and MAGIC [Aharonian et al., 2006; Aleksić et al., 2015].

The right panel of Figure 4.12 presents the Crab Nebula spectrum obtained with both methods and the best-fit results given by a log-parabola curve. The spectrum is reconstructed with at least 10 signal events and a significance higher than 5σ per spectral point. The fit results are found to be equivalent within the t-test probability. The stereo parameters obtained from the Hillas parametrisation of the shower images from this dataset are presented in Figure A.2. As discussed in Chapter 3, we expect the mean scaled width and length to be roughly Gaussian distributed around zero. We also present in the figure the super-soft cuts applied in this analysis. The distribution for both methods are consistent with expectations, indicating that the gains in event reconstruction do not come from any incorrect IRF production.

4.4.1.1 Crab Nebula testing configurations:

We study the performance of the ONN cleaning by restricting this Crab Nebula dataset to particular elevation ranges, observing seasons and noise levels:

- Ranges of elevation angles: $30^\circ - 40^\circ$, $40^\circ - 50^\circ$ and $50^\circ - 90^\circ$ - shown from Figure A.3 to Figure A.5 in Appendix A;
- Ranges of noise level: 100 MHz - 200 MHz, 200 MHz - 300 MHz, 300 MHz - 400 MHz and 400 MHz - 500 MHz - shown from Figure A.6 to Figure A.9 in Appendix A;
- Observing seasons: 2012-2013, 2013-2014, ..., 2016-2017 and 2017-2018 - shown from Figure A.10 to Figure A.15 in Appendix A.

Analysis results are summarised in Table A.2 of Appendix A. Upon analysing every configuration considered in this study, we can conclude that, in general, the ONN can successfully reconstruct more events compared to the traditional image cleaning method. Remarkable gains are observed particularly at low-energies in all testing configurations. An impressive result is shown for configuration $50^\circ - 90^\circ$ (Figure A.5), in which events with energies as low as ~ 65 GeV are reconstructed, which is significantly lower than the sensitivity range of VERITAS reported in the literature (85 GeV - 40 TeV) [Adams et al., 2022]. Additionally, it is worth noting that the ONN consistently shows similar gains in terms of event reconstruction in various observing seasons, proving that the telescopes performance and optical throughput [Adams et al., 2022] do not negatively impact the cleaning.

4.4.2 Monte Carlo data comparison

The consistency of the event reconstruction with the Optimised Next Neighbour image cleaning is validated by comparing results from Monte Carlo simulations to the Crab Nebula dataset². This validation can reveal inherent systematic uncertainties introduced by the cleaning and assure that the application on simulated events and data is consistent. Figures 4.13 and 4.14 present the distribution of the MSCW and MSCL parameters for a Crab Nebula dataset consisting of 41 hours of live-time, zenith angles lower than 25 degrees and recorded during the 2012-2013 observing season. The simulations shown in comparison are produced at a zenith angle of 20 degrees and have a noise level of 200 MHz. Comparisons between data and MC simulations are divided into 6 energy bins ranging from 100 GeV up to 10 TeV. The figures show that the dataset and the Monte Carlo simulations display an overall consistent behaviour. Due to the low photon fluxes above $\gtrsim 2$ TeV, the last two energy bins are dominated by the statistical uncertainties of the dataset, leading the distributions of parameters to differ at higher energy values. Moreover, the leakage of images outside the camera and saturation effects also introduce discrepancies in the distribution observed for the last bin.

The Kolmogorov–Smirnov (KS) test quantifies the distance between an empirical and a reference cumulative distribution function of a sample. Below 500 GeV, the empirical distribution is likely drawn from the simulated one at 3σ . Variations between data and Monte Carlo simulations likely arise since simulated events are produced only in discrete intervals of zenith and noise levels and are, therefore, not exact representations of the data. Moreover, simulations also suffer from limited representations of the atmospheric profiles and an absent or limited depiction of broken electronic channels, shadowing effects, among other factors. For instance, the limited representation of atmospheric profiles already introduces a systematic error of 10% to 15% [Adams et al., 2022]. Regarding data/MC comparisons produced with the afterpulsing cleaning, as presented in Figures A.28 and A.29, a similar behaviour of the curves and KS-tests are obtained. From the cumulative distribution of the stereo parameters, a systematic uncertainty of $< 4\%$ below 1 TeV is obtained. For the AP cleaning, a systematic uncertainty of $< 2\%$ is found below 1 TeV. The data/MC validation indicates that the Optimised Next Neighbour image cleaning does not introduce significant systematic uncertainties in event reconstruction. The comparison of the full set of single telescope shower parameters is shown in Figure 4.15. Distributions are reasonably similar. Shower parameters comparisons for Telescopes 2, 3 and 4 can be found in Figures A.32 - A.34 in Appendix A. A second validation with a 64 hours dataset taken during the 2017-2018 observing season is provided in Figures A.26 and A.27 from Appendix A.

²Data/MC validations are performed with several shower parameters, including MSCW, MSCL, single telescope width and length, image size and number of pixels in the image. In this section, we present results for MSCW and MSCL since these are the shower parameters with the highest impact on the gamma/hadron separation.

CHAPTER 4. IMPLEMENTATION OF THE OPTIMISED NEXT NEIGHBOUR IMAGE CLEANING METHOD FOR THE VERITAS ARRAY

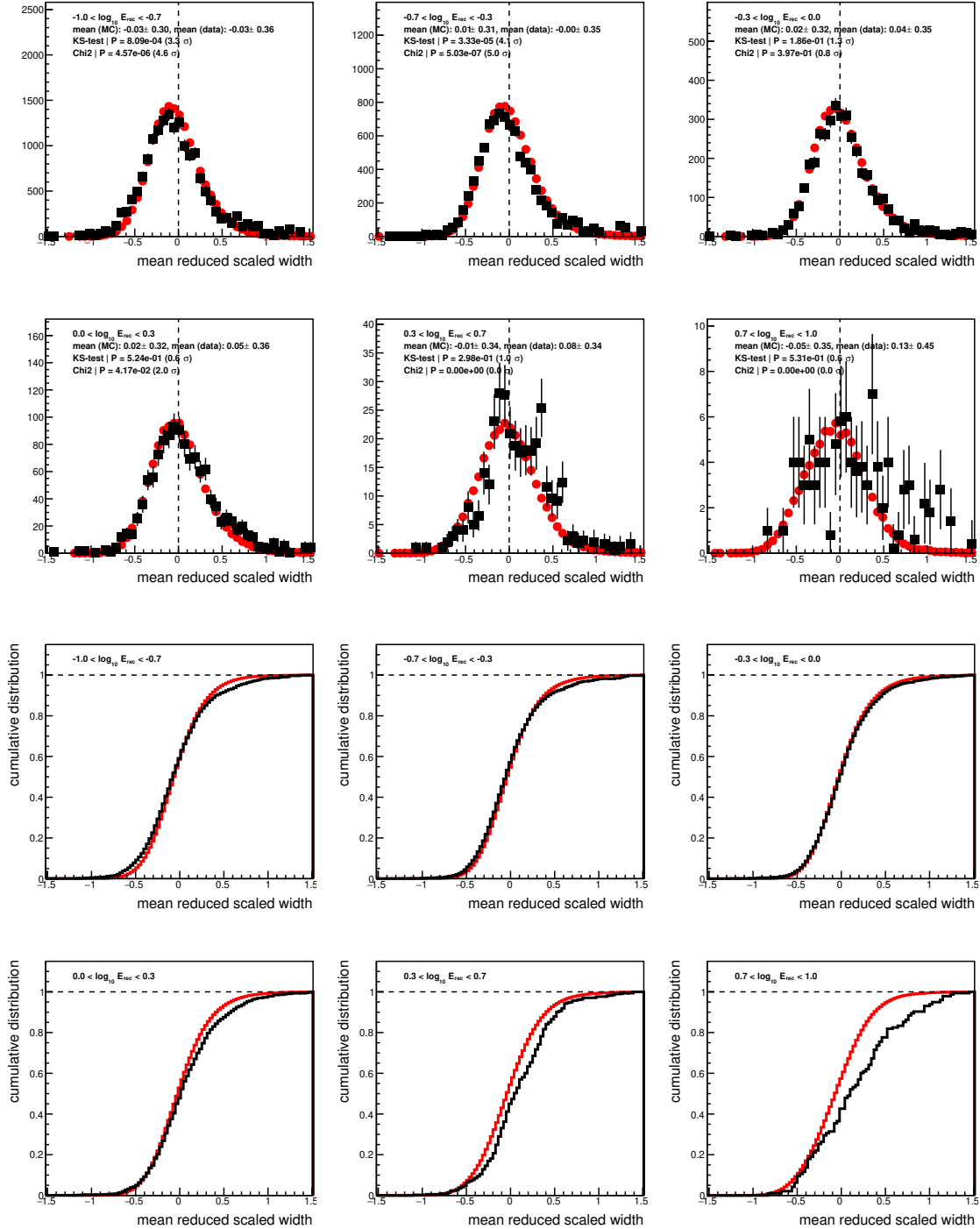


Figure 4.13: Top: Distribution of MSCW for a Crab Nebula dataset (black squares) and simulated gamma-rays (red circles) in arbitrary units. The dataset consists of events with a zenith lower than 25 degrees. Simulated events are produced at a zenith of 20 degrees and a noise level of 200 MHz. The events are separated based on the reconstructed energy E_{rec} (in TeV) in the following ranges: $-1.0 < \log_{10}(E_{rec}) < -0.7$, $-0.7 < \log_{10}(E_{rec}) < -0.3$, $-0.3 < \log_{10}(E_{rec}) < 0.0$, $0.0 < \log_{10}(E_{rec}) < 0.3$, $0.3 < \log_{10}(E_{rec}) < 0.7$, $0.7 < \log_{10}(E_{rec}) < 1.0$. Bottom: cumulative distribution of MSCW for each energy range.

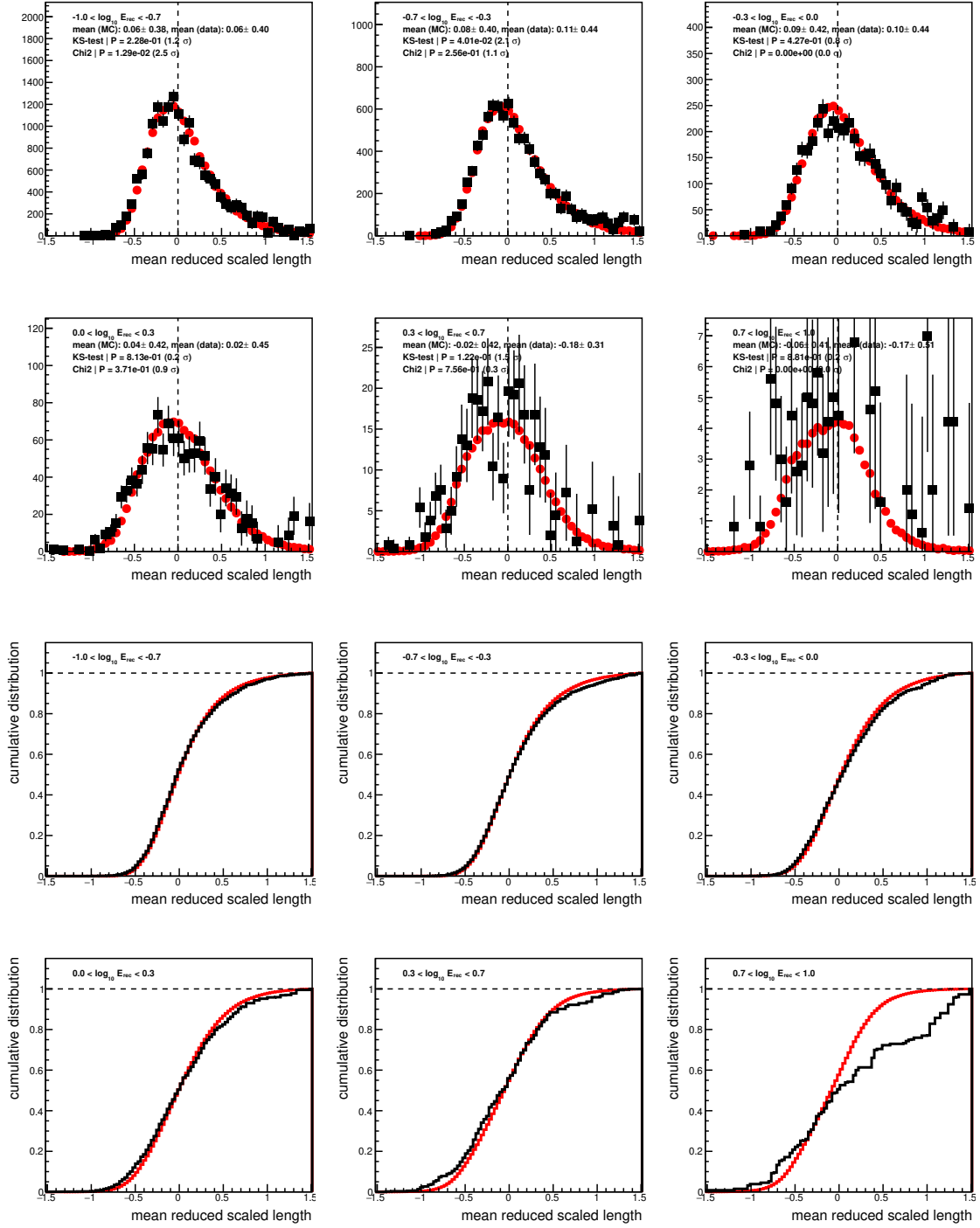


Figure 4.14: Top: Distribution of MSCL for a Crab Nebula dataset (black squares) and simulated gamma-rays (red circles) in arbitrary units. The dataset consists of events with a zenith lower than 25 degrees. Simulated events are produced at a zenith of 20 degrees and a noise level of 200 MHz. The events are separated based on the reconstructed energy E_{rec} (in TeV) in the following ranges: $-1.0 < \log_{10}(E_{\text{rec}}) < -0.7$, $-0.7 < \log_{10}(E_{\text{rec}}) < -0.3$, $-0.3 < \log_{10}(E_{\text{rec}}) < 0.0$, $0.0 < \log_{10}(E_{\text{rec}}) < 0.3$, $0.3 < \log_{10}(E_{\text{rec}}) < 0.7$, $0.7 < \log_{10}(E_{\text{rec}}) < 1.0$. Bottom: cumulative distribution of MSCL for each energy range.

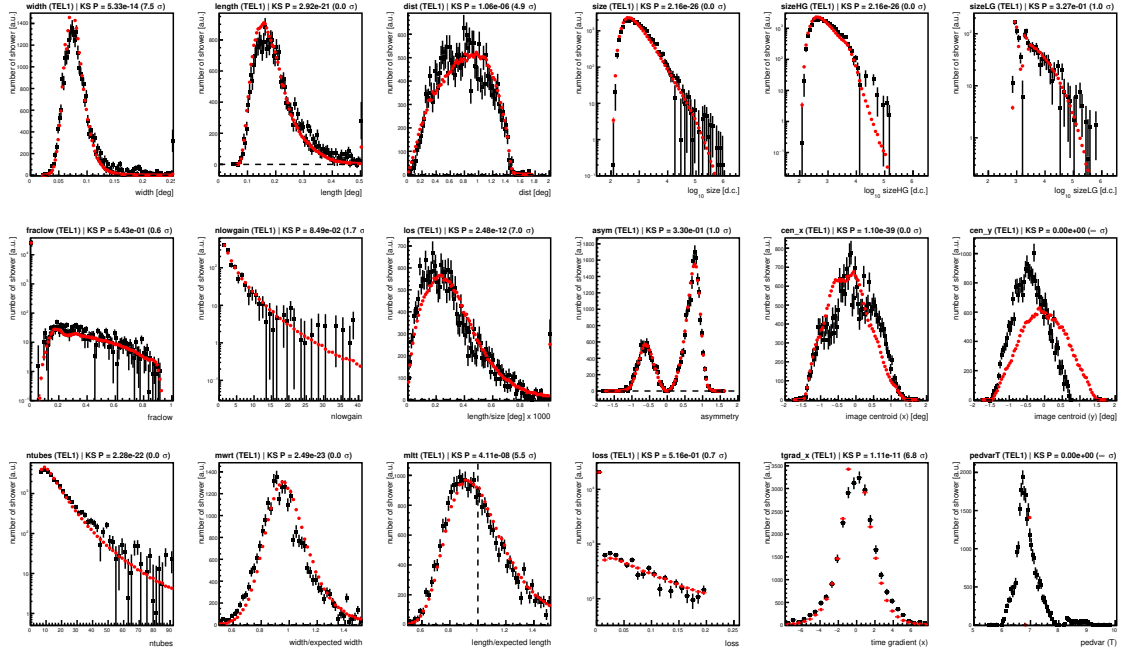


Figure 4.15: Comparison of single telescope (Telescope 1) shower parameters between data and Monte Carlo simulations. From top to bottom and from left to right: width, length, shower core distance, image size, image size (high gain channels), image size (low gain channels), fraction of image size in low gain pixels (fraclow), number of tubes triggering high/low gain (nlowgain), image length per size, shower skew (asymmetry), coordinates of image centroid (x and y directions), number of pixels in the image (ntubes), width and length over expected values, image loss, time gradient, and *pedvars*. Simulation distributions are given in red, while data in black. The difference seen for the centroid position is due to the difference in the distribution of the azimuth of observations. The Y-axis is given in arbitrary units.

4.4.3 PKS 1424+240

PKS 1424+240 is a High-frequency peaked BL Lac object (HBL) showing a synchrotron peak above 10^{15} Hz [Acciari et al., 2009] and an isotropic luminosity of $\sim 10^{44}$ erg s^{-1} above 400 GeV [Archambault et al., 2014]. Blazars SEDs show two characteristic broad peaks, which are interpreted as resulting from synchrotron radiation of accelerated electrons, yielding the low-frequency peak, and inverse Compton scattering emission or possibly hadronic mechanisms, which produce the high-frequency peak. Due to the lack of emission lines in their spectra, blazars redshift are often difficult to constrain and are usually resolved with the stellar emission of the host. Blazars can be classified based on the peak frequency of their emission, with HBLs being the ones where the low peak is within the UV and X-ray bands, and the high frequency peak is located around 100 GeV.

Discovered by VERITAS in 2009 [Acciari et al., 2009], PKS 1424+240 is at an uncertain redshift ($0.24 < z < 1.19$) [Malik et al., 2022; Yang and Wang, 2010] and has exhibited variable flux levels in the VHE regime over the years. These include particular flaring periods in 2009

and 2011. The spectral indices of the power-law fit reported by the VERITAS Collaboration for observations conducted in 2009 and 2011 are $\Gamma = -3.8 \pm 0.3$ [Acciari et al., 2009] and $\Gamma = -4.3 \pm 0.3$ [Archambault et al., 2014], respectively. On the other hand, during a dimmer VHE state in 2013, the HBL was observed with a spectral index of $\Gamma = -4.5 \pm 0.2$ [Archambault et al., 2014]. Combining the datasets from the three epochs, Ref. [Benbow, 2015] finds an index of $\Gamma = -4.2 \pm 0.3$. While in the bright VHE state, the source integral flux resulted in 4.6% of the integrated Crab Nebula emission above 120 GeV, meaning this is a relatively faint source.

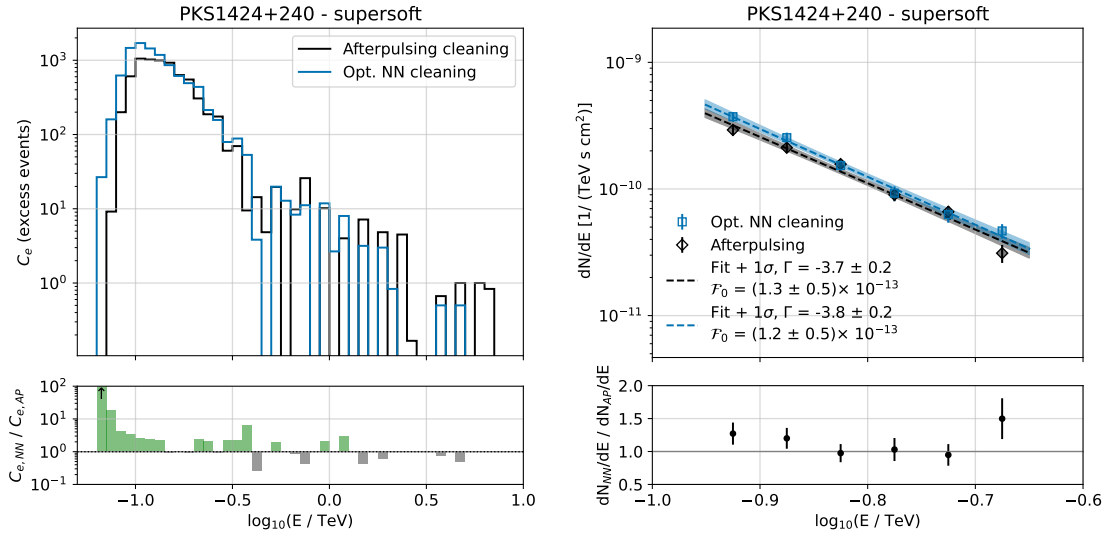


Figure 4.16: Left panel: spectrum of reconstructed source events from PKS 1424+24 with the ONN (blue) and afterpulsing (black) cleaning methods. The lower left plot shows the ratio of the number of reconstructed events by ONN and AP. Bins for which ONN reconstruct more events than AP are given in green and the opposite in grey. Bins at energies < 1 TeV for which there are no reconstructed events for AP but ONN reconstructs at least one source event are marked with the upper black arrows. Right panel: spectrum of PKS 1424+24 and fit ($+1\sigma$) of the data points with a power-law function for ONN (blue) and AP (black). The lower right panel shows the ratio of the reconstructed spectra.

For PKS 1424+24, we collect a total of 172 hours of live-time, taken from 2012 to 2020. The dataset has a pointing offset of 0.5° and a mean elevation of 75.9° . The left panel of Figure 4.16 shows the excess counts spectrum for PKS 1424+24 obtained with the ONN (blue) and AP (black) cleaning methods. We observe a decrease in counts for both methods beyond 1 TeV due to the soft spectrum, with statistical fluctuations dominating above 3 TeV. Similar to the Crab Nebula, the ONN cleaning was able to reconstruct significantly more events in overall when compared to the AP cleaning. Notably, we observed a significant increase in the number of events below 200 GeV with the ONN, with at least ~ 3 times more events. Particularly, the bin centered at 65 GeV is not present in the counts spectrum obtained with AP.

The excess rate per minute shows a noticeable increase of $\sim 40\%$ from 0.66 ± 0.02 with AP to 0.93 ± 0.03 with ONN. Although an increase in the background rate is also noted, the increased

excess rate is a promising factor for probing faint sources that would otherwise require very long exposures for detection. Similarly to what has been discussed for the Crab Nebula, an increase in the background rate will likely deter improvements in the significance level, even if there is a corresponding increase in the gamma-ray rate. For this particular dataset, the significance achieved with the AP cleaning is 28.5σ , while 28.6σ with ONN. The right panel of Figure 4.16 shows the reconstructed spectrum for PKS1424+240 with datapoints with at least 10 events and a significance of 5σ , together with a simple power-law fit. Because the dataset comprises different flux states, the resulting spectral indices should not necessarily be consistent with Ref. [Benbow, 2015].

4.4.4 PG 1553+113

PG 1553+113 is an HBL at redshift $z \simeq 0.5$ [Tavani et al., 2018]. The long-term monitoring of this blazar by Fermi-LAT shows the source exhibits a quasi-periodic trend, with a ~ 2.18 years period in the observer frame for the main peak of the gamma-ray emission [Tavani et al., 2018]. PG1553+113 is likely a binary system composed of two black-holes of masses $10^8 M_{\odot}$ and $10^7 M_{\odot}$ [Tavani et al., 2018]. In the VHE regime, the VERITAS Collaboration reported a power-law spectral index of $\Gamma = -4.33 \pm 0.09$ between 160 and 560 GeV, based on observations in the period of 2010 to 2012 [Aliu et al., 2015]. An integral flux of 6.9% of the Crab Nebula above 200 GeV is also reported. The left panel from Figure 4.17 presents the counts spectrum of PG1553+113. The dataset comprises ~ 92 hours of live-time recorded with a pointing offset 0.5° from the location of PG1553+113. Similar conclusions as taken for the Crab Nebula and PKS1424+240 apply. With ONN, we reconstruct events of energy ~ 75 GeV and ~ 85 GeV, which are absent from the counts spectrum reconstructed with the AP cleaning. The excess rate increased from 2.59 ± 0.03 to 3.47 ± 0.04 per minute, while the background rate doubled with ONN. A similar significance level is achieved.

4.4.5 M87

M87 is a massive radio-loud elliptical galaxy in the Virgo constellation ($z = 0.004$). After a monitoring campaign between 2012 and 2015, when M87 was generally in a low emission state, the MAGIC Collaboration reports that the VHE spectrum can be fitted from ~ 100 GeV to ~ 10 TeV with a simple power-law with an index of -2.41 ± 0.07 [Acciari et al., 2020]. In particular, most recent studies by the H.E.S.S. Collaboration indicate a spectral index of $\Gamma = -2.4 \pm 0.1$ [Aharonian, Ait Benkhali, et al., 2023] for the intermediate emission state observed from 2018 to 2021. The left panel of Figure 4.18 presents the counts spectrum of M87. The dataset comprises approximately 138 hours of live-time with a pointing offset of 0.5° . Once again, it is observed that ONN leads to a higher number of reconstructed events overall. Particularly, energy bins centred at ~ 95 GeV and ~ 105 GeV are present in the counts spectrum reconstructed with the ONN cleaning, but not in that with the AP cleaning. The gamma-ray rate increased from 0.16 ± 0.02 with AP to 0.20 ± 0.03 per minute with ONN, while the background rate more than doubled, rising from 3.160 ± 0.008 to 6.51 ± 0.01 events per minute. A significance level of 7.6σ is achieved with the AP cleaning against 6.7σ with ONN.

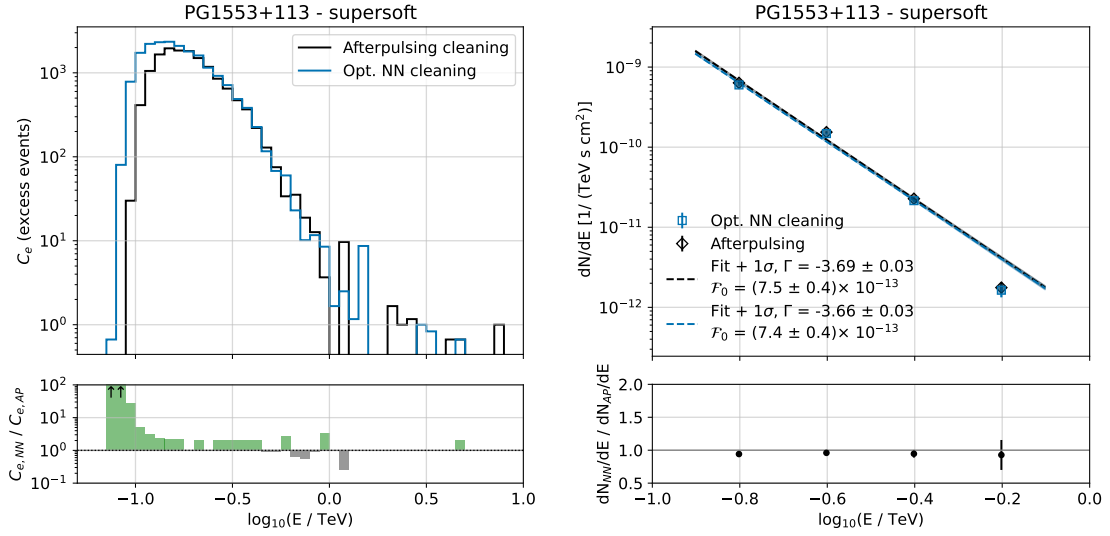


Figure 4.17: Left panel: spectrum of reconstructed source events from PG 1553+113 with the ONN (blue) and afterpulsing (black) cleaning methods. The lower left plot shows the ratio of the number of reconstructed events by ONN and Right panel: spectrum of PG 1553+113 and fit (+ 1σ) of the data points with a power-law function for ONN (blue) and AP (black). The lower right panel shows the ratio of the reconstructed spectra.

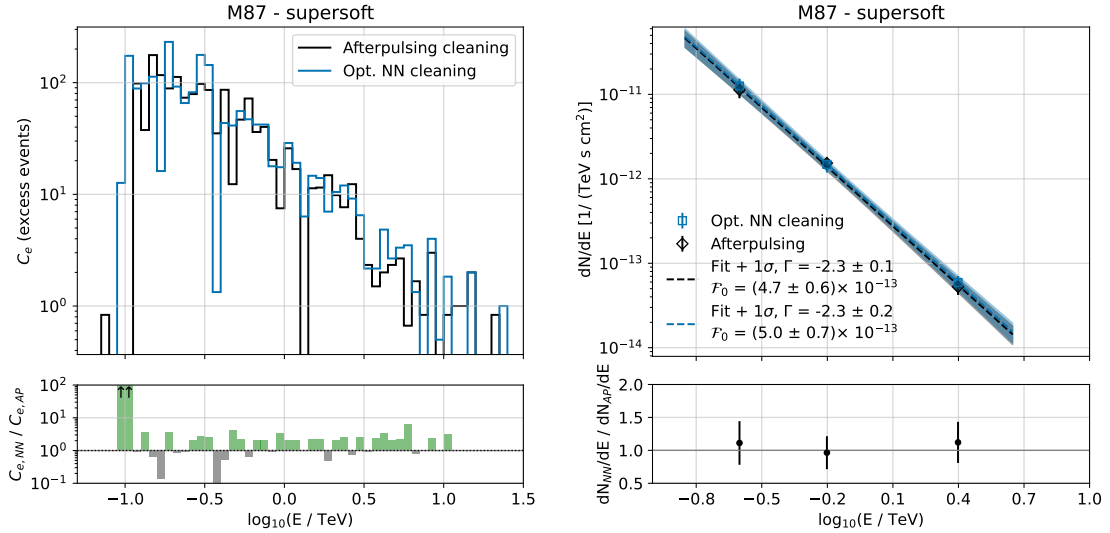


Figure 4.18: Left panel: spectrum of reconstructed source events from M87 with the ONN (blue) and afterpulsing (black) cleaning methods. The lower left plot shows the ratio of the number of reconstructed events by ONN and AP. Right panel: spectrum of M87 and fit (+ 1σ) of the data points with a power-law function for ONN (blue) and AP (black). The lower right panel shows the ratio of the reconstructed spectra.

4.5 The optimised next neighbour image cleaning for runs of short duration

Pedestal events are needed to accurately estimate the noise in a given observation. The lower the number of pedestal events in an observation, the more the IPR is susceptible to statistical fluctuations. This is particularly seen for runs of short duration (< 5 minutes). Figure 4.19 presents the IPR and dynamical contours for a run with a duration of 3 minutes. Due to the limited number of noise measurements from pedestal events above 20 dc, the dynamical contours may exhibit features above this signal range. Since at least 5 entries are required for the construction of H_Q , it is usual in low statistic scenarios ($N_{Q_0} \lesssim 10^6$) to have gaps in the charge range which do not meet this criteria. This also leads to gaps in the contours, which in principle could just be interpolated.

To enhance the statistical significance of our noise measure for short-duration runs, we provide IPR curves by averaging the noise over all pixels over all cameras in the array. In this way, one particular observation has only one IPR curve and one set of dynamical cuts which are applied to all telescopes. We notice from the right panel of Figure 4.19 that we can eliminate the peculiar features above $\gtrsim 20 - 25$ dc (where the curve is just represented as a linear interpolation due to the lack of data in the particular charge range) when averaging the IPR over all telescopes. Particularly, this approach is adopted in case $N_{Q_0} < 10^6$ for the IPR of a single telescope. In practice, only runs shorter than $\lesssim 5$ minutes are affected.

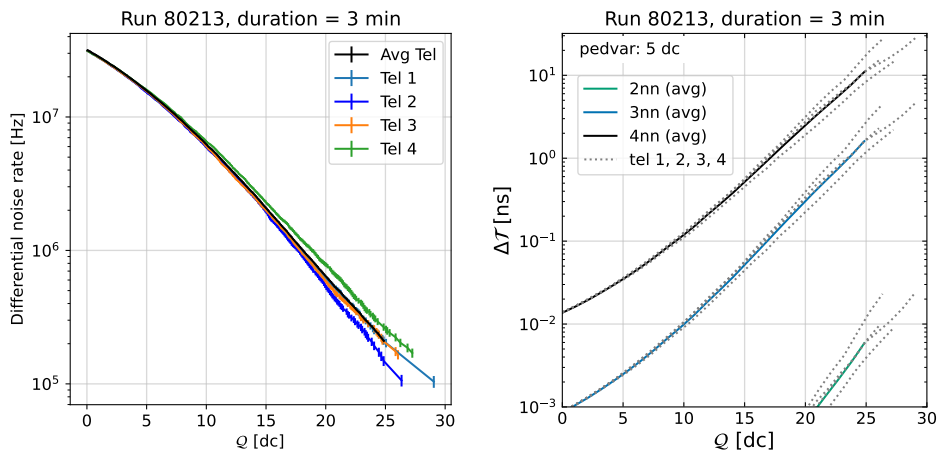


Figure 4.19: Left: Differential noise rate per telescope as a function of pixel charge for a run of 3 minutes. The average over pixels in all telescopes is shown in the black curve. Right: Dynamical cuts for each telescope in the array (grey curves). The contours given by the averaged IPR over all telescopes are shown for multiplicities $n = 2$ (black), 3 (blue) and 4 (green).

4.6 The optimised next neighbour image cleaning for data taken with Reduced High Voltage

To ensure safe operations under bright NSB conditions, the VERITAS array implements safety thresholds that reduce the voltage in the PMTs of the camera. During Reduced High Voltage (RedHV) observations, PMT currents should generally stay below $15\mu\text{A}$. In case this threshold is exceeded, observers are instructed to shut off the cameras. In order to operate under bright moonlight conditions, i.e., when the Moon is from 35% up to 65% illuminated, the voltage in the PMTs is reduced by 81% of the nominal values used during dark conditions (Table 3.1).

Due to the dependence of the cleaning thresholds on noise rates, it is plausible to assume that our method performance may vary when the NSB conditions change significantly. We evaluate the performance of the ONN cleaning in a Crab Nebula dataset obtained strictly with the RedHV mode. The dataset consists of 13 hours of live time collected with a pointing offset of 0.5° . The counts spectrum for this dataset is shown in the left panel of Figure 4.20. We notice an increase of at most a factor of ~ 3.5 in the number of reconstructed events below ~ 300 GeV. On the other hand, above ~ 300 GeV and below ~ 3 TeV, the ONN cleaning generally reconstructs up to 10% less events than the AP technique. Above 3 TeV, the counts spectra are dominated by statistical fluctuations. The spectral indexes of the spectra remains equivalent within errors.

Figures 4.21 and 4.22 present the data/MC comparison for the Reduced High Voltage Crab Nebula dataset below 20 degrees in zenith angle. Due to the low statistics of the dataset above 1 TeV, it is difficult to assess the validation between data and simulations. Systematic uncertainties range from $\lesssim 10\%$ to 12% below 1 TeV. As seen from the RedHV data/MC comparisons obtained for the afterpulsing cleaning (Figures A.30 and A.31 in Appendix A), the distribution of the MSCW parameter appears slightly shifted towards the left for higher energies, indicating that images cleaned with the ONN method are generally wider. This is also observed in the image width distribution in the plot of single telescope parameters, which can be found in Figures A.39 - A.42 in Appendix A.

A probable reason for the poor performance of the ONN cleaning above 300 GeV is the uneven illumination of pixels happening due to the positioning of the Moon. Although guidelines require that the telescopes alignment should be directed roughly 90 degrees away from the Moon, a fraction of the camera is more intensely illuminated as the Moon changes elevation during the progression of the run. This effect is seen in Figure 4.23, which shows the evolution of the image *pedvars* with time for two different runs, one taken under nominal voltage and the other under bright NSB. When averaging the differential noise rate across all the pixels in the camera, the impact of the noise rate gradients are flattened out and not taken into consideration. This suggests that the event reconstruction could be enhanced provided that IPR curves are produced on a per pixel level and/or also account for time dependency.

Based on the measured counts spectra shown in Figure 4.20, it is possible that the gradients are caused due to the varying noise rates associated with the telescope pointing. Depending on the separation angle of the Moon and the camera, shadowing effects could lead to portions of the camera being much darker than others. Since low-energy showers usually produce less extended

images with fewer pixels, the noise gradient in the images would be less pronounced compared to higher-energy showers, which cover larger portions of the camera. On the other hand, it is not possible to completely disregard the possibility that time dependent gradients might also be contributing to a poorer performance of the ONN cleaning.

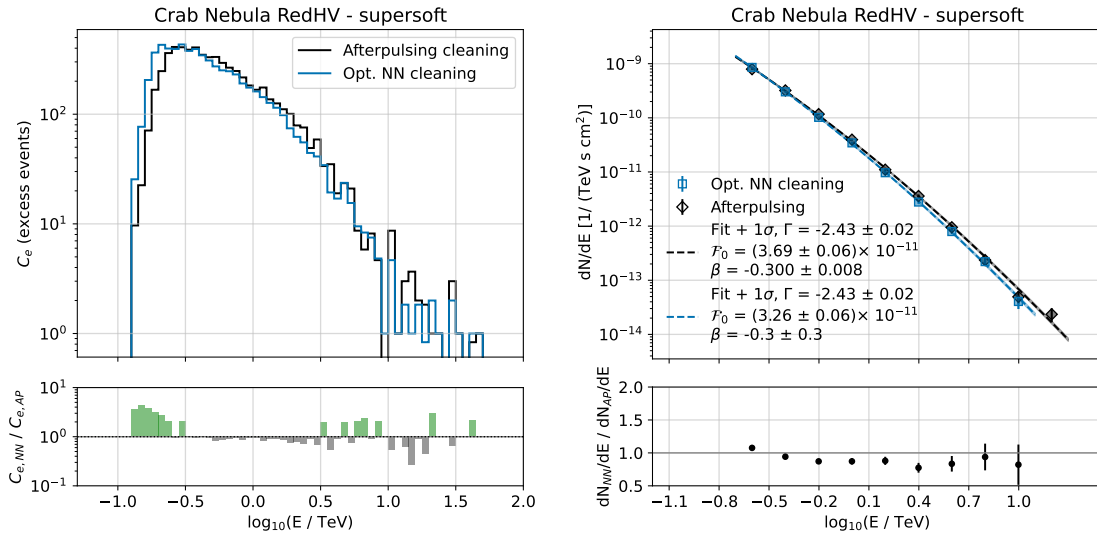


Figure 4.20: Left panel: spectrum of reconstructed source events from the RedHV Crab Nebula dataset with the ONN (blue) and afterpulsing (black) cleaning methods. The lower left plot shows the ratio of the number of reconstructed events by ONN and AP. Bins for which ONN reconstruct more events than AP are given in green and the opposite in grey. Bins at energies < 1 TeV for which there are no reconstructed events for AP but ONN reconstructs at least one source event are marked with the upper black arrows. Right panel: spectrum of the Crab Nebula and fit ($+ 1\sigma$) of the data points with a log-parabola function for ONN (blue) and AP (black). \mathcal{F}_0 is given in units of $\text{cm}^{-2} \text{s}^{-1} \text{TeV}^{-1}$. The lower right panel shows the ratio of the reconstructed spectra.

4.6. THE OPTIMISED NEXT NEIGHBOUR IMAGE CLEANING FOR DATA TAKEN WITH REDUCED HIGH VOLTAGE

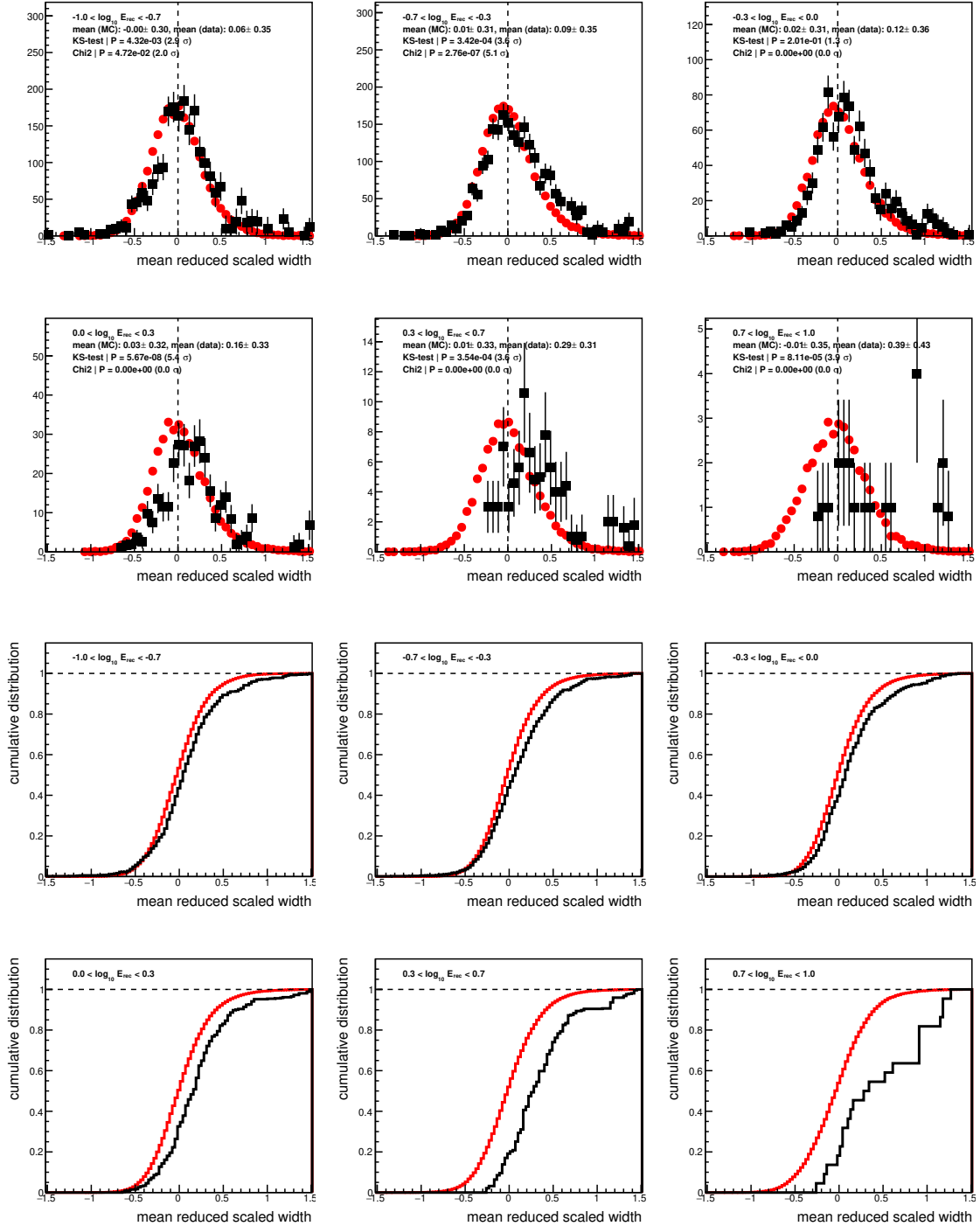


Figure 4.21: Top: Distribution of MSCW for a Reduced High Voltage Crab Nebula dataset (black squares) and simulated gamma-rays (red circles) in arbitrary units. The dataset consists of events with a zenith lower than 25 degrees. Simulated events are produced at a zenith of 20 degrees and a noise level of 200 MHz. The number of events is separated based on the reconstructed energy E_{rec} (in TeV) in the following ranges: $-1.0 < \log_{10}(E_{rec}) < -0.7$, $-0.7 < \log_{10}(E_{rec}) < -0.3$, $-0.3 < \log_{10}(E_{rec}) < 0.0$, $0.0 < \log_{10}(E_{rec}) < 0.3$, $0.3 < \log_{10}(E_{rec}) < 0.7$, $0.7 < \log_{10}(E_{rec}) < 1.0$. Bottom: cumulative distribution of MSCW for each energy range.

CHAPTER 4. IMPLEMENTATION OF THE OPTIMISED NEXT NEIGHBOUR IMAGE CLEANING METHOD FOR THE VERITAS ARRAY

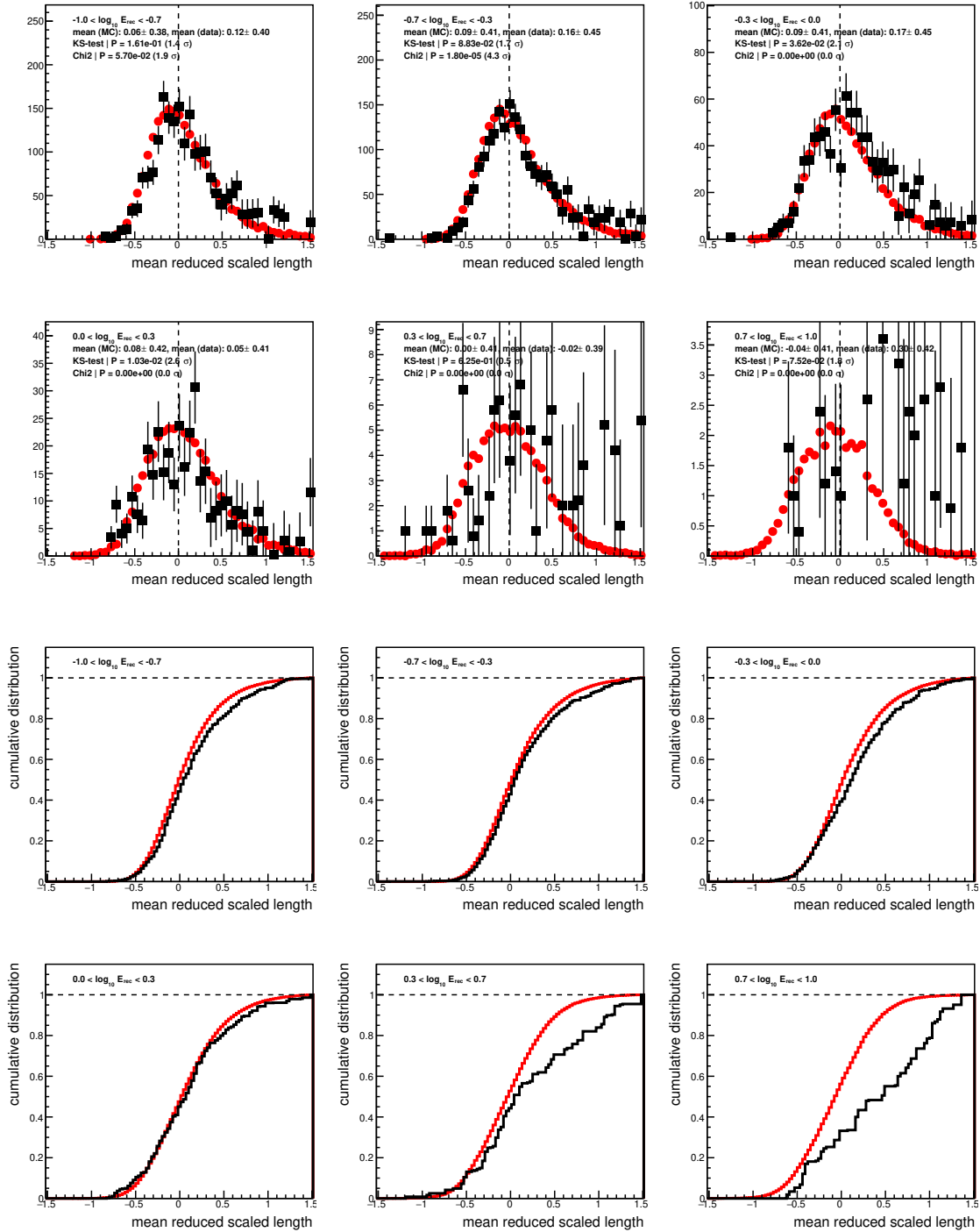


Figure 4.22: Top: Distribution of MSCL for a Reduced High Voltage Crab Nebula dataset (black squares) and simulated gamma-rays (red circles) in arbitrary units. The dataset consists of events with a zenith lower than 25 degrees. Simulated events are produced at a zenith of 20 degrees and a noise level of 200 MHz. The number of events is separated based on the reconstructed energy E_{rec} (in TeV) in the following ranges: $-1.0 < \log_{10}(E_{rec}) < -0.7$, $-0.7 < \log_{10}(E_{rec}) < -0.3$, $-0.3 < \log_{10}(E_{rec}) < 0.0$, $0.0 < \log_{10}(E_{rec}) < 0.3$, $0.3 < \log_{10}(E_{rec}) < 0.7$, $0.7 < \log_{10}(E_{rec}) < 1.0$. Bottom: cumulative distribution of MSCL for each energy range.

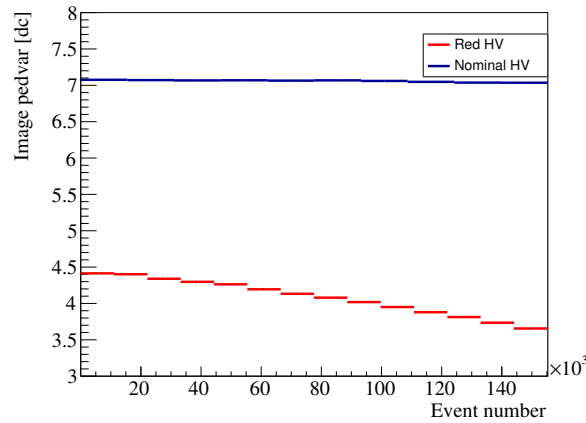


Figure 4.23: Average of *pedvars* in pixels composing a telescope image for a run taken under dark conditions (Nominal HV - blue) and under bright moonlight (Reduced High Voltage - red). The *pedvars* are plotted against the event number. The last event is recorded 30 minutes after the first one. We notice that while the *pedvars* remain fairly constant for the blue curve, it decreases by ~ 1 dc in the RedHV case. This variation could be seen as either a rise or a decline of the curve, depending if the Moon is rising or setting.

In order to test our assumptions, we first compute IPR curves segmented into time intervals. We sampled the curves in intervals of 180 seconds, resulting in 10 curves for a 30-minute run. Given that each 180-second interval contains only about 130 pedestal events recorded per pixel, averaging over the pixels camera results in about 10^4 pedestal events for the IPR calculation. As was discussed for the case of short-duration runs, enough pedestal statistics are needed to have accurate IPR curves, especially at higher signal values. For this reason, we also factor in events with at least one non-triggered telescope. The charge in the cameras from telescopes with no L2 trigger is also recorded during an array trigger. The read-out from non-triggered telescopes should, in principle, be composed of only noise, thus resembling a pedestal event. For this reason, the camera read-out from non-triggered telescopes is also included in the IPR calculation. Figure 4.24 presents the typical differential noise rate calculated in time intervals for a Reduced High Voltage run. For comparison, the Figure also presents the curves computed in time intervals but with only pedestal events (in red), the IPR curves computed with no time intervals but also considering non-triggered telescopes (in blue) and the typical IPR calculation without time intervals and with only pedestal events (in black). As expected, the IPR computation in time intervals and with only pedestal events suffers from very low statistics and therefore the charge range of the curve is reduced, meaning we would lose the reconstruction of several images. The same effects are seen even when considering longer time intervals of 10 minutes, corroborating the use of non-triggered telescopes in the IPR calculation.

The curves computed in time intervals exhibit a higher noise rate above a pixel charge of about 15 digital counts. This increase is likely a result of the non-triggered telescope cameras capturing some Cherenkov light from the particle showers, although still insufficient to provide a L2 trigger. Due to the higher noise rates, dynamical cuts will be more stringent above this threshold. Therefore,

CHAPTER 4. IMPLEMENTATION OF THE OPTIMISED NEXT NEIGHBOUR IMAGE CLEANING METHOD FOR THE VERITAS ARRAY

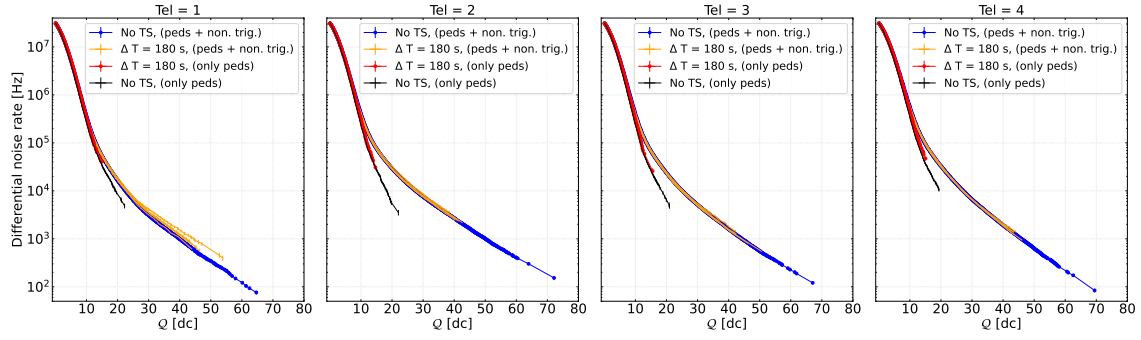


Figure 4.24: Differential noise rate per telescope as a function of pixel charge. The black curve represents the typical IPR calculation as described in the previous sections. The red curve shows an example of the IPR calculation in time slices (TS) of 180 seconds and using only pedestal events. The orange curves show the IPR calculation in time slices (TS) of 180 seconds (the run represented here has a duration of 30 minutes, resulting in 10 time slices), using pedestal events and the camera information from non-triggered telescopes during an L3 trigger. The blue curve is calculated with pedestal events and non-triggered telescopes and with no time-slices (by averaging the noise during the full 30 minutes).

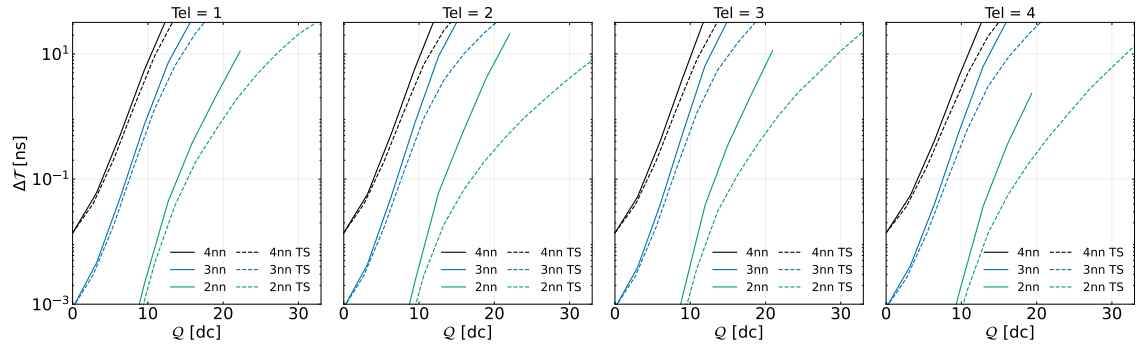


Figure 4.25: Dynamical cuts for each telescope in the array. The contours given by the typical IPR calculation are shown for multiplicities $n = 2$ (black), 3 (blue) and 4 (green) as the solid lines. The contours for the calculation of the IPR in time intervals (for time-slice 1) are shown in the same colors, but in dashed lines.

we can expect a poorer performance from the ONN cleaning in terms of event reconstruction. Figure 4.25 shows the contours for the typical calculation of the IPR curve compared to the ones obtained in time intervals.

While the time variability in moonlight levels across the camera can negatively impact the performance of the ONN cleaning, it is not possible to mitigate its effect by periodically sampling the differential noise rates. The noise rate is overestimated since the non-triggered telescopes contain some significant level of Cherenkov light from the particle showers. Therefore, dynamical cuts become overly strict, leading to a lower efficiency in event reconstruction.

We also consider the scenario where IPR curves are calculated for each individual pixel in the camera. To achieve this, due to also the low statistics when not averaging the IPR across all

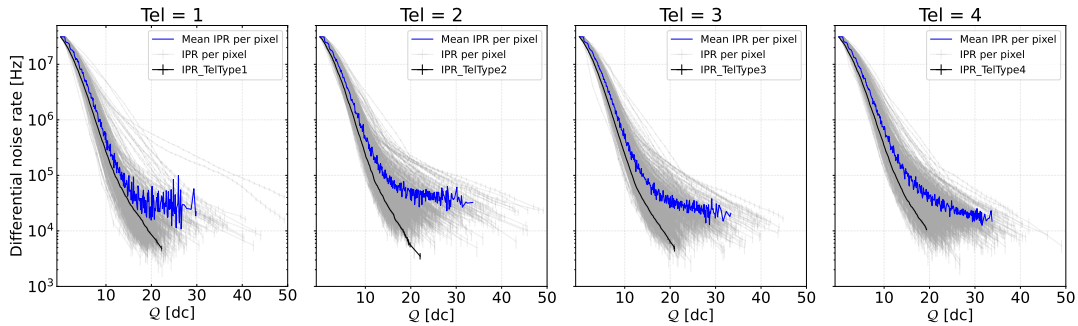


Figure 4.26: Differential noise rate per telescope for individual pixels (grey curves). The black curve represents the typical IPR calculation as described in the previous sections. The figure also shows in blue the average of the individual IPR per pixel for charge values for which there are at least 10 entries (at least 10 pixels with non-zero IPR in the particular charge value).

pixels, we also need to employ the artificial read-out of the charge from non-triggered telescopes. Figure 4.26 shows the IPR per pixel for the same run. We also notice a significant increase in the differential noise rate per pixel, as shown by the average of the curves.

The ONN cleaning is still suitable for data taken for soft and faint sources under reduced high voltage, showing a gain in source events below $\lesssim 3$ TeV. Further developments of the method for Reduced High Voltage data could include, e.g., a library of IPR curves in a discrete range of noise levels that is constructed by joining pedestal events from different data runs.

4.7 Chapter conclusions

In this Chapter, the implementation of the Optimised Next Neighbour Image cleaning for VERITAS is presented. The novel technique has enhanced the event reconstruction from simulations of the CTAO by a factor of at least two below 300 GeV. The results presented here mark the first application of the method to IACT data.

We present the performance of the Optimised Next Neighbour image cleaning on simulated events, test sources and through validations between data and Monte Carlo comparisons. The efficacy of the method is compared with results from the traditional threshold cleaning with the addition of afterpulsing correction.

Below, I summarise my contributions to the development of this project as presented in this Chapter:

- contributing, reviewing and debugging the code on the *EventDisplay* pipeline;
- production of ONN IRFs, including IRFs for performance and code testing;
- validation of the ONN via comparisons of the IRFs with the traditional cleaning;
- calculation of the optimal value for the maximum probability of false group detection;
- validation via Monte Carlo/data comparisons for different observing modes;

- validation of the ONN via comparisons with the traditional cleaning using test sources datasets;
- implementation and testing of the ONN functionality for short runs;
- testing the ONN for data taken with Reduced High Voltage and implementing and testing alternatives for the IPR calculation in this mode.

The main results of this Chapter can be summarised in the following points:

1. The implementation of the Optimised Next Neighbour Image cleaning is available in the *EventDisplay* analysis framework.
2. The noise rate in each observation is measured via pedestal events. For each data run, a differential noise rate is computed. IPR curves represent how often the NSB generates pixels with a charge above a given threshold. Given the differential noise rate of the observation, the optimal set of cleaning thresholds is identified within a parameter space of pixel charge and arrival time. We consider pixel groups of multiplicities $n = 2, 3$ and 4 to construct the final image.
3. Overall, an increased rate of reconstructed events is observed for Monte Carlo simulations. Moreover, higher effective areas and lower energy thresholds are gained for every IRF configuration involving discrete ranges in zenith angles ($40^\circ - 55^\circ$), noise levels (75 MHz - 400 MHz) and observing seasons (2012 - 2018). In the particular case shown in this Chapter, the effective area increased by a factor of at least three below 100 GeV while the energy threshold reduced by $\sim 17\%$. The energy bias below ~ 200 GeV is also less predominantly dominated by high-energy events due to the reduced suppression of low-energy events.
4. The performance of the ONN is tested on a Crab Nebula dataset consisting of 303 hours of live-time observations. This dataset was divided into testing configurations based on elevation angles, noise levels and observing seasons. For all configurations, gains in event reconstruction were seen at least below ~ 300 GeV. For the entire dataset, an increase by a factor of at least 2.5 more events is achieved below 100 GeV. Moreover, the ONN cleaning could reconstruct events at energies until then absent from the counts spectrum calculated with the afterpulsing cleaning. This effect is also observed in every testing configuration. The most remarkable result is the reconstruction of events in energy bins centred at 67 and 75 GeV, which are lower than the official sensitivity range reported by the VERITAS array. Notably, for data collected at lower zenith angles ($< 50^\circ$), additional spectral points are obtained in the flux reconstruction of the Crab Nebula.
5. The validation of the ONN cleaning was given in comparisons between the Crab Nebula dataset and Monte Carlo simulations. For this purpose, we demonstrate that the distributions of the stereo parameters MSCL and MSCW (the most discriminating ones in gamma/hadron separation) are in good agreement between data and simulations. Statistical limitations of

the dataset above this energy hinder comparisons above 5 TeV. For the ONN cleaning, a systematic error of 4% is found up to 1 TeV. This value compares with the 2% found for the afterpulsing cleaning. Simulations are not exact representations of the data since they suffer from physical limitations which introduce additional systematic errors. The ONN cleaning does not introduce significant systematic uncertainties during event reconstruction.

6. The performance of the ONN is also evaluated on a set of known TeV sources expected to be both faint and soft, i.e., they have a spectral index higher than 3. These sources are PKS 1424+240, PG 1553+113, M87, Markarian 501 and 1ES 1118+424. An increased gamma-ray rate and number of source counts are seen in all cases.
7. Background rates were also observed to increase with the ONN cleaning. This increase translated as lower detection significances for most analysed sources. This issue can be addressed by applying gamma/hadron separation cuts that are improved with machine learning techniques. In the case of the Crab Nebula dataset, the significance increased by 148σ with the application of gamma/hadron separation cuts optimised with BDT methods.
8. Due to the low pedestal statistics in the time frame of a few minutes, IPR curves for runs of short duration are averaged over all telescopes ($4 \text{ cameras} \times 499 \text{ pixels}$).
9. The efficacy of the ONN cleaning under Reduced High Voltage settings is tested with an extended Crab Nebula dataset. The ONN can reconstruct more source events below 300 GeV by a factor of at most 3.5. However, between 300 GeV and 3 TeV, the ONN systematically reconstructs at least 10% less events than the afterpulsing cleaning. This discrepancy is likely attributed to noise gradients in the camera that originate from shadowing effects and from the evolution of the Moon's position during an observation. In a first attempt to provide more accurate noise rates, we provided IPR curves segmented in time intervals. To account for the low statistics of pedestal events in short intervals (from 180 seconds up to at least 10 minutes), we include in the noise estimation the pixel charges from telescope cameras that have no L2 trigger during an array read-out. The final IPR curves exhibit noise rates that are much higher above a certain threshold, indicating that the signals in non-triggered cameras likely contain some level of Cherenkov light. Since higher noise rates lead to stricter thresholds, fewer reconstructed events would be obtained with the periodically sampled IPR curves.
10. We also calculate IPR curves for each individual pixel. In this scenario, we also include non-triggered telescopes in the noise estimation due to the low pedestal statistics. As expected, noise rates are also higher on average, which would lead to stricter cleaning thresholds.

Overall, the implementation has demonstrated an exceptional performance in event reconstruction, particularly at low energies ($< 200 - 300 \text{ GeV}$). The Optimised Next Neighbour image cleaning can be especially advantageous for faint and soft sources, which benefit from the improved gamma-ray rate. A higher detection significance can also be achieved when combined with cuts optimised

with machine learning techniques. Despite results seen at higher energies, the ONN cleaning is still suitable for the analysis of data taken with Reduced High Voltage settings, particularly below ~ 300 GeV. Further developments in the implementation of the Optimised Next Neighbour image could be developed to improve its performance for data taken under bright moonlight.

Observations of tidal disruption events with VERITAS

In Section 2.5.1, the prospective role of TDEs as astrophysical accelerators and sources of radiation at VHE was addressed. Certain radiative emission processes that are presumed to power TDEs could produce a detectable radiation at energies greater than 100 MeV. The most obvious scenario that provides the necessary conditions for particle acceleration, and therefore for non-thermal emission, is the formation of relativistic jets due to an accretion disk fuelled by the circularisation of the star's bound debris. In addition, particle acceleration in zones which do not involve jets are also argued to possibly play a key role in the subsequent production of neutrinos and VHE radiation. This is the case, for instance, of collisions of disc outflows with the CNM material, as well as through interactions involving the tidal debris streams [Murase et al., 2020].

Due to the high energies once acquired during acceleration mechanisms, the relativistic protons could produce a gamma-ray signal through hadronic interactions with the surrounding radiation field or with the ambient gas. In these processes, charged and neutral pions are produced. The decay of the charged pions leads to a neutrino signal, while the decay of the neutral pions results in two gamma rays ($p = 98.8\%$). Alternatively, electrons could also be accelerated, giving rise to leptonic interactions. Although the exact role of each mechanism has yet to be clarified for certain presumed classes of shock transients, indications suggest that hadronic processes are favoured at least for the emission of classical novae [Fang et al., 2020]. The coincident detection of neutrinos and electromagnetic radiation in the GeV - TeV energy range would be the smoking gun for hadronic acceleration in TDEs. Nonetheless, it is possible that a detectable neutrino signal, e.g. seen by IceCube, is produced while the gamma rays are obscured in the dense photon and matter fields, leading to a no-detection from gamma-ray observatories [Aartsen et al., 2020]. In this scenario, gamma rays produced alongside neutrinos via hadronic processes would interact via two-photon annihilation with the thermal radiation from the source or via other channels of annihilation with the surrounding matter (see Chapter 2). These interactions then lead to the attenuation of the gamma-ray signal, which is reprocessed into lower energy photons. Nonetheless, there are reports of possible associations of astrophysical IceCube neutrinos with a few radio-detected TDEs that have shown no traceable gamma-ray emission. This is the case, for instance, of TDEs AT2019dsg [Stein et al., 2021], associated with IceCube neutrino IC191001A (59% signalness¹, 200.0 TeV), and AT2019fdr, reported within the 90% localisation region of IC200530A (59% signalness, 82.2 TeV) [Reusch et al., 2022]. The probability of finding a coincident radio-traceable TDE with a

¹Signalness refers to the probability of the neutrino being of astrophysical origin.

bright bolometric luminosity similar to the one derived for AT2019dsg ($10^{44.54 \pm 0.08}$ erg s⁻¹ at peak) is only of 0.2% [Stein et al., 2021], suggesting that TDEs are likely potential sites for particle acceleration (a neutrino of energy ~ 100 TeV would require a parent proton with energy in the PeV regime). In addition, the contribution of jetted TDEs to the diffuse astrophysical neutrino flux is estimated to be at most of 1%, while for non-jetted ones, of 26% (90% C. L.) [Stein and IceCube Collaboration, 2019]. While Fermi-LAT has detected no gamma-ray signal from any of the TDEs associated with astrophysical neutrinos, gamma-ray observatories, both space born and ground based, might still be sensitive to a potential signal given the ideal conditions. A detection could help further probe the potential acceleration mechanisms taking part in such environments.

The investigation of TDEs in high and very high energy gamma rays is still in its early stages. Among the available literature on the events observed above $\gtrsim 100$ MeV, Ref. [Peng et al., 2016] reports the non-detection of HE emission by Fermi-LAT for the relativistic jetted TDEs Swift J1644, Swift J2058.4+0516 and Swift J1112.2-8238. In the same reference, the non-detection is also reported for the nearby event ASASSN-14li. In addition, the VERITAS Collaboration reports the non-detection of Swift J1644 after 28 hours of exposure time on the event [Aliu et al., 2011]. Finally, in 2021, H.E.S.S. reported the non-detection of AT2021uqv, a thermal X-ray (0.3 - 1.0 keV) event showing a brief radio emission [Burrows et al., 2005]. The particular subset of jetted TDEs observed directly on-axis or slightly off-axis, such as Swift J1644, Swift J1112.28238 and AT2022cmc [Andreoni et al., 2022], are the most promising candidates for searches of VHE gamma-ray radiation. However, as discussed in Chapter 2, the inferred volumetric rate of on-axis jetted TDEs represents a very small fraction of the total expected rate of events [Teboul and Metzger, 2023].

Since almost six years after the disruption of Swift J1112.28238, AT2022cmc has been the only event to show clear signs of relativistic jet emission. X-ray observations yield a corresponding peak isotropic luminosity of 10^{48} erg s⁻¹ [Pasham et al., 2022] and a jet Lorentz factor of $\Gamma \sim 10 - 100$ [Yao et al., 2024], revealing the extreme energetic nature of this source. AT2022cmc was observable above 30 degrees in elevation by the VERITAS array during its eruption. However, due to its high redshift ($z = 1.19$), it was not a suitable candidate for VHE follow-up as it was predicted that any VHE emission would be heavily attenuated by the EBL [Franceschini and Rodighiero, 2017]². At this redshift, almost all radiation above ~ 100 GeV would be suppressed en route to Earth.

Generally, TDEs exhibiting other non-thermal emission components besides clear on-axis relativistic jets, such as radio and non-thermal X-ray fluxes, are also good candidates for VHE searches. Overall, it is critical to acknowledge that the main challenge when observing TDEs in high and very high energies is the internal absorption of gamma rays by two-photon annihilation. This process takes part due to the dense environment composed of thermal photons of lower energy. Additionally, gamma rays can also be attenuated by interacting with the ambient nuclei, although this is a less relevant channel of attenuation. For instance, studies suggest that TeV gamma rays in a generic

²For results presented throughout this chapter, I consistently use Ref. [Franceschini and Rodighiero, 2017] to model the optical depth from EBL attenuation

TDE scenario should be heavily attenuated by two-photon annihilation interactions in the first ~ 90 days post disruption [Fang et al., 2020].

Within the scope of my doctoral research, I assumed a key role in establishing the first follow-up program for TDEs at VHE within the VERITAS Collaboration. My contributions included

- writing and submitting Target of Opportunity (ToO) observations of TDEs,
- following up on alerts from The Astronomer’s Telegram³ (ATEL) and the Transient Name Server⁴ (TNS),
- triggering candidates for observations and
- communicating with the VERITAS Time Allocation Committee (TAC) to schedule and plan observations.

In addition, I conducted a multiwavelength and internal absorption analysis of each observed TDE event, which complemented the VERITAS observations and provided insights regarding the processes of gamma-ray attenuation. With this study, new adjustments on the ToO program can be introduced in order to improve the use of telescope time and the selection of potential candidates for observation.

In this chapter I present the details of the ToO proposal for the observation of TDEs with VERITAS and an introduction to the triggered events in section 5.1. VERITAS and Fermi-LAT results are presented in Section 5.2 and a study on the estimation of the internal attenuation in Section 5.3. I also present an updated analysis of Swift J1644 in Section 5.4. Conclusions of this work are presented in Section 5.5. The methods used for the multiwavelength analysis are given in Appendix B.

5.1 Target of Opportunity observations of tidal disruption events

Target of Opportunity Observations for the VERITAS array are requested for astrophysical events which may occur at an unknown point in time (or at least not entirely predictable or constrained timeframe). The actual event position and disruption time might be unanticipated, as seen in phenomena such as TDEs and GRBs. Alternatively, the target may be known in advance, but its flux is expected to change within a time interval of high uncertainty. This is the case, for example, of recurrent novae such as RS Ophiuchi. Depending on the transient class, e.g. GRBs and FBOTs, urgent or immediate observations are required. Conversely, a more deliberate approach to observations may occur in case the transient class exhibits extended light curves that last weeks or months, which is the case of TDEs. ToO proposals must include specific triggering conditions and detailed observation plans. The final decision on whether the candidate will be observed or not relies on

³The Astronomer’s Telegram is an online platform that distributes information on recent astronomical observations. Available at: <https://astronomerstelegram.org/>

⁴Since 2016, the Transient Name Server is the official tool from the International Astronomical Union for reporting new astronomical transients, such as TDEs, FBOTs and SNe candidates. Available at: <https://www.wis-tns.org/>

the TAC. Factors such as the observing schedule, program priorities and the candidate’s scientific interest are taken into account in this decision.

Since 2021, a dedicated ToO proposal titled ”Target of opportunity observations of tidal disruption events” was established within the Astroparticle, Transient, Optical, Multi-Messenger (ATOMM) Science Group of the VERITAS Collaboration. The proposal requests 60 hours of dark time observations (moonlight $\lesssim 65\%$) in case ATEs and/or the TNS reports a TDE alert, which is simply a discovery report containing information such as redshift, classification, source position, etc. These alerts serve the purpose to inform interested astronomers of a new event as quickly as possible, therefore triggering swift follow-up observations. The total of 60 hours assigned per observing season are expected to be evenly distributed among the follow-up of 3 TDEs, resulting in 20 hours per TDE candidate. These 20 hours are then equally divided into 3 dark runs (DRs)⁵. In order for the TAC to approve the allocated time, the TDE must satisfy the criteria summarised in Table 5.1.

As of the time of writing this thesis, the TNS database reports 34 TDEs since the start of the 2021-2022 observing season, resulting in an average rate of approximately one TDE alert per month. Reports were made by optical instruments such as the ZTF [Bellm et al., 2018], the Asteroid Terrestrial-impact Last Alert System (ATLAS) [Heinze et al., 2018; K. W. Smith et al., 2020; Tonry et al., 2018] and ASAS-SN [Kochanek et al., 2017; Shappee et al., 2014], with ZTF being responsible for 19 of these alerts. In particular, ZTF and VERITAS can provide a comprehensive optical and gamma-ray follow-up of astronomical events due to their overlapping FoV.

The scarce literature combined with the limited observations of TDEs at high and very high energies result in poor modelling constraints for gamma rays. Current observations by IACTs, as will be described in this chapter, are mainly based on the identification of minimal (short-lived or faint) non-thermal emission signatures. The criteria are then often based on the observational properties distinguished for the known relativistic events. These properties include a power-law decaying X-ray emission, a relatively long-lasting peaked radio synchrotron flux and associations with astrophysical neutrinos (from AT2019dsg and AT2019fdr). However, due to the long time-scales of the light curve, the identification of the thermal or non-thermal origin of the X-ray component and whether the radio flux can be associated or not with synchrotron emission from the transient (instead of from the host) is often issued months after the discovery. This happens similarly with the disclosure of the transient’s classification as a TDE, which typically happens about a few weeks to months after the initial trigger. This is due to the long-term underlying TDE features which distinguish them from AGNi and SNe (namely, a smooth power-law decay over the course of months, a hot blue continuum and a rise time in the order of weeks). This delay combined with the scarce number of clearly relativistic candidates requires more relaxed trigger criteria. For instance, providing upper-limits on the gamma-ray flux of TDEs that have a detected radio and/or X-ray emission - even if for a short period and if this emission is later on confirmed as non-thermal - can already provide interesting constraints, e.g. on the neutrino fluence when assuming hadronic interactions. These arguments were critical in the triggering decisions made for this ToO proposal.

⁵A dark run comprises the period when observatories can actually conduct observations, meaning when the moonlight is at an acceptable level. It usually lasts for three weeks with an interval of about one week until the start of the next dark run.

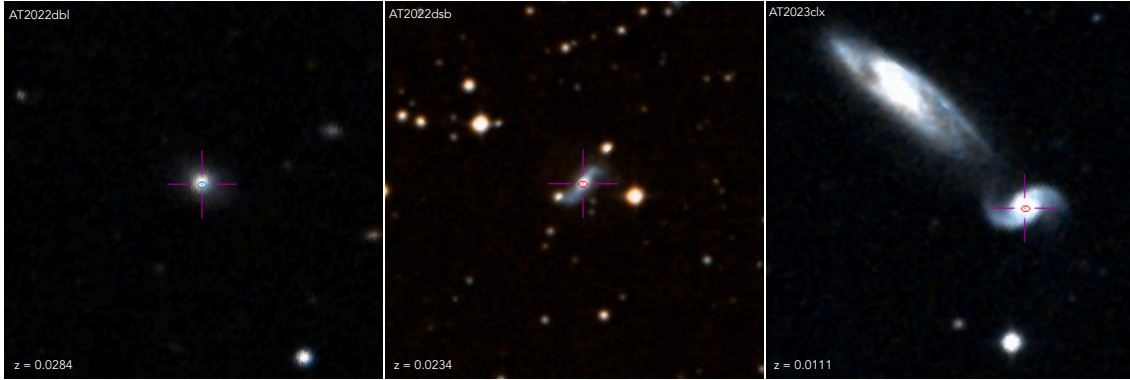


Figure 5.1: Optical images of host galaxies for AT2022dbl, AT2022dsb and AT2023clx, obtained with SDSS. The position of the host galaxy is highlighted by the red cross.

In fact, so far only a handful of events exhibited radio luminosities above 10^{40} erg s⁻¹ [Alexander et al., 2020]. For this reason, we consider for this proposal that TDEs with a confirmed radio detection are especially worth pursuing.

During the observing seasons of 2021-2022 and 2022-2023, the follow-up of 3 TDEs that fit our criteria was possible: AT2022dbl, AT2023dsb and AT2023clx. Figure 5.1 presents optical images of the respective host galaxies obtained with the Sloan Digital Sky Survey (SDSS, [Gunn et al., 2006]). For TDEs AT2022dsb and AT2023clx, allocating a total of 20 hours was not possible because of the early monsoon shutdown.

Trigger criteria	
Redshift	< 0.5
Elevation	> 30 degrees
Time period	< 3 months post-optical peak
Request	20 hours in 3 Dark Runs

Table 5.1: Summary of the trigger criteria for the Target of Opportunity observations of TDEs within the VERITAS Collaboration: redshift < 0.5, a time period of less than 3 months post-optical peak and an elevation greater than 30 degrees to guarantee the lowest possible energy threshold and highest sensitivity. In case of an accepted trigger, 20 hours of observing time will be equally scheduled into three consecutive dark runs.

	Unit	AT2022dbl	AT2022dsb	AT2023clx
R. A. (J2000)	[hms]	12:20:45.01	15:42:21.74	11:40:09.40
DEC (J2000)	[dms]	+49:33:04.68	-22:40:14.04	+15:19:38.54
Redshift		0.0284	0.0234	0.0111
Distance	[Mpc]	124.80	102.95	48.98
Discovery date		2022-02-22	2022-03-01	2023-02-23
Peak mag		16.93	17.04	16.07
Host Galaxy		WISEA J122045.05+493304.7	ESO 583-G004	NGC 3799

Table 5.2: TDE summary table: sky position in right Ascension (R. A.) and declination (DEC), redshift, distance, discovery date, peak optical magnitude, ZTF ID and host galaxy for AT2022dbl (wis-tns.org/object/2022dbl), AT2022dsb (wis-tns.org/object/2022dsb) and AT2023clx (wis-tns.org/object/2023clx). Information is retrieved from the respective TNS entry linked in this caption. The distance is calculated assuming the Planck 2018 cosmology parameters [Aghanim et al., 2020].

The multi-wavelength data showcased in this Chapter consist of observations from a variety of telescopes and instruments which cover a wide range of the electromagnetic spectrum. The dataset for each TDE was constructed using publicly accessible data analysis tools. In Appendix B, I describe the methods for data collection, reduction and analysis in three main sections: *a*) optical and ultra-violet (OUV) instruments: ZTF, ATLAS, ASAS-SN and Swift-UVOT, *b*) X-rays and radio telescopes and *c*) gamma-ray instruments: Fermi-LAT and VERITAS. Table B.1 from Appendix B presents a summary of the filters from the OUV instruments outlined in this Chapter. Magnitudes presented in this thesis are reported in the AB system [Oke, 1974]. Below, I provide a literature review for AT2022dbl, AT2022dsb, and AT2023clx. A summary of the properties from these TDEs is presented in Table 5.2.

5.1.1 AT2022dbl

AT2022dbl is a TDE located at a distance of 125 Mpc ($z = 0.0284$). It was first detected by the ATLAS optical survey in January 2022 with an AB magnitude of 20.01. The spectrum of AT2022dbl displays broad Hydrogen and Helium emission features, as well as a blue continuum. Subsequent detections by ZTF showed that the optical magnitude reached a peak of $m_{AB} = 16.93$, approximately 20 days after the initial discovery.

The Neil Gehrels Swift Observatory [Angelini et al., 2024] conducted UV and X-ray observations, which led to the detection of a long-lasting UV signal from Swift-UVOT since near the optical peak. Only flux ULs were derived by Swift-XRT in the energy range of 0.3 - 10 keV. However, even with no detection, the existence of an energetic X-ray component that is heavily absorbed

cannot be ruled out. The Karl G. Jansky Very Large Array (VLA) [Lacy et al., 2020] reported a potential radio signal of $32 \pm 7 \mu\text{Jy}$ at 15.0 GHz, located approximately 0.4 arcsec away from the optical position of AT2022dbl⁶. Given that the VLA has an angular resolution of 0.13 arcsec, this emission is strongly suggested to be associated with the event. Because of the lack of further reports, it is not possible to debate on the astrophysical origin of the detection by VLA. Combined with the absence of X-ray emission, AT2022dbl is classified as a thermal TDE. Nonetheless, based on previous discussions, we still deem it a good candidate for VHE follow-up.

5.1.2 AT2022dsb

AT2022dsb was discovered by ASAS-SN with a magnitude of $m_{AB} = 17.3$ in the ESO 583-G004 galaxy ($z = 0.0235$), a type II AGN [Y.-P. Chen et al., 2022]. The spectral analysis of AT2022dsb indicates the presence of Hydrogen and Helium emission lines and a blue continuum. The extended ROentgen Survey with an Imaging Telescope Array (eROSITA) [Merloni et al., 2024] detected the ultra-soft X-ray emission (0.2 - 8 keV) from AT2022dsb approximately 14 days before its peak optical brightness [Malyali et al., 2023]. In a work published about a year after the detection, Ref. [Malyali et al., 2023] reports that the eROSITA detection was best fitted by a blackbody spectrum with a temperature of $k_B T = 47^{+5}_{-5}$ eV, which is consistent with the typical temperature observed in previous X-ray bright TDEs ($\sim 10^5$ K) [R. Saxton et al., 2021]. The early X-ray emission is attributed to the recent formation of an accretion disk assembled from the circularisation of the earliest fallback stream [Malyali et al., 2023]. As observed by the X-ray Multi-Mirror Mission (XMM-Newton, 0.2 - 2 keV) [Schartel et al., 2022] approximately 19 days and 173 days after the eROSITA observations, the X-ray flux in the 0.2 - 2 keV energy range decreased by a factor of about 39. This flux is best fit by a power-law spectrum with a photon index of $2.7^{+0.3}_{-0.3}$. Because no major change in the flux is observed in XMM detections spaced by a period of ~ 150 days, Ref. [Malyali et al., 2023] argues that the XMM detection is probably dominated by diffuse X-ray emission of the CNM environment of the host galaxy and is unrelated to the accretion triggered by the TDE. This is motivated by the low-luminosity AGN nature of the host galaxy, which could have been responsible for boosting the density of material surrounding the disk and leading to a higher reprocessing level of the disk emission. Swift-XRT (0.3 - 10 keV) monitoring observations did not show any significant X-ray emission above background levels for about 200 days after the initial eROSITA detection.

Most TDEs are identified by optical instruments without displaying transient X-ray emission. The reprocessing of the X-ray radiation could be caused in regions such as the debris envelope formed around the disk. On the other hand, it is important to also understand the observational constraints that might be linked to the TDEs being obscured in X-rays. For the subset of X-ray bright TDEs, targeted observations typically commence around or after the events have reached their peak optical brightness. This delay is likely a result of the large number of transients discovered through optical surveys, leading to X-ray follow-up observations being initiated only when

⁶<https://www.wis-tns.org/astronotes/astronote/2022-57>

there are strong indications that the event is indeed a TDE. Typically, this classification occurs near or after the optical peak of the event (about a few weeks after the first detection).

Moreover, according to Ref. [Malyali et al., 2023], among the TDEs detected in X-rays before their optical counterpart, it is also possible that the estimated unabsorbed X-ray flux and intrinsic luminosity might be oversimplified. For example, factors such as the underestimation of the absorption component from the stellar debris or from the host galaxy could result in the overestimation of the flux of the event.

In radio wavebands, AT2022dsb was detected by the Australia Telescope Compact Array (ATCA) at frequencies of 5.5 GHz and 9.0 GHz [Goodwin et al., 2022]. Considering the transient nature of the source and the absence of prior radio detections from the event's location, it is strongly suggested that the radio emission is associated with the TDE rather than with the host galaxy.

Optical detections of AT2022dsb persisted for about ~ 3 months after the event reached its peak brightness. During the monitoring campaign, AT2022dsb was detected in the ultraviolet range by UVOT. No detection was seen in the Swift-XRT campaign.

5.1.3 AT2023clx

AT2023clx was discovered by the ASAS-SN optical survey with a magnitude of $m_{AB} = 16.3$. The event happened at the galaxy NGC 3799 and is one of the nearest detected TDEs, located at 49 Mpc ($z = 0.0111$). The host galaxy is noted as a potential AGN by the Milliquas catalogue [Flesch, 2023]. Spectroscopic analysis of AT2023clx revealed characteristic Hydrogen emission lines and a blue continuum [Zhu et al., 2023].

The event reached its peak brightness in approximately 10 ± 2.5 days after disruption, making it one of the fastest-rising TDEs recorded to date [Charalampopoulos et al., 2024]. This fast temporal light curve characteristic suggests that the disruption originated from a star of extremely low mass $< 0.1 M_{\odot}$ by a black hole with a mass of about $10^6 M_{\odot}$. The impact parameter (fraction of star disrupted) is estimated at $\sim 80\%$ [Charalampopoulos et al., 2024].

No X-ray detections were reported for this candidate and a Swift-XRT analysis results also in no detection. Similar to AT2022dbl, the existence of a heavily absorbed X-ray component cannot be ruled out. The Arcminute Microkelvin Imager - Large Array (AMI-LA) [Grainge et al., 2012] reported a potential radio detection at a central frequency of 3 GHz within the reported optical position of AT2023clx [Sfaradi et al., 2023]. This detection results in a flux density of 0.40 ± 0.08 mJy after 4 hours of observations about the same day as the first detection by Swift-UVOT. No further radio detections have been reported.

5.2 VERITAS and Fermi-LAT results

In this section, I present VERITAS and Fermi-LAT analysis results for AT2022dbl, AT2022dsb and AT2023clx.

VERITAS

The VERITAS observation summary for each event is shown in Table 5.3, while data analysis results are presented in Table 5.4. No detection was found for AT2022dbl, AT2022dsb or AT2023clx, yielding flux ULs above the energy threshold of 108 GeV (95% C. L.). Significance and excess skymaps are presented in Figures 5.2, 5.4 and 5.6 for AT2022dbl, AT2022dsb and AT2023clx, respectively. Flux ULs for a power-law spectral index of $\Gamma = -2$ correspond to ~ 0.1 , 0.1 and 0.3% of the integral Crab flux for AT2022dbl, AT2022dsb, and AT2023clx, respectively. These values are calculated assuming a log-parabola description of the Crab Nebula spectrum [Meagher, 2015]. At least about 1000 hours would be necessary to achieve a detection at this flux UL level (the VERITAS sensitivity is presented in Figure 3.20).

	Unit	AT2022dbl	AT2022dsb	AT2023clx
Live-time	[h]	20.91	14.61	12.13
Mean elevation	[degrees]	65.26	34.35	68.42
Trigger rate	[Hz]	147.31	74.94	145.12
Mean noise rate	[MHz]	270	389	310

Table 5.3: Summary of VERITAS observations of TDE candidates: total live-time, mean elevation, trigger rate and mean noise rate.

Fermi-LAT

The Fermi-LAT light curve was divided into two time periods: the first one, $t_{\text{LAT},1}$, spans from the discovery date up to 20 days post optical peak, while the second one, $t_{\text{LAT},2}$, extends from 20 days post-peak until the last day of either optical or ultra-violet detection. The period $t_{\text{LAT},1}$ is presumed to be under the highest level of attenuation due to the increased brightness of the lower energy photon field. On the other hand, for $t_{\text{LAT},2}$ the effects of attenuation should be dimmer. The periods $t_{\text{LAT},1}$ and $t_{\text{LAT},2}$ for each event are presented in Table 5.5. The Fermi-LAT analysis results in a test statistics of $TS = 0.0$ for AT2022dbl, AT2022dsb and AT2023clx. Therefore, no significant emission is derived for any candidate. Flux ULs in the energy range of 100 MeV up to 300 GeV were derived and can be found in Table 5.5.

Figures 5.3, 5.5 and 5.7 present the multiwavelength light curves for AT2022dbl, AT2022dsb and AT2023clx, respectively. The light curve derived from VERITAS observations is given in a single time period enclosing the complete course of observations (due to the live-time in the order of \sim hours).

	AT2022dbl	AT2022dsb	AT2023clx
N_{ON}	4454	711	2827
N_{OFF}	4447.50	747.33	2739.83
N_s	6.5	-36.33	87.17
S (σ)	0.1	-1.2	1.5
excess/min	0.01 ± 0.06	-0.04 ± 0.03	0.11 ± 0.07
$\Phi_{\text{VTS}}^{\text{UL}}$ (95% C. L., 0.1 - 10 TeV) ($\text{erg cm}^{-2} \text{ s}^{-1}$, $\Gamma = 2$)	$7.81 \cdot 10^{-13}$	$4.76 \cdot 10^{-13}$	$1.71 \cdot 10^{-12}$
$\Phi_{\text{VTS}}^{\text{UL}}$ (95% C. L., 0.1 - 10 TeV) ($\text{erg cm}^{-2} \text{ s}^{-1}$, $\Gamma = 3$)	$1.83 \cdot 10^{-12}$	$9.44 \cdot 10^{-13}$	$5.19 \cdot 10^{-12}$

Table 5.4: VERITAS analysis results: number of events from the ON region, N_{ON} , number of events from the OFF region, N_{OFF} , number of excess events, N_s , significance, excess rate and flux ULs at 95% C. L. corrected for EBL attenuation. Flux ULs are provided considering a power-law spectrum with indices of $\Gamma = 2$ and $\Gamma = 3$ (above the energy threshold of 108 GeV and below 10 TeV).

	AT2022dbl	AT2022dsb	AT2023clx
$t_{\text{LAT},1}$ (MJD)	59615 - 59658	59627 - 59661	59986 - 60017
$t_{\text{LAT},2}$ (MJD)	59658 - 59766	59661 - 59831	60017 - 60117
$\Phi_{\text{LAT},1}^{\text{UL}}$ (95% C. L., 0.1 - 300 GeV) ($\text{erg cm}^{-2} \text{ s}^{-1}$, $\Gamma = 2$)	$2.37 \cdot 10^{-14}$	$9.41 \cdot 10^{-15}$	$1.46 \cdot 10^{-13}$
$\Phi_{\text{LAT},1}^{\text{UL}}$ (95% C. L., 0.1 - 300 GeV) ($\text{erg cm}^{-2} \text{ s}^{-1}$, $\Gamma = 2$)	$1.92 \cdot 10^{-14}$	$1.82 \cdot 10^{-14}$	$5.22 \cdot 10^{-14}$

Table 5.5: Time periods used for the derivation of Fermi-LAT flux upper limits, in Modified Julian Dates (MJD): 1) $t_{\text{LAT},1}$: discovery date up to 20 days post optical peak, 2) $t_{\text{LAT},2}$: 20 days post optical peak up until last day of optical or UV detection. Since there is no significant detection for any candidate, upper limits are derived for each time period: $\text{UL}_{\text{LAT},1}$ and $\text{UL}_{\text{LAT},2}$, at 95% C. L. (spectra assumed as a power-law with index $\Gamma = 2$) at the energy range $100 \text{ MeV} < E < 300 \text{ GeV}$.

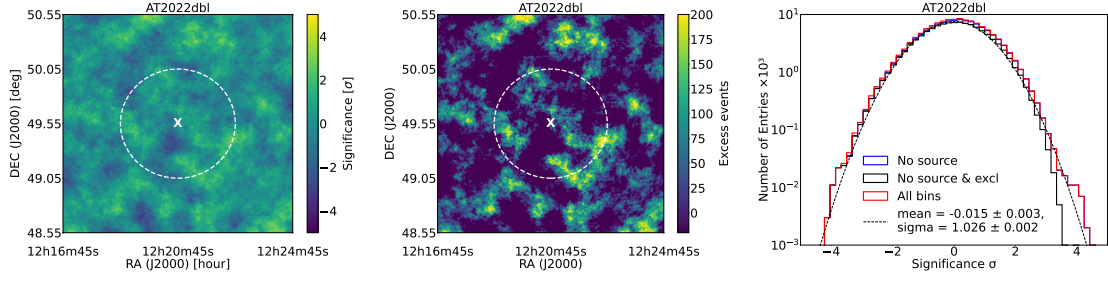


Figure 5.2: Significance map (**left panel**), excess events map (**middle panel**) and significances distribution (**right panel**) for AT2022dbl. The white cross and the white circle represent respectively the position of the TDE and a circular region of 0.5° . Significance distributions are presented for the entire skymap (red histogram), without source region (blue histogram) and without source and exclusions regions (black histogram with Gaussian fit).

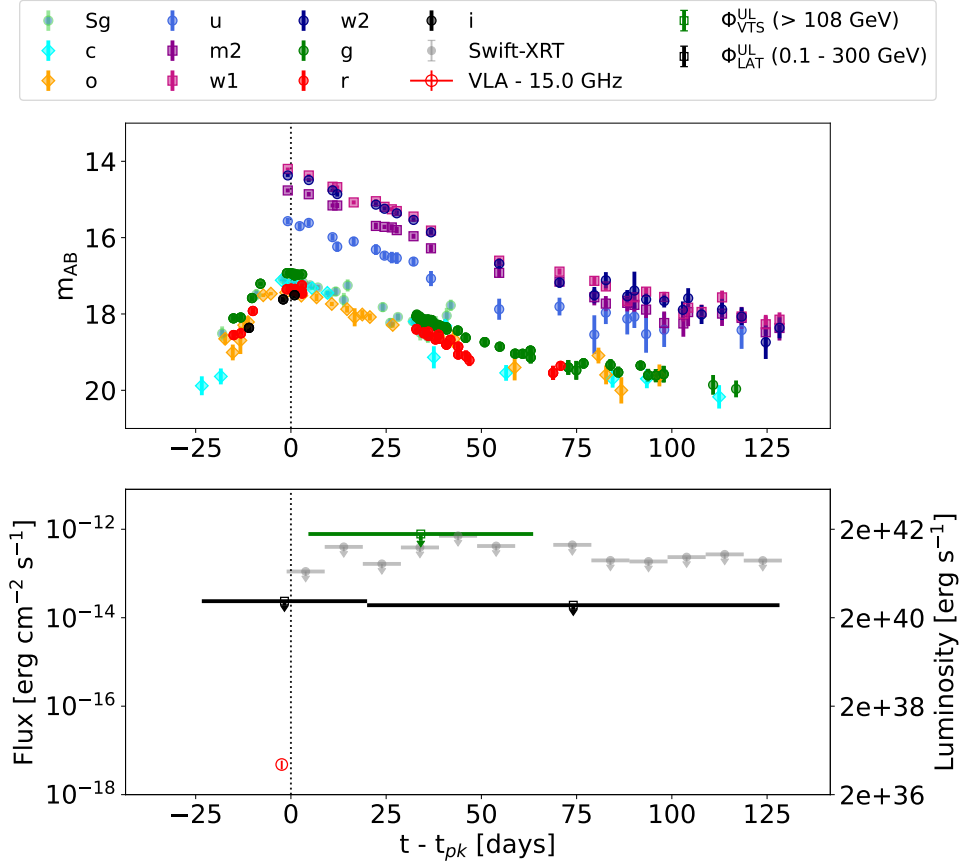


Figure 5.3: Multi-wavelength light curve for AT2022dbl. **Upper panel:** optical and UV magnitudes obtained by ZTF (filters: green g , red r and infra-red i), ASAS-SN (filter: green Sg), ATLAS (filters: orange o and cyan c filters) and Swift-UVOT (filters: u , $w1$, $w2$ and $m2$). **Lower panel:** upper limits from Swift-XRT ($0.3 - 10$ keV), VERITAS (108 GeV $< E < 10$ TeV, 95% C. L.; $\Gamma = 2$) and Fermi-LAT (100 MeV $< E < 300$ GeV, 95% C. L.; $\Gamma = 2$). Flux levels are given on the left side of the y-axis, while luminosities on the right side. Fermi-LAT flux ULs are given in the time periods $t_{LAT,1}$ and $t_{LAT,2}$. A detection by the VLA radio telescope is also shown in the lower panel.

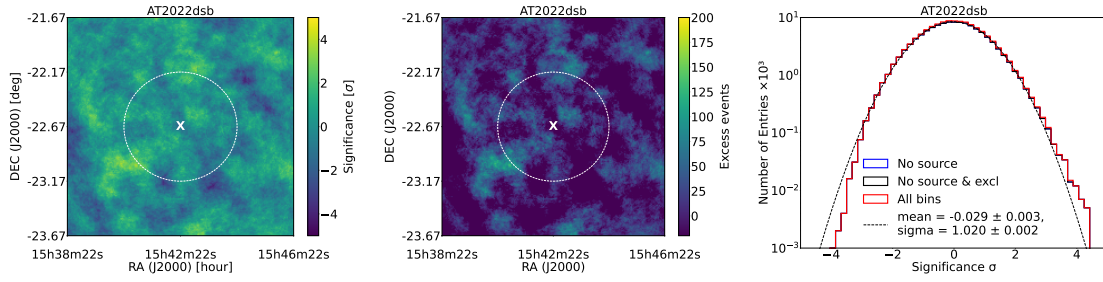


Figure 5.4: Significance map (**left panel**), excess events map (**middle panel**) and significances distribution (**right panel**) for AT2022dsb. The white cross and the white circle represent respectively the position of the TDE and a circular region of 0.5° . Significance distributions are presented for the entire skymap (red histogram), without source region (blue histogram) and without source and exclusions regions (black histogram with Gaussian fit).

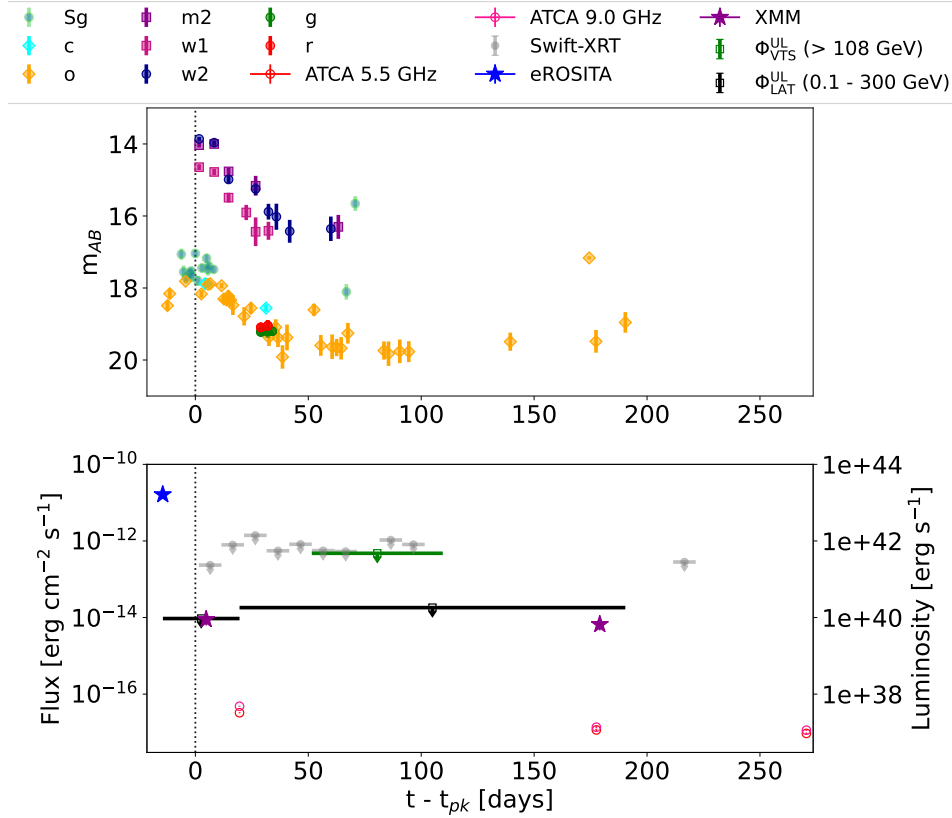


Figure 5.5: Multi-wavelength light curve for AT2022dsb. **Upper panel:** optical and UV magnitudes obtained by ZTF (filters: green g , red r and infra-red i), ASAS-SN (filter: green Sg), ATLAS (filters: orange o and cyan c filters) and Swift-UVOT (filters: $w1$, $w2$ and $m2$). **Lower panel:** upper limits from Swift-XRT (0.3 - 10 keV), VERITAS (108 GeV $< E < 10$ TeV, 95% C. L.; $\Gamma = 2$) and Fermi-LAT (100 MeV $< E < 300$ GeV, 95% C. L.; $\Gamma = 2$). Flux levels are given on the left side of the y-axis, while luminosities on the right side. Fermi-LAT flux ULs are given in the time periods $t_{LAT,1}$ and $t_{LAT,2}$. Detections by eROSITA (blue star), XMM (purple star) and ATCA (red and pink circles) are also presented in the lower panel.

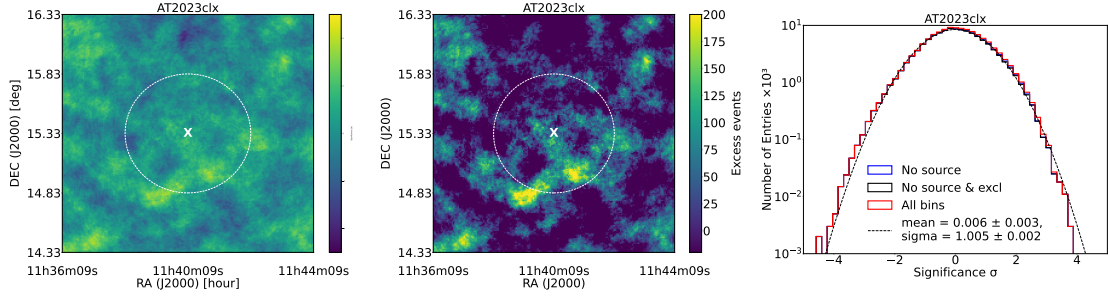


Figure 5.6: Significance map (**left panel**), excess events map (**middle panel**) and significances distribution (**right panel**) for **AT2023clx**. The white cross and the white circle represent respectively the position of the TDE and a circular region of 0.5° . Significance distributions are presented for the entire skymap (red histogram), without source region (blue histogram) and without source and exclusions regions (black histogram with Gaussian fit).

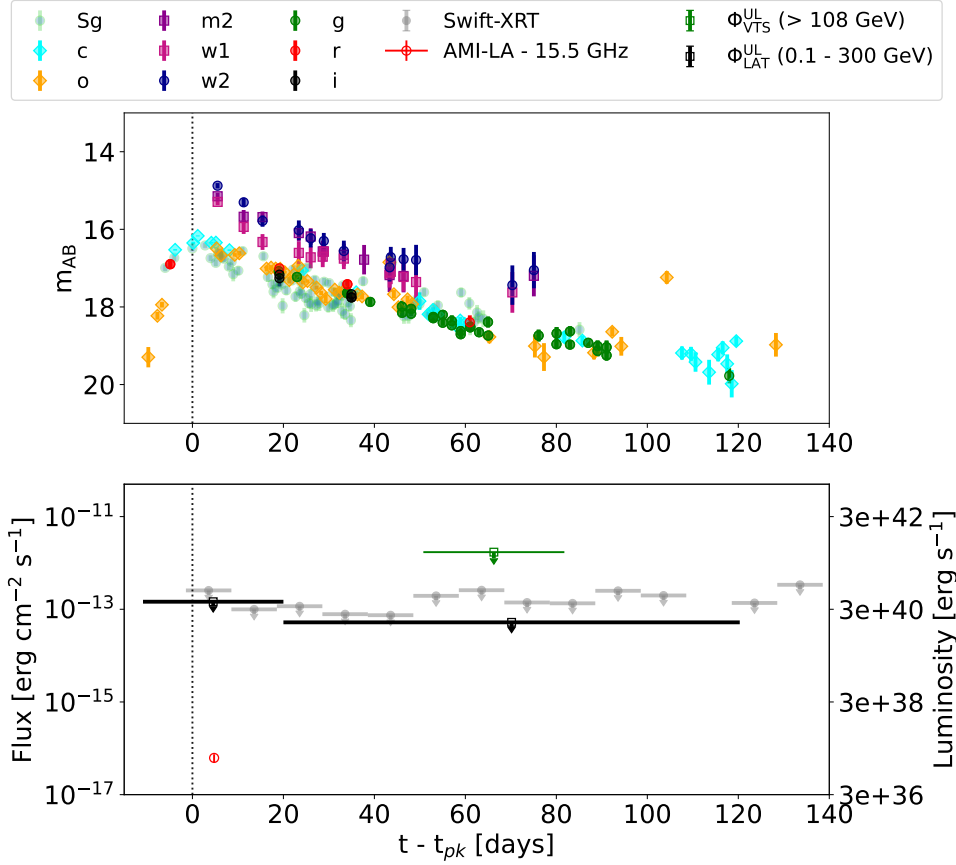


Figure 5.7: Multi-wavelength light curve for **AT2023clx**. **Upper panel**: optical and UV magnitudes obtained by ZTF (filters: green g , red r and infra-red i), ASAS-SN (filter: green Sg), ATLAS (filters: orange o and cyan c filters) and Swift-UVOT (filters: $w1$, $w2$ and $m2$). **Lower panel**: upper limits from Swift-XRT ($0.3 - 10$ keV), VERITAS (108 GeV $< E < 10$ TeV, 95% C. L.; $\Gamma = 2$) and Fermi-LAT (100 MeV $< E < 300$ GeV, 95% C. L.; $\Gamma = 2$). Flux levels are given on the left side of the y-axis, while luminosities on the right side. Fermi-LAT flux ULs are given in the time periods $t_{LAT,1}$ and $t_{LAT,2}$. The detection by AMI-LA is presented in the lower panel.

5.3 Modelling the internal gamma-ray attenuation for AT2022dbl and AT2022dsb

As previously discussed, one of the main challenges posed for the search of VHE emission from shock-powered transients is the internal absorption of gamma rays due to interactions with nuclei and lower energy ambient photons (the dominant absorption interaction) from the dense environment of the event. To quantify the extent of internal gamma-ray attenuation, the rate of $\gamma\gamma$ pair-production based on the available OUV dataset for each event is computed. Due to the very faint luminosity of AT2023c1x, the analysis in this section centres on events AT2022dsb and AT2022dbl.

Inspired by previous works, such as in Refs. [van Velzen, Gezari, et al., 2021] and [Yuan and Winter, 2023], we assume that a single blackbody spectrum (Equation 2.10) can reasonably describe the observed OUV radiation. Nonetheless, it is important to note that such assumption is a simplified approach for the characterisation of the thermal emission for the TDE scenario, since it does not account for non-spherical geometries and implies isotropic emission. Optical radiation from TDEs can arise, e.g., due to the reprocessing of X-ray radiation from the inner disk [Loeb and Ulmer, 1997], collisions between the streams of bound debris [Piran et al., 2015] and disk outflows [Roth et al., 2020]. In contrast to the modelling presented in this chapter, these radiative emission mechanisms are not necessarily isotropic, and they pose modelling complexities. Nevertheless, the choice for the blackbody characterisation of the OUV emission has proven to be successful in describing several events, such as in Refs. [van Velzen, Gezari, et al., 2021] and [van Velzen, Pasham, et al., 2021]. For instance, AT2019fdr, also detected in the infra-red region, is well fitted as a composite of two blackbodies, comprising a spectrum given by the OUV and a second one by the infra-red radiation [Reusch et al., 2022]. In practice, even if this choice represents an oversimplification of the TDE scenario, it usually provides a reasonable description of the data and it also allows us to make reasonable assumptions on the particle interaction rates based on the observed photometry without focusing on a particular acceleration zone (exemplified in Figure 2.16). Naturally, more sophisticated numerical and analytical models should be developed to better quantify the potential gamma-ray emission and attenuation taking place in these events. However, this is out of the scope of this work.

Upon selecting the blackbody characterisation, it is necessary to determine the radius that describe the emission. The size of a spherical radiation zone which is larger than the typical acceleration region, R_{acc} , is considered, i.e., $R > R_{\text{acc}} \sim 10^{12} - 10^{16}$ cm (Section 2.5.1.3, [Winter and Lunardini, 2023]). At this radius, the high-energy particles, which may have been accelerated anisotropically, would already be under the influence of the magnetic fields.

The fit of the soft X-ray component observed in TDEs have radii which align with the thermal emission from the inner radius of the accretion disk [Gezari et al., 2009; van Velzen et al., 2019]. On the other hand, the fitted blackbody radius for the OUV components are usually 10 to 100 times larger than the expected size of the nascent debris disk [van Velzen, Gezari, et al., 2021]. The disk's initial size is typically 100 - 1000 times larger than the Schwarzschild radius of the central black hole and roughly corresponds to the tidal radius of the system. For a black hole of mass $10^6 M_{\odot}$ and a sun-like star, the tidal radius for disruption is $r_t \approx 7 \cdot 10^{12}$ cm (from the Equation 2.21).

Considering the known population of thermal TDEs, it is observed that the blackbody radius at the peak of OUV luminosity ranges from $\sim 10^{14}$ to 10^{16} cm [van Velzen, Gezari, et al., 2021]. Based on this information, radii up to $\sim 10^{16}$ cm should serve as a reasonable test set.

The choices for blackbody radii:

For effective particle acceleration to occur, protons must be magnetically confined in the acceleration region. A simple estimate of the confinement radius for a given magnetic field strength can be obtained using the Larmor formula, as shown in Equation 2.22. For magnetic fields of the order of a few percent of Gauss, and assuming $R_L = 5 \cdot 10^{14}$ cm, protons of energy $E_p \lesssim 10$ PeV would be magnetically confined. This proton energy exceeds the threshold necessary for the production of gamma rays of mean energy $E < 10$ TeV via the π^0 channel of photohadronic interactions.

The optical depth is evaluated assuming four distinct radii for the blackbody emission, arranged in order of decreasing compactness: $R_0 = 5.0 \cdot 10^{14}$ cm, $R_1 = 1.0 \cdot 10^{15}$ cm, $R_2 = 5.0 \cdot 10^{15}$ cm and $R_3 = 1.0 \cdot 10^{16}$ cm. The choice of a few per cent of Gauss for the strength of the magnetic fields is justified since general relativistic magnetohydrodynamics simulations of TDEs find Gauss-scale magnetic fluxes of the order of $\sim 10^{31}$ G cm⁻² [L. Dai et al., 2018]. At a distance of $\sim 10^{16}$ cm, the magnetic field strength could then be $B \simeq 0.08$ G.

5.3.1 Results of the blackbody characterisation of the OUV components for AT2022dbl and AT2022dsb

In order to calculate the target photon density for $\gamma\gamma$ attenuation, I derive the time-dependent bolometric luminosity from the direct observations of the OUV components with the Python-based program *Superbol* [Nicholl, 2018]. This code generates the bolometric light curve by applying polynomial fits to the multiband data and extrapolating these fits to a set of common reference times. These reference times are selected based on the observation dates from the filter with the most detections for each TDE.

The reliability in deriving bolometric luminosity leans on selecting filters with sufficient data points, as polynomial fits for filters with $\lesssim 4$ data points yield imprecise estimations of the rise and decay of the light curve. The pseudo-bolometric approach is employed for the calculation of the bolometric luminosity. In this method, the flux is integrated across the selected filters that present a detection in a given reference time. Section B.1 of Appendix B provides a more detailed description of this calculation.

Figure 5.8 shows the time-dependent bolometric luminosity, L_{bol} , alongside the upper limits from VERITAS and Fermi-LAT for AT2022dbl and AT2022dsb (considering a spectral index of $\Gamma = 2$). Additionally, a power-law fit is applied with a fixed index of $-5/3$ to project the bolometric luminosity to dates beyond the last recorded OUV detection (this index is a canonical scaling of the light curve at $t > t_{pk}$, as discussed in Chapter 2). Table 5.6 lists the peak value of bolometric luminosity, L_{peak} , along with the ratio of upper limits from VERITAS and Fermi-LAT. The results from the pseudo-bolometric integration are comparable to the typical luminosities of TDEs detected in radio and soft X-rays ($\sim 10^{42} - 10^{45}$ erg s⁻¹), which corroborates that this method provides a reasonable approximation.

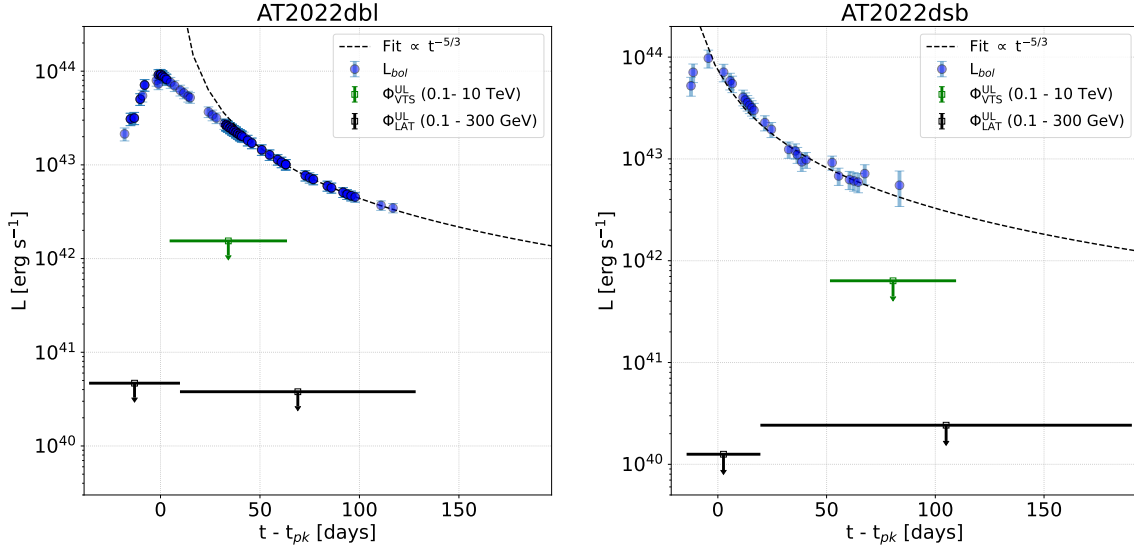


Figure 5.8: Bolometric luminosity (blue points) of AT2022dbl (right) and AT2022dsb (left). A fit of the light curve with a power-law with the canonical index of $-5/3$ is shown as the black dashed curve (done by including points that are within 50 (for AT2022dsb) and 20 (for AT2022dbl) days after the peak). Luminosity ULs by VERITAS ($\Gamma = 2$, $108 \text{ GeV} < E < 10 \text{ TeV}$) and Fermi-LAT ($\Gamma = 2$, $100 \text{ MeV} < E < 300 \text{ GeV}$) are shown in green and black, respectively, both for 95% C. L.

	$L_{\text{peak}} [\text{erg s}^{-1}]$	$L_{\text{VTS}}/L_{\text{bol}}$	$L_{t_{\text{LAT},1}}/L_{\text{bol}}$	$L_{t_{\text{LAT},2}}/L_{\text{bol}}$
AT2022dbl	$9.20 \cdot 10^{43}$	0.06	0.001	0.004
AT2022dsb	$9.76 \cdot 10^{43}$	0.1	0.0002	0.008

Table 5.6: Peak luminosity L_{peak} , and fraction of upper-limits given by VERITAS and Fermi-LAT in comparison to the bolometric luminosity at the time of VERITAS observations and Fermi-LAT analysis periods ($t_{\text{LAT},1}$ and $t_{\text{LAT},2}$).

5.3.2 Optical depth from $\gamma\gamma$ attenuation

A pure absorption factor in the radiation transfer equation affects the source intensity by $e^{-\tau_{\gamma\gamma}}$, and depends on the optical depth (Equation 2.9) for the corresponding target photon field. For $\tau_{\gamma\gamma} = 1$, the source flux would be reduced by a factor of about $\sim 40\%$. Considering internal absorption and a constant source function, the term becomes $(1 - e^{-\tau_{\gamma\gamma}})/\tau_{\gamma\gamma}$. In this section, the $\gamma\gamma$ annihilation between gamma rays and lower energy photons composing the OUV and X-ray blackbody spectra is examined.

Figures 5.9 and 5.10 show the optical depth for AT2022dbl and AT2022dsb as a function of the energy at the time of the UV peak and at the median time of VERITAS observations. The calculation of the optical depth for radii $5.0 \cdot 10^{15} \text{ cm}$ and $1.0 \cdot 10^{16} \text{ cm}$ at both times considered here was performed with the Astrophysical Multi-Messenger Modeling (AM³) software for the

simulation of the multi-messenger emission from astrophysical sources⁷ [Klinger et al., 2023]. For AT2022dsb, an additional blackbody with a temperature of 42 eV was also considered in this calculation, based on the observed X-ray detection by eROSITA. For AT2022dbl, even though no X-ray detection was identified, we still include an additional blackbody at the same temperature (42 eV) to account for a possible obscured X-ray component.

At the time of UV peak for AT2022dbl, $\tau_{\gamma\gamma} \geq 1$ for energies above $\gtrsim 3$ GeV ($\gtrsim 11$ GeV) when considering the blackbody radius R_0 (R_3). At the time of VERITAS observations, the gamma-ray emission would be heavily attenuated above ~ 3 GeV (14 GeV) for R_0 (R_3). Consequently, within the energy range where VERITAS is sensitive (~ 80 GeV to 40 TeV), a persistent attenuation of the gamma-ray emission would be taking place.

A similar result is observed for AT2022dsb, with $\tau_{\gamma\gamma} \geq 1$ for $E \gtrsim 2$ GeV ($\gtrsim 16$ GeV) when considering the compact radius R_0 (least compact R_3) at the time of UV peak. Because the median date of VERITAS observations were performed 80 days after the UV peak, the density of the target photon field had sufficiently decreased, resulting in a reduced attenuation within the sensitivity range of VERITAS. At the date of VERITAS observations, $\tau_{\gamma\gamma} \geq 1$ at $E \gtrsim 2$ GeV ($E \gtrsim 12$ GeV) for R_0 (R_3).

A lower attenuation is also observed within the sensitivity range of Fermi-LAT. Increasing the emission radius while keeping the luminosity constant, results in reduced rates of pair-production interaction, leading to lower attenuation. As expected, the attenuation level is greater during the peak UV time, coinciding with the peak bolometric luminosity, when the target photon field is much denser. Also as expected, the optical depth decreases over time, suggesting that the medium becomes less optically thick at certain energies.

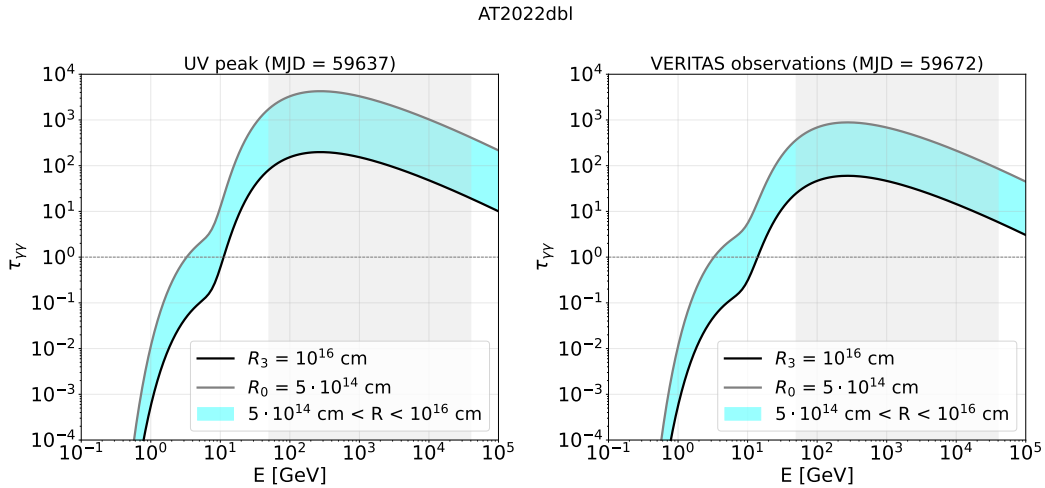


Figure 5.9: Optical depth for candidate AT2022dbl for $R_0 = 5.0 \cdot 10^{14}$ cm (gray line) and $R_3 = 1.0 \cdot 10^{16}$ cm (black line) at the time of UV peak (left plot) and at the time of VERITAS observations (right plot). The gray shaded area indicates the energy range of 0.05 TeV - 40 TeV.

⁷Results were produced following the baseline template for TDEs provided at <https://gitlab.desy.de/am3/> and with the orientation of Dr. Chengchao Yuan.

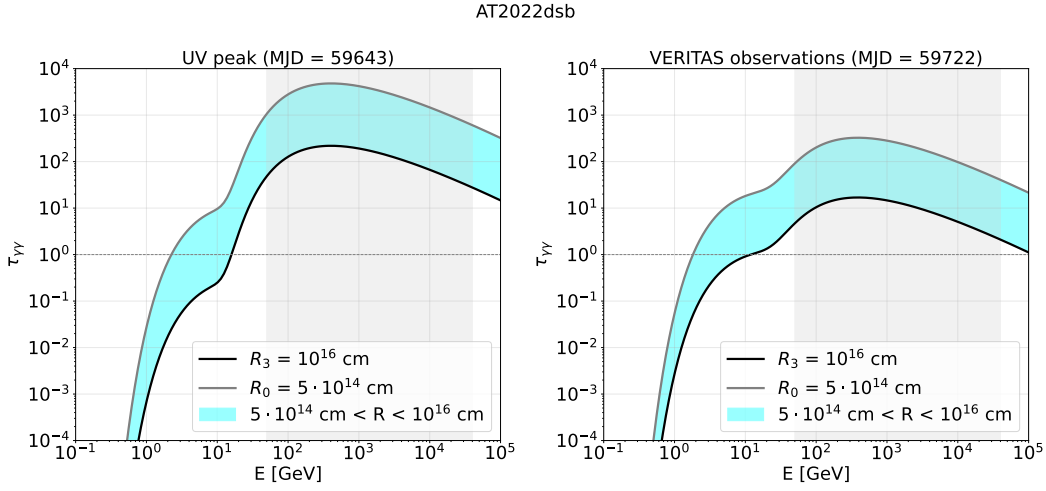


Figure 5.10: Optical depth for AT2022dsb between $R_0 = 5.0 \cdot 10^{14}$ cm (gray line) and $R_3 = 1.0 \cdot 10^{16}$ cm (black line) at the time of UV peak (left plot) and at the time of VERITAS observations (right plot). The gray shaded area indicates the energy range of 0.05 TeV - 40 TeV.

5.3.3 Time evolution of the optical depth

In order to identify possible time windows with a lower absorption level, the evolution of the optical depth up to 150 days after the peak of the UV lightcurve is calculated. This can be achieved by considering that $\tau_{\gamma\gamma} \propto n_{\gamma} \propto L_{\text{bol}}$, as seen in Equations 2.9 and 2.11. The time range is partitioned into 1-day bins. In order to calculate L_{bol} at each day, the bolometric light curve is interpolated into our set of desired dates. As a resort to deal with the lack of detections in the entire considered range, L_{bol} is extrapolated to later times by using the fit of the light curve with a power-law function with the canonical index of $-5/3$. Figures 5.11 and 5.12 show the optical depth as a function of time for gamma-ray energies spanning from 100 MeV up to 100 TeV. The red line provides the contour at which $\tau_{\gamma\gamma} = 1$. We can expect a high attenuation level for the region enclosed by this curve.

For AT2022dbl, the radiation zone remained essentially optically thick ($\tau_{\gamma\gamma} \gg 1$) for all considered values of R_i at the time of VERITAS observations. Moreover, the event also remains optically thick at the VERITAS sensitivity range for the most compact values of radii (R_0 , R_1 and R_2) throughout the 150 days post UV peak. However, for R_3 , $\tau_{\gamma\gamma} < 1$ between 20 TeV and 40 TeV around 100 days after the UV peak brightness (about 30 days before the last UV detection).

For AT2022dsb, R_0 and R_1 show a similar behavior as for AT2022dbl, with the medium remaining optically thick at the VERITAS sensitivity range for the entire duration considered here. However, for R_3 , a small energy window above ~ 20 TeV is available. Upper limits on the size of the radiation zone would be required in order to make more precise predictions of energy range for which attenuation is at its maximum. For both events, the radius $R \sim 10^{16}$ cm is the only choice for which the radiation zone is optically thin for gamma rays in the GeV range ($\lesssim 10$ GeV). However, values higher than R_3 , are not typically derived for thermal TDEs [van Velzen, Gezari, et al., 2021], indicating that the emission attenuation should indeed be expected.

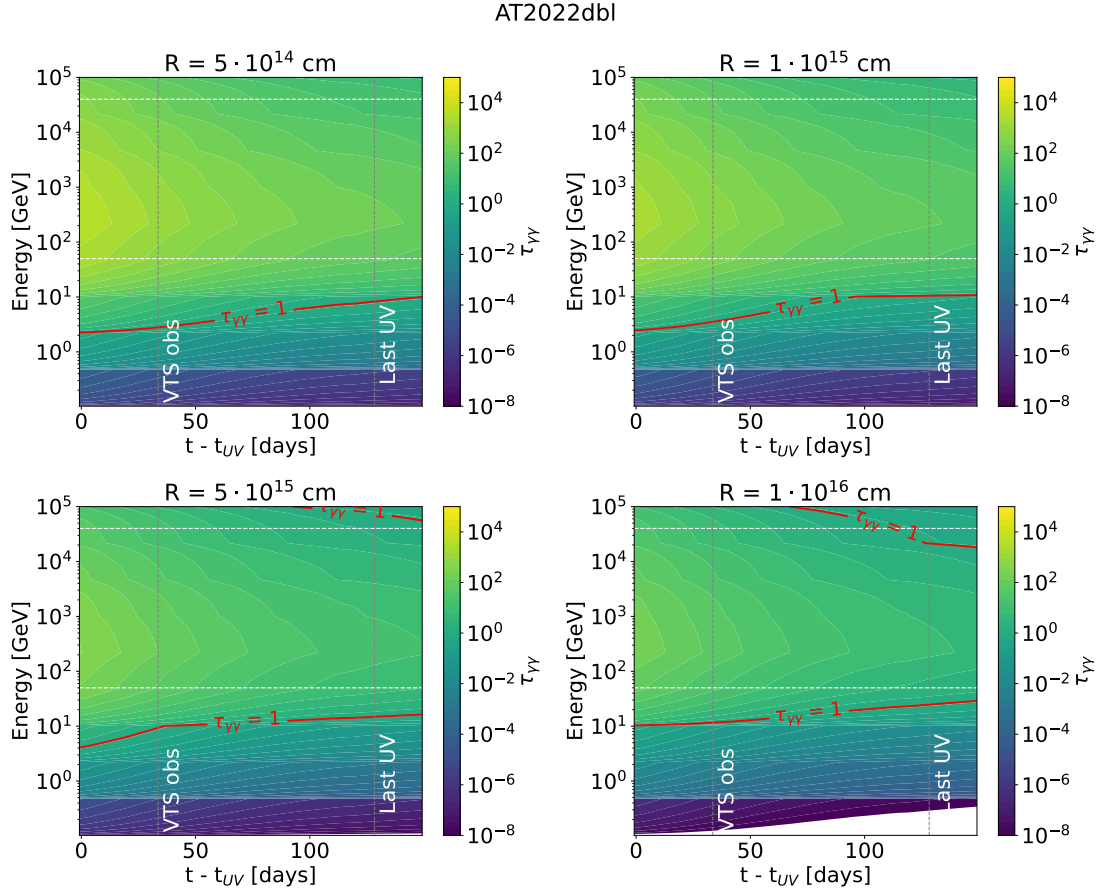


Figure 5.11: Time evolution of the optical depth for AT2022dbl at R_i , $i \in 0, 1, 2, 3$. The x-axis represents days after the UV peak (t_{UV}). The red line shows the contour where $\tau_{\gamma\gamma} = 1$. The dates of VERITAS observations and the last UV detection are also shown as grey dashed lines. White dashed lines represent the energy range of 50 GeV - 40 TeV.

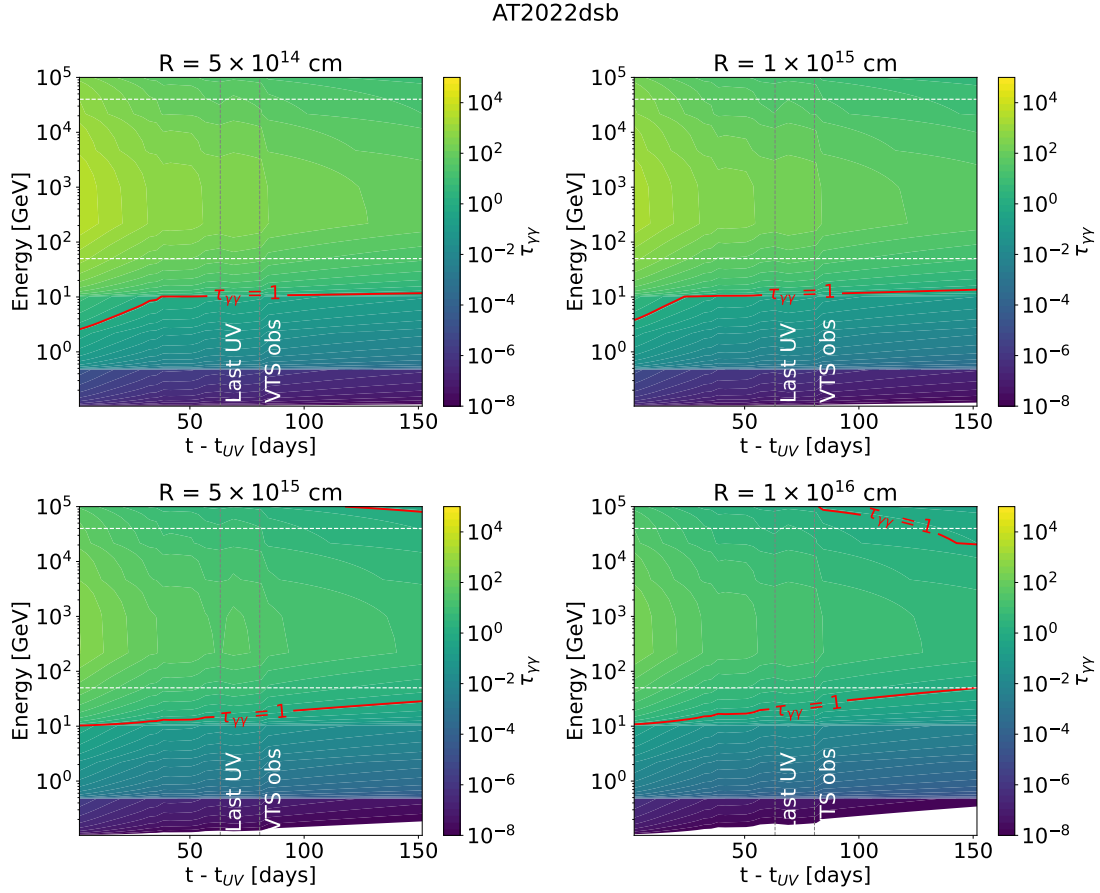


Figure 5.12: Time evolution of the optical depth for AT2022dsb at R_i , $i \in 0, 1, 2, 3$. The x-axis represents days after the UV peak (t_{UV}). The red line shows the contour where $\tau_{\gamma\gamma} = 1$. The dates of VERITAS observations and the last UV detection are also shown as grey dashed lines. White dashed lines represent the energy range of 50 GeV - 40 TeV.

5.3.4 Broadband gamma-ray flux ULs for AT2022dbi and AT2022dsb

Figures 5.13 and 5.14 present the gamma-ray flux ULs for AT2022dbi and AT2022dsb, assuming the conservative scenario in which the attenuation is due to a blackbody spectrum of radius R_0 , representing the highest level of absorption. The grey shaded area displays the energy range where $\tau_{\gamma\gamma} < 1$ at the time of peak UV luminosity. The results presented in this chapter show that the flux would be significantly suppressed at the energy range outside the shaded area.

5.3.5 Upper limits on the proton luminosity

The flux ULs derived from VERITAS observations provide interesting clues into the scenario of shock acceleration. We can study the flux ULs with methods derived for classical novae that have shown direct evidence of shock acceleration, such as V906 Car [Aydi et al., 2020] and ASASSN-16ma [K.-L. Li et al., 2017] (here, I refer to section 2.5.4).

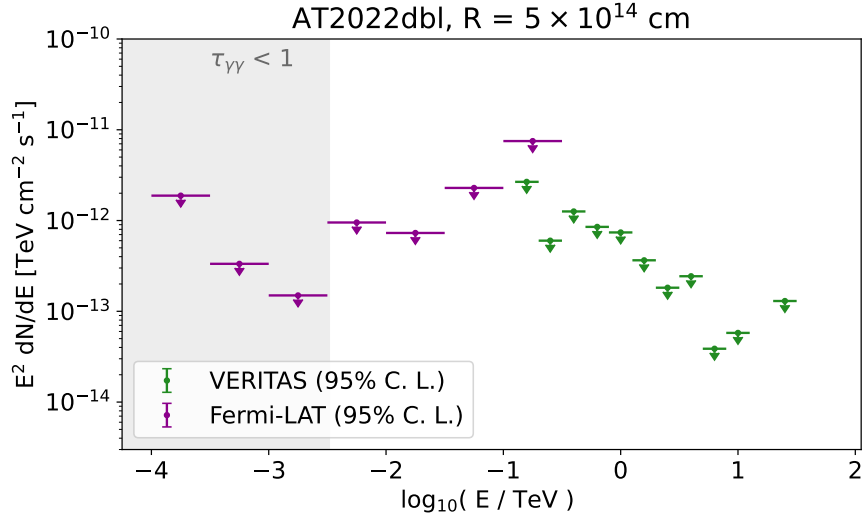


Figure 5.13: Broadband gamma ray flux ULs (Fermi-LAT in magenta and VERITAS in green) for AT2022dbl. Considering the peak luminosity and blackbody emission radius R_0 , the energy range for which $\tau_{\gamma\gamma} < 1$ is depicted as the gray shaded area.

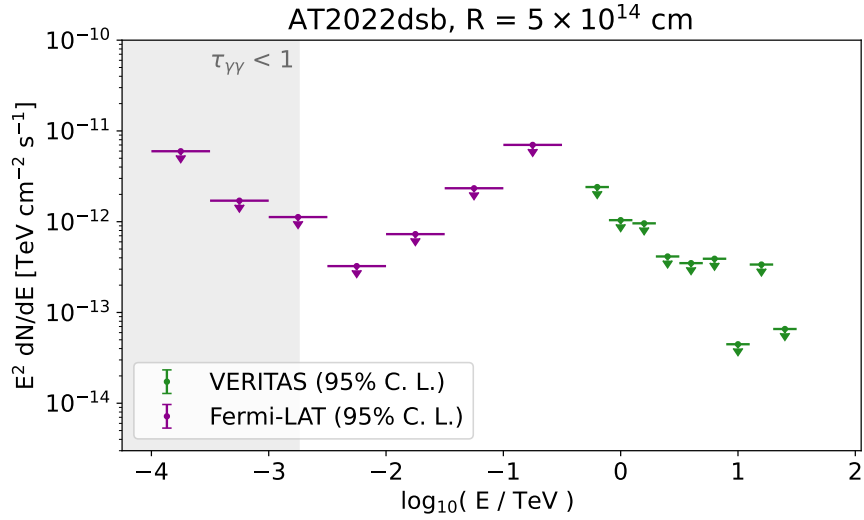


Figure 5.14: Broadband gamma-ray flux ULs (Fermi-LAT in magenta and VERITAS in green) for AT2022dsb. Considering the peak luminosity and black-body emission radius R_0 , the energy range for which $\tau_{\gamma\gamma} < 1$ is depicted as the gray shaded area.

According to references [Yuan and Winter, 2023] and [Winter and Lunardini, 2023], the expected rate of pp interactions in thermal TDEs is sub-dominant in respect to $p\gamma$ at higher proton energies ($t_{p\gamma}^{-1} \gg t_{pp}^{-1}$). The mean free path, λ , for a proton in a radiation field target characterised by a mean photon density n_γ can be described as

$$\lambda = \frac{1}{\sigma_{p\gamma} n_\gamma}, \quad (5.1)$$

where $\sigma_{p\gamma} = 5 \cdot 10^{-28} \text{ cm}^2$ [Razzaque et al., 2003]. A reasonable assumption is that the OUV blackbody spectrum derived in this section also serves as a photon target for $p\gamma$ interactions. Protons with energies in the PeV range would be required to produce gamma rays via interactions with the OUV spectrum derived for AT2022dbl and AT2022dsb (Table 5.7)⁸. Table 5.7 presents the mean free path for AT2022dbl and AT2022dsb at the time of VERITAS observations. Knowing that this interaction has an inelasticity of 0.2 [Aharonian, 2004] (the fraction of proton energy transferred to secondary particles), the conversion efficiency can be approximated to $f_{p\gamma} = 1 - e^{-\frac{0.2R}{\lambda}}$, also presented in the Table 5.7. A pion production efficiency of $f_{p\gamma} \sim 1$ is found for both events, i.e., the medium is optically thick for photo-meson production.

Adopting equation 2.23, I find the upper limits on the proton luminosity, L_p . Since $e^{-\tau_{p\gamma}} > 1$, L_p is shown as the average of the proton luminosity in this interval. With a certain efficiency of particle acceleration in shocks, an upper limit on the shock luminosity could also be imposed based on L_p . Because setting values on this efficiency would require a new set of assumptions on the shock conditions, I refrain from imposing such upper limits. A detection of a signal would lead to further conclusions on the effectiveness of particle acceleration.

	λ	$f_{p\gamma}$	$\langle E_{\text{OUV}} \rangle$	$E_{p,\text{th}}$	L_p
Unit	[cm]		[eV]	[PeV]	[erg s ⁻¹]
AT2022dbl	$1.8 \cdot 10^{13}$	0.99	4.1	17	$4 \cdot 10^{44}$
AT2022dsb	$5.4 \cdot 10^{13}$	0.84	2.8	24	$1 \cdot 10^{44}$

Table 5.7: Proton mean free path, λ , pion conversion efficiency, $f_{p\gamma}$, mean energy of the OUV photon target, $\langle E_{\text{OUV}} \rangle$, energy threshold of protons for π^0 production in $p\gamma$ interactions, $E_{p,\text{th}}$, and upper limit on proton luminosity, L_p , for AT2022dbl and AT2022dsb.

The results in this chapter reveal the need for a revised strategy in our approach to observing TDEs in the VHE regime. While our initial procedure involved a minimal search for non-thermal emission signatures in TDE candidates, there is a substantial challenge in the follow-up of events by Cherenkov instruments: a remarkably high level of internal attenuation. Furthermore, this internal attenuation can be expected to be aggravated by subsequent attenuation effects by the EBL and other channels which are typically less efficient. Further developments to constrain the time- and

⁸A π^0 production will take place in $p\gamma$ interactions above the energy threshold given by: $4E_p \langle E_{\text{OUV}} \rangle = m_\pi c^4 (2m_p + m_\pi)$, with $\langle E_{\text{OUV}} \rangle$ representing the mean energy of the photon target field.

geometry-dependent gamma-ray emission and internal attenuation effects are needed to refine the TDE observing follow-up strategy. Such an approach could allow us to maximise the scientific potential of our observations within the constraints of available scheduling.

5.4 Updating the VERITAS results on Swift J1644

In Chapter 4, I introduced the Optimised Next Neighbour technique, a novel image cleaning method that considers the time structure of the Cherenkov pulse in the pixels. This method allows for an increased sensitivity in the lowest energies and an increased gamma-ray rate, particularly for soft and faint sources (spectral index $\gtrsim 3$). Because the disruption occurred in 2011, applying the Optimised Next Neighbour image cleaning in this dataset is not possible since the estimation of the background via pedestal events was only introduced in 2012. Before 2012, non-triggered telescopes from array triggers were used for this purpose. The Afterpulsing method, also described in Chapter 4, already provides an overall improvement in sensitivity regarding the conventional threshold cleaning.

For this analysis, the same dataset used in Ref. [Aliu et al., 2011] is considered (Figure 5.15), which is equivalent to ~ 25 hours of data that pass the quality selection criteria. The gamma-hadron separation is provided via cuts optimised for soft sources (ref. Appendix B, with an offset cut of $\theta^2 < 0.08$ degree²). The background is estimated with the reflected regions method. The source flux is assumed to follow a power-law spectrum with a photon index of $\Gamma = 3.0$. In a similar manner as in Ref. [Aliu et al., 2011], the analysis is divided into three time intervals: *a*) Total, including all observations for Swift J1644 - from March 29 to April 15, 2011, *b*) flaring period, when the TDE was observed to be particularly intense in X-rays, from March 29 to March 31, 2011 and *c*) Low period, when the TDE is observed with relatively low X-ray flux states, from April 1 to April 15, 2011. A more comprehensive description of Swift J1644 can be found in Chapter 2.

Results of the analysis are presented in Table 5.8. Compared to Ref. [Aliu et al., 2011], we notice an overall reduction in the gamma-ray rate and significance (still no detection) for each time period. This can be likely attributed to the different gamma/hadron separation cuts applied. For instance, in the analysis presented in Ref. [Aliu et al., 2011], a limiting reconstruction offset of 0.1° has been applied, while in this section the most updated gamma/hadron separation criteria used by the Collaboration are employed. In order to compare with the previous work, flux ULs are presented above 500 GeV with EBL correction at 99% C. L. (Table 5.8, results presented in the publication assume the same confidence level but show the flux upper limits without correcting for EBL attenuation. However, Swift 1644 has a redshift of $z = 0.35$, so EBL attenuation effects should become relevant above ~ 300 GeV.).

	Total	Flaring	Low
N_{ON}	452	44	408
N_{OFF}	443.00	48.33	394.67
N_s	9.00	-4.33	13.33
Significance	0.4	-0.6	0.6
excess/min	0.006 ± 0.01	-0.02 ± 0.04	0.01 ± 0.02
$\Phi_{95\%}^{\text{UL}}$ (99% C.L.) [erg/cm ² /s]	$2.38 \cdot 10^{-12}$	$4.29 \cdot 10^{-12}$	$2.80 \cdot 10^{-12}$
$\Phi_{95\%}^{\text{UL} \dagger}$ (99% C.L.) [erg/cm ² /s]	$1.4 \cdot 10^{-12}$	$3.1 \cdot 10^{-12}$	$1.5 \cdot 10^{-12}$

Table 5.8: Results for VERITAS analysis of Swift J1644 using the Afterpulsing cleaning method: number of ON (N_{ON}), OFF (N_{OFF}) and excess events ($N_s = N_{\text{ON}} - \alpha N_{\text{OFF}}$), significance of detection, gamma ray rate, flux ULs for 99% C. L. above 500 GeV and upper limits for 99% C. L. above 500 GeV provided from Ref. [Aliu et al., 2011][†].

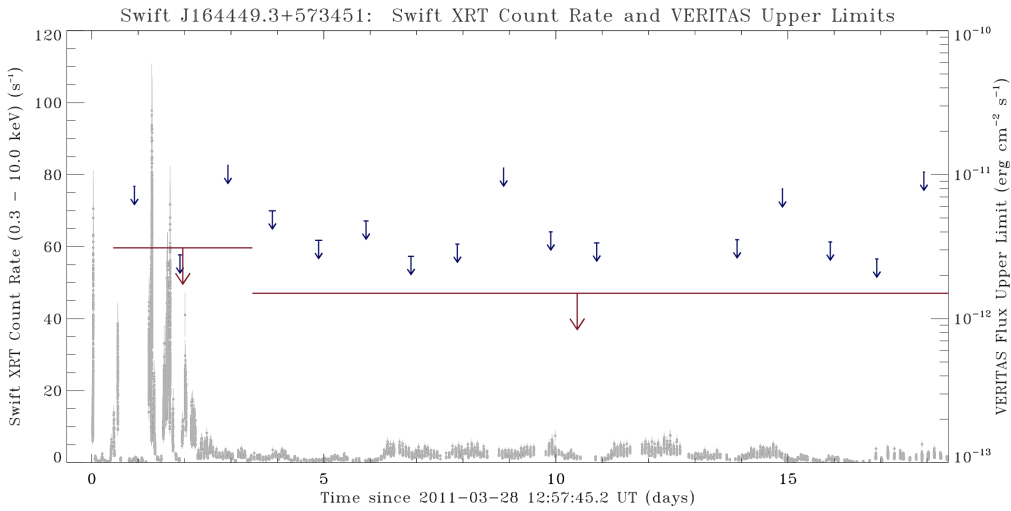


Figure 5.15: VERITAS flux ULs and Swift-XRT count rates in the interval of 0.3 - 10 keV for Swift J1644. VERITAS flux ULs are given in bins of one day and as a joint UL on the flaring period (from 2011 March 29 to March 31) and lower-state period (2011 April 1 to April 15). Figure from: [Aliu et al., 2011]

5.5 Chapter conclusions and final remarks

A ToO proposal dedicated to monitoring TDEs has been in force within VERITAS since 2021. The trigger criteria initially consist of minimal observational constraints (maximum redshift, minimum elevation and live-time). Although restrictions should also be placed on the selection of the best candidates for gamma-ray emission, the scarce literature and the very few observations of TDEs in the VHE regime make this difficult to achieve. We, therefore, selected events as long as they displayed at least radio or X-ray emission, albeit quick and faint. We argue that imposing gamma-ray upper limits even on TDEs later on classified as fully thermal is still worth pursuing due to the shortage of VHE observations of this particular class of events. Since the start of the proposal, three TDEs were accepted for gamma-ray follow-up with VERITAS: AT2022dbl, AT2022dsb and AT2023clx. These events exhibited at least a short potential radio detection around the peak of the OUV light curve. In conclusion, the light curves from all the events are consistent with thermal emission.

No HE (100 MeV - 300 GeV) or VHE (≥ 100 GeV) components were detected by Fermi-LAT or VERITAS for any of the events triggered by the proposal. The flux ULs were derived considering EBL absorption. In order to estimate the attenuation level for each event, the OUV emission is characterised with a blackbody spectrum and the optical depth for $\gamma\gamma$ interactions is calculated. The blackbody luminosity is estimated based on the OUV photometry for each event. Compared to the luminosity ULs provided by VERITAS (above ~ 108 GeV), a gamma-ray fraction of at most 6% (10%) of the bolometric luminosity is found for AT2022dbl (AT2022dsb). I consider four distinct radii for the blackbody emission, arranged in decreasing order of compactness: $R_0 = 5.0 \cdot 10^{14}$ cm, $R_1 = 1.0 \cdot 10^{15}$ cm, $R_2 = 5.0 \cdot 10^{15}$ cm and $R_3 = 1.0 \cdot 10^{16}$ cm. This model is evidently a simplification of the TDE scenario, given the expected complexity of the environment. However, there is enough evidence in the literature to assume this characterisation for typical thermal TDEs (e.g. Ref. [van Velzen, Gezari, et al., 2021]). Considering the most compact case (R_0), we see that at the time of the UV peak, gamma-ray emission above a few GeV is almost completely attenuated ($\tau_{\gamma\gamma} > 1$) for AT2022dbl and AT2022dsb. At the time of the VERITAS observations, a lower attenuation rate is obtained, as expected. However, $\tau_{\gamma\gamma} > 1$ in a similar energy range for both events. I also derived the optical depth of attenuation up to 150 days after the UV peak of each event. In both cases, for the most compact radius, the environment remained optically thick ($\tau_{\gamma\gamma} > 1$) for almost the entire period considered. The VERITAS luminosity ULs were used to set upper limits on the proton luminosity, resulting in $1.6 \cdot 10^{43}$ erg s $^{-1}$ ($1.5 \cdot 10^{43}$ erg s $^{-1}$) for AT2022dbl (AT2022dsb).

I employed an improved image cleaning method (afterpulsing method, described in Chapter 4) to provide a new analysis of the Swift J1644 data collected with the VERITAS array. No detection is found and flux ULs are derived with EBL correction due to redshift of Swift J1644 ($z = 0.35$).

In addition to the internal attenuation, delays in classification and limited real-time reports of non-thermal emission in the X-ray and radio bands also constrain the refinement of the trigger criteria. Based on the results presented in this Chapter, events that show clear signs of active particle acceleration remain as natural candidates for follow-up campaigns. On the other hand,

new research on the time- and geometry-dependent VHE emission could help improve the follow-up strategy for thermal events. The study of TDEs in a multi-messenger approach has gained a lot of attention in recent years, particularly since the recent association claims with astrophysical neutrinos with energies of ~ 100 TeV. It is proposed in the literature that the non-thermal emission of TDEs might be fuelled by shock interactions, which already have direct evidence to play a role in many other classes of transients. Although the most promising candidates are very rare, up until now it cannot be ruled out that given the optimal observing conditions, the non-thermal mechanisms could be strong enough to produce a detectable gamma-ray signal.

The importance of the TDE ToO proposal has been recognised by the VERITAS Collaboration and the project should be in operation until at least June of 2024. Monitoring new events should improve significantly with new large-scale radio surveys, such as the Square Kilometer Array (SKA) [Weltman et al., 2020] and the next generation of the VLA [Di Francesco et al., 2019], which could provide the detection of hundreds of new TDEs per year. Moreover, the Vera Rubin observatory [Brough et al., 2020] should also increase the rate of event discovery by a factor of $\sim 10^3$.

VERITAS Observations of GRB 221009A

Gamma-ray bursts are among the most energetic astrophysical phenomena in the Universe. They present extreme luminosities and in highly variable time-scales. GRBs also serve as potential sites for accelerating cosmic rays to extremely high energies. It is proposed that the initial (prompt) emission stems from internal shocks within the jet, caused by collisions between shells of material moving at different velocities. The subsequent afterglow is proposed to originate from the deceleration of the jet as it encounters the surrounding matter (Chapter 2). The observed VHE emission from some events has been proposed to originate from IC scenarios, either internal or external. Internal IC is believed to arise from the up-scatter of the synchrotron radiation emitted by the same population of electrons accelerated in the external and internal shocks.

GRB 221009A was the brightest gamma-ray burst detected to date, with an outstanding isotropic-equivalent energy of $\sim 10^{55}$ erg (8 keV – 40 MeV), as measured by the Fermi-GBM on October 9, 2022, at $T_0 = 13:16:59$ UTC [Lesage et al., 2023] (these energetics correspond to a isotropic-equivalent luminosity of $9.9 \cdot 10^{53}$ erg s $^{-1}$). GRB 221009A was a long-lasting event (≥ 900 seconds) at 753 Mpc ($z = 0.151$). Detections of an extended X-ray light curve by Swift-XRT and other X-ray instruments were reported [Williams et al., 2023]. The X-ray afterglow of the event exhibited a brightness at $T_0 + 4.5$ ks that surpassed any previous GRBs detected by Swift-XRT by more than an order of magnitude. Additionally, only 1 in 10000 long GRBs exhibited a similar energy to GRB 221009A in a simulation of randomly generated bursts, showing the exceptional nature of this event [Williams et al., 2023]. A detection by Fermi-LAT with a highest energy of 99.3 GeV was identified after 240 seconds from the GBM trigger [Pillera et al., 2022].

VERITAS observations of GRB 221009A started ~ 37 hours after the initial trigger by GBM, resulting in 23.6 hours of live-time. During the first night of observations by VERITAS, the Moon reached a peak illumination of 99%, with an inferred NSB rate of > 350 MHz. As a result, the first ~ 2.9 hours of observations were conducted under bright moonlight conditions, which require special strategies to circumvent the limits imposed by the intense NSB. Under bright moonlight, the sky can be approximately 100 brighter than during dark conditions. The intense NSB not only worsens the quality of the data but also generates high PMT currents ($> 10 \mu\text{A}$), degrading their dynodes and photocathodes.

One way to ensure the safe operation of the PMTs under such conditions is to decrease their overall gain by reducing the HV by 80%. As previously mentioned, this observation mode is referred to as Reduced High Voltage (RedHV). Nevertheless, even with reduced HV, the current in

the PMTs is still much higher than the safety thresholds ($\sim 15 \mu A$) when the moon illumination is above 65%. In this case, cameras are covered by a plate with SCHOTT UG-11 UV filters [Archambault et al., 2017], which reduces the amount of light transmitted to the camera. This mode is referred to as UVF.

Although the performance of UVF observations had previously been thoroughly evaluated [Archambault et al., 2017], the plate had not been used since at least 2020 and had not undergone any kind of maintenance for a long time. Due to the urgency of the observations, it was not possible to properly clean the plate. For this reason, it is expected that the filter’s absorption performance had changed and a new calibration correction factor should be applied.

In this chapter, I describe observations of the VERITAS array taken under bright moonlight in section 6.1, the corrections applied on the reconstruction of events in section 6.2 and VERITAS observations and preliminary results on GRB 221009A in section 6.4.

6.1 UVF observations with the VERITAS array

Figure 6.1 (left panel) presents a picture of the UV plate employed by VERITAS. It consists of 499 absorptive filters (one for each PMT) composed of transition-metal-doped glass. As the light passes through the filters, it gets absorbed and scattered. Consequently, the filters effectively reduce the transmission of the light to the camera.

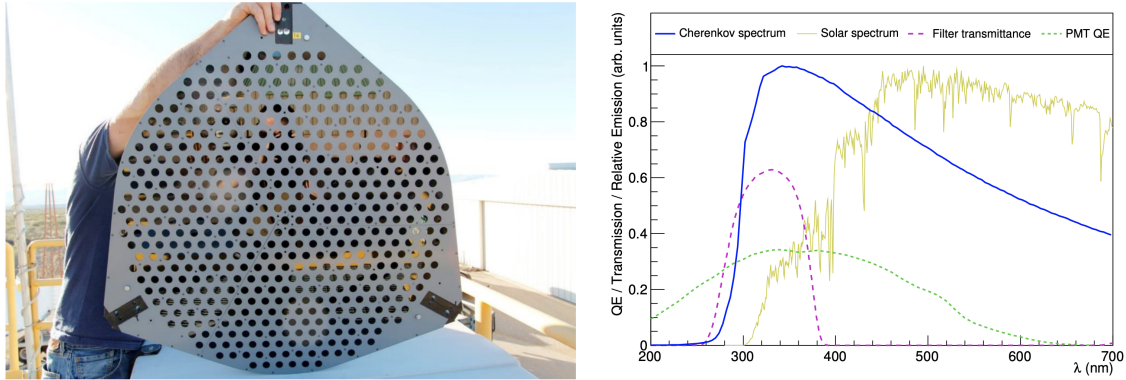


Figure 6.1: Left: Plate used for UVF observing mode with VERITAS. It is composed of 499 UV filters, one for each PMT in the camera. Each filter has a diameter of 22 mm. Right: Filter transmission (dashed pink line), along with the Cherenkov emission for a 500 GeV simulated gamma ray (blue solid line). The figure also shows the PMT quantum efficiency (green dashed line) and the solar spectrum at ground level (orange solid line), assumed to be similar to the lunar spectrum. Figures adapted from: [Archambault et al., 2017].

The total transmittance of the UV filter for normal incidence is presented in Figure 6.1 (right panel). For comparison, the figure also shows the Cherenkov emission expected from a simulated gamma ray with an energy of 500 GeV and the solar spectrum at ground level, which is predicted to be similar to the lunar spectrum since moonlight is essentially reflected sunlight. The filters block $\sim 96\%$ of the solar spectrum while allowing the passage of $\sim 17\%$ of the Cherenkov light. The

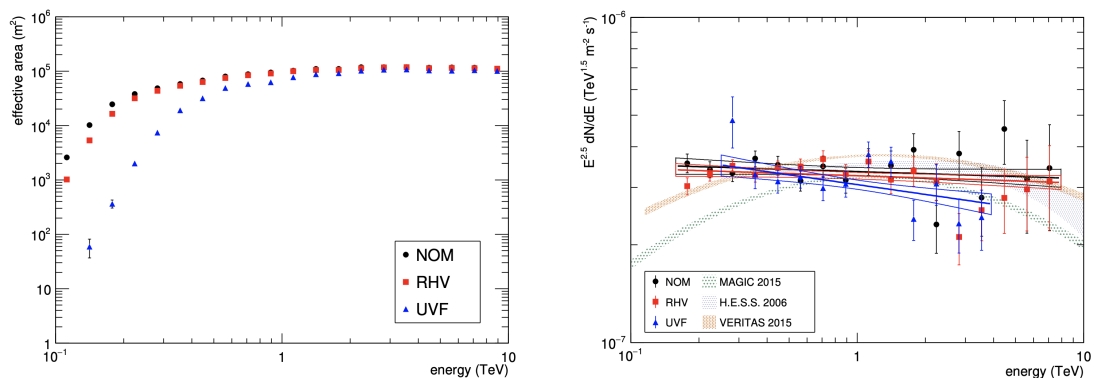


Figure 6.2: Left: Effective areas at zenith = 20 degrees for data taken under nominal (NOM), reduced high voltage (RHV) and UVF observing modes. Right: Power-law fit + 1σ contours of the reconstructed Crab Nebula spectrum for the nominal (NOM), reduced high voltage (RHV) and UVF observing modes. Spectra from MAGIC [Aleksić et al., 2015], H.E.S.S. [Aharonian et al., 2006] and VERITAS (Nominal mode 2015) [Meagher, 2015] are also depicted. Figures adapted from: [Archambault et al., 2017].

UVF observing mode allows up to a 13% increase in annual exposure above 160 GeV [Archambault et al., 2017].

Comparing with the nominal observing configuration, the UVF mode is significantly less sensitive than the nominal mode, as seen by a reduction of 40% in effective areas. The deterioration in the sensitivity likely comes from the poorer event reconstruction caused by the lower light level from the showers which achieve the camera and due to the suppression of many events. The validation of UVF mode is given by the analysis of Crab Nebula data and is presented in Figure 6.2. This is done by comparing Crab Nebula datasets taken under UVF, nominal and RedHV modes. The Crab Nebula spectrum obtained with UVF observations agree within uncertainties to the nominal dataset.

6.2 Corrections for UV Filter Observations with EventDisplay

Over time, IACTs are exposed to several external factors which deteriorate their optical and electronic response. That is the case of the ageing process of PMTs, which have their spectral sensitivity degraded, e.g., due to charge accumulation as they operate in HV mode. Moreover, weather conditions, such as variations in temperature, snow and rain, also affect the reflectivity of the mirrors. In Chapter 3 (section 3.1.3), the throughput calibration methods for the VERITAS telescopes [Adams et al., 2022] have been discussed. These corrections are necessary to guarantee the correct reconstruction of the Cherenkov signal. In summary, the throughput calibration depends on the PMTs gain (g) and quantum efficiency (QE) and on the reflectivity of the mirrors (r).

The final throughput calibration, which indicates how much the PMT charge is underestimated, is given by $s = g \cdot r$. This factor is used to calibrate the reconstructed signal in the PMTs by correcting the trace integration. When this correction is introduced, it is necessary to update the

telescopes IRFs. Figure 3.5 from Chapter 3 shows the dependence of s with time for each telescope.

To correct the effect of the UV filter, we introduce a new factor, u , into the throughput correction: $s' = u \cdot g \cdot r = u \cdot s$. As previously mentioned, this filter has undergone no maintenance for a significant period of time, and its current effective transmission is unknown. We use the new s' to reconstruct a Crab Nebula dataset with 358 minutes of data and a mean elevation of $\sim 50^\circ$ taken under UVF mode with the plate in the same state as during observations of GRB 221009A. We then compare the corrected Crab Nebula spectrum with literature values. We test different values of u until the corrected Crab Nebula spectrum reasonably matches the literature reference. This is done by testing the following values: $u \in \{0.85, 0.80, 0.78, 0.75, 0.70, 0.65, 0.60\}$. For a given value of u , the charge is $(1 - u)\%$ lower due to the accumulation of dust and dirt and increased filter absorption.

Initially, the values of $u = 0.85$ and $u = 0.65$, provided a significant divergence in the reconstructed spectrum of the UVF Crab Nebula dataset compared to the literature. This indicates that u should likely be in the interval $0.65 < u < 0.85$. Since the production of IRFs is computationally expensive, the number of tested values were limited until a reasonable correction was found.

Figure 6.3 present a power-law (PL) fit (and 1σ error) of the UVF Crab Nebula dataset with the different values of u mentioned above. Because the energy threshold of the UVF observations is higher than in the nominal case (spectral points were only reconstructed above ~ 600 GeV), a power-law fit (rather than a log-parabola fit, as discussed in Chapter 4) provides a reasonable description of the dataset. We compare the UVF Crab Nebula fit results with the previously published nominal flux of the source, available in Reference [Meagher, 2015] (fitted in the reference with a log-parabola function).

u	Γ	$\mathcal{F}_0 (\cdot 10^{-11})$	$\chi^2/\text{n.d.f}$
1.0	2.55 ± 0.09	2.2 ± 0.1	1.64
0.85	2.31 ± 0.09	2.3 ± 0.2	0.56
0.80	2.37 ± 0.08	2.6 ± 0.2	0.76
0.78	2.36 ± 0.09	2.8 ± 0.2	0.47
0.75	2.30 ± 0.07	2.5 ± 0.2	1.42
0.70	2.29 ± 0.07	2.7 ± 0.2	1.14
0.65	2.19 ± 0.07	2.8 ± 0.2	2.93
0.60	2.16 ± 0.08	3.1 ± 0.3	1.03

Table 6.1: Parameters from the fit of the Crab Nebula spectrum assuming a fit given by a power-law function: $\mathcal{F}_0 \left(\frac{E}{\text{TeV}}\right)^{-\Gamma}$. \mathcal{F}_0 is given in units of $\text{cm}^{-2} \text{s}^{-1} \text{TeV}^{-1}$. The γ /hadron separation cuts are optimised for a spectrum with a power-law index of 2. Values used for additional throughput correction (u): 1.00 (no correction), 0.85, 0.80, 0.78, 0.75, 0.70, 0.65 and 0.60. The goodness of the fit is given as the χ^2 by the number of degrees of freedom (n.d.f.).

Table 6.1 presents the fit results, including the case where the spectrum has no additional correction ($u = 1.0$). The value $u = 0.78$ is selected based on visual inspection and how closely the

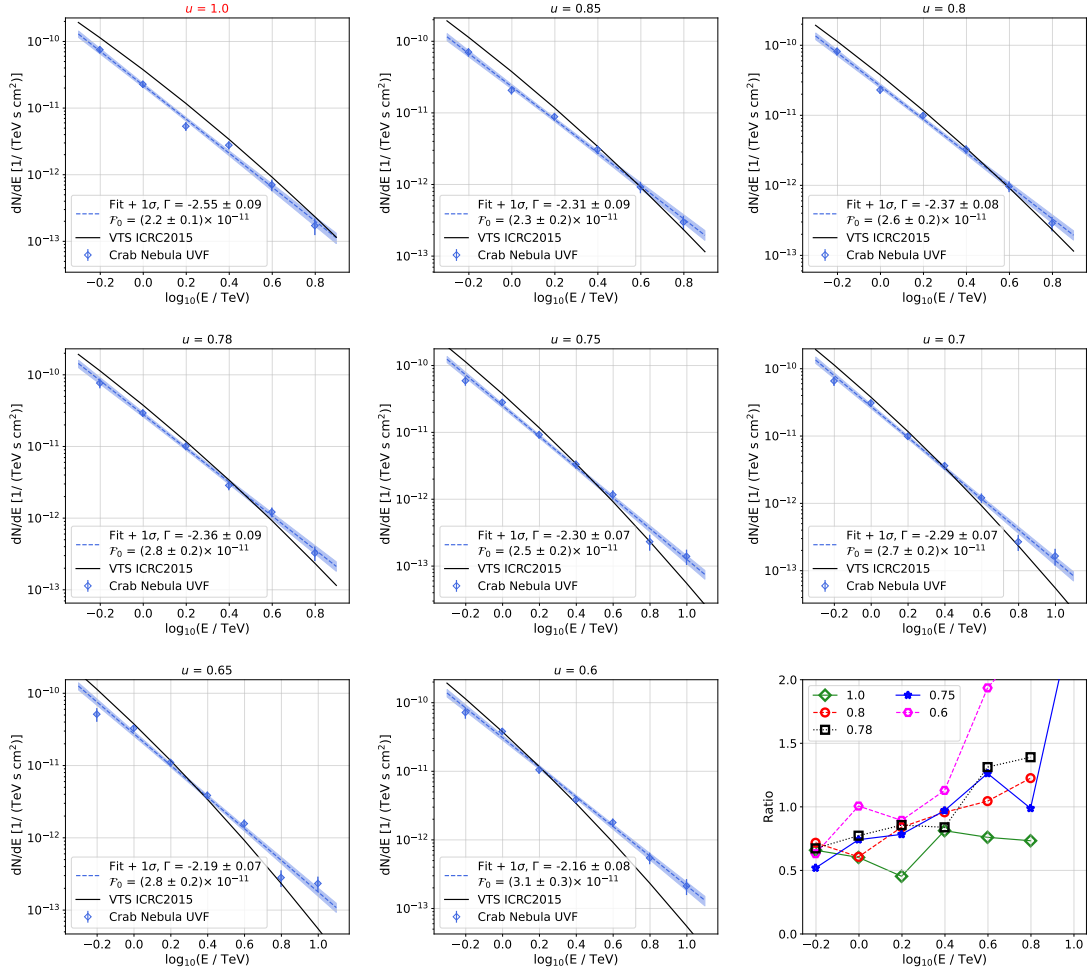


Figure 6.3: Fit and standard deviation of the Crab Nebula Spectrum assuming a power-law function. The values assumed for the extra correction are $u = 1.00$ (no UVF correction), 0.85, 0.80, 0.78, 0.75, 0.70, 0.65 and 0.60. The solid blue line (VTS ICRC2015) represents the literature fit extracted from Ref. [Meagher, 2015]. The last panel shows the ratio between the flux points and the reference spectrum for different values of u .

spectral index matches the expected values from Ref. [Meagher, 2015] (2.467 ± 0.006) while still providing a reasonable $\chi^2/n.d.f.$

Figure 6.4 presents the comparison of the original UVF effective area (from the literature) with the one constructed with the additional u factor. The energy threshold of the new IRFs is quite low, at ~ 610 GeV (against ~ 300 GeV from the literature). This low value is also aggravated by the higher noise level during the observations of GRB 221009A (~ 350 MHz). The same set of IRFs corrected with the u factor but at a noise level of 200 Hz and at a zenith of 20 degrees yield an energy threshold of ~ 300 GeV.

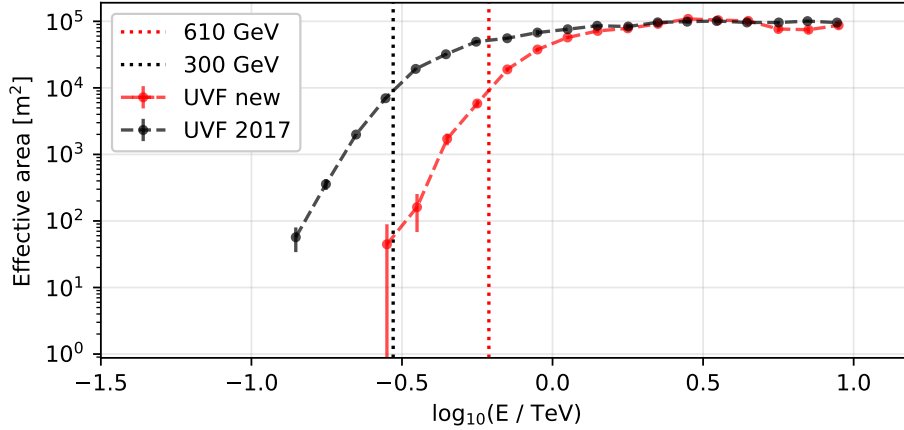


Figure 6.4: Comparison of updated UVF effective areas to the literature reference (zenith = 20 degrees, noise = 200 Hz, taken from [Archambault et al., 2017]). The updated one corresponds to a noise level of 350 MHz and a zenith of 35 degrees. The dotted lines represent the energy threshold of the updated (610 GeV) and literature (300 GeV) IRFs.

6.3 The VERITAS GRB follow-up program

Since 2006, VERITAS has implemented a dedicated program to the observation of GRBs. During this period, over 200 bursts have been followed up [Ribeiro, 2023]. Alerts are received via GCN in the format of real-time coordinates (via *Notices*) or follow-up reports (*Circulars*). Although a pre-filtering is performed regarding the burst distance, brightness and position, the final follow-up decision is attributed to the observers since additional properties such as sky visibility and weather conditions should be assessed.

Figure 6.5 presents the distribution of GRB triggered by Swift or Fermi-LAT that have been followed-up by VERITAS. Although Swift triggers are more common, priority is given to Fermi-LAT due to the presence of the HE component. The observing criteria can be summarised as follows:

- Triggers by only Fermi-GBM (150 keV - 30 MeV) and in case the position is known with an uncertainty of less than 5° : observe up to 1 hour after the initial trigger.
- Triggers by BAT (15 - 150 keV), XRT (0.2-10 keV) and LAT (20 - 300 GeV): observe up to 3 hours after the initial trigger. Some bursts bright in the VHE regime (e.g., GRB 190829A and GRB 190114C [Derishev and Piran, 2019]) have also exhibited a bright and extended afterglow in the X-ray band (XRT flux $\sim 10^{-11}$ - 10^{-10} erg s $^{-1}$ cm $^{-2}$). For this reason, the inferred XRT flux, when available, is used as a filtering condition to trigger the VERITAS GRB proposal. Observations of GRBs exhibiting an X-ray flux higher than 10^{-11} erg s $^{-1}$ cm $^{-2}$ will continue as long as this threshold is still valid.

With this protocol, events that are well localised and are also promising VHE candidates are prioritised. The typical delay time is in the order of 10^2 - 10^4 seconds and depends on several

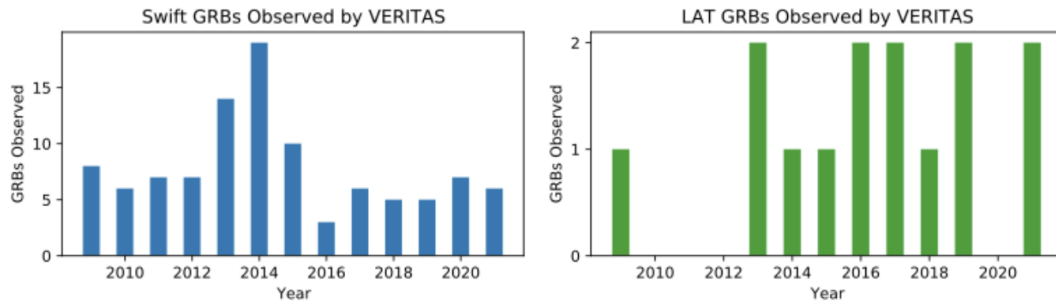


Figure 6.5: Distribution of GRBs followed up by VERITAS based on triggers by Swift (right) and Fermi-LAT (left). Figure from: [Ribeiro, 2023].

factors, such as the observer’s response and telescope slew time. Although no GRB has been detected by VERITAS so far (March 2024), important constraints regarding the environment of the burst progenitor and emission mechanisms have been provided with flux ULs [Abeysekara et al., 2018; Aliu et al., 2014].

6.4 GRB 221009A in very high energies

GRB 221009A was not only an exceptional event in the X-ray band but also provided the first VHE gamma-ray detection beyond 10 TeV from a GRB, as reported by the The Large High Altitude Air Shower Observatory (LHAASO) Collaboration [Cao et al., 2019; The LHAASO Collaboration, 2023]. LHAASO interconnects three detectors at 4410 meters above sea level at the Province of Sichuan, China. The sub-arrays are composed by the Water Cherenkov Detector Array (WCDA, with an area of 78000 m²), the Kilometer Squared Array (KM2A, with an area of 1.3 km²) and the Wide Field-of-view Cherenkov Telescopes Array (WFCTA) [Di Sciascio, 2016]. In particular, KM2A comprises plastic scintillators used to measure the electromagnetic and muonic components of photon and cosmic-ray showers.

From $T_0 + 230$ s, when the initial detection occurred, up to $T_0 + 900$ seconds, when the last emission was observed, LHAASO-KM2A registered 142 gamma rays above 3 TeV with a significance above 20σ . In addition, the LHAASO-WCDA also reported the detection ($> 100\sigma$) of over 5000 events above 500 GeV within 2000 seconds from the first GBM trigger [Huang et al., 2022]. A maximum photon energy of $12.5^{+3.2}_{-2.4}$ is reported by KM2A after correcting for EBL absorption and given a power-law with exponential cutoff for the spectrum fit. Figure 6.6 presents the light curve and significance sky-map measured by KM2A.

The study of the LHAASO spectrum of GRB 221009A results in interesting physical implications regarding emission zones and mechanisms. The events spectrum does not show any softening until ~ 10 TeV, which contradicts KN predictions and challenges SSC emission models for the afterglow, as was also observed for GRB 190829A [The LHAASO Collaboration, 2023]. In the provided reference, possible explanations for the observed spectrum are discussed.

H.E.S.S. reported the non-detection of GRB 221009A with a flux upper limit of $9.7 \cdot 10^{-12}$ erg s⁻¹ cm⁻² above 650 GeV (95% C. L.) considering the entire dataset ($S = -0.7\sigma$) [Aharonian,

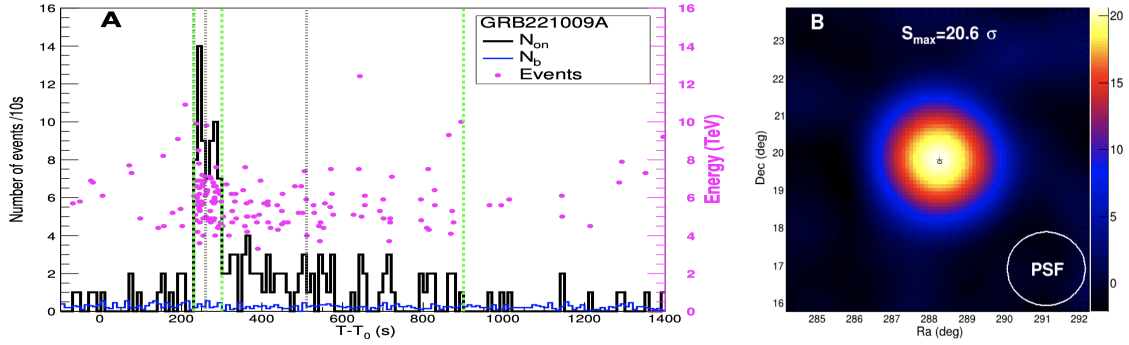


Figure 6.6: Light curve (left) and significance map (right) of GRB 221009A obtained by LHAASO-KM2A. Left: The black histogram shows events from the source region centred on the GRB, while the blue histogram shows the number of background events. The pink dots show the energy of the events. Right: Significance map of GRB 221009A as measured by LHAASO-KM2A. The cross (circle) denotes the position and error of the event as seen by LHAASO-KM2A (Fermi-LAT). Figure adapted from: [The LHAASO Collaboration, 2023]

Benkhali, et al., 2023]. For the first night of observations, starting at $\sim T_0 + 52.8$ h and ending at $T_0 + 53.5$ h, a flux UL of $4.06 \cdot 10^{-11}$ erg s $^{-1}$ cm $^{-2}$ above 650 GeV (95% C. L.) is found.

6.4.1 VERITAS Observations of GRB 221009A

In this section, I describe the observations of GRB 221009A by VERITAS. This is an ongoing analysis and further results are expected to be part of a future publication.

Due to the moon phase happening from October 6th, 2022 to October 13th, 2022, special VERITAS observations (for this night, no observations were scheduled due to moonlight) for GRB 221009A started on $T_0 + 1.35 \cdot 10^5$ seconds (~ 37 hours). On the first day of observations (October 11th, 2022), 177 minutes of live-time were collected under the UVF mode. These observations are the most critical ones, as they are the earliest after the trigger alert by Fermi-GBM. In the following three days, it was possible to allocate nominal and RedHV observations, while the moonlight illumination remained in a level of $\sim 50\%$ - 65% . Starting from the fourth night onwards, all observations were conducted using the nominal voltage (until October 30th, 2022). The summary of observations for each observing mode is presented in Table 6.2.

Observing date	Observing mode	Exposure (minutes)	Mean elevation (degrees)
11-10-2022	UVF	177	51.6
12-10-2022	RedHV	85	64.6
13-10-2022	Nominal	49	68.5
13-10-2022	RedHV	40	56.5
14-10-2022	Nominal	87	64.7
14-10-2022	RedHV	41	47.5
16-10-2022 - 30-10-2022	Nominal	937	56.7
Total	-	1416	58.6

Table 6.2: Summary of VERITAS observations of GRB 221009A: observing date, observing mode, total exposure in minutes and mean elevation of the period. Night 11.10.2022 corresponds to a time interval of $(T_0 + 1.34 \cdot 10^5 \text{ s} — T_0 + 1.46 \cdot 10^5)$.

Reconstruction methods and analysis results:

The analysis is performed within the *EventDisplay* [Maier and Holder, 2017] framework, adopting the afterpulsing image cleaning method. The background is estimated with the reflected regions method and the gamma/hadron separation is performed with *soft* cuts, which are optimised for soft ($\Gamma > 3$) sources.

Following this analysis, no detection from GRB 221009A is found. The significance for the entire dataset is 0.9σ , while it yields 0.4σ for the first observing night. Excess events maps and significance maps are presented in Figures 6.7 and 6.8 for the first night of observations and for the entire dataset, respectively.

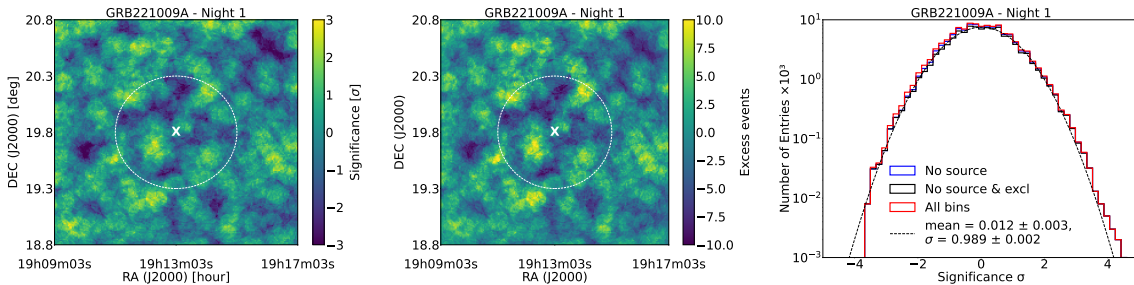


Figure 6.7: **Night 1**: Significance map (**left panel**), excess events map (**middle panel**) and significances distribution (**right panel**) for GRB 221009A. The white cross and the white circle represent respectively the position of the event and a radius of 0.5° . Significance distributions are presented for all regions (red histogram), without source region (blue histogram) and without source and exclusions regions (black histogram with Gaussian fit).

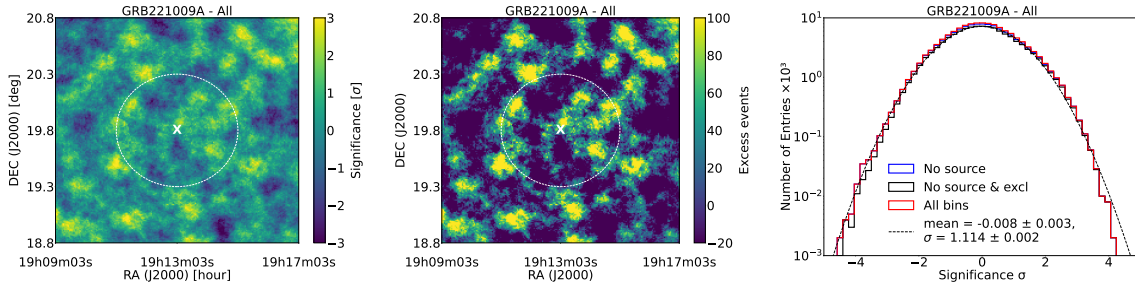


Figure 6.8: **Total dataset:** Significance map (**left panel**), excess events map (**middle panel**) and significances distribution (**right panel**) for GRB 221009A. The white cross and the white circle represent respectively the position of the event and a 0.5° circle. Significance distributions are presented for all regions (red histogram), without source region (blue histogram) and without source and exclusions regions (black histogram with Gaussian fit).

The flux upper limits (95% C. L.) above the energy threshold of the observations (610 GeV) are calculated assuming a spectrum given by a power-law function and using the *Rolke 2001* [Rolke and Lopez, 2001] likelihood ratio test statistic for setting limits on faint signals. We also compute the upper limits with no EBL absorption (adopting the model from *Franceschini et al. 2017* [Franceschini and Rodighiero, 2017]). Power-law spectra with indices of $\Gamma = 2$ and $\Gamma = 3$ are considered. Analysis results are presented in Table 6.3. Gamma-ray flux ULs for GRB 221009A are presented in Figure 6.9.

Period	N_{ON}	N_{OFF}	N_{S}	$S (\sigma)$	Γ	$\Phi_{95\%}^{\text{UL}}$ [erg cm $^{-2}$ s $^{-1}$]
Night 1	13	11.33	1.67	0.4	2	$1.0 \cdot 10^{-11}$
					3	$4.9 \cdot 10^{-11}$
Total	2838	2788.90	49.10	0.9	2	$2.5 \cdot 10^{-11}$
					3	$8.7 \cdot 10^{-11}$

Table 6.3: Summary of VERITAS flux UL for GRB 221009A: observing period, N_{ON} , N_{OFF} , N_{S} , significance (S) and flux UL for a given power-law index. All flux ULs are given at 95% C. L. and above the energy threshold of 610 GeV up to 10 TeV.

Comparison with H.E.S.S. results:

As described in Ref. [Aharonian, Benkhali, et al., 2023], the SED in the range of radio up to X-rays is consistent with synchrotron emission originating from a single electron population. Because the synchrotron spectrum peaks at energy levels beyond the range covered by the X-ray instruments, Klein Nishina effects would suppress any inverse Compton component. By adapting a

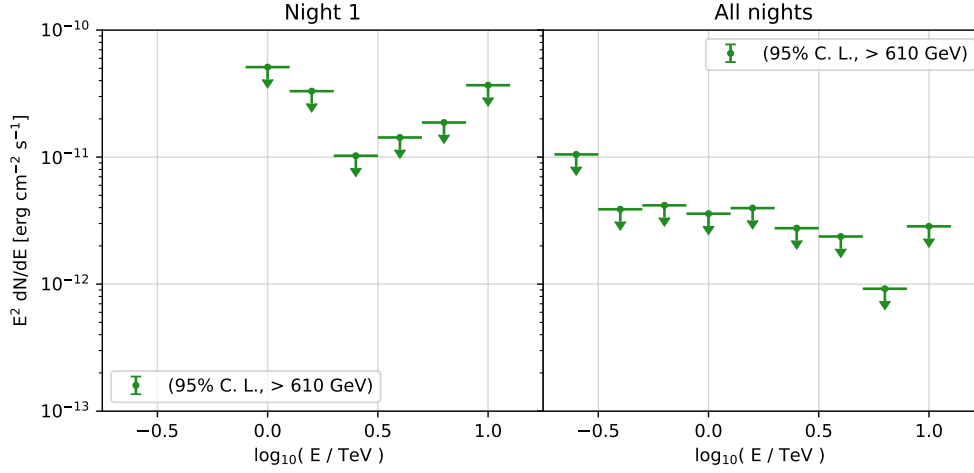


Figure 6.9: Flux upper limits at 95% C. L. above 610 GeV for GRB 221009A considering the entire period of VERITAS observations (left) and the first night of observations (right).

SSC model to match the flux ULs by H.E.S.S., it is found that the SED should not be IC-dominated. The flux ULs by the H.E.S.S. Collaboration ($\Gamma = 2$) result in $4.06 \cdot 10^{-11} \text{ erg cm}^{-2} \text{ s}^{-1}$ in the period of $T_0 + 1.901 \cdot 10^5 \text{ s} - 1.920 \cdot 10^5 \text{ s}$ (On Oct 11 2022, referred to in this thesis as "Night 1" and corresponding to roughly ~ 15 hours after the start of VERITAS observations). The higher flux UL achieved by VERITAS is likely due to the higher level of moonlight during observations, which increases the energy threshold. Nonetheless, VERITAS flux ULs are comparable to ones found by H.E.S.S., supporting the conclusion that the spectrum is not IC-dominated.

6.5 Chapter conclusions

GRB 221009A was an extraordinary astrophysical event at redshift 0.151. It displayed an outstanding isotropic equivalent energy ($\sim 10^{55} \text{ erg}$ at 8 keV – 40 MeV) and luminosity ($9.9 \cdot 10^{53} \text{ erg s}^{-1}$).

VERITAS observations of GRB 221009A could only start about 37 hours after the initial GBM trigger due to the high level of moon illumination. Because the PMT currents would exceed the safety thresholds, the camera was covered with a plate containing 499 UV filters aligned with each PMT. This plate absorbs most of the moonlight ($\sim 96\%$) while still transmitting a reasonable portion of the Cherenkov spectrum. A total of 23.6 hours of live-time were taken for GRB 221009A. The first ~ 2.9 hours are taken with the UVF mode, while the remaining was taken under Reduced High Voltage or nominal mode. Because UVF observations had not been conducted for a few years, the UV plate had accumulated dirt and dust due to the lack of maintenance.

Similarly to the throughput factors already accounted for, the increased Cherenkov absorption of the plate will also translate into the suppression of the PMT signal. As a result, the existing UVF IRFs provide an inaccurate event reconstruction. In order to correct for this lack of maintenance, I introduce an additional factor to the throughput calibration, now given by $s' = u \cdot s$, with u

accounting for the loss in PMT signal from the plate and s describing the typical correction for the observing season. In order to find the best value of u , I use a UVF Crab Nebula dataset taken with the UV plate in the exact conditions. I test values of $u \in (0.85, 0.80, 0.78, 0.75, 0.70, 0.65, 0.60)$. Because the production of IRFs is computationally expensive, I limit the number of test values until a reasonable value u for which the fit of the Crab Nebula spectrum approaches the literature reference is found. The value that provides a reasonable correction is $u = 0.78$ ($\chi^2/\text{n.d.f} = 0.47$, power-law spectral index = 2.36 ± 0.09).

The VERITAS analysis of GRB 221009A is performed with IRFs produced with the new throughput factor. No detection is found on either the first night of observations ($S = 0.4\sigma$) or considering the entire dataset ($S = 0.9\sigma$). Flux ULs corrected for EBL absorption are found for the first night and for the entire dataset. We compare the results obtained by VERITAS with the publication by the H.E.S.S. Collaboration. VERITAS flux ULS are less strict than those found by H.E.S.S. This is likely due to the lower energy threshold achieved by VERITAS due to the UVF observing mode.

Observations of fast blue optical transients with VERITAS

The identification of SNe presenting fast-developing timescales and extreme luminosities has gained rising attention only since relatively recent optical discoveries, such as the events AT2018cow and AT2018lug (the "Koala") [Ho et al., 2020]. For this reason, observations of FBOTs in the VHE regime are scarce. Although the census of known FBOTs discovered through optical surveys has substantially increased in the past few years, only AT2018cow has triggered follow-up observations in the TeV range. Observations of AT2018cow by the H.E.S.S. Collaboration yielded only flux upper limits above the energy threshold of 220 GeV (95% C. L.) [de Naurois, 2018]. These results were achieved after 2.4 hours of live-time and after a mono analysis with telescope CT5. In addition, the VERITAS Collaboration also reports the non-detection of SLSNe SN2015b and SN2017eg after 1.0 h and 1.8 h of live-time, respectively [Acharyya et al., 2023]. In the following section, the first ToO proposal for the observation of FBOTs by IACTs is described. This program aims to raise attention to the scientific potential of FBOTs as a new class of astrophysical accelerators, ensuring that follow-up observations are triggered as quickly as possible as new events are identified via optical surveys.

7.1 Target of opportunity observations of fast blue optical transients with VERITAS

In 2022, a ToO follow-up program for FBOTs was established through a partnership between the VERITAS and H.E.S.S. Collaborations. A communication channel was created with the goal of monitoring ATEls and TNS alerts, as well as conducting discussions on the feasibility of each candidate. The triggering criteria primarily depend on the optical characteristics of the event, including absolute magnitude, rise time, and decay time. The criteria used in this proposal, which has been adopted by both Collaborations, are summarised in Table 7.1. In order to explore the widest range of optical features, candidates are divided into two categories: FBOTs within a close range that meet a minimum luminosity requirement (Class 1), and FBOTs at a greater distance which are exceptionally bright (Class 2). In both scenarios, follow-up observations should be conducted during the ascension of the light curve or immediately after the optical peak (within a maximum of 2 days), when the gamma-ray emission is anticipated to be the highest. Similar to the ToO proposal for TDEs, the TAC of VERITAS is responsible for granting approval for triggers. Should a trigger be approved, the event is observed nightly up until either 10 or 15 hours are

collected, depending on the observing schedule of the respective dark run. Compared to TDEs, FBOTs require much faster responses in terms of proposal triggering. The response has to be fast enough that the peak of the light curve is not missed, but not fast enough to require triggering decisions directly by the observers.

		Case 1	Case 2
Trigger criteria	Distance	$\lesssim 80$ Mpc ($z \lesssim 0.02$)	$\lesssim 150$ Mpc ($z \lesssim 0.03$)
	Rise time	< 5 days (1 mag/day)	< 5 days (1 mag/day)
	Peak absolute magnitude	$-20 < M_{\text{peak}} < -17.5$	$M_{\text{peak}} < -20$
	Minimum elevation	30 degrees	30 degrees
VERITAS observations	Time-frame	< 2 days post optical peak	
	Time per trigger	2 hours/night until a total of 10 or 15 hours	

Table 7.1: Trigger criteria for FBOTs ToO: minimum distance, rise time, minimum brightness (peak absolute magnitude) and minimum elevation. Conditions for VERITAS observations: light curve should be at no more than 2 days post optical peak. In case of an accepted trigger, take 2 hours of live-time on the event until 10 or 15 hours is completed (depending on the scientific interest of the FBOT and on the observing schedule).

An overview of the FBOT alerts since the start of the proposal can be found in Table 7.2. As of the writing of this thesis, VERITAS has followed-up one event, AT2023ufx.

Event	Triggered	Trigger rejection reason	TNS entry
AT2023ufx	yes	-	[2023ufx]
AT2023iuc	-	redshift	[2023iuc]
AT2023xje	-	brightness	[2023xje]
AT2023uqf	-	redshift	[2023uqf]
AT2023vth	-	redshift	[2023vth]
AT2023yoo	-	brightness	[2023yoo]
AT2023aub	-	visibility	[2023aub]
AT2023zcu	-	visibility	[2023zcu]
SN2024ggi	-	visibility	[2024ggi]

Table 7.2: List of FBOT alerts since the implementation of the ToO proposal by H.E.S.S. and VERITAS. For each event, it is listed whether there was a positive trigger or the trigger rejection reason by VERITAS. The last column provides a link to the TNS entry of each event.

7.2 AT2023ufx

AT2023ufx¹ was a fast rising transient at ~ 44 Mpc ($z = 0.01$), discovered by ATLAS on October 6th, 2023 with a magnitude of 17.55 ± 0.09 (o-filter). Figure 7.1 presents the optical light curve for this event. The following features characterise AT2023ufx as an FBOT candidate:

- Blue color: $g-r \sim -0.13$.
- Fast rise: within four days, the absolute magnitude had a rise from ~ -15.6 to ~ -17.3 (equivalent to about -0.5 mag/day).
- Peak magnitude and timescale: the rise to the peak occurred 6.0 ± 0.5 days after the initial detection. The peak magnitude based on ZTF g-band is of $M_{\text{peak}} = -18.4$.

Although the rise time-scale did not reach -1.0 mag/day, it was still a compelling candidate for observations, mainly due to its distance.

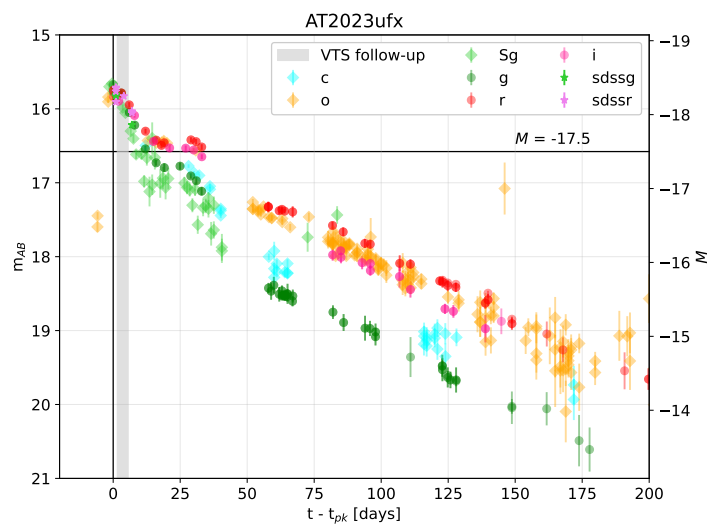


Figure 7.1: Light curve for AT2023ufx. Filters by ZTF: green (g), red (r) and infrared (i), ATLAS cyan (c) and orange (o), SDSS green (sdssg) and SDSS red (sdssr) and ASAS-SN (Sg). The VERITAS observing period is shown as the grey region.

AT2023ufx originated from a core-collapse supernova at a distance of ~ 0.8 kpc from the center of the galaxy SDSS J082451.43+211743.3 [Tucker et al., 2024]. The host is classified as a metal-poor ($\sim 0.1 Z_{\odot}$) dwarf galaxy ($\sim 10^{6.4} M_{\odot}$). The mass of the envelope inferred for AT2023ufx is in the range of $0.5 M_{\odot} - 1.5 M_{\odot}$ [Tucker et al., 2024], which could be explained as a result of strong stellar winds stripping mass away or due to interactions with a nearby stellar companion. Fast outflows in the order of 5000 km s^{-1} are also estimated based on the spectroscopic analysis [Tucker et al., 2024]. Overall, AT2023ufx exhibited several features of an FBOT candidate, triggering observations by VERITAS.

¹www.wis-tns.org/astronotes/astronote/2023-268

7.2.1 VERITAS results for AT2023ufx

VERITAS observations on AT2023ufx started on October, 14th, 2023, approximately 7 days after the initial trigger and ~ 2 days after the optical peak from ZTF. The data analysis methods are the same as the ones described in section B.0.3 of appendix B. The dataset consists of 6.85 hours of live-time (due to observing schedule constraints) with a mean elevation of 50.2 degrees. VERITAS analysis methods are described in Section B.0.3.2. No detection was found for AT2023ufx, and a dataset significance of 0.6σ is derived ($N_{\text{ON}} = 591$, $\alpha N_{\text{OFF}} = 575.50$ and $N_s = 15.50$). An excess rate of 0.05 ± 0.09 gamma/min is inferred. Figure 7.2 presents the significance and excess events skymaps for AT2023ufx. Assuming a power law spectrum of index 2, flux ULs at 95% C. L. below 10 TeV and above an energy threshold of 140 GeV yield $\Phi_{95\%}^{\text{UL}} = 2.23 \cdot 10^{-12}$ erg cm $^{-2}$ s $^{-1}$ (corrected for EBL attenuation).

Assuming the light curve is binned in intervals of 1, 5 and 10 days, the Fermi-LAT analysis of AT2023ufx comprising the period of 10 days before the optical peak and up to 20 days after VERITAS observations yields no detection (in the energy range of 100 MeV - 300 GeV). Fermi-LAT analysis methods are described in Section B.0.3.1. The flux ULs for gamma rays are presented in Figure 7.3.

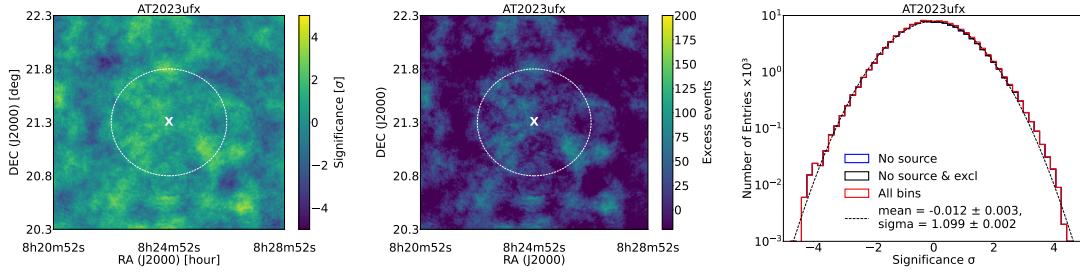


Figure 7.2: Significance map (**left panel**), excess events map (**middle panel**) and significances distribution (**right panel**) for AT2023ufx. The white cross and the white circle represent respectively the position of the event and a 0.5° region. Significance distributions are presented for all regions (red histogram), without source region (blue histogram) and without source and exclusions regions (black histogram with Gaussian fit).

7.3 Conclusions and future prospects

FBOTs have attracted increasing attention as potential sites for cosmic-ray acceleration. Shock interactions could be triggered as the star's ejecta encounters the progenitor's envelope, resulting in a bright and fast burst of light. As a result, these interactions may also lead to the emission of gamma rays as the relativistic particles interact with the ambient matter and radiation field. This chapter describes the first ToO follow-up program of FBOTs in the VHE regime. In order to focus on the widest range of candidates, the trigger criteria for this program are divided into two groups: bright events that are nearby and events that are slightly further away but exceptionally bright. In both cases, candidates should also exhibit a fast development of the light curve. As part of this

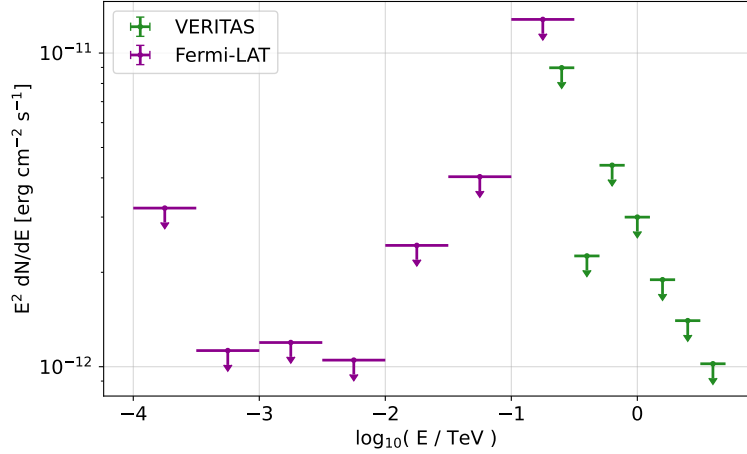


Figure 7.3: Upper limits by VERITAS and Fermi-LAT for AT2023ufx.

program, the VERITAS array conducted observations on AT2023ufx. Since the event featured a peak absolute luminosity of ~ -18.4 and a very low redshift ($z = 0.01$), it was triggered under the first case of the proposal. Further analysis of AT2023ufx indicates this is likely a core-collapse supernova exhibiting a thin envelope [Tucker et al., 2024]. The VERITAS analysis of AT2023ufx results in no detection. Flux ULs were derived above the energy threshold of 140 GeV (95% C. L.). Additionally, no detection was observed by Fermi-LAT in the energy range of 100 MeV - 300 GeV when the light curve was analysed in intervals of 1, 5, and 10 days.

Similar to TDEs, the absorption mechanisms of gamma rays by the surrounding matter and radiation fields could also be a significant factor in this scenario. The extent of absorption would vary for each event, but it is reasonable to assume that for typical luminosities greater than $\sim 10^{40}$ erg s $^{-1}$, a substantial fraction of a potential gamma-ray emission would be suppressed in the GeV - TeV regime. Even in the absence of VHE detection by VERITAS, establishing upper limits would still be valuable to constrain the emission. The ToO proposal presented in this chapter is established at least until the end of the 2023 - 2024 observing season. The onset of the future Vera Rubin Observatory is expected to significantly increase the known census of FBOTs [Megias Homar et al., 2023], highlighting the importance of future searches of gamma-ray signals from this transient class as a wider selection of fast and bright events becomes available.

Summary and outlook

This thesis focused on the search for VHE emission from various astrophysical transients. The high luminosities observed by optical, UV, and occasionally X-ray instruments, suggest that some transient classes could be powered by shock interactions capable of accelerating particles to relativistic energies. Nonetheless, there have been no detections of TDEs and FBOTs in high or very high energy ranges to date. Notably, only in recent years have observations of TDEs and FBOTs by IACTs gained increasing attention and, as a consequence, the field suffers not only from the low statistics of observed events but also from a shortage of viable candidates for follow-up observations. In addition, the potential gamma-ray emission is possibly heavily attenuated, or the mechanisms driving these events might not be strong enough to produce a detectable non-thermal component above ~ 100 MeV. Extensive observations by IACTs on viable candidates - and thus achieving a better telescope sensitivity through advancements in analysis techniques - could substantially enhance our understanding of the non-thermal scenario in transient phenomena.

The thesis starts by providing a comprehensive review of gamma-ray astrophysics in the VHE regime, followed by discussions on the current VHE picture of TDEs, FBOTs and GRBs. Following, a description of the VERITAS array is provided, including the data acquisition process, instrument calibration and event reconstruction methods. I present the implementation of a novel image cleaning method that enhances the sensitivity of the VERITAS array in the GeV range. Unlike the traditional cleaning, which consistently applies a $5\sigma/2.5\sigma$ (above the pedestal variance) pixel charge threshold to ensure that most noise is removed, the Optimised Next Neighbour technique determines dynamical threshold contours in the parameter space of the group minimum charge and the maximum difference in arrival time of Cherenkov pulses. This method is based on the principle that pixels containing Cherenkov light from showers should exhibit a correlated distribution of pulse arrival times. However, the random noise also contaminates neighbouring pixels within a short time frame. Removing these noise-induced pixels is crucial in the analysis chain of IACTs, as their presence can introduce significant bias in image parameterisation. We account for the probability of such contamination occurring, setting it low enough to guarantee that most recorded events are not reconstructed with a "fake" group. I show that a probability of 0.05% significantly improves the rate of event reconstruction without affecting the distribution of simulated image parameters.

One of the key advantages of the ONN cleaning over the traditional approach is that the cleaning thresholds are tailored to each specific observation. These thresholds are based on the pixel noise rate and inferred from pedestal events, implying that observations taken under higher NSB are cleaned with stricter thresholds, while darker conditions allow for more lenient criteria. This

represents a significant improvement over the traditional method, since the cleaning cuts adapt to the noise level.

The performance of the ONN method was first evaluated with simulated gamma-ray events. By incorporating the time information, the minimum pixel charge required to form an image is reduced, enabling simulated events in the lower range of VERITAS sensitivity ($\sim 50 - 100$ GeV) that were previously suppressed by the traditional cleaning to be successfully reconstructed. When comparing IRFs produced with the ONN and conventional methods, we notice an increase in effective areas for every Monte Carlo configuration produced with different noise levels and zenith angles. This result was also consistent across observing seasons. Consequently, the energy threshold of the telescopes is lowered in each configuration. Specifically, the effective areas increased by a factor of approximately $\lesssim 3$ below 100 GeV at a zenith angle of 40° degrees and a noise level of 200 MHz. This configuration resulted in a reduction of the energy threshold by roughly 17%.

Following, I present results of the ONN method on an extensive Crab Nebula dataset of over 300 hours. This dataset is divided in observing seasons and in ranges of zenith angles ($30^\circ - 40^\circ$, $40^\circ - 50^\circ$ and $50^\circ - 90^\circ$) and noise levels (100 MHz - 200 MHz, 200 MHz - 300 MHz, 300 MHz - 400 MHz and 400 MHz - 500 MHz). I show that in overall an increased number of reconstructed excess events was observed below approximately 300 GeV in every configuration. Particularly in some cases, the ONN method reconstructed events at energies ($\lesssim 75$ GeV) which were completely suppressed by the traditional cleaning method. An additional spectral point at an energy of ~ 300 GeV was obtained in configurations which include events recorded during observations with an elevation lower than $\sim 50^\circ$. In addition, I show that the application of the ONN cleaning to a set of five faint and soft sources also yielded remarkable results in terms of event reconstruction. Although the significance was lower in a few cases, this issue can be addressed with gamma/hadron separation cuts derived from machine learning techniques. A good agreement was observed in the Monte Carlo/data comparison, with a systematic uncertainty of 4% below 1 TeV, compared to 2% with the afterpulsing method. This result further validates the effectiveness of the ONN method. Lastly, I describe the implementation of the ONN for observations with a short duration. Due to the lower statistics in pedestal events, we adopt IPR curves averaged over all telescopes. This mode comes into practice when the noise rate histogram presents less than 10^6 entries.

I analysed the efficiency of the ONN cleaning method for data taken under reduced high voltage mode with Crab Nebula data. An increase by a factor of 3.5 in event reconstruction below approximately 300 GeV is achieved. However, above ~ 300 GeV and below 3 TeV, the ONN method systematically reconstructed fewer events than the afterpulsing method. The Monte Carlo/data comparison shows that the parameters MSCW and MSCL from Crab Nebula images are larger in respect to the simulations. One reason for the poorer performance could be the varying illumination of the Moon across different parts of the camera, which introduces noise gradients. However, the noise rates employed for deriving the cleaning cuts are averaged over all camera pixels and over the entire observation duration, which is not suitable under very bright moonlight.

I explored whether deriving a new set of cuts in shorter time intervals (of either 3 or 10 minutes) could improve the cleaning performance. The reduced pedestal statistics within these short intervals result in a lower maximum pixel charge. To improve statistics, I include the charge information

from telescope cameras that do not contain an L1 trigger during the recording of an event (i.e., even when only two or three telescopes participate in an array trigger, the read-out of the charge in all four cameras is performed. In these cases, we have either one or two telescopes which do not meet the L1 threshold, but, in practice, they might have collected some Cherenkov light). The inclusion of these signals significantly increased the IPRs above a few dozen digital counts, likely due to "contamination" of the non-triggered telescopes with some Cherenkov light from the showers. The higher noise rates lead threshold cuts to be more stringent, which would suppress even more events. I also investigated the behaviour of IPR curve per pixel. Nonetheless, this method also suffers from low statistics of pedestal events and produces more stringent cuts when including the charge information from non-triggered telescopes. In summary, while the ONN cleaning method has significantly increased event reconstruction in below ~ 300 GeV for nominal observations, noise rate variations and insufficient pedestal statistics hinder the performance for Reduced High Voltage data. Further optimisations to the cleaning approach are necessary to address the latter.

In the following chapter, I introduce the ToO program for TDE follow-up with VERITAS. This program has been in place since the start of the 2021/2022 observing season. I present the follow-up campaigns for thermal TDEs AT2022dbl, AT2022dsb and AT2023clx. In order to reach the lowest energy threshold, I apply the ONN cleaning method to the analysis of each event. No detection is found in a VERITAS analysis of each TDE. Flux upper limits are established at 95% C. L. above the energy threshold of 108 GeV. In addition, no detection is found in a Fermi-LAT analysis comprising two main periods of the light curve: one under the highest absorption level (from the discovery + 20 days) and the second at a lower attenuation level (from discovery + 20 days until the last day of optical or UV detection).

I present the optical depth for gamma-ray annihilation with ambient thermal photons by characterising the observed OUV photometry with a blackbody spectrum. A blackbody radius is assumed to be large enough to ensure that anisotropically accelerated particles have sufficient time to isotropise in magnetic fields. For AT2022dbl and AT2022dsb, the results indicate that gamma rays above ~ 10 GeV would be suppressed at the source for radiation zone radii spanning from $5 \cdot 10^{14}$ cm and $1 \cdot 10^{16}$ cm. Furthermore, gamma rays in the VERITAS sensitivity range would be almost completely attenuated by the OUV photosphere for at least 150 days after the optical peak. It is worth noting that even though the study presented in this thesis indicates a severe level of attenuation, the blackbody characterisation is an oversimplified representation of the TDE scenario. A possible VHE emission might still escape and produce a detectable signal under different conditions.

In the following chapter, I present the revision of IRFs for the VERITAS UVF observing mode. GRB 221009A was a nearby event ($z = 0.151$) with an extraordinary isotropic-equivalent luminosity of $9.9 \cdot 10^{53}$ erg s^{-1} , as seen by Fermi-GBM. It triggered extensive follow-up campaigns across the electromagnetic spectrum. Nonetheless, VERITAS observations were hindered by a high level of moon illumination ($\gtrsim 99\%$) in the ~ 40 hours post the initial trigger by Fermi-GBM. To start observations as soon as possible, a UV filter cover was placed to protect the telescope's cameras. VERITAS observations of GRB 221009A commenced ~ 37 hours after the GBM trigger, with the first ~ 2.9 hours being conducted with a UV camera cover. Although appropriate IRFs were

available for the analysis of data taken under the UVF mode, the cover had not been maintained for a long time, indicating that the actual absorption capacity of the filters should have deviated significantly from the manufacturer’s specifications. Consequently, the pre-existing IRFs would not ensure an accurate event reconstruction.

To address this issue, I applied an additional correction factor, u , which accounts for the extra unknown absorption by the filter, to the throughput correction of the telescopes. The validation was done with a Crab Nebula dataset taken with the filter in the exact conditions as for the observations of GRB 221009A. I determine a factor of $u = 0.78$ by comparing the literature spectrum fit of the Crab Nebula with the one reconstructed with different values of u . I produced new IRFs with the additional u factor. I present the analysis of the data of GRB 221009A using the corrected UVF IRFs. No detection was found, and flux upper limits were set for the first night of observations and for the entire dataset, which comprises ~ 23.6 hours of live-time in the span of ~ 29 days after the initial GBM trigger. Flux upper limits for the first night are comparable to the results obtained by H.E.S.S. in a similar time window.

The final transient class discussed in this thesis are FBOTs. FBOTs have gained increasing attention in recent years following the detection of a few highly energetic SNe exhibiting very short time-scales. I present the first ToO proposal for FBOT follow-up with VERITAS and discuss the trigger criteria. Given the rapid timescales in which FBOTs operate, the trigger decision must be quick to ensure that observations can capture the peak of the optical light curve. I present the VERITAS follow-up campaign for AT2023ufx, which started ~ 2 days after the optical peak seen by ZTF. About 6.85 hours of live-time were collected. The VERITAS analysis of AT2023ufx resulted in no detection, and flux upper limits were derived. In addition, no detection is found in a Fermi-LAT analysis comprising a period of 10 days before the optical peak and up to 20 days after VERITAS observations when the light curve is binned in intervals of 1, 5 and 10 days. I emphasise the growing interest in the VHE regime for this class of transients. Similar to TDEs, ToO proposals focus on selecting the most extreme candidates. The possibilities of follow-up are further constrained since the rate of exotic events such as AT2018cow and AT2018lug is expected to be $\lesssim 0.1\%$ of the local core-collapse SN [Ho et al., 2023].

In conclusion, this thesis has presented different follow-up programs for transient events with the VERITAS array. I have discussed their current status and analysis results for events approved for follow-up. Each program is at a different stage of development, with the VERITAS GRB follow-up program being well-established since 2006 and having provided gamma-ray observations of over 200 bursts [Ribeiro, 2023]. Some of the main constraints for GRB follow-up are the required rapid response time, the telescopes slew time and the telescope’s duty cycle, which restrict the timely follow-up of bursts. In addition, the lack of artificially triggered observations should mainly affect short GRBs ($\lesssim 2$ seconds), as human-in-the-loop triggers create additional delays. On top of that, the limitations of sky surveys, which are responsible for providing the initial triggers, also play a role in creating observation delays, as factors such as the instrument’s response time and the time required for alert creation and circularisation have to be considered.

In contrast, the TDE and FBOT follow-up programs are in their initial stages, with fewer than a handful of events observed so far. Several factors influence the follow-up for each proposal. For

TDEs, the low rate of events presenting relativistic jets ($\sim 10^{-2} - 1 \text{ Gpc}^{-3} \text{ yr}^{-1}$) [Donley et al., 2002; Gezari et al., 2008; Magorrian and Tremaine, 1999; Teboul and Metzger, 2023] and delays in the classification are important constraints. Since the TDE discovery is usually provided in optical bands, distinguishing these events from AGNi and SNe is a long-term task, which is further limited by the uncertainty of the optimal observation window to avoid gamma-ray annihilation. Nonetheless, TDE light curves can extend over several months, allowing for a deliberate approach in accepting the follow-up. A careful estimation of the most viable observation windows, which are under the lowest levels of gamma-ray annihilation, could enhance the proposal, particularly for events showing only thermal OUV and X-ray components. On the other hand, FBOTs also require much faster responses, as the brightest periods of their light curves are enclosed in time-scales of a few days. In this case, the proposal is limited by similar factors as discussed for GRBs.

The implementation of the Optimised Next Neighbor image cleaning method has enhanced the sensitivity of the VERITAS array, particularly in the GeV range, and has shown promising results across different observation configurations. Although no VHE emission was detected from the TDEs and FBOTs discussed in this thesis, the establishment of flux upper limits and the comprehensive analysis techniques and corrections developed have helped to provide a starting basis for future transient research with VERITAS. Looking forward, the development of multimessenger astrophysics presents exciting possibilities for transient research. Coordinated gamma-ray observations combined with neutrinos and gravitational waves alerts could provide deeper insights into the mechanisms driving transient phenomena. The further collaboration between different observatories and the development of advanced data analysis techniques will be essential in maximising the scientific potential of the field. Additionally, future optical sky surveys, such as the Vera C. Rubin Observatory, will play a crucial role in identifying new transient candidates for follow-up, providing fast alerts via detailed light curves, and promoting timely follow-up observations with the CTAO and other facilities. The upcoming CTAO will be the most advanced ground-based gamma-ray observatory, and its unprecedented sensitivity (Figure 3.21) and wider field of view will ensure the extensive follow-up of several transient events. Advanced follow-up techniques for ToO observations are being developed for the CTAO. For instance, the implementation of the Transient Handler [Egberts et al., 2022] will allow for an efficient trigger mechanism for key science projects, such as high-energy neutrinos, GRBs and gravitational waves. The Transient Handler will manage the incoming alerts and process them to arrive at a decision of whether or not to conduct observations of transient phenomena. For instance, the system was designed to generate a scheduling block in less than 5 seconds after receiving a GRB alert from a Broker System [Egberts et al., 2022].

In summary, continued efforts in alert follow-up techniques, combined with improvements in telescope sensitivity through analysis methods, have the potential to overcome the obstacles in following-up transient events. These advances will be crucial in enhancing our understanding of the non-thermal processes driving the energetic emission from transient phenomena and performing VHE follow-ups.

Supplementary material for Chapter 3

This section of supplementary materials includes additional figures (A.3 - A.15) for the testing of the following Crab Nebula configurations described in Chapter 4:

- Ranges of zenith angles: $30^\circ - 40^\circ$, $40^\circ - 50^\circ$ and $50^\circ - 90^\circ$ - shown in Figures A.3 - A.5;
- Ranges of noise level: 100 MHz - 200 MHz, 200 MHz - 300 MHz, 300 MHz - 400 MHz and 400 MHz - 500 MHz - shown in Figures A.6 - A.9;
- Observing seasons: 2012-2013, 2013-2014, ..., 2016-2017 and 2017-2018 - shown in Figures A.10 - A.15.

All configurations were analysed with a respective Crab Nebula dataset with super-soft cuts for the gamma-hadron separation and reflective regions method for the background estimation [Berge et al., 2007].

Additionally, we also present the counts rate and spectrum fit for Markarian 501 and blazar 1ES 1118+424 in Figures A.17 and A.16, respectively. Markarian 501 is a nearby bright HBL showing extreme spectral variability at a redshift of $z = 0.034$ [Ahnen et al., 2018]. The variability is observed from radio wavelengths to VHE, with a characteristic time interval of 5 up to 25 days for the flares observed in the TeV range. Moreover, a lag of < 0.4 (1σ) is measured for the correlation between the TeV and X-ray curves, consistent with emission from the synchrotron self-Compton process [Arbet-Engels et al., 2021]. The VERITAS Collaboration found a spectral index of $\Gamma = 2.7 \pm 0.2$ for the power-law fit of the spectrum, measured after a short-term multi-wavelength study in 2009 [Acciari et al., 2011]. The second source considered in this appendix, 1ES 1118+424, is another blazar with quasi-featureless spectra and redshift of $z \sim 0.2$ [Dorigo Jones et al., 2022]. For 1ES 1118+424 only upper limits (99% C. L. , > 100 GeV) are found for the spectrum.

To complement the study of the ONN performance on IRFs, we bring in this appendix effective areas, energy bias and energy and angular resolutions for zenith angles 40 and 55 degrees, noise levels 75, 200 and 400 MHz and observing seasons 2012-2013 and 2017-2018 (Figures A.18 - A.24). We also present in Figure A.25 a set of IRFs produced for Reduced High Voltage simulation at 45 degrees zenith and 450 MHz noise level.

Tables A.1 and A.2 presents a summary of the results obtained for each test source and in each test configuration. The configuration column contains internal references to the corresponding Figure.

Configuration:	T (h)	N_s	N_{ON}	N_{OFF}	S (σ)	gamma/min	bkg/min	E_{\uparrow} (GeV)
Crab Nebula	303	235311.53	349523	113983.50	498.7	13.00 ± 0.03	6.29 ± 0.01	67, 75
	303	197340.81	244781	47345.50	556.8	10.89 ± 0.03	2.612 ± 0.005	
PKS 1424+240	173	9472.1	103611	93951.00	28.6	0.93 ± 0.03	9.06 ± 0.01	67
	173	6782.94	54325	47447.17	28.5	0.66 ± 0.02	4.578 ± 0.009	
PG 1553+113	92	19090.92	53199	34040.00	87.7	3.47 ± 0.04	6.17 ± 0.01	75, 85
	92	14280.79	31002	16687.83	89.9	2.59 ± 0.03	3.02 ± 0.01	
M87	139	1578.27	55886	54199.34	6.7	0.20 ± 0.03	6.51 ± 0.01	94, 106
	139	1294.35	27670	26323.00	7.6	0.16 ± 0.02	3.160 ± 0.008	
Crab RedHV	13	6195.12	7218	1020.83	107.6	7.7 ± 0.1	1.27 ± 0.02	-
	13	5975.0	6725	748.50	111.6	7.5 ± 0.1	0.94 ± 0.01	
Mrk501	103	18160.06	57125	38887.17	79.2	2.97 ± 0.04	6.32 ± 0.01	67, 75
	103	16221.55	36154	19892.67	94.1	2.65 ± 0.03	3.235 ± 0.009	
1ES 1118+424	37	395.99	13592	13169.67	3.4	0.19 ± 0.06	5.98 ± 0.02	75, 150
	37	261.94	7055	6779.50	3.1	0.12 ± 0.04	3.08 ± 0.02	

Table A.1: Results of source analysis with the application of ONN (blue) and AP cleaning methods (black): live-time in hours, N_s : number of source events, N_{ON} : number of events in ON region, N_{OFF} : number of events in OFF region, S : significance of detection, gamma-ray rate and background rate. E_{\uparrow} represents the bins in which the ONN analysis reconstruct events which are absent from the spectrum generated by AP.

Configuration:	T (h)	N _s	N _{ON}	N _{OFF}	S (σ)	gamma/min	bkg/min	E _† (GeV)
30° - 40°	27	8709.01	13796	5076.83	90.3	5.43 ± 0.07	3.16 ± 0.02	266, 299
	27	7178.52	9003	1820.83	104.7	4.47 ± 0.06	1.13 ± 0.01	
40° - 50°	31	16442.54	24770	8310.83	130.0	8.9 ± 0.09	4.49 ± 0.02	150, 188
	31	13717.67	16973	3248.83	147.3	7.42 ± 0.07	1.76 ± 0.01	
50° - 90°	197	185786.96	275653	89686.67	443.6	15.79 ± 0.05	7.61 ± 0.01	67, 75
	197	156745.34	194567	37746.17	495.8	13.31 ± 0.04	3.204 ± 0.007	
(100 - 200) MHz	21	26441.34	28107	9974.00	132.8	14.8 ± 0.1	8.12 ± 0.03	67, 75
	21	18938.44	19622	4093.17	152.5	12.6 ± 0.1	3.33 ± 0.02	
(200 - 300) MHz	135	165594.62	175498	59301.67	344.4	14.45 ± 0.05	7.37 ± 0.01	75, 84
	135	119449.39	123567	24656.33	390.3	12.3 ± 0.04	3.066 ± 0.008	
(300 - 400) MHz	116	82870.49	120198.0	223518.0	302.9	12.02 ± 0.05	5.40 ± 0.01	75, 84, 94
	116	68324.64	83868.0	93074.0	332.1	9.91 ± 0.04	2.248 ± 0.007	
(400 - 500) MHz	22	12733.01	17903.0	30958.0	122.5	9.7 ± 0.1	3.91 ± 0.02	84
	22	10206.72	12351.0	12840.0	130.8	7.74 ± 0.09	1.62 ± 0.01	
2012 - 2013	41	34351.26	53092.0	112220.0	183.5	14.19 ± 0.1	7.72 ± 0.02	75, 67
	41	29394.88	36972.0	45372.0	211.1	12.13 ± 0.08	3.12 ± 0.02	
2013 - 2014	34	34500.18	52612.0	108454.0	186.2	17.3 ± 0.1	9.04 ± 0.03	75, 84
	34	29463.23	36779.0	43807.0	213.4	14.8 ± 0.1	3.65 ± 0.02	
2014 - 2015	13	9691.91	15413.0	34258.0	95.0	12.7 ± 0.2	7.49 ± 0.04	84
	13	8377.83	10635.0	13516.0	111.4	11.0 ± 0.1	2.96 ± 0.03	
2015 - 2016	29	23678.95	35478.0	70653.0	156.9	13.9 ± 0.1	6.93 ± 0.03	84
	29	20295.9	25108.0	28815.0	179.2	11.94 ± 0.09	2.83 ± 0.02	

2016 - 2017	20	14314.39	21635.0	43836.0	121.0	12.0 ± 0.1	6.12 ± 0.03	84
	20	11886.61	14836.0	17661.0	135.6	10.0 ± 0.1	2.47 ± 0.02	
2017 - 2018	64	50098.43	73598.0	140716.0	232.6	13.12 ± 0.07	6.13 ± 0.02	75, 84
	64	41524.4	51677.0	60794.0	254.3	10.87 ± 0.06	2.65 ± 0.01	

Table A.2: Results of test configuration analysis with the application of ONN (blue) and AP cleaning methods (black): live-time in hours, N_s : number of source events, N_{ON} : number of events in ON region, N_{OFF} : number of events in OFF region, S : significance of detection, gamma-ray rate and background rate. E_{\uparrow} represents the bins in which the ONN analysis reconstruct events which are absent from the spectrum generated by AP. Rows in blue represent the configuration in ranges o elevation, rows in green, the configuration in noise levels (in units of MHz) and rows in grey, the configuration in observing season.

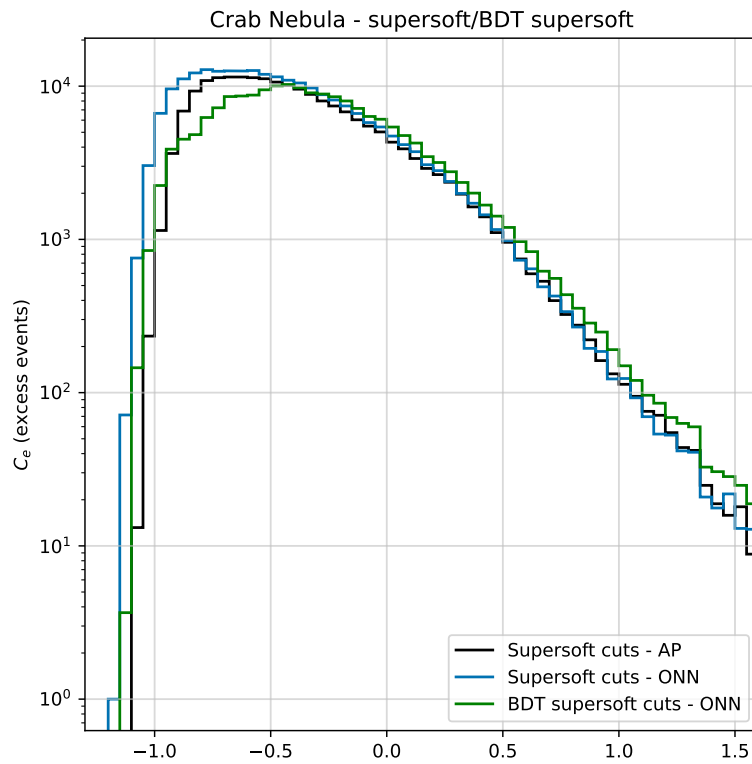


Figure A.1: Spectrum of reconstructed source events from the Crab Nebula with *supersoft* box cuts and *supersoft* cuts derived with BDTs [Krause et al., 2017]. Blue histogram: Counts reconstructed with the ONN cleaning and *supersoft* box cuts. Green histogram: Counts reconstructed with the ONN cleaning and *supersoft* BDT cuts. Black histogram: Counts reconstructed with the Afterpulsing cleaning and *supersoft* box cuts.

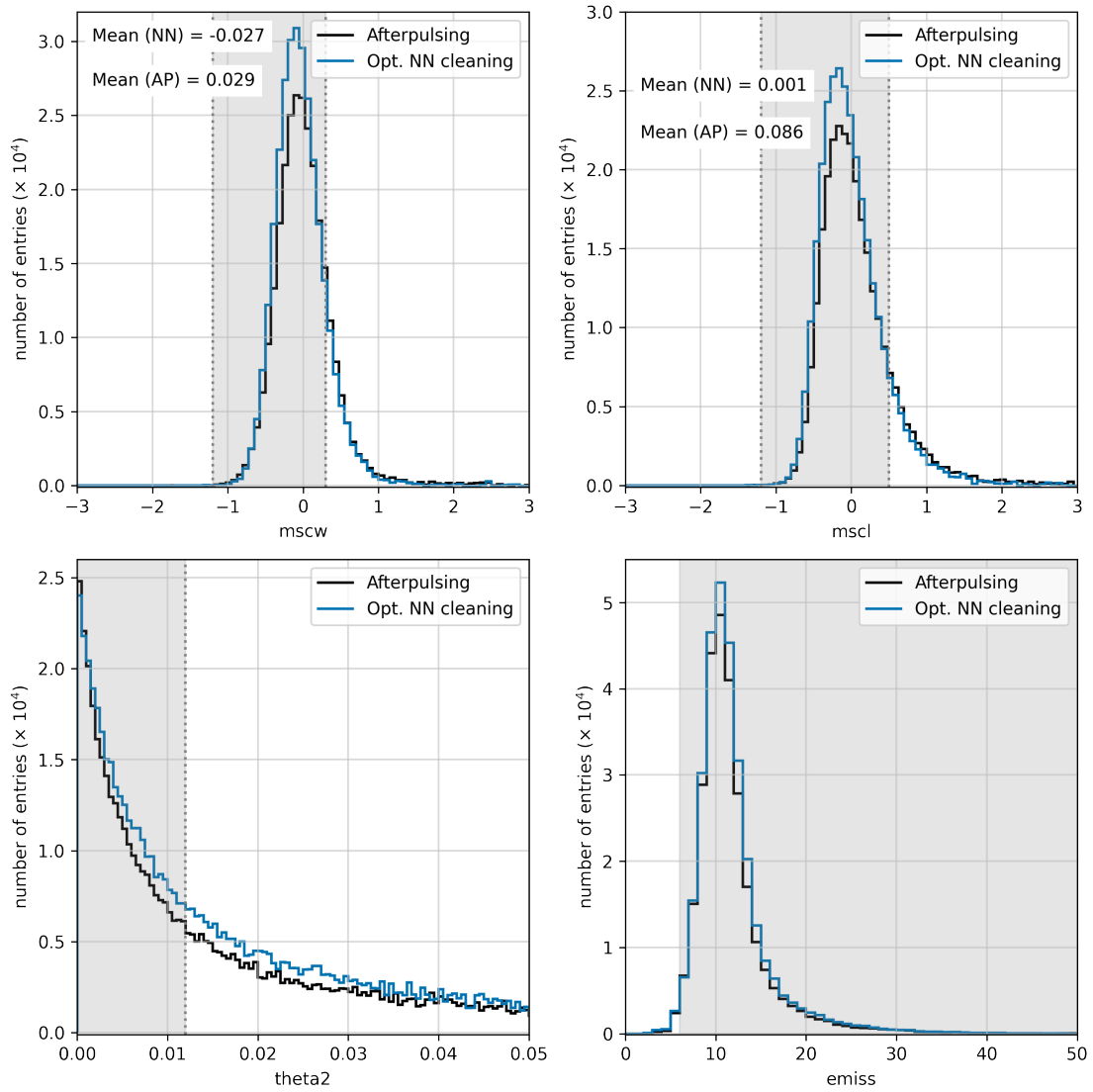


Figure A.2: Stereo parameters for the ONN (blue) and afterpulsing (black) for the full Crab Nebula dataset presented in Figure 4.12: MSCW, MSCL, squared offset from source position (θ^2) (theta2) and emission height (emiss). The super-soft cuts applied are shown in grey.

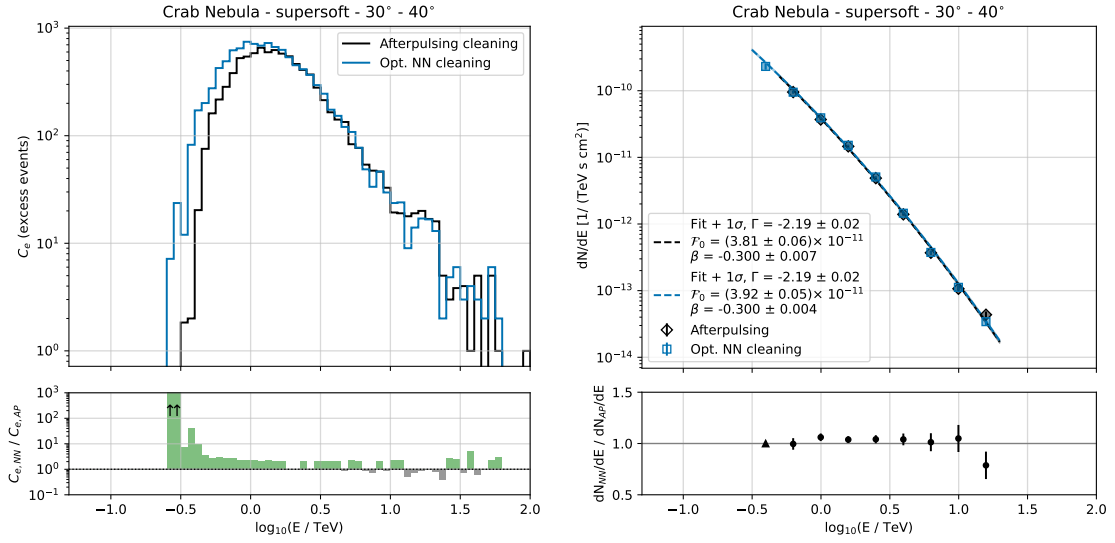


Figure A.3: Left panel: spectrum of reconstructed source events from the Crab Nebula with the ONN (blue) and afterpulsing (black) cleaning methods **for elevation angles higher than 30° and lower than 40°**. The lower left plot shows the ratio of the number of reconstructed events by ONN and AP. Bins for which ONN reconstruct more events than AP are given in green and the opposite in grey. Bins at energies < 1 TeV for which there are no reconstructed events for AP but ONN reconstructs at least ten source events are marked with the upper black arrows. Right panel: spectrum of the Crab Nebula and fit (+ 1 σ) of the data points with a log-parabola function for ONN (blue) and AP (black). \mathcal{F}_0 is given in units of $\text{cm}^{-2} \text{s}^{-1} \text{TeV}^{-1}$. Spextrum points are shown for > 10 source events and for a significance of at least 5 σ . The lower right panel shows the ratio of the reconstructed spectra.

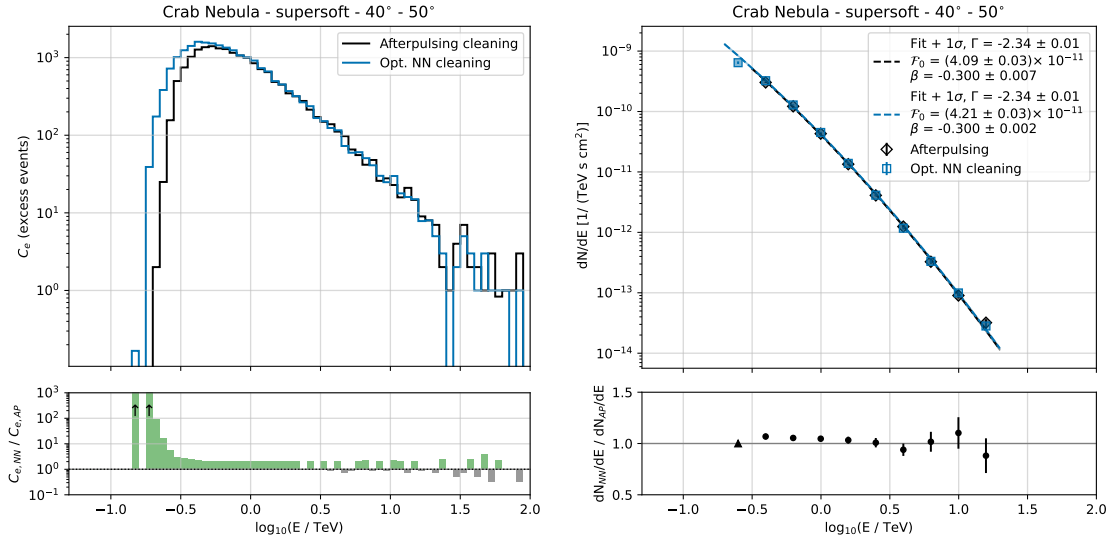


Figure A.4: Left panel: spectrum of reconstructed source events from the Crab Nebula with the ONN (blue) and afterpulsing (black) cleaning methods **for elevation angles higher than 40° and lower than 50°**. The lower left plot shows the ratio of the number of reconstructed events by ONN and AP. Bins for which ONN reconstruct more events than AP are given in green and the opposite in grey. Bins at energies < 1 TeV for which there are no reconstructed events for AP but ONN reconstructs at least ten source events are marked with the upper black arrows. Right panel: spectrum of the Crab Nebula and fit (+ 1 σ) of the data points with a log-parabola function for ONN (blue) and AP (black). \mathcal{F}_0 is given in units of $\text{cm}^{-2} \text{s}^{-1} \text{TeV}^{-1}$. Spextrum points are shown for > 10 source events and for a significance of at least 5 σ . The lower right panel shows the ratio of the reconstructed spectra.

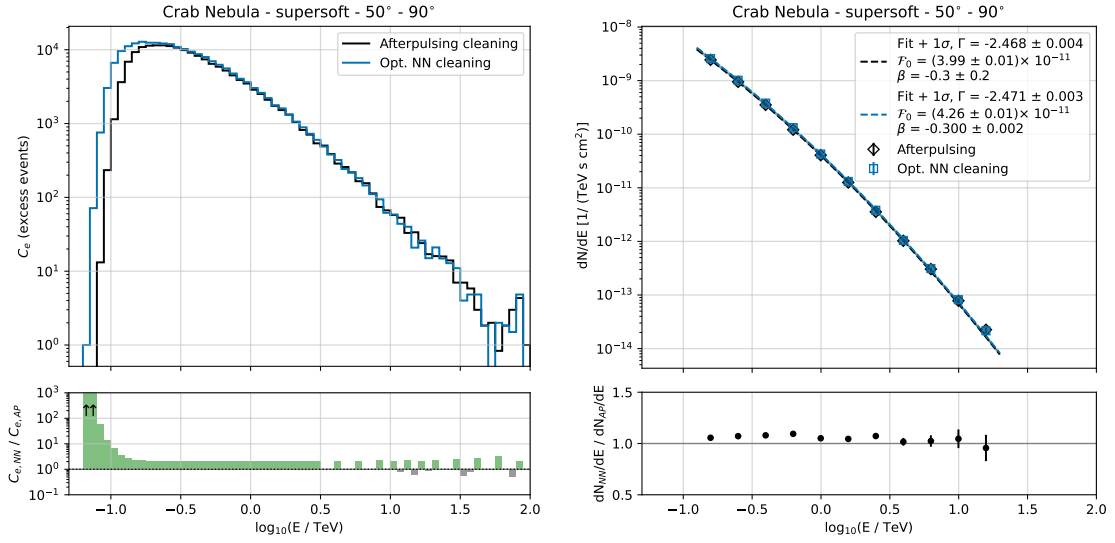


Figure A.5: Left panel: spectrum of reconstructed source events from the Crab Nebula with the ONN (blue) and afterpulsing (black) cleaning methods **for elevation angles higher than 50° and lower than 90°** . The lower left plot shows the ratio of the number of reconstructed events by ONN and AP. Bins for which ONN reconstruct more events than AP are given in green and the opposite in grey. Bins at energies < 1 TeV for which there are no reconstructed events for AP but ONN reconstructs at least ten source events are marked with the upper black arrows. Right panel: spectrum of the Crab Nebula and fit ($+ 1\sigma$) of the data points with a log-parabola function for ONN (blue) and AP (black). \mathcal{F}_0 is given in units of $\text{cm}^{-2} \text{s}^{-1} \text{TeV}^{-1}$. Spextrum points are shown for > 10 source events and for a significance of at least 5σ . The lower right panel shows the ratio of the reconstructed spectra.

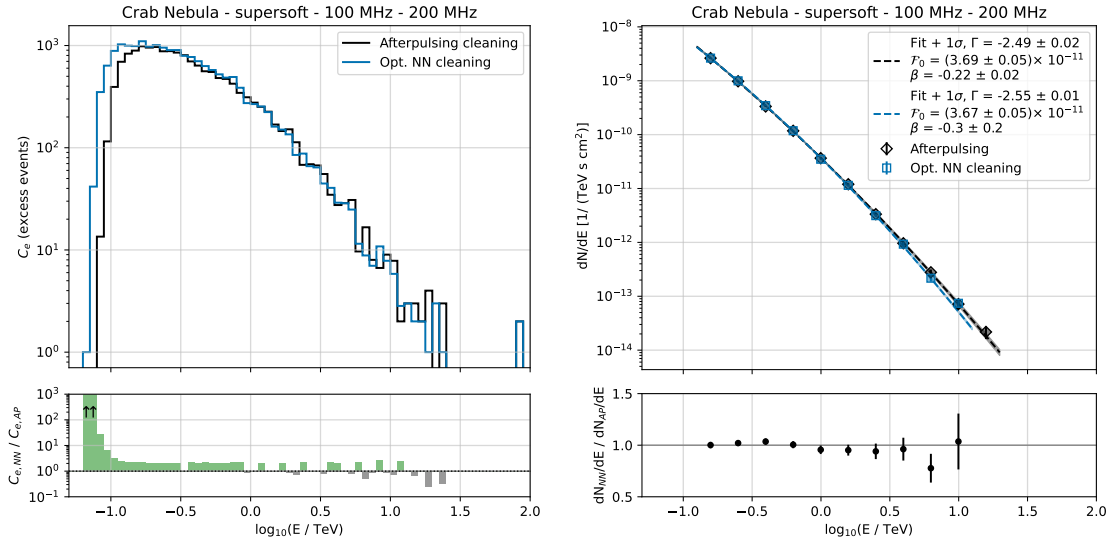


Figure A.6: Left panel: spectrum of reconstructed source events from the Crab Nebula with the ONN (blue) and afterpulsing (black) cleaning methods **for noise levels higher than 100 MHz and lower than 200 MHz**. The lower left plot shows the ratio of the number of reconstructed events by ONN and AP. Bins for which ONN reconstruct more events than AP are given in green and the opposite in grey. Bins at energies < 1 TeV for which there are no reconstructed events for AP but ONN reconstructs at least ten source events are marked with the upper black arrows. Right panel: spectrum of the Crab Nebula and fit ($+ 1\sigma$) of the data points with a log-parabola function for ONN (blue) and AP (black). \mathcal{F}_0 is given in units of $\text{cm}^{-2} \text{s}^{-1} \text{TeV}^{-1}$. Spextrum points are shown for > 10 source events and for a significance of at least 5σ . The lower right panel shows the ratio of the reconstructed spectra.

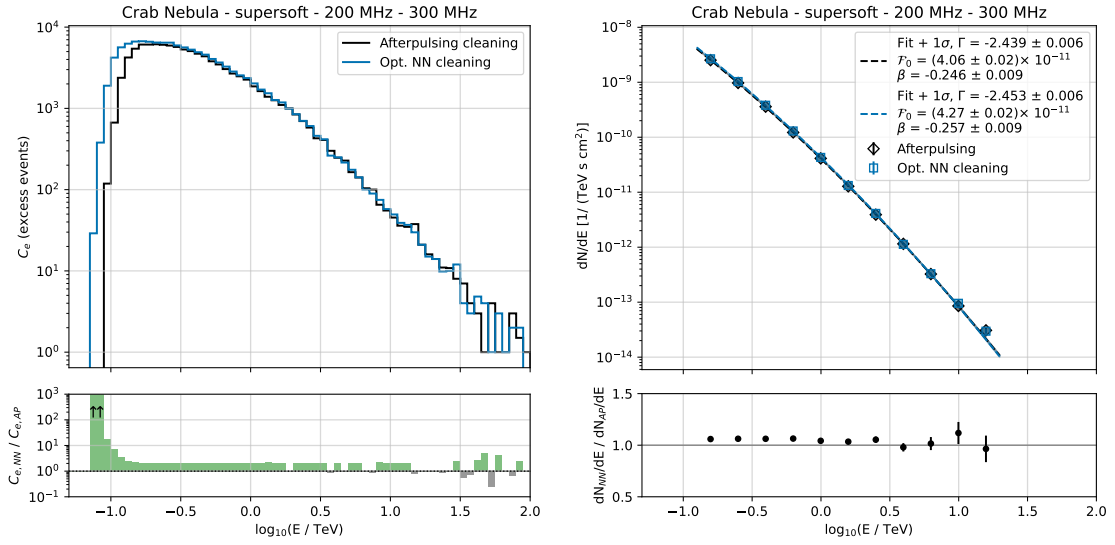


Figure A.7: Left panel: spectrum of reconstructed source events from the Crab Nebula with the ONN (blue) and afterpulsing (black) cleaning methods **for noise levels higher than 200 MHz and lower than 300 MHz**. The lower left plot shows the ratio of the number of reconstructed events by ONN and AP. Bins for which ONN reconstruct more events than AP are given in green and the opposite in grey. Bins at energies < 1 TeV for which there are no reconstructed events for AP but ONN reconstructs at least ten source events are marked with the upper black arrows. Right panel: spectrum of the Crab Nebula and fit ($+ 1\sigma$) of the data points with a log-parabola function for ONN (blue) and AP (black). \mathcal{F}_0 is given in units of $\text{cm}^{-2} \text{s}^{-1} \text{TeV}^{-1}$. Spextrum points are shown for > 10 source events and for a significance of at least 5σ . The lower right panel shows the ratio of the reconstructed spectra.

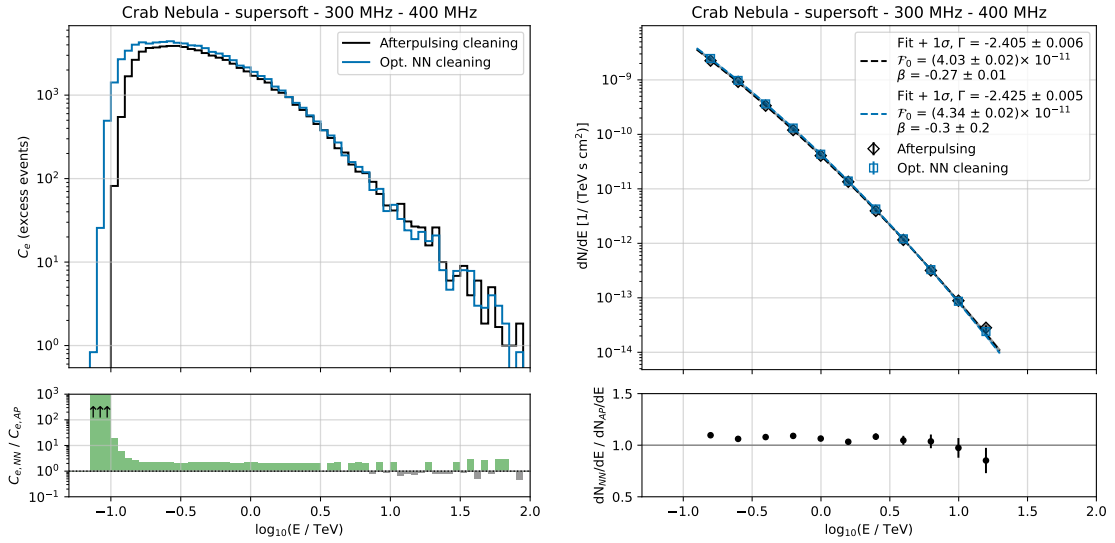


Figure A.8: Left panel: spectrum of reconstructed source events from the Crab Nebula with the ONN (blue) and afterpulsing (black) cleaning methods **for noise levels higher than 300 MHz and lower than 400 MHz**. The lower left plot shows the ratio of the number of reconstructed events by ONN and AP. Bins for which ONN reconstruct more events than AP are given in green and the opposite in grey. Bins at energies < 1 TeV for which there are no reconstructed events for AP but ONN reconstructs at least ten source events are marked with the upper black arrows. Right panel: spectrum of the Crab Nebula and fit ($+ 1\sigma$) of the data points with a log-parabola function for ONN (blue) and AP (black). \mathcal{F}_0 is given in units of $\text{cm}^{-2} \text{s}^{-1} \text{TeV}^{-1}$. Spextrum points are shown for > 10 source events and for a significance of at least 5σ . The lower right panel shows the ratio of the reconstructed spectra.

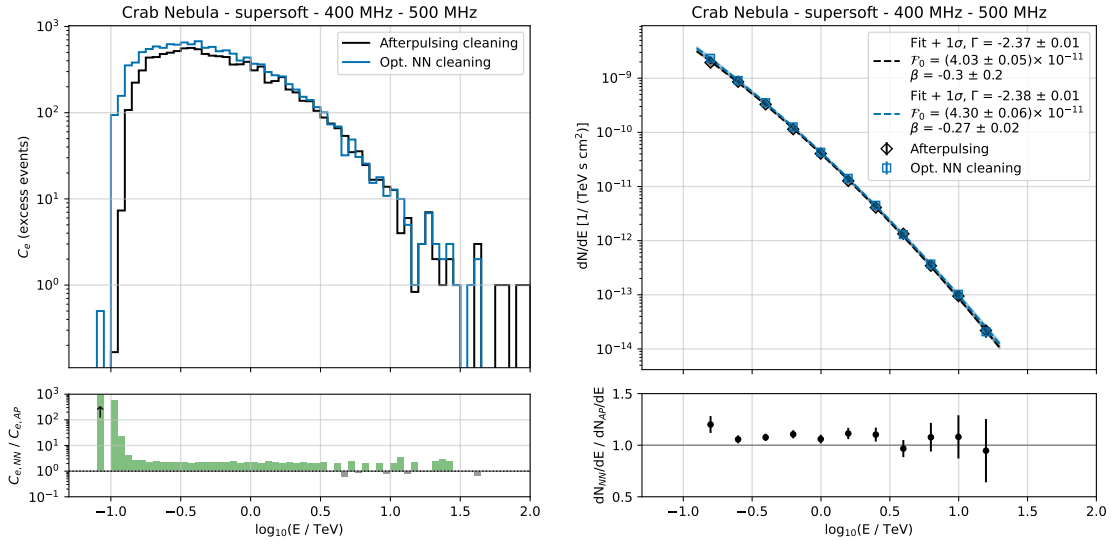


Figure A.9: Left panel: spectrum of reconstructed source events from the Crab Nebula with the ONN (blue) and afterpulsing (black) cleaning methods **for noise levels higher than 400 MHz and lower than 500 MHz**. The lower left plot shows the ratio of the number of reconstructed events by ONN and AP. Bins for which ONN reconstruct more events than AP are given in green and the opposite in grey. Bins at energies < 1 TeV for which there are no reconstructed events for AP but ONN reconstructs at least ten source events are marked with the upper black arrows. Right panel: spectrum of the Crab Nebula and fit ($+ 1\sigma$) of the data points with a log-parabola function for ONN (blue) and AP (black). \mathcal{F}_0 is given in units of $\text{cm}^{-2} \text{s}^{-1} \text{TeV}^{-1}$. Spextrum points are shown for > 10 source events and for a significance of at least 5σ . The lower right panel shows the ratio of the reconstructed spectra.

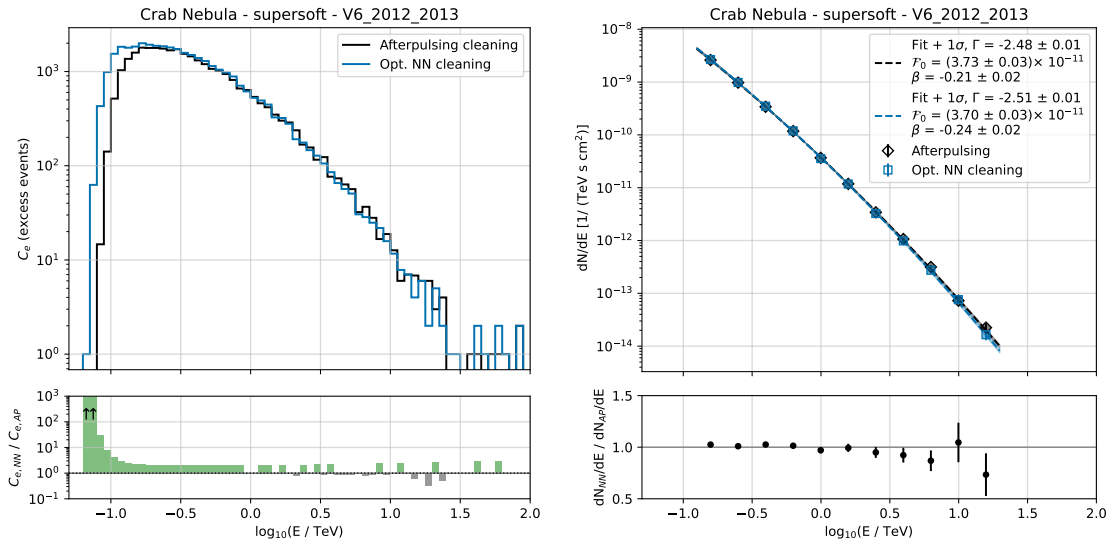


Figure A.10: Left panel: spectrum of reconstructed source events from the Crab Nebula with the ONN (blue) and afterpulsing (black) cleaning methods **for the 2012 - 2013 observing season**. The lower left plot shows the ratio of the number of reconstructed events by ONN and AP. Bins for which ONN reconstruct more events than AP are given in green and the opposite in grey. Bins at energies < 1 TeV for which there are no reconstructed events for AP but ONN reconstructs at least ten source events are marked with the upper black arrows. Right panel: spectrum of the Crab Nebula and fit (+ 1σ) of the data points with a log-parabola function for ONN (blue) and AP (black). \mathcal{F}_0 is given in units of $\text{cm}^{-2} \text{s}^{-1} \text{TeV}^{-1}$. Spextrum points are shown for > 10 source events and for a significance of at least 5σ . The lower right panel shows the ratio of the reconstructed spectra.

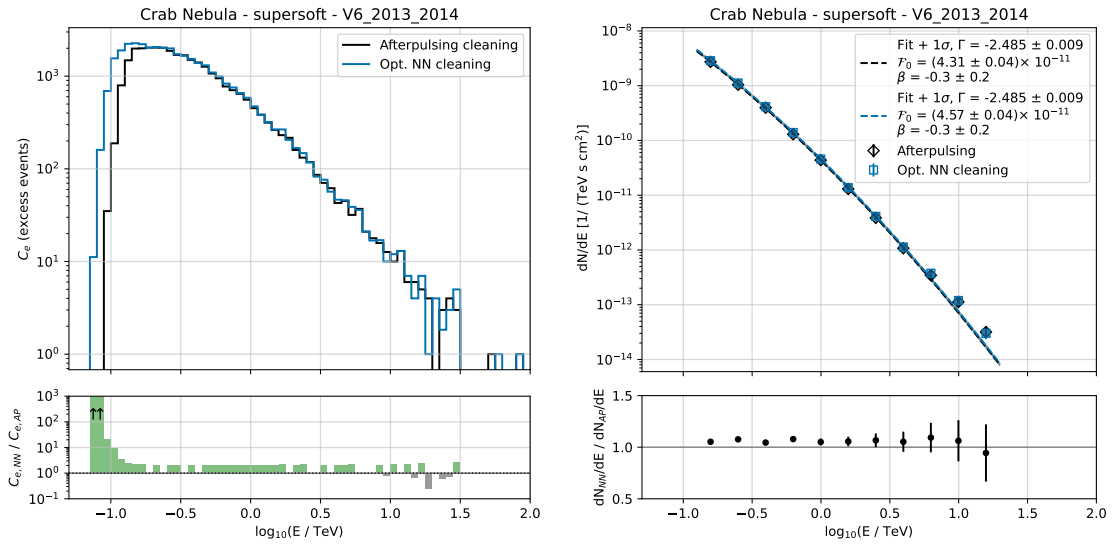


Figure A.11: Left panel: spectrum of reconstructed source events from the Crab Nebula with the ONN (blue) and afterpulsing (black) cleaning methods **for the 2013 - 2014 observing season**. The lower left plot shows the ratio of the number of reconstructed events by ONN and AP. Bins for which ONN reconstruct more events than AP are given in green and the opposite in grey. Bins at energies < 1 TeV for which there are no reconstructed events for AP but ONN reconstructs at least ten source events are marked with the upper black arrows. Right panel: spectrum of the Crab Nebula and fit ($+ 1\sigma$) of the data points with a log-parabola function for ONN (blue) and AP (black). \mathcal{F}_0 is given in units of $\text{cm}^{-2} \text{s}^{-1} \text{TeV}^{-1}$. Spextrum points are shown for > 10 source events and for a significance of at least 5σ . The lower right panel shows the ratio of the reconstructed spectra.

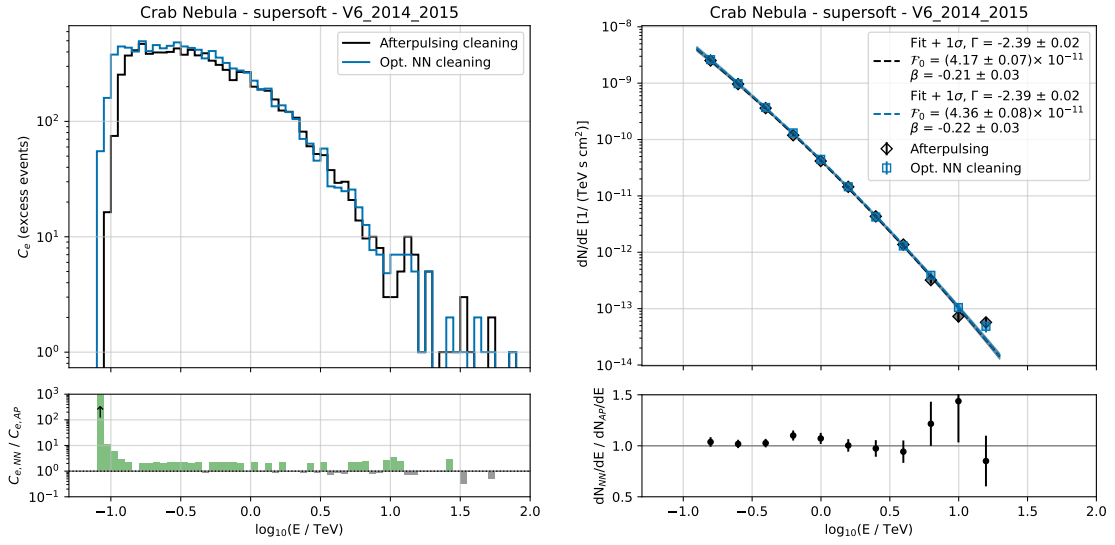


Figure A.12: Left panel: spectrum of reconstructed source events from the Crab Nebula with the ONN (blue) and afterpulsing (black) cleaning methods **for the 2014 - 2015 observing season**. The lower left plot shows the ratio of the number of reconstructed events by ONN and AP. Bins for which ONN reconstruct more events than AP are given in green and the opposite in grey. Bins at energies < 1 TeV for which there are no reconstructed events for AP but ONN reconstructs at least ten source events are marked with the upper black arrows. Right panel: spectrum of the Crab Nebula and fit ($+ 1\sigma$) of the data points with a log-parabola function for ONN (blue) and AP (black). \mathcal{F}_0 is given in units of $\text{cm}^{-2} \text{s}^{-1} \text{TeV}^{-1}$. Spextrum points are shown for > 10 source events and for a significance of at least 5σ . The lower right panel shows the ratio of the reconstructed spectra.

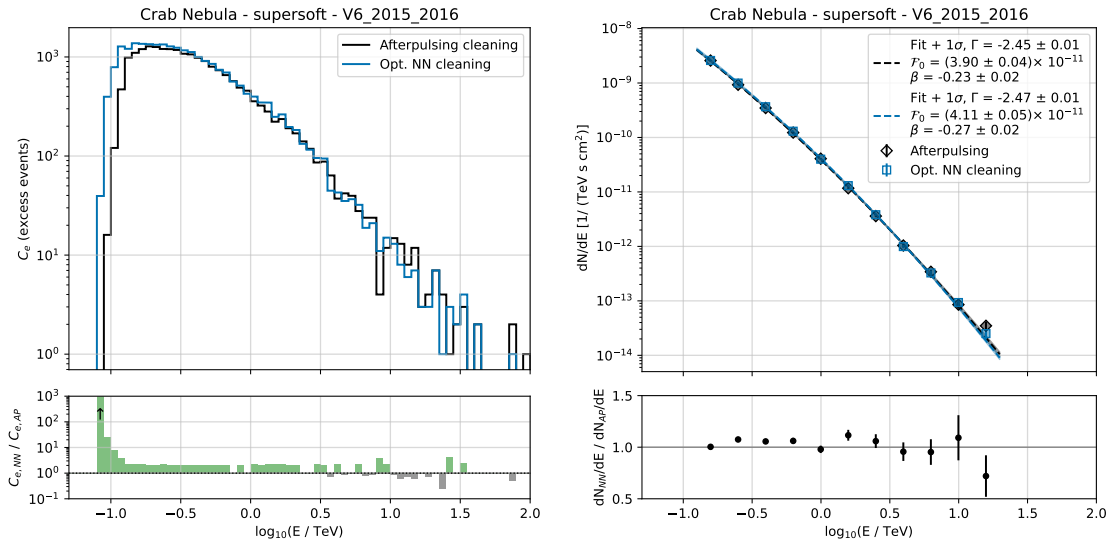


Figure A.13: Left panel: spectrum of reconstructed source events from the Crab Nebula with the ONN (blue) and afterpulsing (black) cleaning methods **for the 2015 - 2016 observing season**. The lower left plot shows the ratio of the number of reconstructed events by ONN and AP. Bins for which ONN reconstruct more events than AP are given in green and the opposite in grey. Bins at energies < 1 TeV for which there are no reconstructed events for AP but ONN reconstructs at least ten source events are marked with the upper black arrows. Right panel: spectrum of the Crab Nebula and fit ($+ 1\sigma$) of the data points with a log-parabola function for ONN (blue) and AP (black). \mathcal{F}_0 is given in units of $\text{cm}^{-2} \text{s}^{-1} \text{TeV}^{-1}$. Spextrum points are shown for > 10 source events and for a significance of at least 5σ . The lower right panel shows the ratio of the reconstructed spectra.

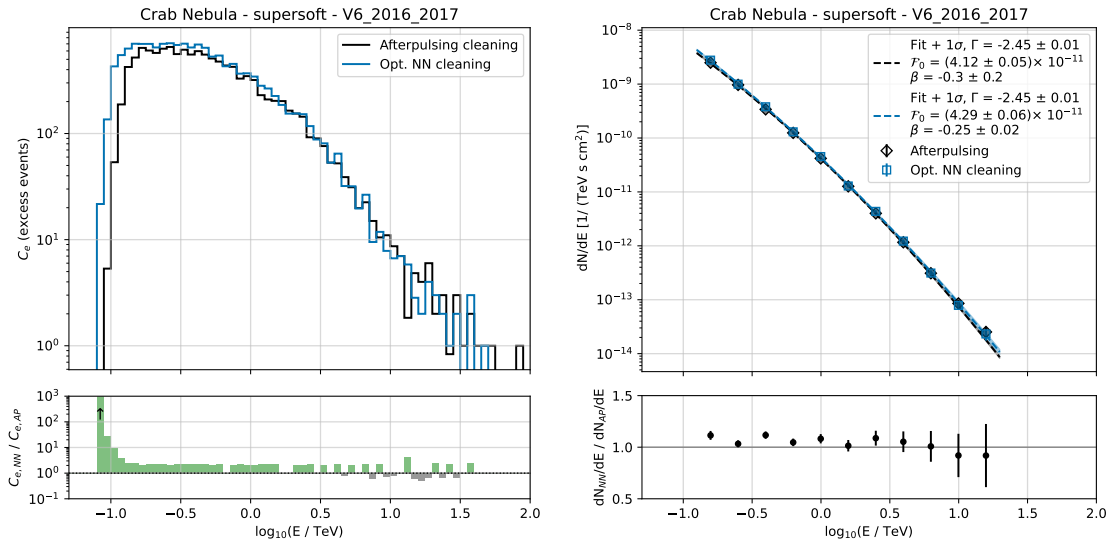


Figure A.14: Left panel: spectrum of reconstructed source events from the Crab Nebula with the ONN (blue) and afterpulsing (black) cleaning methods **for the 2016 - 2017 observing season**. The lower left plot shows the ratio of the number of reconstructed events by ONN and AP. Bins for which ONN reconstruct more events than AP are given in green and the opposite in grey. Bins at energies < 1 TeV for which there are no reconstructed events for AP but ONN reconstructs at least ten source events are marked with the upper black arrows. Right panel: spectrum of the Crab Nebula and fit ($+ 1\sigma$) of the data points with a log-parabola function for ONN (blue) and AP (black). \mathcal{F}_0 is given in units of $\text{cm}^{-2} \text{s}^{-1} \text{TeV}^{-1}$. Spextrum points are shown for > 10 source events and for a significance of at least 5σ . The lower right panel shows the ratio of the reconstructed spectra.

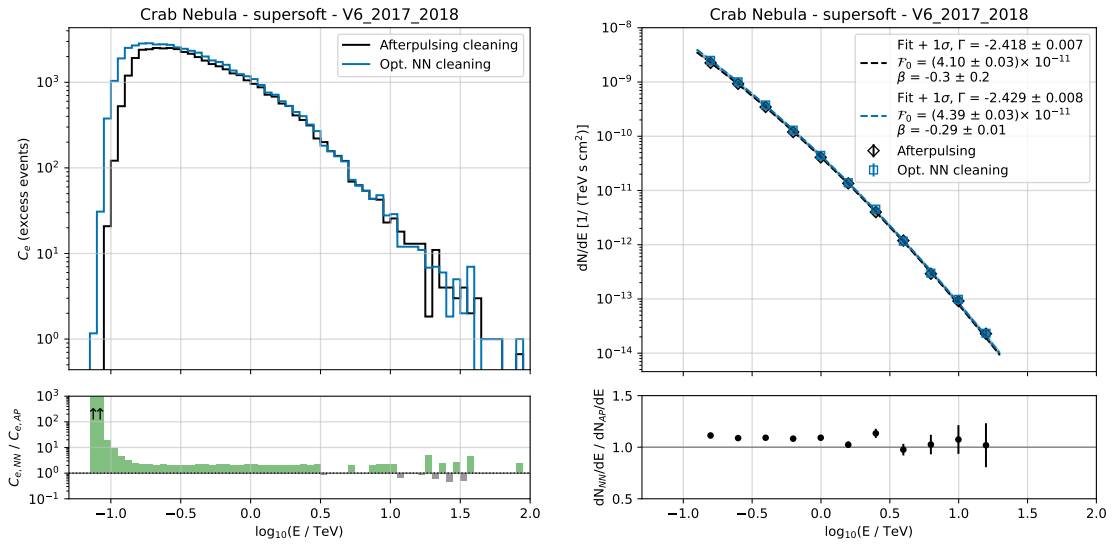


Figure A.15: Left panel: spectrum of reconstructed source events from the Crab Nebula with the ONN (blue) and afterpulsing (black) cleaning methods **for the 2017 - 2018 observing season**. The lower left plot shows the ratio of the number of reconstructed events by ONN and AP. Bins for which ONN reconstruct more events than AP are given in green and the opposite in grey. Bins at energies < 1 TeV for which there are no reconstructed events for AP but ONN reconstructs at least ten source events are marked with the upper black arrows. Right panel: spectrum of the Crab Nebula and fit ($+ 1\sigma$) of the data points with a log-parabola function for ONN (blue) and AP (black). \mathcal{F}_0 is given in units of $\text{cm}^{-2} \text{s}^{-1} \text{TeV}^{-1}$. Spextrum points are shown for > 10 source events and for a significance of at least 5σ . The lower right panel shows the ratio of the reconstructed spectra.

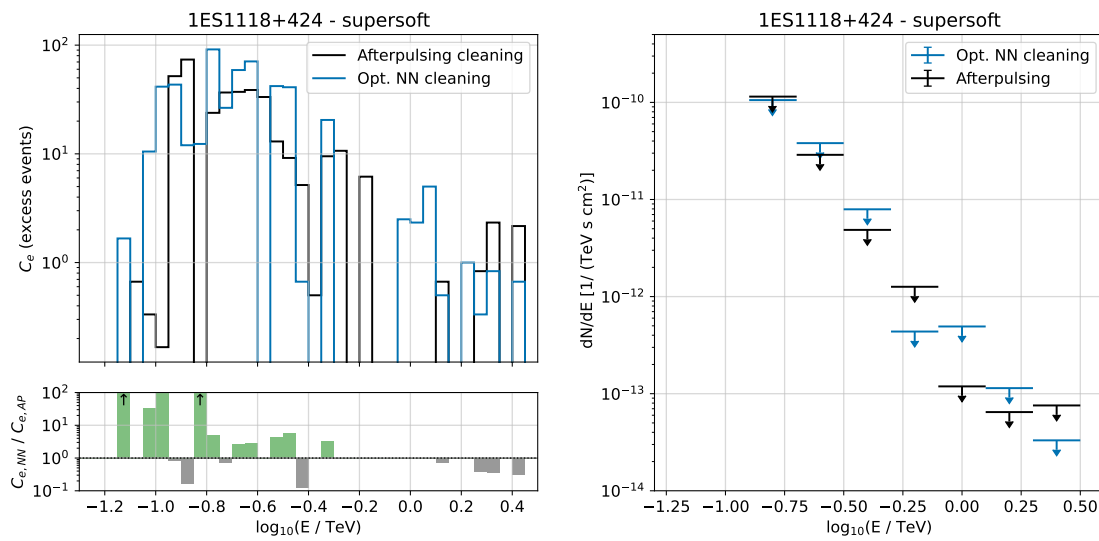


Figure A.16: Left panel: spectrum of reconstructed source events from **1ES 1118+424** with the ONN (blue) and afterpulsing (black) cleaning methods. The lower left plot shows the ratio of the number of reconstructed events by ONN and AP. Bins for which ONN reconstruct more events than AP are given in green and the opposite in grey. Bins at energies < 1 TeV for which there are no reconstructed events for AP but ONN reconstructs at least ten source events are marked with the upper black arrows. Right panel: upper limits (95% C. L., above 100 GeV) of 1ES 1118+424.

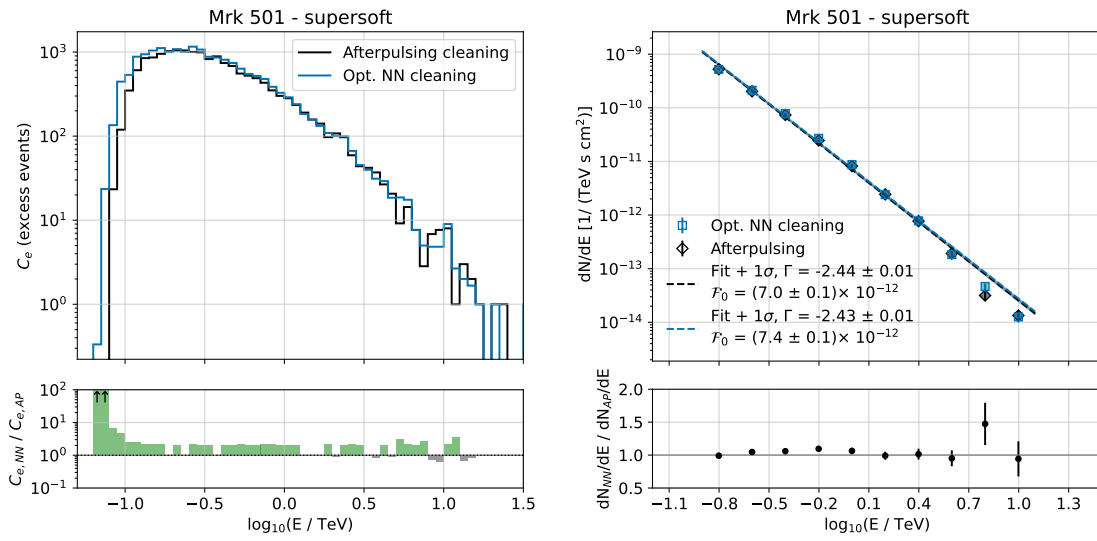


Figure A.17: Left panel: spectrum of reconstructed source events for **Markarian 501** with the ONN (blue) and afterpulsing (black) cleaning methods. The lower left plot shows the ratio of the number of reconstructed events by ONN and AP. Bins for which ONN reconstruct more events than AP are given in green and the opposite in grey. Bins at energies < 1 TeV for which there are no reconstructed events for AP but ONN reconstructs at least ten source events are marked with the upper black arrows. Right panel: spectrum of Markarian 501 and fit of data points with a power-law for ONN (blue) and AP (black). The lower right panel shows the ratio of the reconstructed spectrum at a specific energy between ONN and AP. The source counts spectra and the estimated fluxes are given after super-soft box cuts for the gamma/hadron separation.

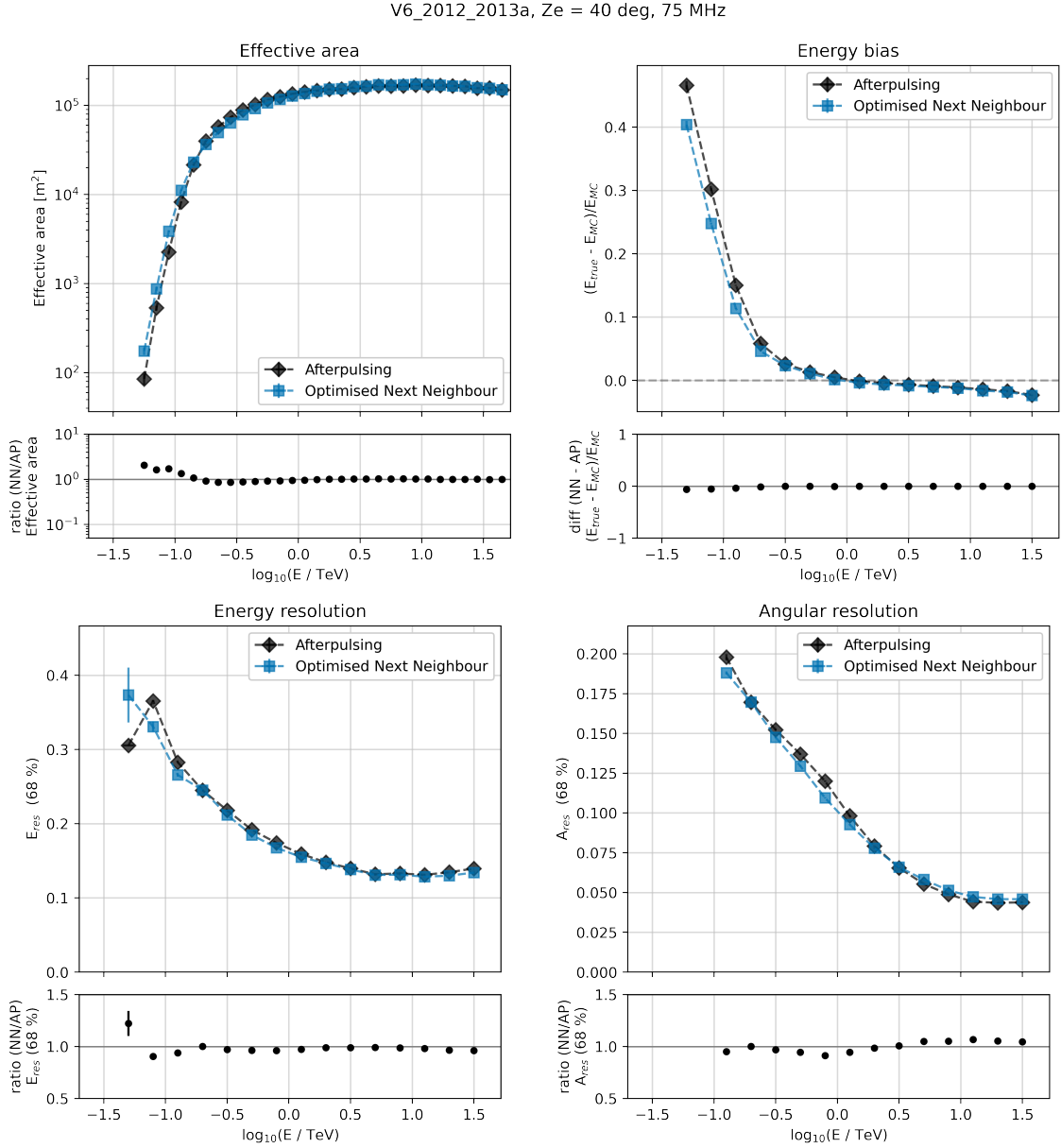


Figure A.18: Set of IRFs for the **2012-2013 observing season, with super-soft cuts, at zenith = 40 degrees and noise level = 75 MHz** for the ONN (blue squares) and afterpulsing (black diamonds): upper left: effective area, upper right: energy bias, lower left: energy resolution and lower right: angular resolution.

V6_2012_2013a, Ze = 40 deg, 400 MHz

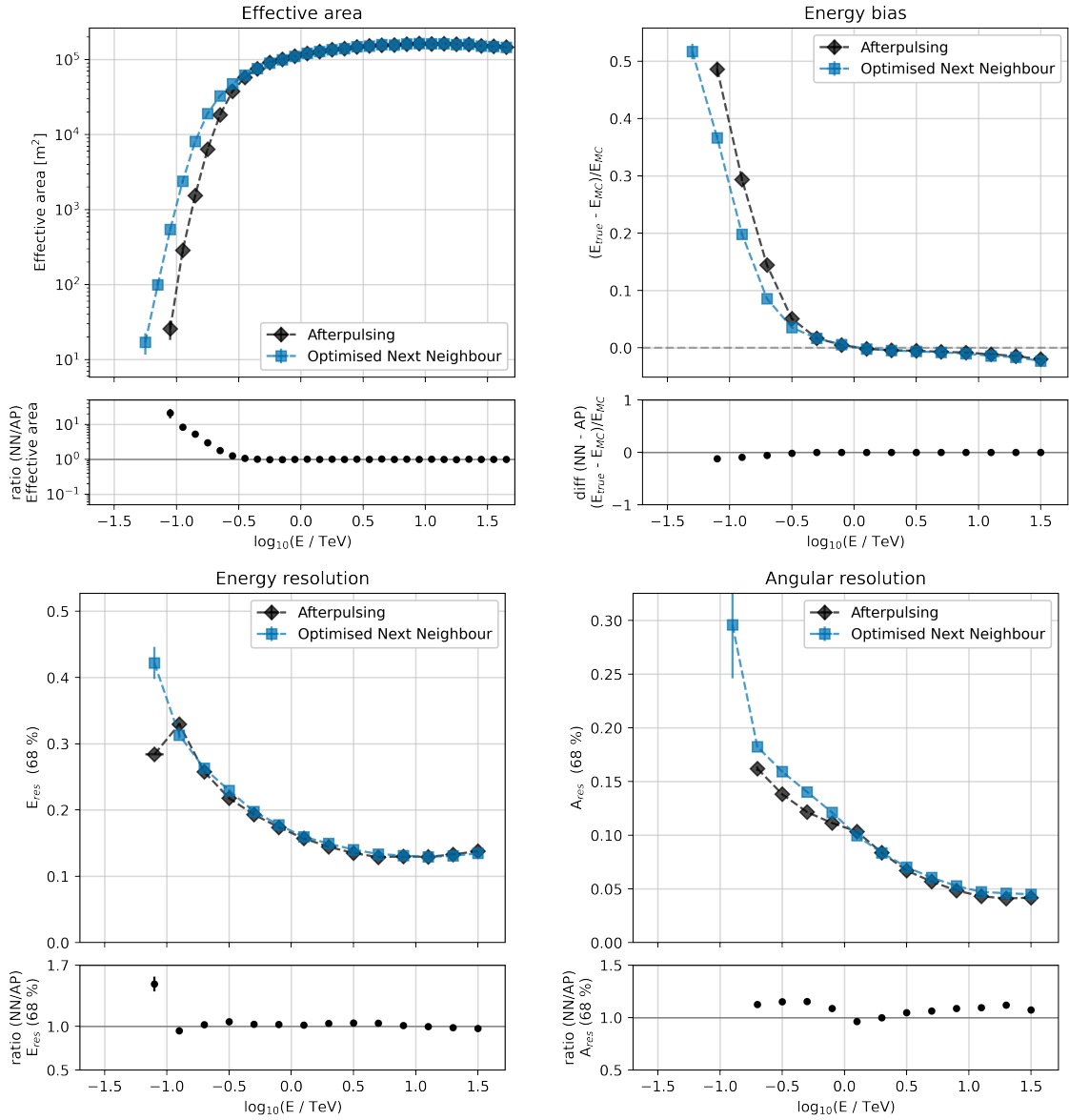


Figure A.19: Set of IRFs for the **2012-2013 observing season, with super-soft cuts, at zenith = 40 degrees and noise level = 400 MHz** for the ONN (blue squares) and afterpulsing (black diamonds): upper left: effective area, upper right: energy bias, lower left: energy resolution and lower right: angular resolution.

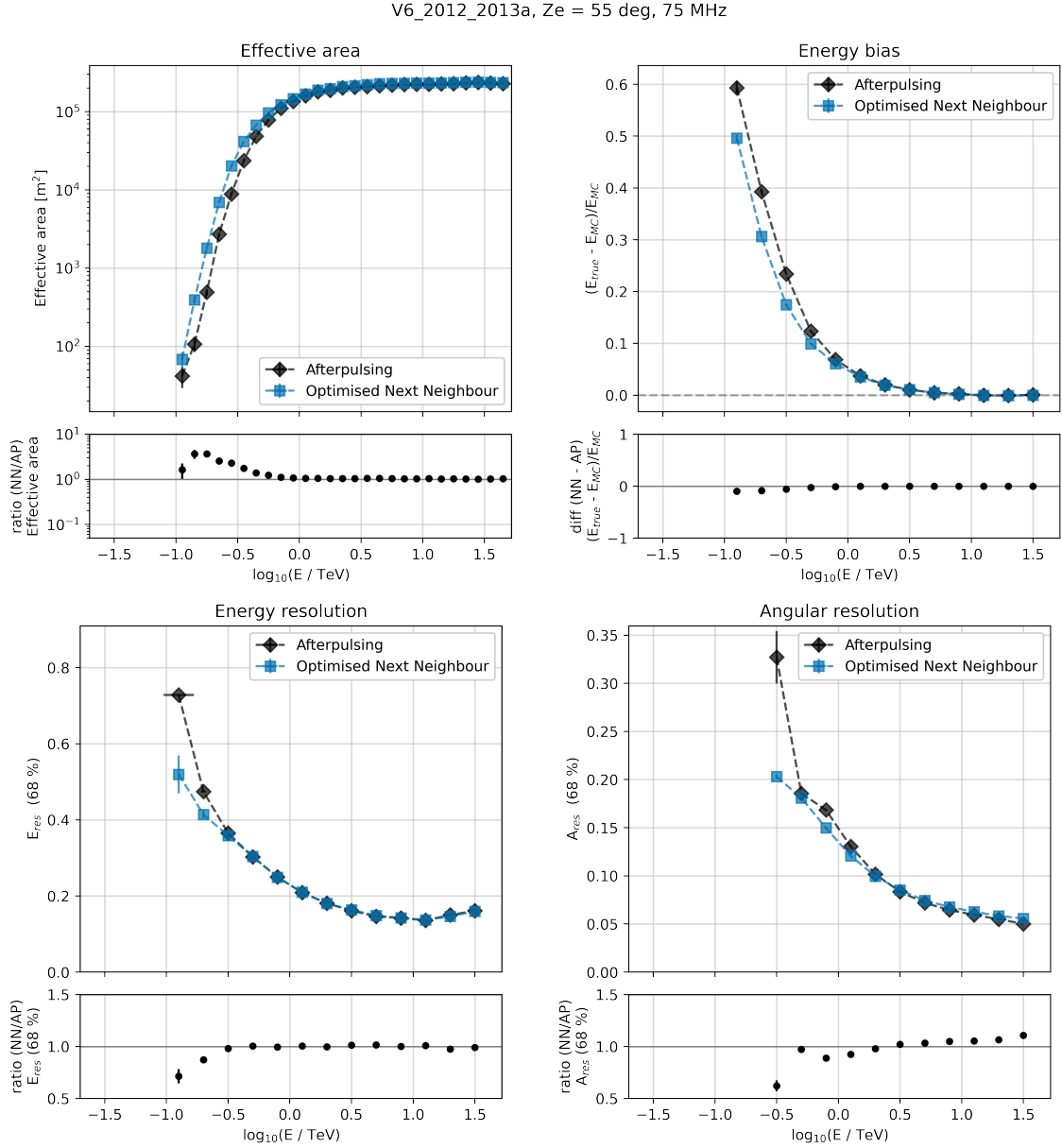


Figure A.20: Set of IRFs for the **2012-2013 observing season, with super-soft cuts, at zenith = 55 degrees and noise level = 75 MHz** for the ONN (blue squares) and afterpulsing (black diamonds): upper left: effective area, upper right: energy bias, lower left: energy resolution and lower right: angular resolution.

V6_2012_2013a, Ze = 55 deg, 200 MHz

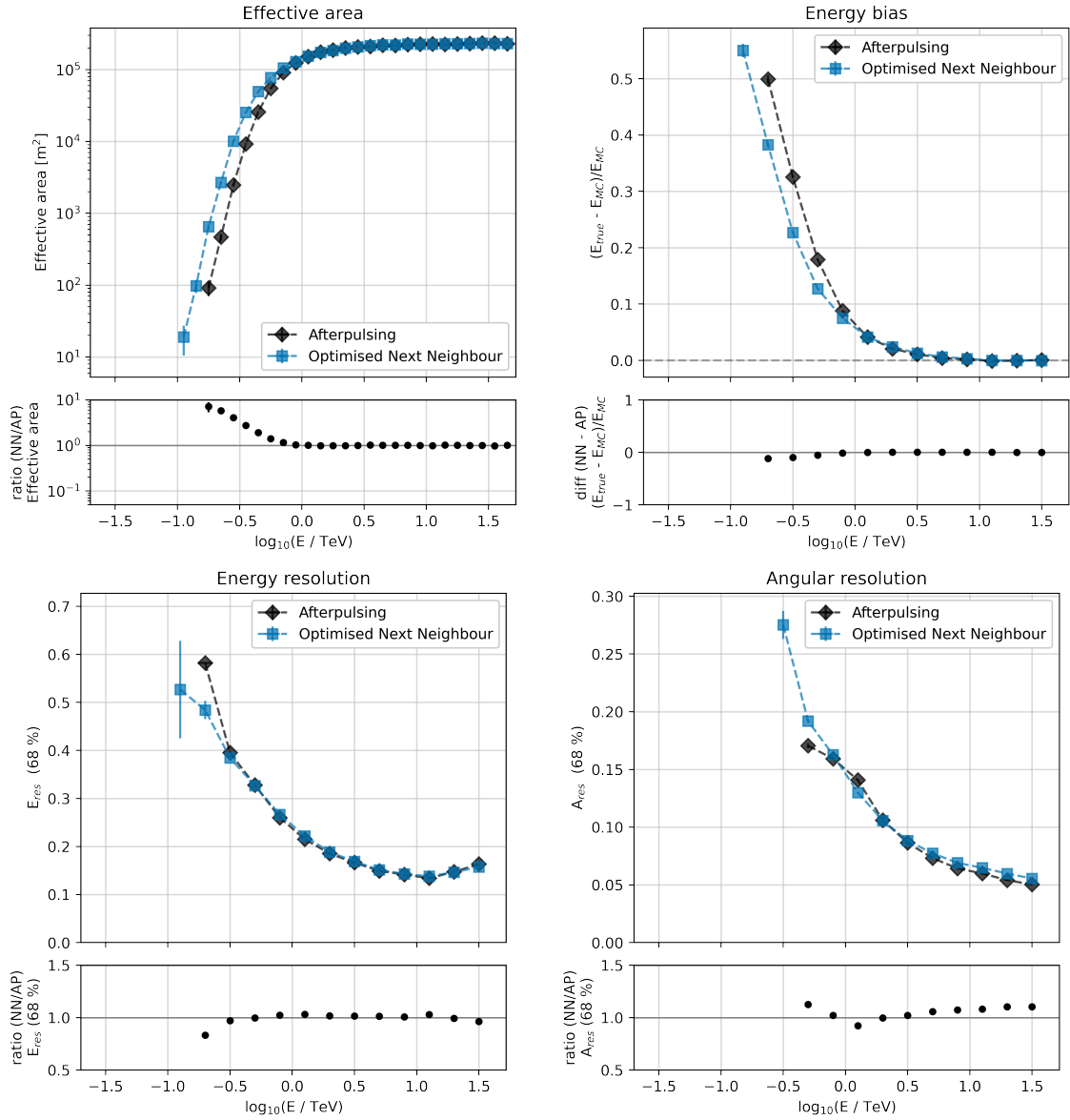


Figure A.21: Set of IRFs for the **2012-2013 observing season, with super-soft cuts, at zenith = 55 degrees and noise level = 200 MHz** for the ONN (blue squares) and afterpulsing (black diamonds): upper left: effective area, upper right: energy bias, lower left: energy resolution and lower right: angular resolution.

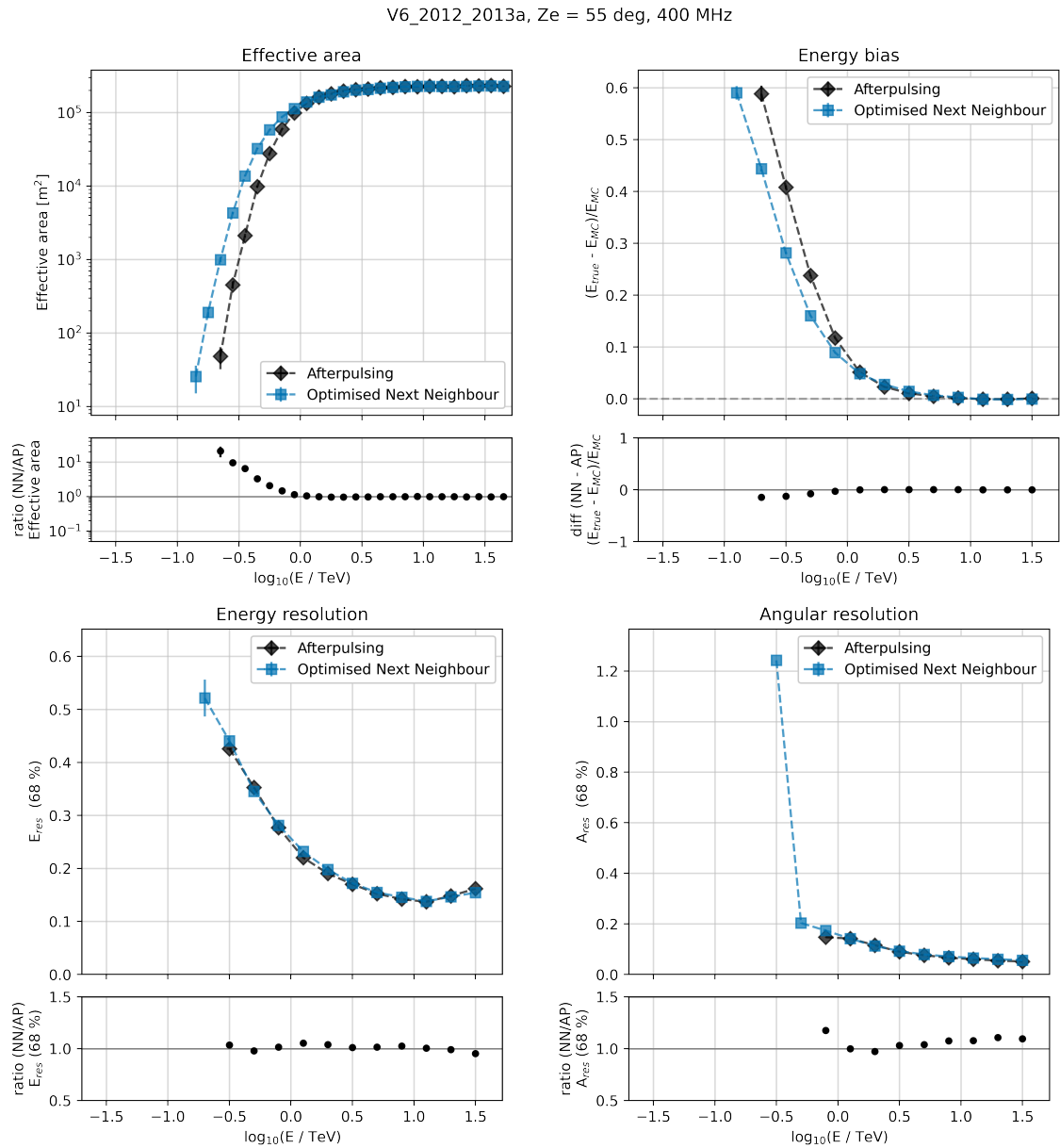


Figure A.22: Set of IRFs for the **2012-2013 observing season, with super-soft cuts, at zenith = 55 degrees and noise level = 400 MHz** for the ONN (blue squares) and afterpulsing (black diamonds): upper left: effective area, upper right: energy bias, lower left: energy resolution and lower right: angular resolution.

V6_2017_2018, Ze = 40 deg, 200 MHz

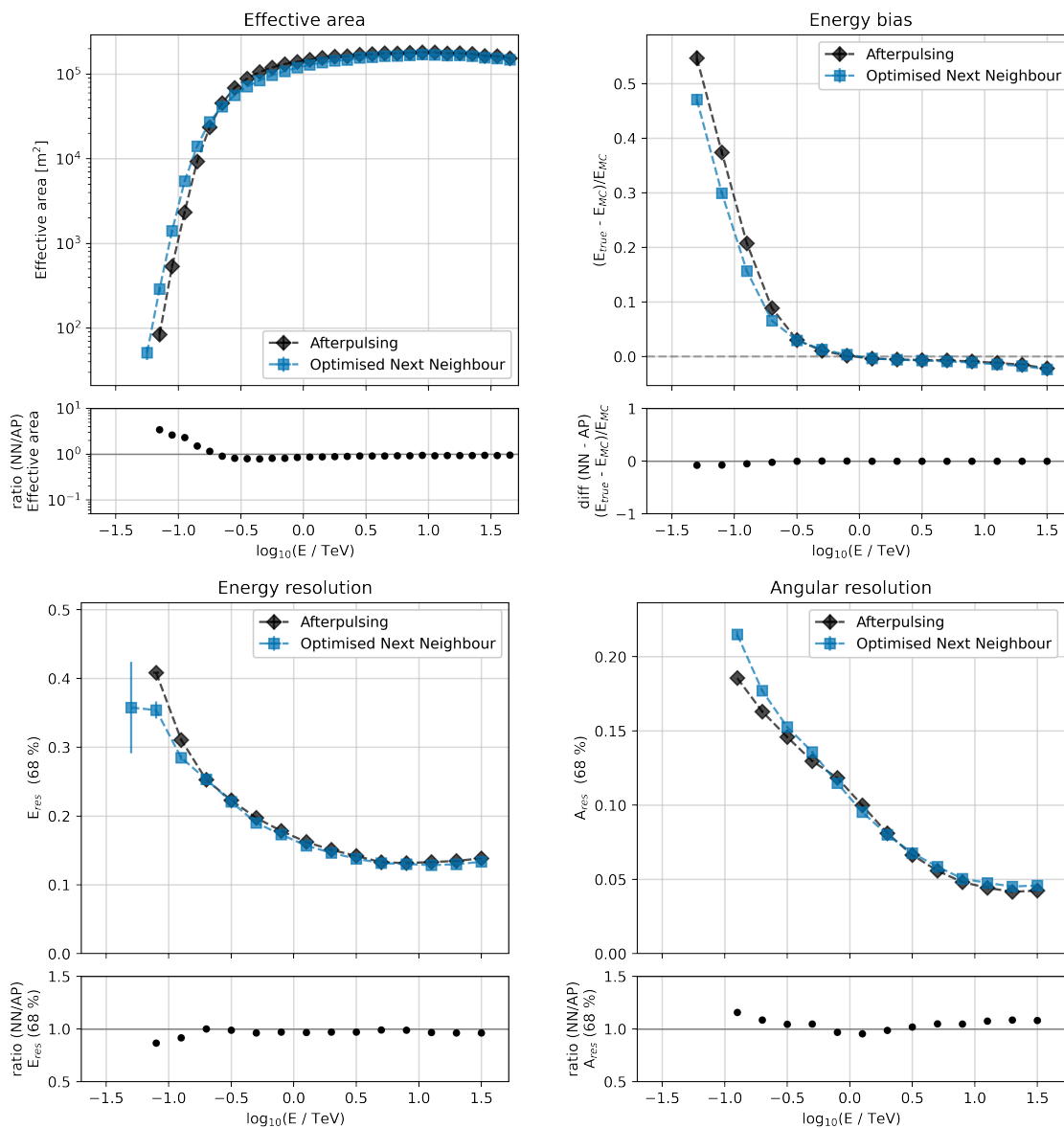


Figure A.23: Set of IRFs for the **2017-2018 observing season, with super-soft cuts, at zenith = 55 degrees and noise level = 200 MHz** for the ONN (blue squares) and afterpulsing (black diamonds): upper left: effective area, upper right: energy bias, lower left: energy resolution and lower right: angular resolution.

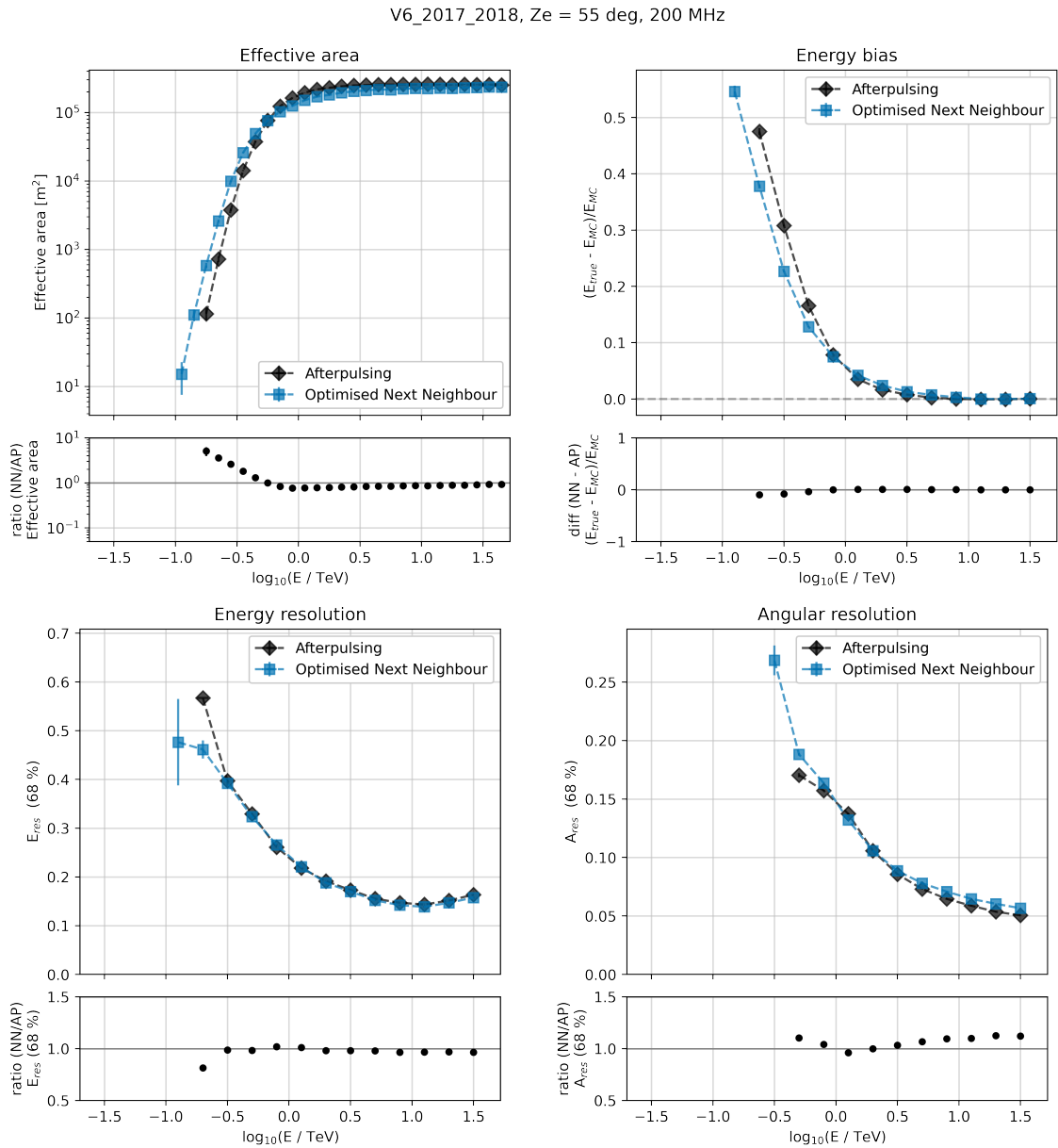


Figure A.24: Set of IRFs for the **2017-2018 observing season, with super-soft cuts, at zenith = 55 degrees and noise level = 200 MHz** for the ONN (blue squares) and afterpulsing (black diamonds): upper left: effective area, upper right: energy bias, lower left: energy resolution and lower right: angular resolution.

V6_2012_2013a, Ze = 45 deg, 450 MHz

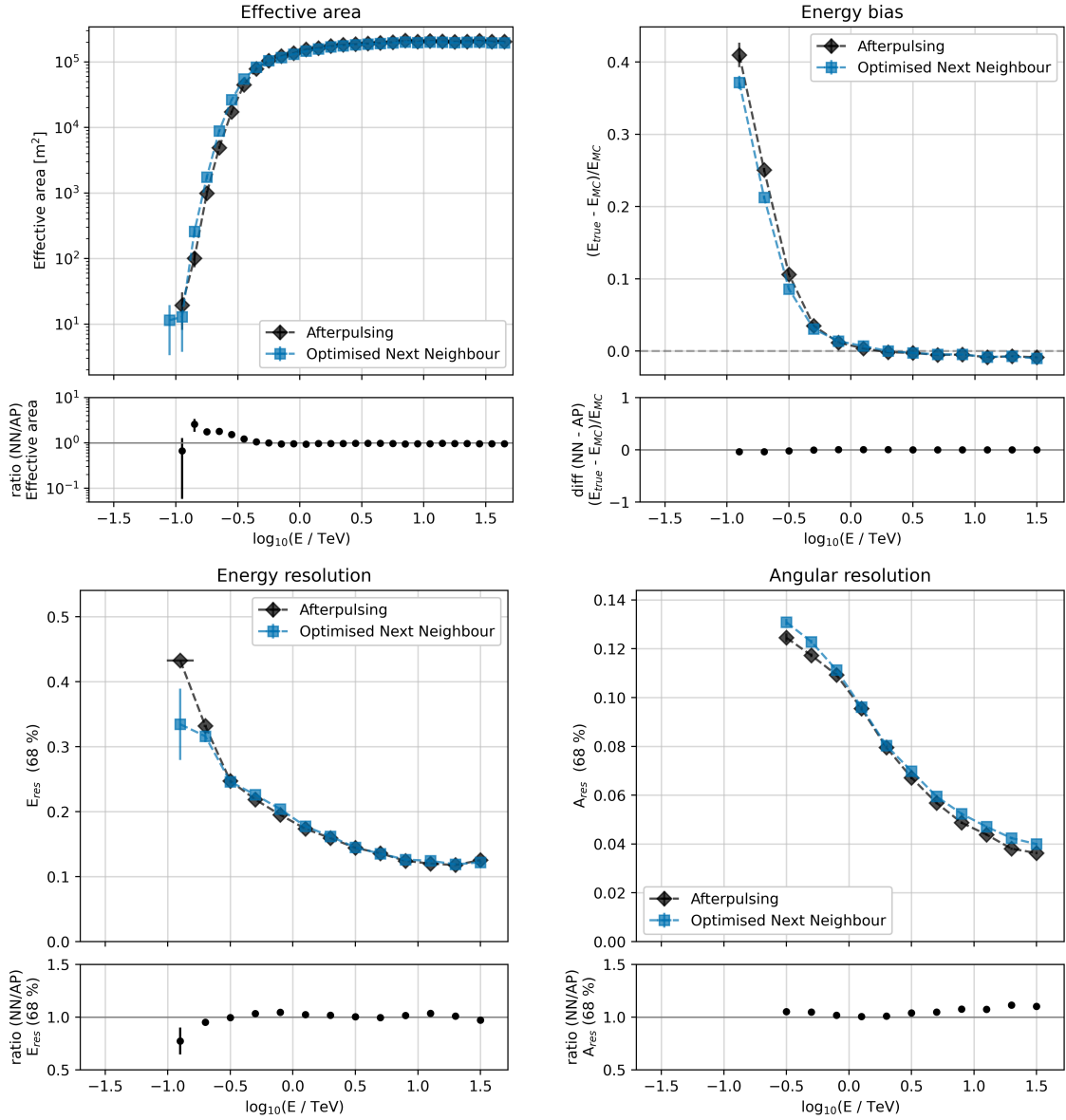


Figure A.25: Set of **Reduced High Voltage IRFs** for the **2012-2013** observing season, at **zenith = 45 degrees** and **noise level = 450 MHz** for the ONN (blue squares) and afterpulsing (black diamonds): upper left: effective area, upper right: energy bias, lower left: energy resolution and lower right: angular resolution.

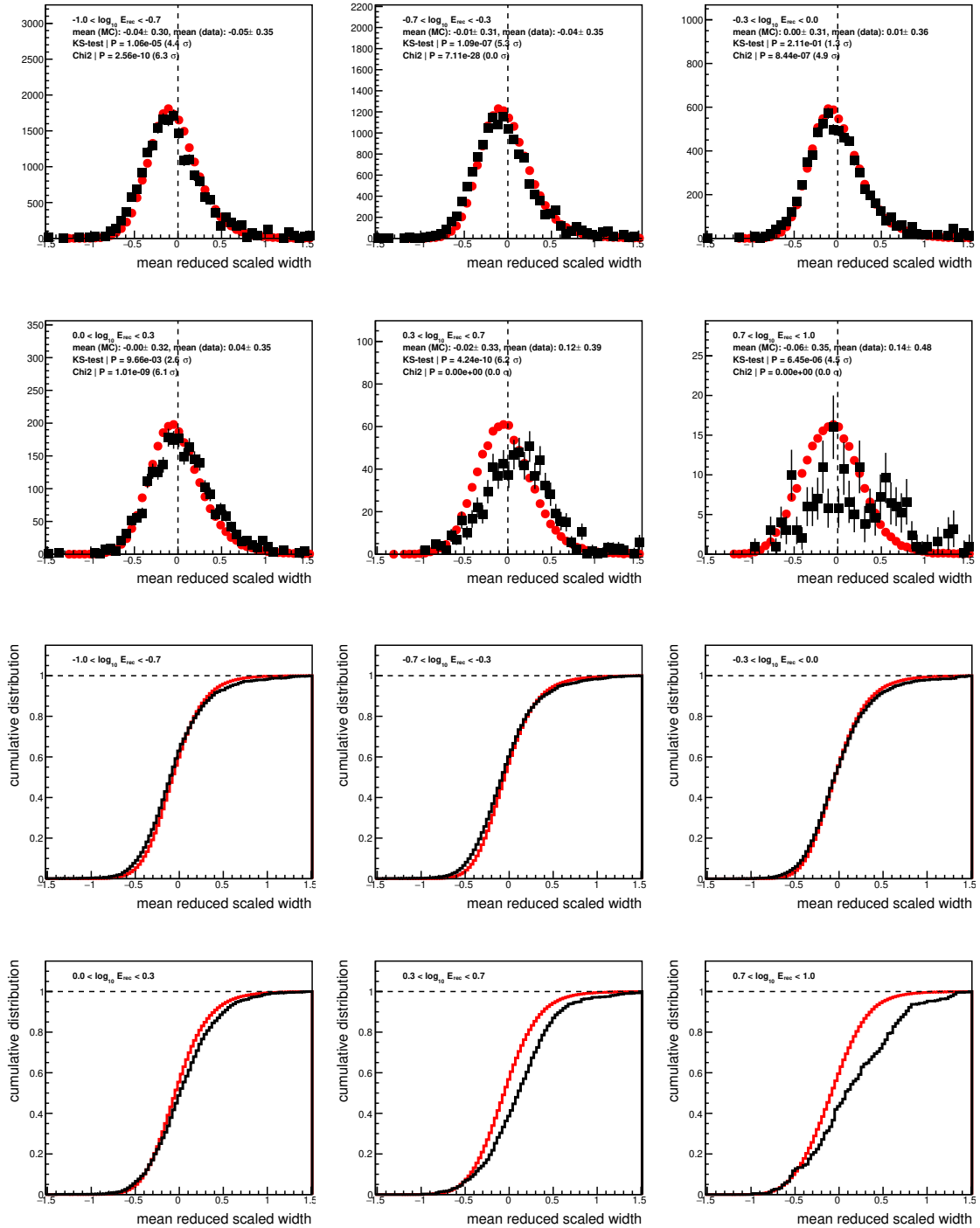


Figure A.26: Top: Distribution of MSCW for a Crab Nebula dataset (black squares) and simulated gamma-rays (red circles) reconstructed with the **Optimised Next Neighbour**. The Crab Nebula dataset consists of events taken in the **2017-2018** observing season with a zenith lower than 25 degrees. Simulated events are produced at a zenith of 20 degrees and a noise level of 200 MHz. The number of events is separated based on the reconstructed energy E_{rec} (in TeV) in the following ranges: $-1.0 < \log_{10}(E_{rec}) < -0.7$, $-0.7 < \log_{10}(E_{rec}) < -0.3$, $-0.3 < \log_{10}(E_{rec}) < -0.0$, $0.0 < \log_{10}(E_{rec}) < 0.3$, $0.3 < \log_{10}(E_{rec}) < 0.7$, $0.7 < \log_{10}(E_{rec}) < 1.0$. Bottom: cumulative distribution of MSCW for each energy range.

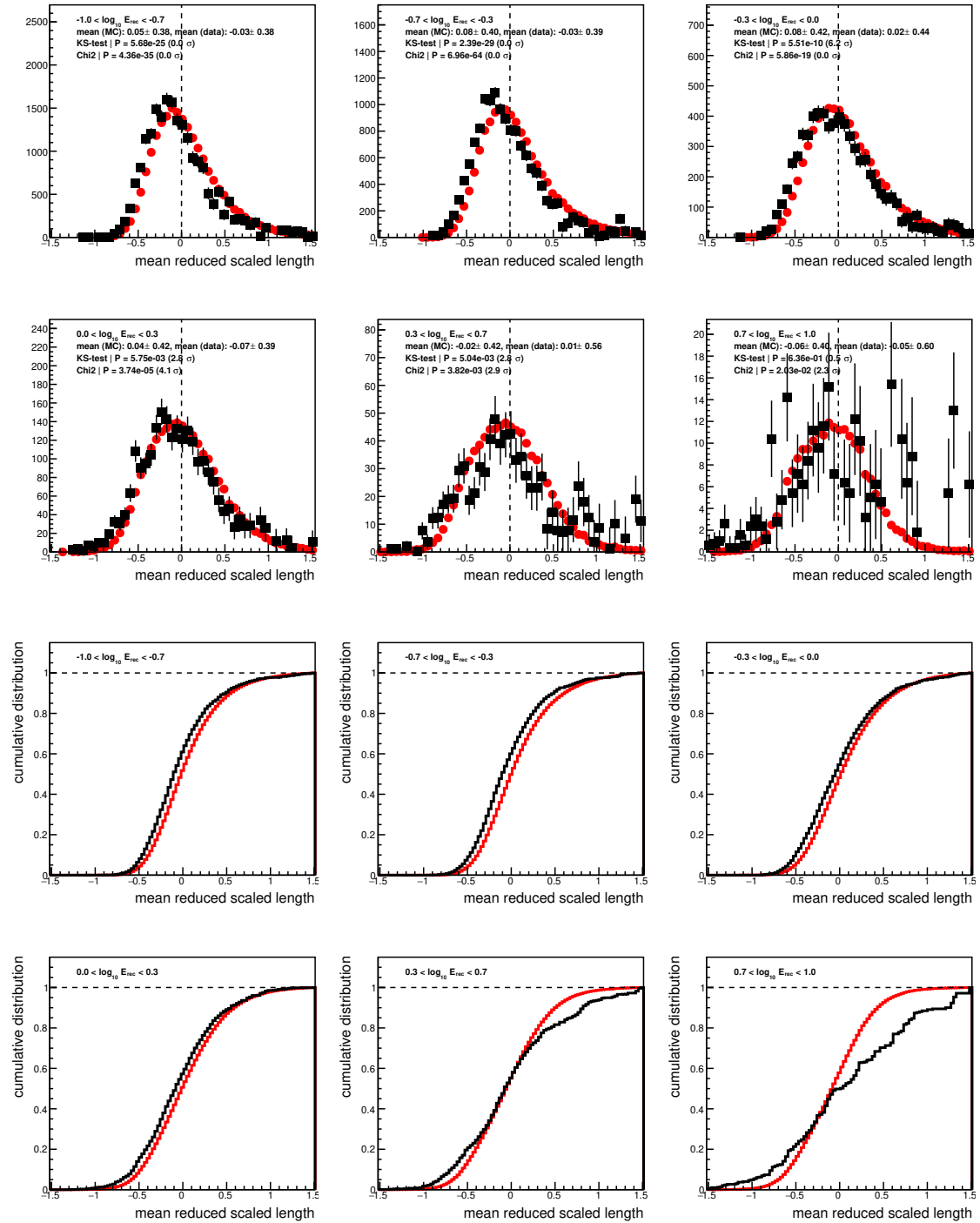


Figure A.27: Top: Distribution of MSCL for a Crab Nebula dataset (black squares) and simulated gamma-rays (red circles) reconstructed with the **Optimised Next Neighbour** image cleaning. The Crab Nebula dataset consists of events taken in the **2017-2018** observing season with a zenith lower than 25 degrees. Simulated events are produced at a zenith of 20 degrees and a noise level of 200 MHz. The number of events is separated based on the reconstructed energy E_{rec} (in TeV) in the following ranges: $-1.0 < \log_{10}(E_{rec}) < -0.7$, $-0.7 < \log_{10}(E_{rec}) < -0.3$, $-0.3 < \log_{10}(E_{rec}) < -0.0$, $0.0 < \log_{10}(E_{rec}) < 0.3$, $0.3 < \log_{10}(E_{rec}) < 0.7$, $0.7 < \log_{10}(E_{rec}) < 1.0$. Bottom: cumulative distribution of MSCL for each energy range.

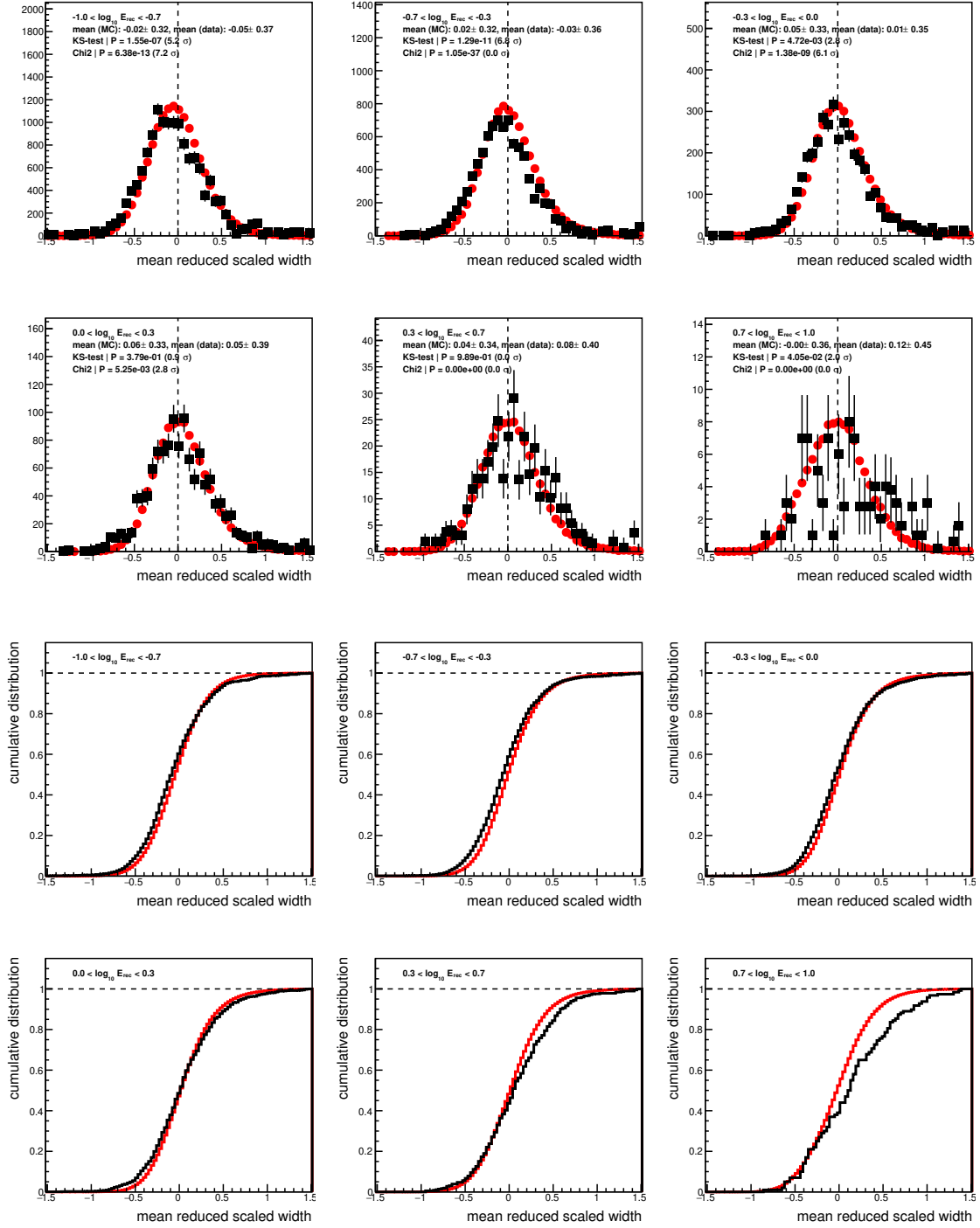


Figure A.28: Top: Distribution of MSCW for a Crab Nebula dataset (black squares) and simulated gamma-rays (red circles) reconstructed with the **afterpulsing** image cleaning. The Crab Nebula dataset consists of events with a zenith lower than 25 degrees. Simulated events are produced at a zenith of 20 degrees and a noise level of 200 MHz. The number of events is separated based on the reconstructed energy E_{rec} (in TeV) in the following ranges: $-1.0 < \log_{10}(E_{rec}) < -0.7$, $-0.7 < \log_{10}(E_{rec}) < -0.3$, $-0.3 < \log_{10}(E_{rec}) < -0.0$, $0.0 < \log_{10}(E_{rec}) < 0.3$, $0.3 < \log_{10}(E_{rec}) < 0.7$, $0.7 < \log_{10}(E_{rec}) < 1.0$. Bottom: cumulative distribution of MSCW for each energy range.

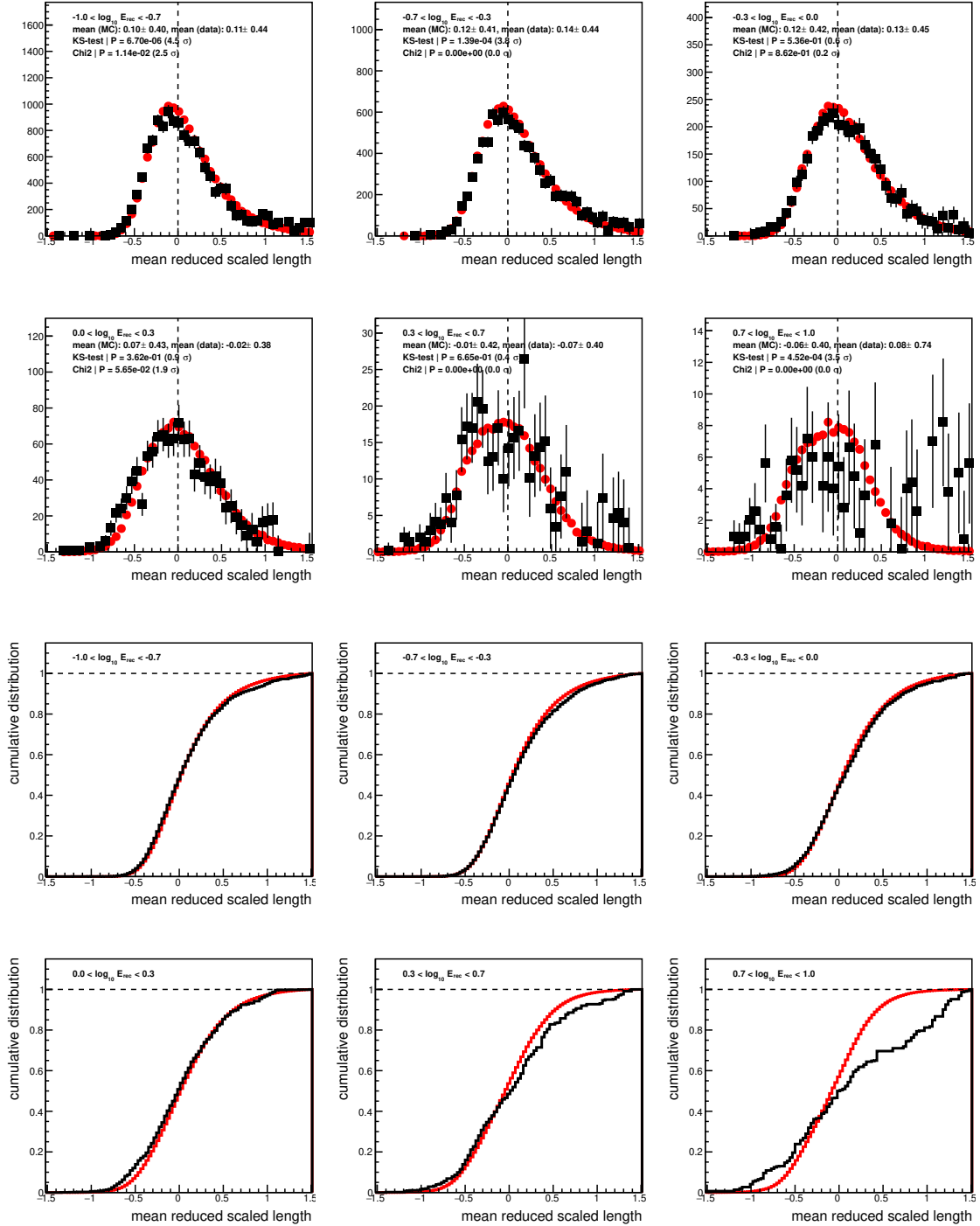


Figure A.29: Top: Distribution of MSLC for a Crab Nebula dataset (black squares) and simulated gamma-rays (red circles) reconstructed with the **afterpulsing** image cleaning. The Crab Nebula dataset consists of events with a zenith lower than 25 degrees. Simulated events are produced at a zenith of 20 degrees and a noise level of 200 MHz. The number of events is separated based on the reconstructed energy E_{rec} (in TeV) in the following ranges: $-1.0 < \log_{10}(E_{rec}) < -0.7$, $-0.7 < \log_{10}(E_{rec}) < -0.3$, $-0.3 < \log_{10}(E_{rec}) < -0.0$, $0.0 < \log_{10}(E_{rec}) < 0.3$, $0.3 < \log_{10}(E_{rec}) < 0.7$, $0.7 < \log_{10}(E_{rec}) < 1.0$. Bottom: cumulative distribution of MSCW for each energy range.

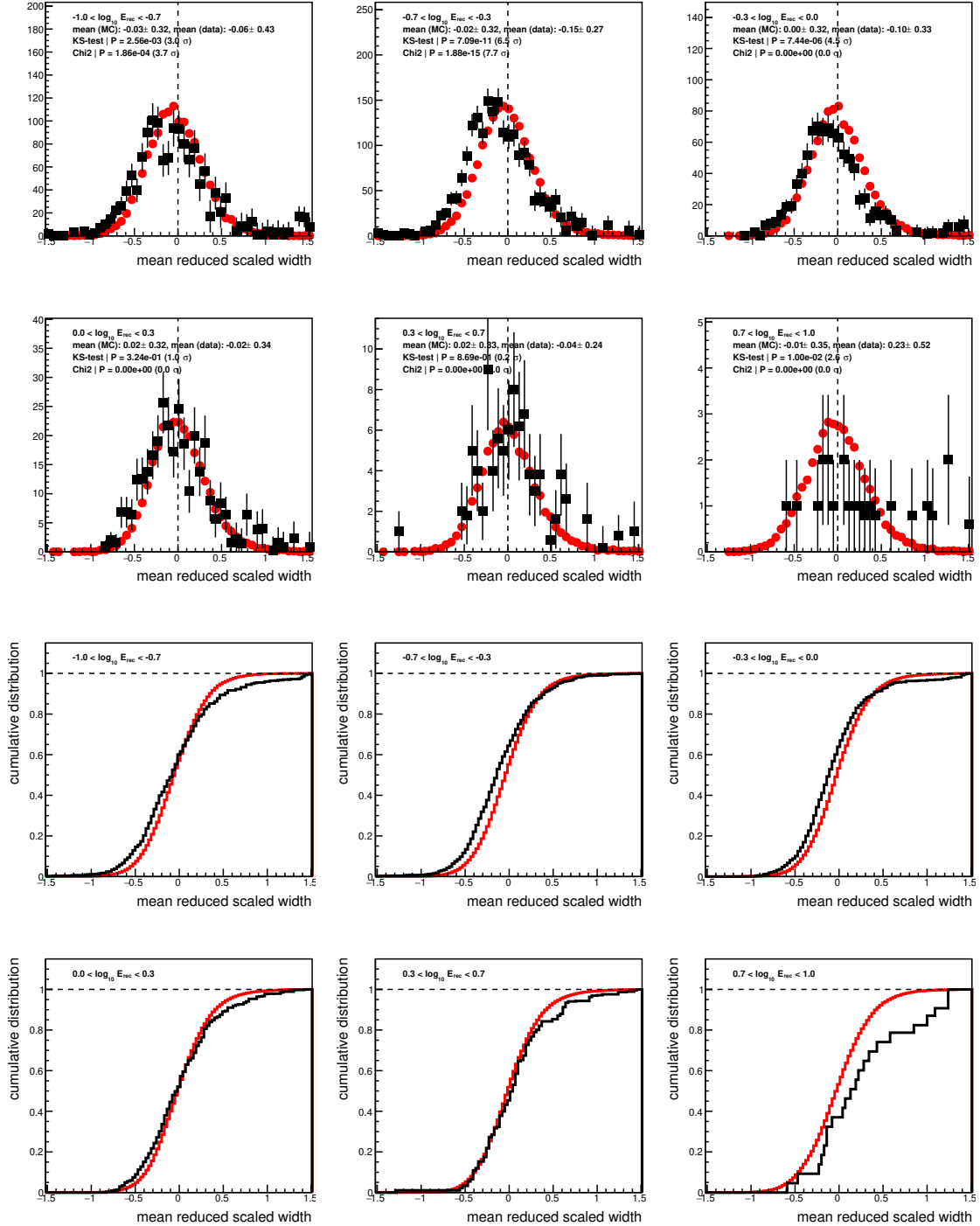


Figure A.30: Top: Distribution of MSCW for a **RedHIV** Crab Nebula dataset (black squares) and simulated gamma-rays (red circles) reconstructed with the **afterpulsing** image cleaning. The Crab Nebula dataset consists of events with a zenith lower than 25 degrees. Simulated events are produced at a zenith of 20 degrees and a noise level of 200 MHz. The number of events is separated based on the reconstructed energy E_{rec} (in TeV) in the following ranges: $-1.0 < \log_{10}(E_{rec}) < -0.7$, $-0.7 < \log_{10}(E_{rec}) < -0.3$, $-0.3 < \log_{10}(E_{rec}) < -0.0$, $0.0 < \log_{10}(E_{rec}) < 0.3$, $0.3 < \log_{10}(E_{rec}) < 0.7$, $0.7 < \log_{10}(E_{rec}) < 1.0$. Bottom: cumulative distribution of MSCW for each energy range.

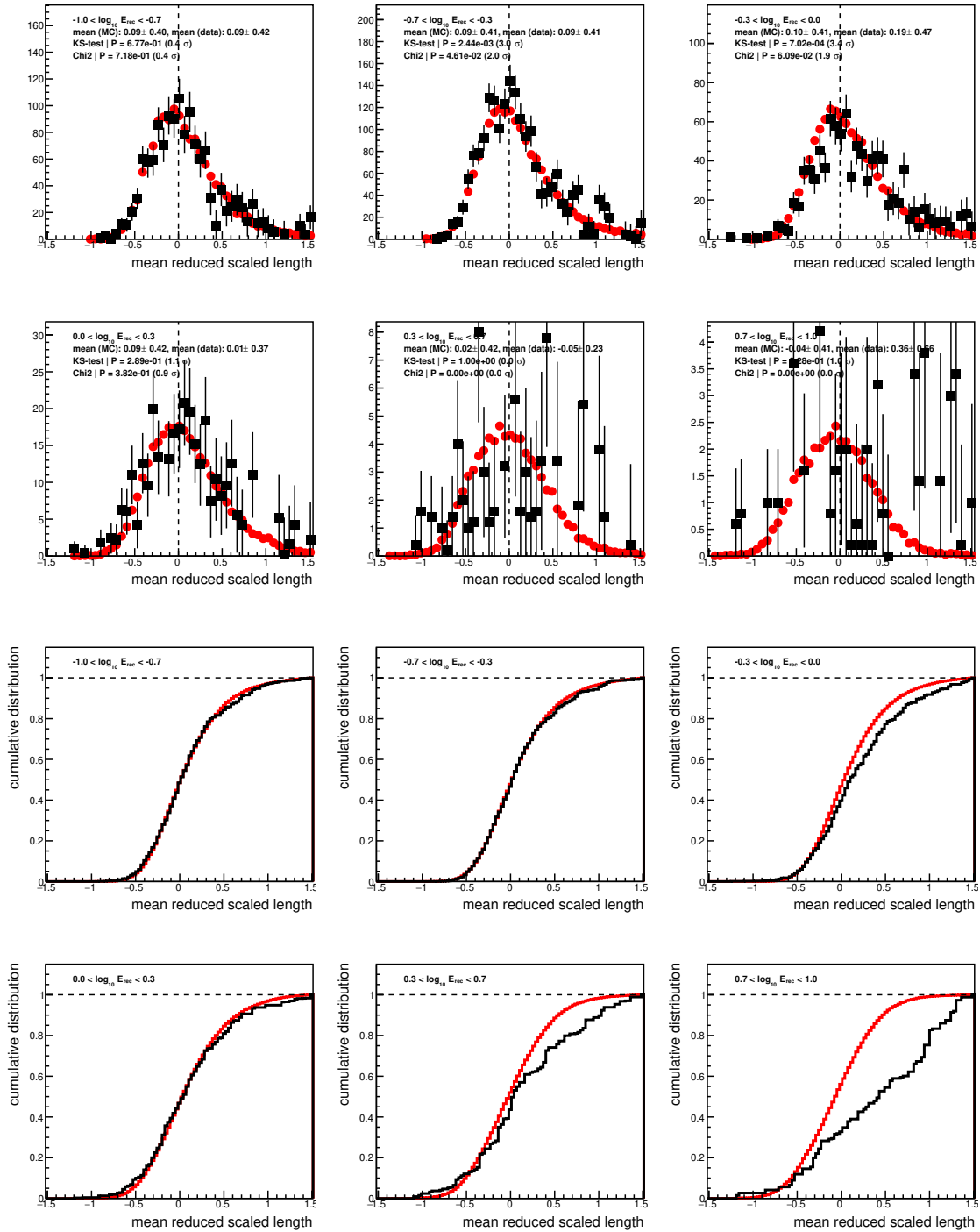


Figure A.31: Top: Distribution of MSCW for a **RedHV** Crab Nebula dataset (black squares) and simulated gamma-rays (red circles) reconstructed with the **afterpulsing** image cleaning. The Crab Nebula dataset consists of events with a zenith lower than 25 degrees. Simulated events are produced at a zenith of 20 degrees and a noise level of 200 MHz. The number of events is separated based on the reconstructed energy E_{rec} (in TeV) in the following ranges: $-1.0 < \log_{10}(E_{rec}) < -0.7$, $-0.7 < \log_{10}(E_{rec}) < -0.3$, $-0.3 < \log_{10}(E_{rec}) < -0.0$, $0.0 < \log_{10}(E_{rec}) < 0.3$, $0.3 < \log_{10}(E_{rec}) < 0.7$, $0.7 < \log_{10}(E_{rec}) < 1.0$. Bottom: cumulative distribution of MSCW for each energy range.

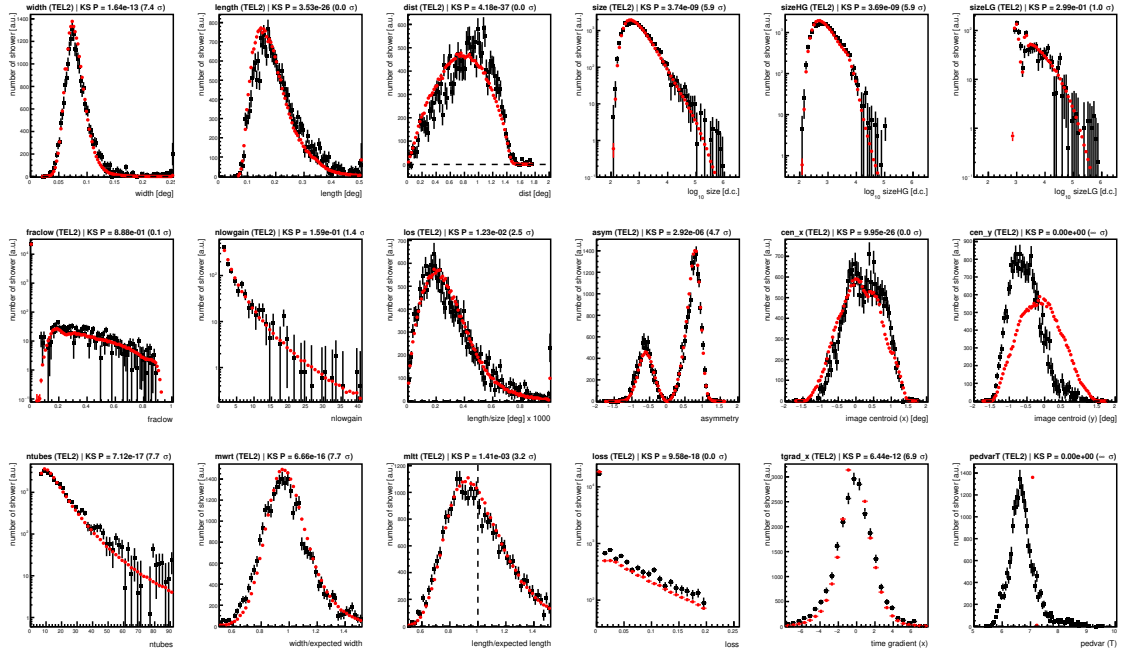


Figure A.32: Comparison of single telescope (**Telescope 2**) shower parameters between data and Monte Carlo simulations with the with the **Optimised Next Neighbour** cleaning cleaning. From top to bottom and from left to right: width, length, shower core distance, image size, image size (high gain channels), image size (low gain channels), fraclow, nlowgain, length per size, asymmetry, coordinates of image centroid (x and y directions), number of pixels in the image, mwrt, mlrt, image loss, image gradient, and *pedvars*. Simulation distributions are given in red, while data in black. Parameter distributions are given in arbitrary units.

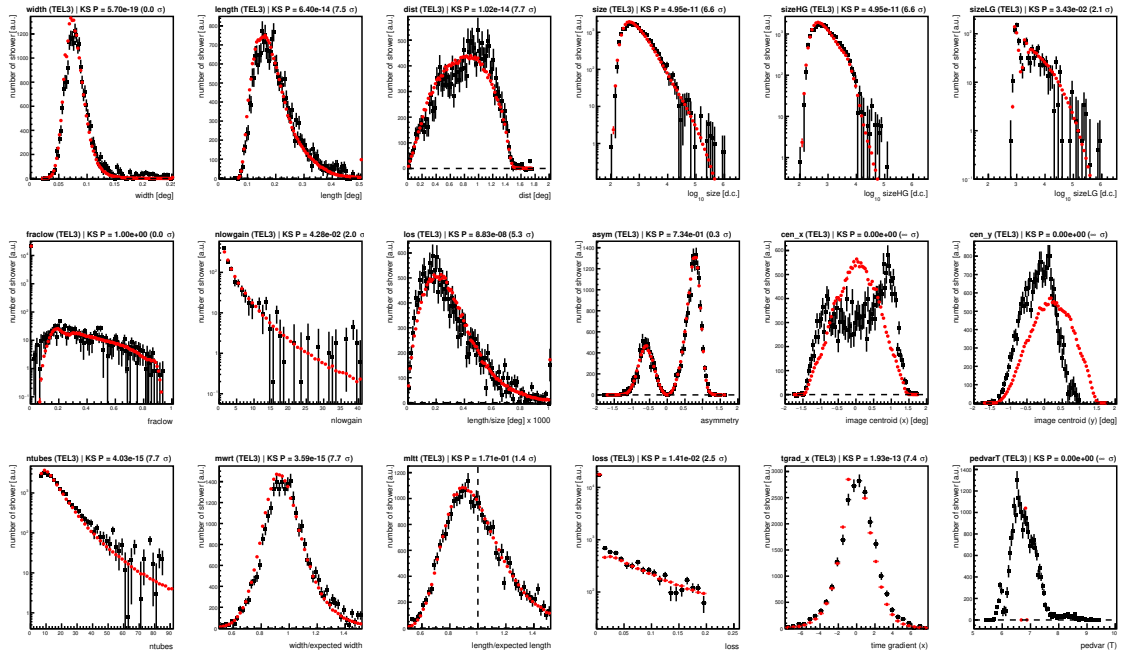


Figure A.33: Comparison of single telescope (**Telescope 3**) shower parameters between data and Monte Carlo simulations with the **Optimised Next Neighbour** cleaning. From top to bottom and from left to right: width, length, shower core distance, image size, image size (high gain channels), image size (low gain channels), fraclow, nlowgain, length per size, asymmetry, coordinates of image centroid (x and y directions), number of pixels in the image, mwrt, mltt, image loss, image gradient, and *pedvars*. Simulation distributions are given in red, while data in black. Parameter distributions are given in arbitrary units.

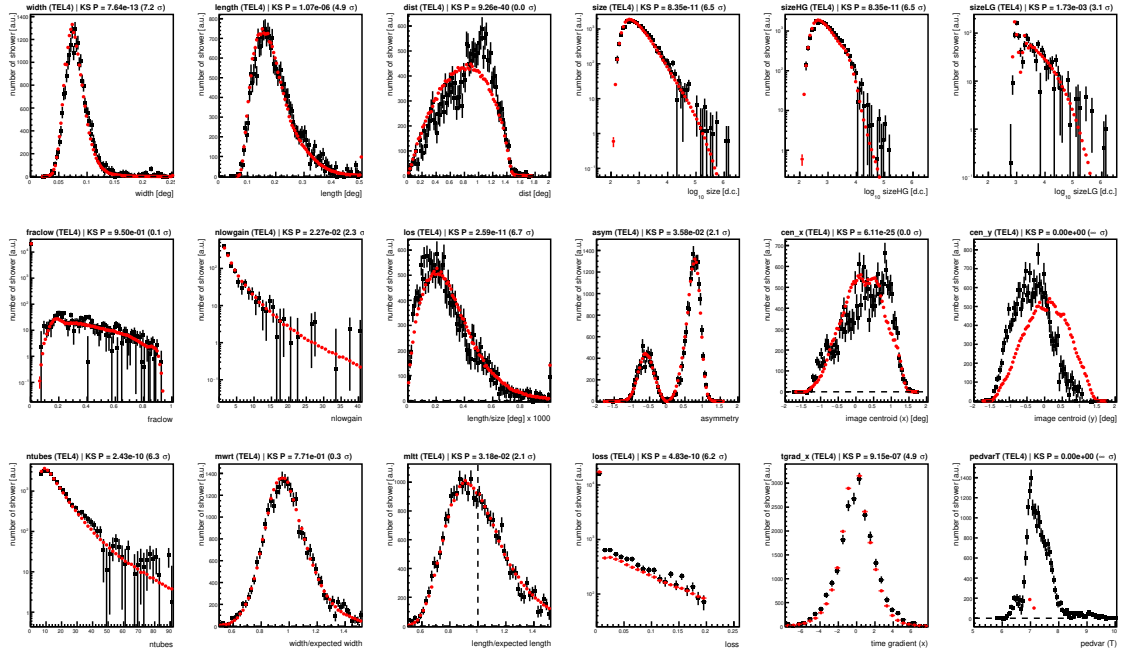


Figure A.34: Comparison of single telescope (**Telescope 4**) shower parameters between data and Monte Carlo simulations with the **Optimised Next Neighbour** cleaning. From top to bottom and from left to right: width, length, shower core distance, image size, image size (high gain channels), image size (low gain channels), fraclow, nlowgain, length per size, asymmetry, coordinates of image centroid (x and y directions), number of pixels in the image, mwrt, mlrt, image loss, image gradient, and *pedvars*. Simulation distributions are given in red, while data in black. Parameter distributions are given in arbitrary units.

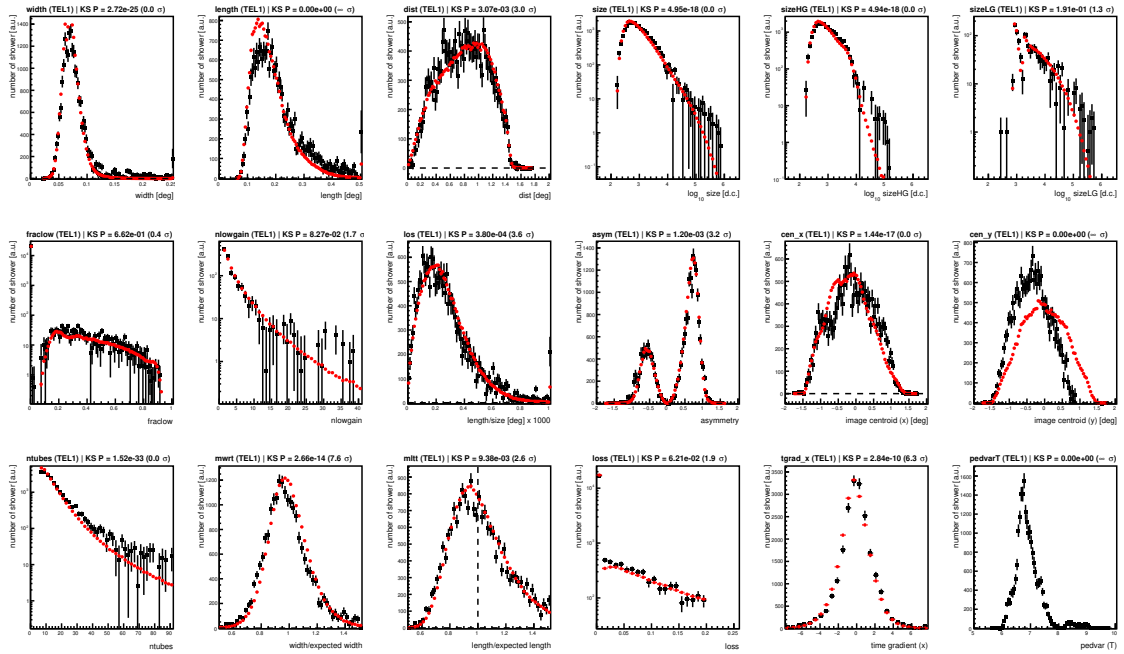


Figure A.35: Comparison of single telescope (**Telescope 1**) shower parameters between data and Monte Carlo simulations with the **afterpulsing** cleaning. From top to bottom and from left to right: width, length, shower core distance, image size, image size (high gain channels), image size (low gain channels), fraclow, nlowgain, length per size, asymmetry, coordinates of image centroid (x and y directions), number of pixels in the image, mwrt, mltt, image loss, image gradient, and *pedvars*. Simulation distributions are given in red, while data in black. Parameter distributions are given in arbitrary units.

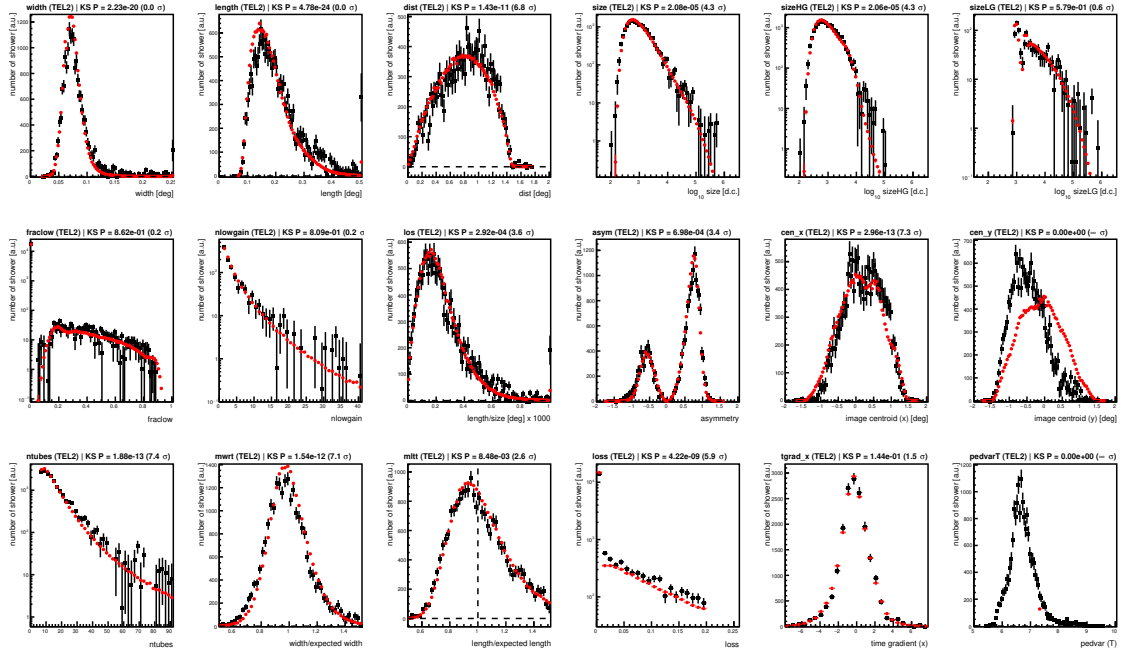


Figure A.36: Comparison of single telescope (**Telescope 2**) shower parameters between data and Monte Carlo simulations with the **afterpulsing** cleaning. From top to bottom and from left to right: width, length, shower core distance, image size, image size (high gain channels), image size (low gain channels), fraclow, nlowgain, length per size, asymmetry, coordinates of image centroid (x and y directions), number of pixels in the image, mwrt, mltt, image loss, image gradient, and *pedvars*. Simulation distributions are given in red, while data in black. Parameter distributions are given in arbitrary units.

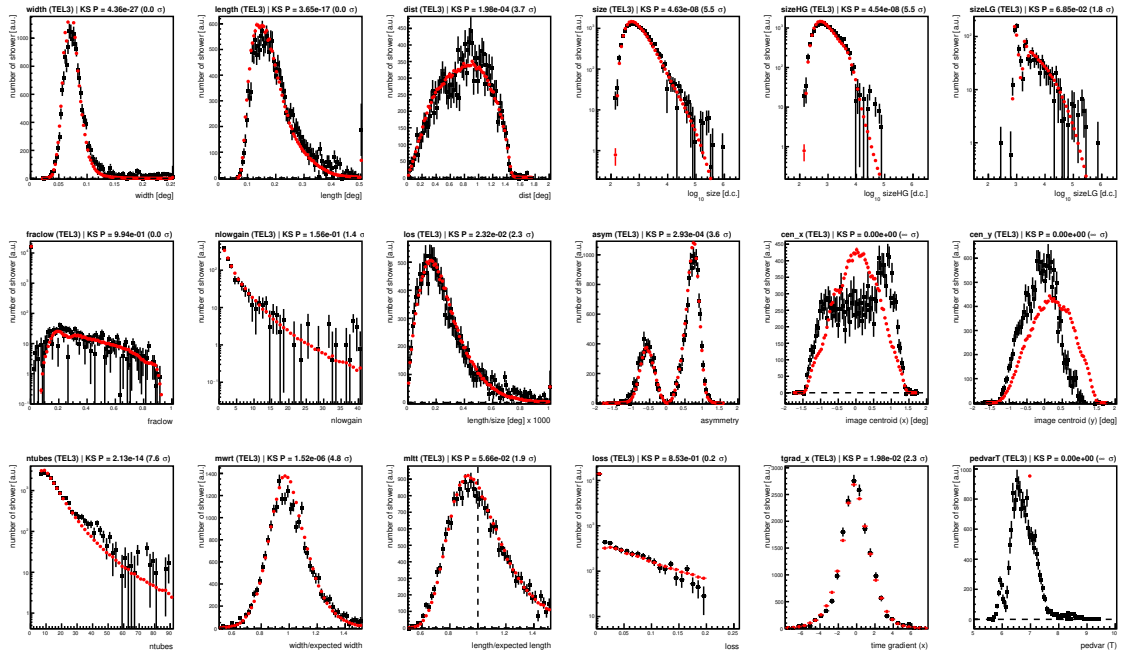


Figure A.37: Comparison of single telescope (**Telescope 3**) shower parameters between data and Monte Carlo simulations with the **afterpulsing** cleaning. From top to bottom and from left to right: width, length, shower core distance, image size, image size (high gain channels), image size (low gain channels), fraclow, nlowgain, length per size, asymmetry, coordinates of image centroid (x and y directions), number of pixels in the image, mwrt, mltt, image loss, image gradient, and *pedvars*. Simulation distributions are given in red, while data in black. Parameter distributions are given in arbitrary units.

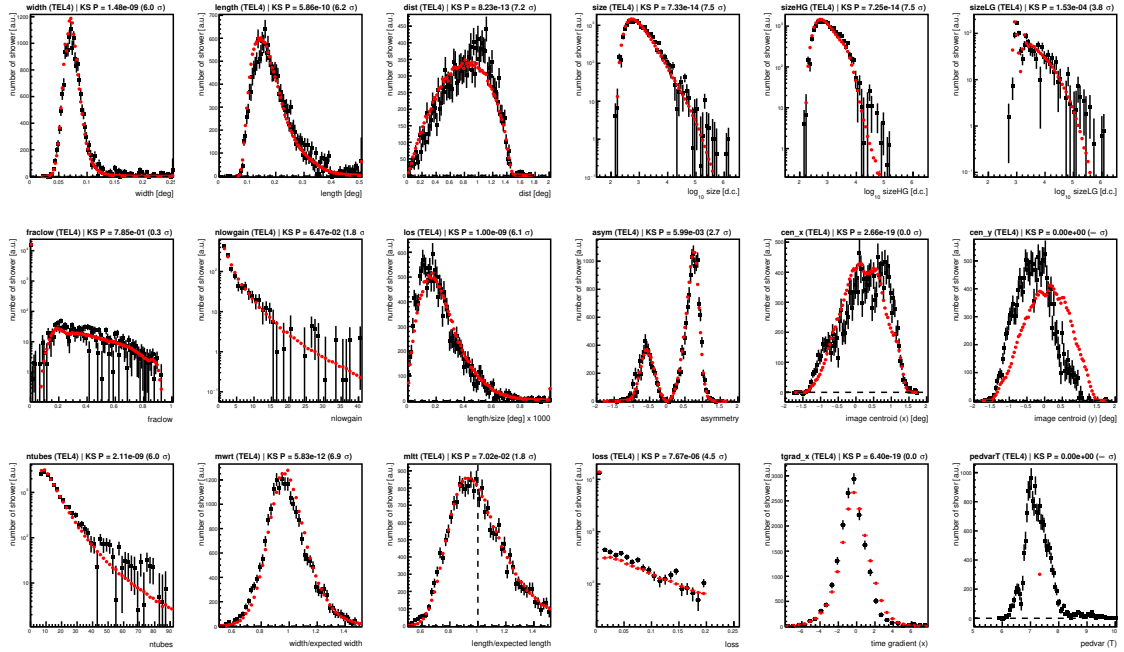


Figure A.38: Comparison of single telescope (**Telescope 4**) shower parameters between data and Monte Carlo simulations with the **afterpulsing** cleaning. From top to bottom and from left to right: width, length, shower core distance, image size, image size (high gain channels), image size (low gain channels), fraclow, nlowgain, length per size, asymmetry, coordinates of image centroid (x and y directions), number of pixels in the image, mwrt, mltt, image loss, image gradient, and *pedvars*. Simulation distributions are given in red, while data in black. Parameter distributions are given in arbitrary units.

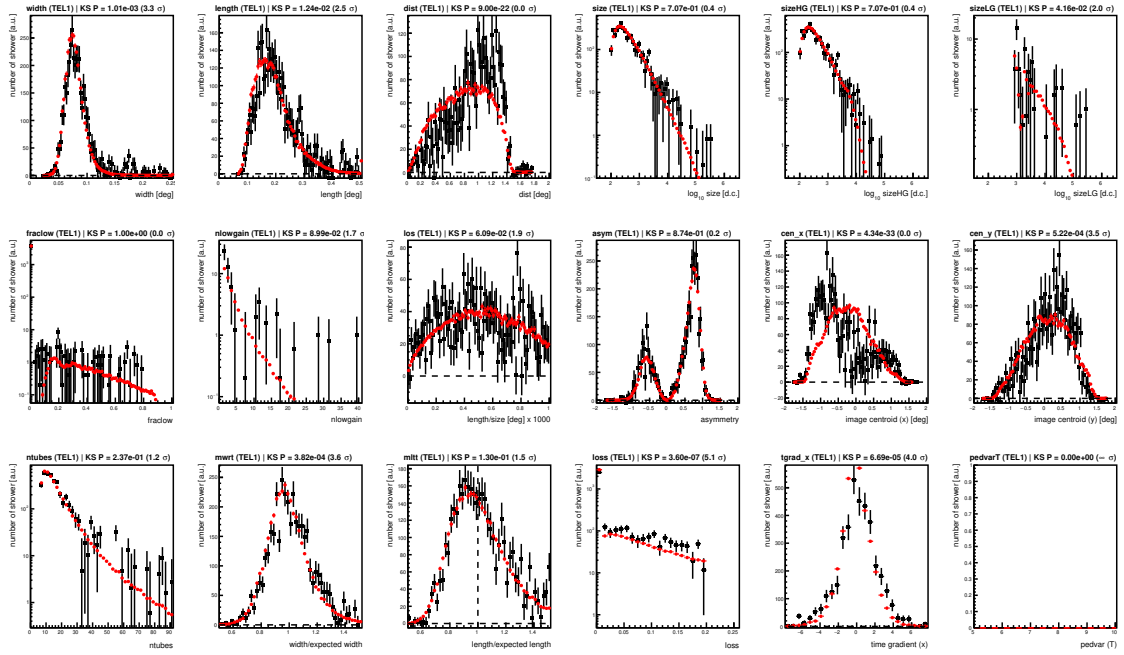


Figure A.39: Comparison of single telescope (**Telescope 1**) shower parameters between a dataset of **Reduced High Voltage** data and Monte Carlo simulations with the **Optimised Next Neighbour** image cleaning. From top to bottom and from left to right: width, length, shower core distance, image size, image size (high gain channels), image size (low gain channels), fraclow, nlowgain, length per size, asymmetry, coordinates of image centroid (x and y directions), number of pixels in the image, mwrt, mlrt, image loss, image gradient, and *pedvars*. Simulation distributions are given in red, while data in black. Parameter distributions are given in arbitrary units. *Pedvars* are typically lower than 5 dc in RedHV runs.

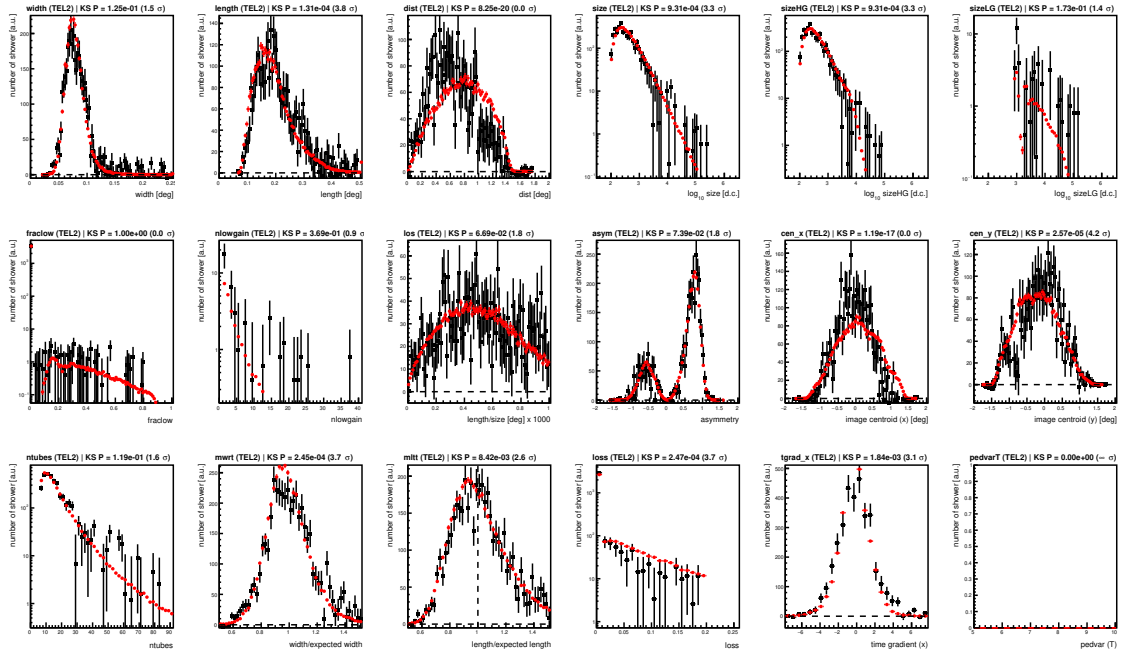


Figure A.40: Comparison of single telescope (**Telescope 2**) shower parameters between a dataset of **Reduced High Voltage** data and Monte Carlo simulations with the **Optimised Next Neighbour** image cleaning. From top to bottom and from left to right: width, length, shower core distance, image size, image size (high gain channels), image size (low gain channels), fraclow, nlowgain, length per size, asymmetry, coordinates of image centroid (x and y directions), number of pixels in the image, mwrt, mltt, image loss, image gradient, and *pedvars*. Simulation distributions are given in red, while data in black. Parameter distributions are given in arbitrary units. *Pedvars* are typically lower than 5 dc in RedHV runs.

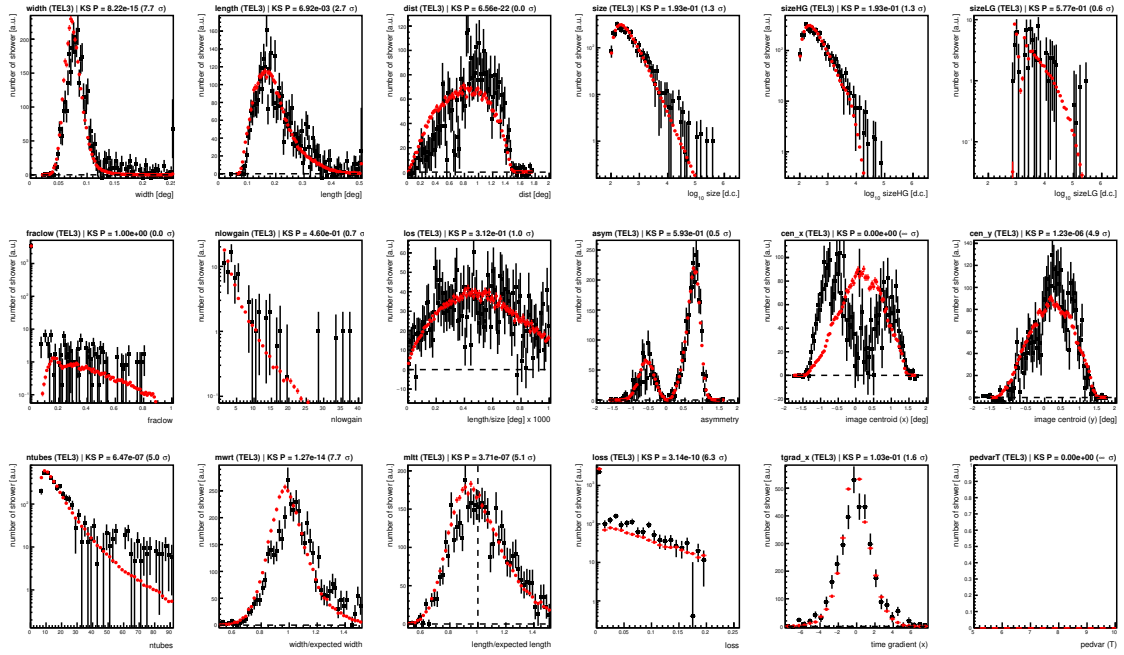


Figure A.41: Comparison of single telescope (**Telescope 3**) shower parameters between a dataset of **Reduced High Voltage** data and Monte Carlo simulations with the **Optimised Next Neighbour** image cleaning. From top to bottom and from left to right: width, length, shower core distance, image size, image size (high gain channels), image size (low gain channels), fraclow, nlowgain, length per size, asymmetry, coordinates of image centroid (x and y directions), number of pixels in the image, mwrt, mltt, image loss, image gradient, and *pedvars*. Simulation distributions are given in red, while data in black. Parameter distributions are given in arbitrary units. *Pedvars* are typically lower than 5 dc in RedHV runs.

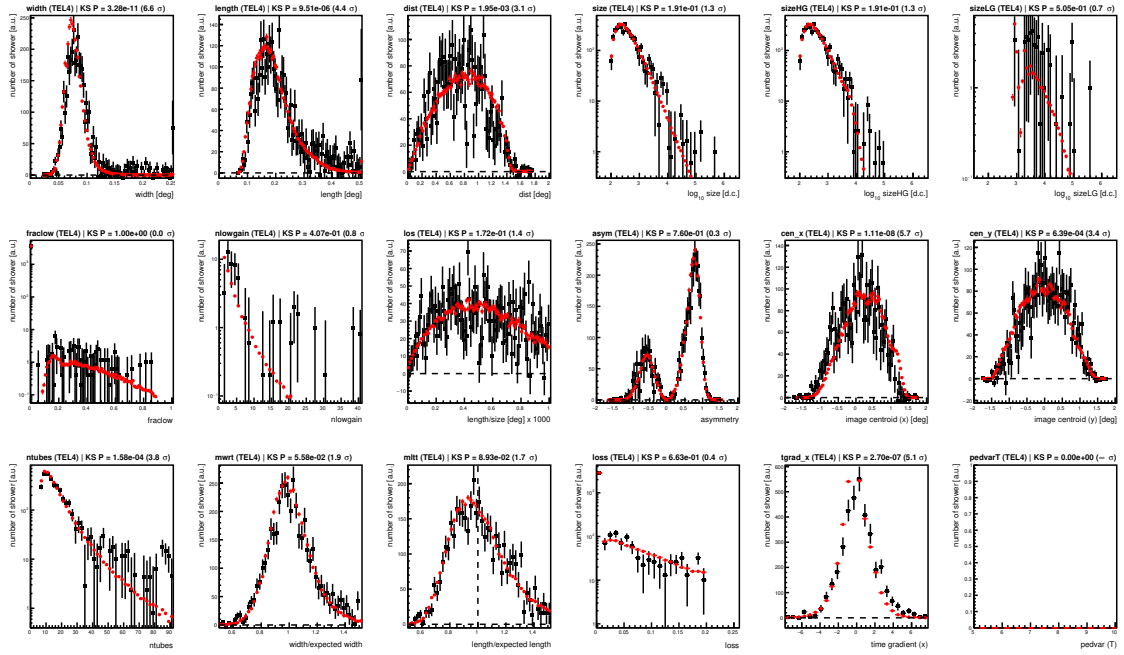


Figure A.42: Comparison of single telescope (**Telescope 4**) shower parameters between a dataset of **Reduced High Voltage** data and Monte Carlo simulations with the **Optimised Next Neighbour** image cleaning. From top to bottom and from left to right: width, length, shower core distance, image size, image size (high gain channels), image size (low gain channels), fraclow, nlowgain, length per size, asymmetry, coordinates of image centroid (x and y directions), number of pixels in the image, mwrt, mltt, image loss, image gradient, and *pedvars*. Simulation distributions are given in red, while data in black. Parameter distributions are given in arbitrary units. *Pedvars* are typically lower than 5 dc in RedHV runs.

Multiwavelength analysis methods for tidal disruption events

This appendix describes the methods employed to assemble the multiwavelength dataset for the analysis presented in Chapter 5. It includes data from different telescopes and instruments across the electromagnetic spectrum. The data collection and reduction techniques are grouped into three sections: *a)* optical and UV, *b)* X-rays and radio, and *c)* gamma-rays. A summary of the properties of the filters from each instrument is given in Table B.1.

B.0.1 Optical and UV instruments

B.0.1.1 Zwicky Transient Facility

ZTF [Bellm et al., 2018] is a fully automated, wide-field survey that systematically explores the transient optical Northern sky. It has three filters: two in visible bands, green and red (g and r), and one in infrared (i). ZTF is attached to the Samuel Oschin Telescope at the Palomar Observatory and consists of a camera with 16 Charge Coupled Devices (CCD), each containing 6144×6160 pixels. This enables each exposure to cover an area of 47 squared degrees. The survey is designed to image the entire northern sky in three nights, scanning the plane of the Milky Way twice each night. The reported median limiting magnitudes (5σ) are 20.8 mag in g -band, 20.6 mag in the r -band, and 19.9 in the i -band [Bellm et al., 2018]. Data from the ZTF was obtained with the `ztfquery` [Rigault, 2018] python package.

B.0.1.2 All-Sky Automated Survey for Supernovae

ASAS-SN [Kochanek et al., 2017] consists of 24 telescopes distributed around the globe, which allows the survey of the entire visible sky every night, regardless of weather conditions. The first unit, deployed at the Hawaii station of the Las Cumbres Observatory, comprises four 14-cm telescopes. Additional units are located in Chile, South Africa, the United States, and China. ASAS-SN employs two different filters - S_g (the same green filter employed by SDSS and V (visual band) - and has a limiting apparent magnitude of $m_{AB} \sim 18$. The instrument's primary goal is to detect new supernovae and other transient sources. To retrieve the data from ASAS-SN, I used the publicly accessible tool Sky Patrol¹ by employing the aperture photometry image subtraction method without the addition of the reference flux (from host galaxies).

¹<https://asas-sn.osu.edu/>

B.0.1.3 The Asteroid Terrestrial-impact Last Alert System

ATLAS is a system that comprises four 0.5-meter telescopes. Its primary objective is to detect potential asteroid impacts on Earth by conducting an all-sky survey on a nightly basis. Two of the telescopes are located in the Haleakala Observatory in the Hawaiian Islands, one in the Sutherland Observatory in South Africa, and one in El Sauce Observatory, Chile. The system has been operational since 2015, with two filters (cyan and orange). To retrieve data, I used the ATLAS forced photometry server² with the method of image subtraction to obtain a light curve for a point-like transient, with no host flux added [Shingles et al., 2021].

B.0.1.4 Swift Ultra-violet Optical Telescope

For the UV band, data was obtained from Swift-UVOT [Romig et al., 2005], a 30 cm modified Ritchey-Chretien UV/optical telescope onboard the SWIFT Observatory. UVOT is co-aligned with Swift-XRT, which allows for simultaneous ultraviolet and optical coverage with six filters (m2, w1, w2, u, V and B) in the band from 170 nm up to 650 nm in a 17' × 17' field of view. Despite its narrow aperture, UVOT offers the advantage of not needing corrections for atmospheric extinction, diffraction, and background. The photometry was measured with the UVOTMAGHIST³ routine from the HEASOFT⁴ v6.31.1 package [Nasa High Energy Astrophysics Science Archive Research Center (Heasarc), 2014]. This tool provides the magnitude history versus time by performing photometry for a source in every UVOT sky image file. We use an aperture of 5'' for the source region and a nearby source-free circular region with an aperture of 50'' for the background estimation. For the host subtraction, we perform the same analysis on host images taken before the disruption of the star or when the TDE flare had already faded to a non-detection in optical bands. The analysis was performed for the filters m2, w2, w1 and u. An example of an image showing the source and background regions for AT2023clx can be seen in Figure B.1.

B.0.2 X-ray and radio

B.0.2.1 Swift-XRT products

The Swift-XRT [Burrows et al., 2005] is a Wolter Type I [Pareschi et al., 2021] X-ray telescope with 12 nested mirrors on board of the Neil Gehrels Swift Observatory. It has been in operation since 2004, and its primary goal is to monitor the X-ray afterglow of GRBs. Upper limits and data points for Swift-XRT are obtained using version 1.10 of XRT products from version 3.0 of the *swifttools* API⁷ [Evans et al., 2007; Evans et al., 2009]. The duration of the bin length is set to 10 days.

²<https://fallingstar-data.com/forcedphot/>

³<https://heasarc.gsfc.nasa.gov/lheasoft/help/uvotmaghist.html>

⁴<https://heasarc.gsfc.nasa.gov/ftools>

⁶<http://svo2.cab.inta-csic.es/svo/theory/fps/index.php>

⁶<https://svo.cab.inta-csic.es/main/index.php>

⁷<https://www.swift.ac.uk/API/>

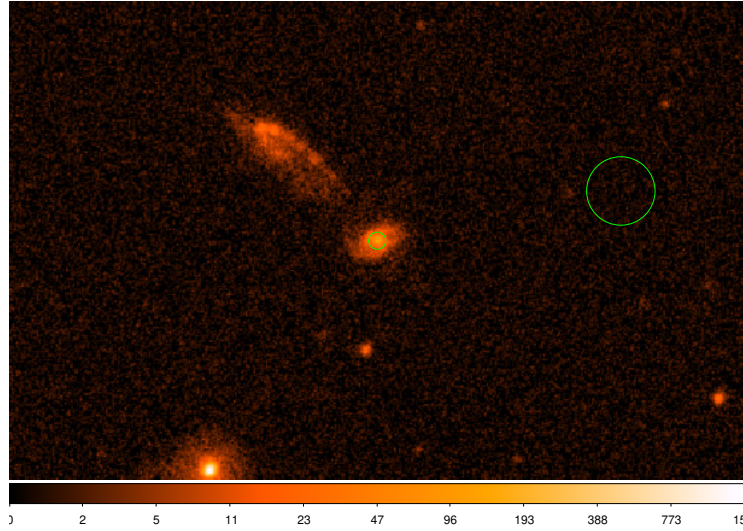


Figure B.1: Example of a Swift-UVOT image for AT2023clx, with a 5'' aperture circular region around the source position and a 50'' aperture circular region for the background estimation. The color pallet represents number of counts.

The significance of a detection per time bin is defined as C/\sqrt{B} , where C is the number of counts in the source region and B is the number of background events expected in the source region. The minimum accepted significance for detection is set as 5σ . Upper limits are given in the confidence level of the minimum required significance, i.e. all bins without a 5σ detection are plotted as upper limits with 5σ confidence level. For non-contiguous observation, which spans multiple snapshots or observations, bins that lie entirely in periods with no Swift-XRT observations are not shown. We extract light curves using events between 0.3 and 10 keV. To convert Swift-XRT count rates to flux, the mission count rate simulator tool WebPIMMS⁸ is employed.

B.0.2.2 Radio and other X-ray instruments

We retrieve radio and X-ray detections from ATELS and the TNS. Radio detections by the Very Large Array (VLA) for AT2022dbl [Sfaradi et al., 2022; Sfaradi et al., 2022] and a possible detection by the Australia Telescope Compact Array (ATCA) for AT2023clx [Sfaradi et al., 2023] have been reported in ATELS. Additionally, data from eROSITA and the XMM-Newton for AT2022dsb are available in Ref. [Malyali et al., 2023].

B.0.3 Gamma rays

B.0.3.1 Fermi-LAT

The gamma-ray band is analysed in the range $100 \text{ MeV} < E < 300 \text{ GeV}$ with Fermi-LAT. The analysis is divided into two distinct periods. The first period, referred to as $t_{\text{LAT},1}$, spans from discovery until 20 days after the optical peak. This period is expected to be approximately under

⁸<https://heasarc.gsfc.nasa.gov/cgi-bin/Tools/w3pimms/w3pimms.pl>

Instrument	Filter name	λ_c (nm)
ZTF	g	480.59
	r	643.59
	i	795.44
ATLAS	c	537.10
	o	691.23
ASAS-SN	Sg	474.73
Swift-UVOT	uvw1	262.93
	uvw1	196.74
	uvm2	225.98
	u	346.85

Table B.1: Filters used in the multiwavelength analysis of TDEs: filter name and central wavelength, λ_c , between the two points defining the full width at half maximum. The filter information are retrieved from the Filter Profile Service⁵ website, provided by the Spanish Virtual Observatory⁶.

the highest level of attenuation of the event due to the brightness of the lower energy photon field. In contrast, the second phase, $t_{\text{LAT},2}$, extends from 20 days post-peak until the last day of either optical or UV detection. In this second phase, the effects of attenuation should be dimmer. Table 5.5 shows these intervals for each candidate.

Data retrieval is performed with the Fermi-LAT API Data Query tool⁹, using the photon event class format derived from the Pass 8 event selection (P8R3SOURCE) [Bruehl et al., 2018]. The Pass 8 analysis includes improved data processing and calibration schemes, which enhance energy dispersion correction, reducing systematic uncertainties at all energies and providing an energy resolution of $< 10\%$ between 1 and 100 GeV. The search parameters cover a circular radius of 30 degrees, centred in the transient coordinates derived from OUV observations.

Events collected by the Fermi-LAT instrument are classified based on the quality of their reconstruction and their photon probability. A specific set of IRFs characterise the instrument response to the different event classes. In Pass 8, the IRF class TRANSIENT exhibits the most lenient selection criteria. It is suited for analysing short-duration events, such as GRBs, for which higher photon statistics are preferable and a higher background fraction and broader PSF are tolerated. Conversely, the most rigorous photon selection, denoted as ULTRACLEAN or ULTRACLEAN-VETO, provides a lower level of background contamination at the cost of a lower effective area,

⁹<https://fermi.gsfc.nasa.gov/cgi-bin/ssc/LAT/LATDataQuery.cgi>

particularly ensuing at low energies. In this case, background fluxes are typically equal to or lower than the diffusive gamma-ray background, and this class is generally recommended for diffuse emission studies.

In this thesis, we use the intermediate class SOURCE (P8R3_SOURCE_V3) in Pass 8, which is recommended for most analyses of point sources on medium to long time scales. In comparison, ULTRACLEANVETO has a background rate that is 15% to 20% lower than the background of the intermediate class SOURCE below 10 GeV, and 50% lower at 200 GeV.

Within each class, events are partitioned into event types considering two conversion modes: Front and Back, depending on the position of the Tracker layer where photon-to-pair conversion happened. The Tracker comprises 12 layers of tungsten converters in the front section and four layers in the back section. Photons that convert in the front section have better angular resolution than those in the back. This is because thicker material is more likely to cause multiple-scattering. The introduction of the conversion type partition allows for separate treatment of front and back events, each with their respective set of IRFs. Additionally, within Pass 8, events are partitioned regarding the quality of their reconstructed energy and direction. The partition is divided into quartiles, from the lowest quality quartile in energy and PSF (EDISP0 and PSF0) to the best quality quartile (EDISP3 and PSF3). The events for this analysis are selected based on event type 128, which requires that events are at least on the second (second to worst quality, > EDISP1 + PSF1) quartile of the reconstructed energy.

This analysis is done with the *fermipy*¹⁰ package (version 1.2) [Wood et al., 2017]. Spectral models are taken from the LAT 14-year Source Catalog [Abdollahi et al., 2020], and galactic and extragalactic diffuse emission models are given by the default files available within *fermipy*: `gll_iem_v07.fits` and `iso_P8R3_SOURCEV3_v1.txt`, respectively. This analysis performs a likelihood fit of every flux normalisation and shape parameters of the spectral and spatial models composing the ROI, creating an initial estimate for the emission. The fit provides the test statistics, TS , which compares the likelihood of the ROI model with and without (null hypothesis) the source of interest:

$$TS = -2 \ln \left(\frac{L_{\max,0}}{L_{\max,s}} \right). \quad (\text{B.1})$$

In Equation B.1, $L_{\max,0}/L_{\max,s}$ is the ratio between L_0 , the maximum likelihood of the null-hypothesis, given by the baseline model of the ROI without the inclusion of the source, and L_s , the maximum likelihood obtained with the inclusion of the source. If the target source does not improve the fit of the model to the data, we can expect TS close to 0 or very low. Because TS follows a χ^2 distribution, we can use the Gaussian approximation [Wilson and Hilferty, 1931] to calculate the significance of the source by simply taking \sqrt{TS} . A detection can be claimed for $TS \geq 25$.

Following the optimisation, we excluded sources that are too faint to be detected within the dataset. Namely, we remove every source with $TS < 3$ and a predicted number of counts, N_{pred} , lower than 3. All spectral parameters for the diffuse emission models and sources within 3° from

¹⁰<https://fermipy.readthedocs.io/en/latest/>

the transient coordinates and bright sources at any location with $TS > 10$ are kept free. With this refined model, a secondary likelihood fit is conducted. The optimisation provides $TS \sim 0$ for AT2022dbl, AT2022dsb and AT2023clx. Therefore, no significant emission is derived for any candidate. Flux ULs are calculated for 95% C. L. for $t_{\text{LAT},1}$ and $t_{\text{LAT},2}$ and are shown in Table 5.5, assuming that the spectrum of the source follows a power-law with index $\Gamma = 3$. Flux ULs are derived in the energy range of $100 \text{ MeV} < E < 300 \text{ GeV}$ (95% C. L.) for each of the periods considered.

B.0.3.2 VERITAS

The VERITAS analysis is conducted within the *EventDisplay* [Maier and Holder, 2017] framework. The image cleaning is performed with the Optimised Next Neighbour method, detailed in Chapter 4. The gamma/hadron separation is executed with *soft* cuts, which are optimised for sources with high spectral index ($\Gamma > 3$) and provide the lowest possible energy threshold:

- $-1.2 < \text{MSCW} < 0.3$
- $-1.2 < \text{MSCL} < 0.5$
- Emission height $> 6 \text{ km}$
- $\theta^2 < 0.008 \text{ degrees}^2$

Since the spectral form of the source is unknown, we assume it follows a power-law with indexes $\Gamma = 3$ and $\Gamma = 2$ for the flux derivation. The background is estimated with six reflected regions. A more comprehensive description of all the steps concerning the VERITAS analysis is given in Chapter 3. A summary of VERITAS observations for each TDE candidate: total exposure time, mean elevation, trigger rate and mean noise rate are shown in Table 5.3. The results for the VERITAS analysis: number of events from the ON region (N_{on}), number of events from the OFF region (N_{off}), number of source events, (N_s), significance, S , excess events rate and upper limits (95% C. L.) considering power-law spectra with indexes $\Gamma = 2$ and $\Gamma = 3$ are presented in Table 5.4. The energy threshold of the observation is 108 GeV, and is calculated as 10% of the maximum of the effective areas the observing season. The flux ULs are calculated using the Rolke [Rolke and Lopez, 2001] method (Section 3.4.2). Figure B.2 presents the time evolution of the dataset significance for each event. No signal was observed for AT2022dbl, AT2022dsb and AT2023clx.

Flux ULs are given after correction by the attenuation from the EBL, using the model presented in reference [Franceschini and Rodighiero, 2017]. Given the absorbed (index *abs*) flux UL measured by VERITAS, the intrinsic flux UL (index *intr*, before attenuation by the EBL) is found as:

$$E^2 \frac{dN_{\text{abs}}}{dE}(E) = E^2 \frac{dN_{\text{intr}}}{dE}(E) \cdot e^{-\tau_{\text{EBL}}(z,E)}, \quad (\text{B.2})$$

where τ_{EBL} corresponds to the optical depth provided in Figure 2.4. Alternatively, when considering the integrated flux UL:

$$\int_{E_{min}}^{E_{max}} E^2 \frac{dN_{abs}}{dE}(E) dE = \int_{E_{min}}^{E_{max}} E^2 \frac{dN_{intr}}{dE}(E) \cdot e^{-\tau_{EBL}(z,E)} dE. \quad (\text{B.3})$$

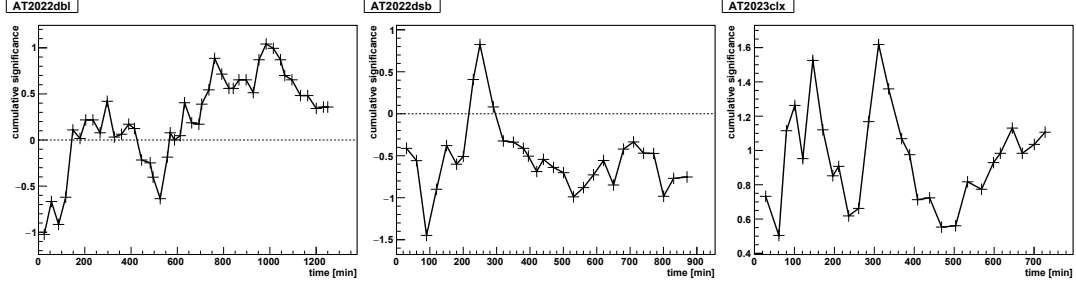


Figure B.2: Time evolution of the VERITAS analysis significance for each event dataset.

B.1 Methods for bolometric light curve calculation

Superbol [Nicholl, 2018] presents two methods for calculating the bolometric light curves: the pseudo-bolometric approach, which integrates the flux across the detected filters, and a full bolometric calculation that involves fitting a blackbody spectrum and extending it to undetected wavelengths. With the second method, estimates for the blackbody radius and temperature are also provided. Figure B.3 lists the extrapolated filters for each TDE. Because the data-points only represent the tail portion of the blackbody spectrum, making the estimation of the peak wavelength more difficult, the pseudo-bolometric approach is employed, which still provides a good approximation of the bolometric luminosity.

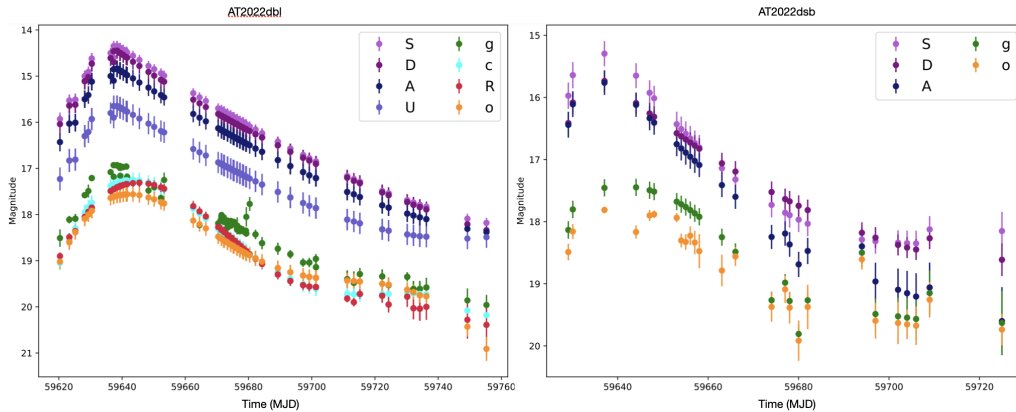


Figure B.3: Interpolated light curves for AT2022dbl (left) and AT2022dsb (right) using the *Superbol* Python-based code [Nicholl, 2018]. Times are given in MJD and magnitudes in the AB system. The represented filters are from Swift-UVOT (S = w2, D = m2, A = w1, u), ZTF (g = green, R = red, i = infrared), ATLAS (o = orange, c = cyan) and ASAS-SN (g = green, joined with ZTF's green filter). The nomenclature in the legend follows the standard one from *Superbol*. The filter of reference is ZTF-g and ATLAS-o for AT2022dbl and AT2022dsb, respectively.

B.2 Photometry tables

AT2022dbl - OUV photometry

band	MJD	Mag	Δ Mag	band	MJD	Mag	Δ Mag	band	MJD	Mag	Δ Mag
Sg	59620.36	18.51	0.19	Sg	59629.35	17.49	0.14	Sg	59636.37	17.08	0.06
Sg	59637.35	17.18	0.07	Sg	59639.43	17.16	0.05	Sg	59641.62	17.18	0.06
Sg	59643.45	17.25	0.08	Sg	59645.48	17.31	0.06	Sg	59648.36	17.48	0.07
Sg	59650.17	17.41	0.12	Sg	59652.3	17.64	0.19	Sg	59653.31	17.25	0.16
Sg	59662.52	17.82	0.12	Sg	59664.5	18.23	0.13	Sg	59666.51	18.08	0.09
Sg	59670.41	18.19	0.1	Sg	59672.36	18.49	0.2	Sg	59674.36	18.6	0.16
Sg	59676.44	18.24	0.18	Sg	59679.31	18.05	0.21	Sg	59680.38	17.77	0.15
c	59589.06	20.33	0.3	c	59615.02	19.88	0.25	c	59620.01	19.64	0.21
c	59635.99	17.12	0.02	c	59638.98	17.18	0.03	c	59643.98	17.32	0.04
c	59647.97	17.45	0.06	c	59670.94	18.2	0.06	c	59675.93	19.14	0.29
c	59678.93	18.31	0.18	c	59694.9	19.54	0.21	c	59722.86	19.7	0.23
c	59731.85	19.7	0.25	c	59750.82	20.17	0.31	o	59565.15	19.83	0.29
o	59621.14	18.65	0.14	o	59623.14	19.01	0.21	o	59625.14	18.69	0.36
o	59626.14	18.29	0.16	o	59627.14	18.21	0.14	o	59631.14	17.51	0.05
o	59633.14	17.47	0.04	o	59637.14	17.44	0.04	o	59641.14	17.52	0.04
o	59645.14	17.56	0.1	o	59649.14	17.74	0.05	o	59653.14	17.88	0.09
o	59655.14	18.09	0.24	o	59657.14	18.01	0.11	o	59659.14	18.08	0.09
o	59665.14	18.29	0.07	o	59677.14	18.59	0.12	o	59681.14	18.66	0.23
o	59697.14	19.4	0.34	o	59719.14	19.09	0.21	o	59721.14	19.6	0.25
o	59725.14	20.0	0.34	o	59735.14	19.61	0.29	o	59967.14	20.06	0.32
u	59637.58	15.57	0.08	u	59640.71	15.7	0.1	u	59643.09	15.61	0.1

band	MJD	Mag	Δ Mag	band	MJD	Mag	Δ Mag	band	MJD	Mag	Δ Mag
u	59649.34	15.99	0.09	u	59650.57	16.24	0.13	u	59654.89	16.1	0.12
u	59660.72	16.31	0.14	u	59662.98	16.47	0.1	u	59664.89	16.52	0.15
u	59666.2	16.54	0.15	u	59670.6	16.63	0.11	u	59675.18	17.07	0.2
u	59693.08	17.88	0.28	u	59708.91	17.81	0.23	u	59718.06	18.54	0.51
u	59721.08	17.96	0.3	u	59726.71	18.13	0.41	u	59728.57	18.07	0.3
u	59731.65	18.53	0.49	u	59736.4	18.41	0.45	u	59756.72	18.42	0.49
w1	59637.58	14.76	0.05	w1	59643.09	14.86	0.06	w1	59649.33	15.16	0.05
w1	59650.57	15.16	0.07	w1	59660.72	15.69	0.09	w1	59662.97	15.72	0.06
w1	59664.89	15.73	0.08	w1	59666.2	15.8	0.09	w1	59670.59	15.96	0.06
w1	59675.18	16.28	0.1	w1	59693.08	16.92	0.13	w1	59708.91	17.15	0.13
w1	59718.06	17.56	0.21	w1	59721.08	17.73	0.2	w1	59726.71	17.71	0.22
w1	59728.57	17.76	0.21	w1	59731.65	17.89	0.22	w1	59736.39	18.24	0.3
w1	59741.43	18.25	0.35	w1	59742.69	17.95	0.37	w1	59751.59	17.99	0.32
w1	59756.72	18.1	0.29	w1	59763.05	18.48	0.42	w1	59766.66	18.37	0.33
w2	59637.59	14.2	0.04	w2	59643.1	14.37	0.04	w2	59649.34	14.67	0.04
w2	59650.57	14.68	0.04	w2	59654.89	15.08	0.05	w2	59660.72	15.05	0.05
w2	59662.98	15.19	0.04	w2	59664.89	15.26	0.05	w2	59666.2	15.3	0.06
w2	59670.6	15.45	0.04	w2	59675.18	15.81	0.06	w2	59693.08	16.6	0.08
w2	59708.92	16.89	0.08	w2	59718.06	17.13	0.11	w2	59721.08	17.28	0.11
w2	59726.71	17.66	0.16	w2	59728.57	17.56	0.13	w2	59731.65	17.41	0.12
w2	59736.4	17.55	0.13	w2	59741.43	17.99	0.2	w2	59742.69	17.83	0.25
w2	59746.21	17.95	0.19	w2	59751.59	17.57	0.18	w2	59756.72	18.07	0.2
w2	59763.06	18.27	0.25	w2	59766.67	18.15	0.19	m2	59637.59	14.37	0.04
m2	59643.1	14.49	0.05	m2	59649.34	14.76	0.04	m2	59650.57	14.86	0.07
m2	59660.73	15.14	0.06	m2	59662.99	15.24	0.04	m2	59666.2	15.36	0.06

band	MJD	Mag	Δ Mag	band	MJD	Mag	Δ Mag	band	MJD	Mag	Δ Mag
m2	59670.6	15.54	0.05	m2	59675.19	15.86	0.07	m2	59693.09	16.68	0.12
m2	59708.92	17.18	0.14	m2	59718.07	17.51	0.21	m2	59721.09	17.11	0.21
m2	59726.71	17.54	0.17	m2	59728.58	17.39	0.5	m2	59731.66	17.62	0.16
m2	59736.4	17.66	0.17	m2	59741.3	17.89	0.22	m2	59742.7	17.59	0.26
m2	59746.21	18.01	0.25	m2	59751.59	17.88	0.28	m2	59756.73	18.07	0.24
m2	59763.06	18.74	0.44	m2	59766.68	18.36	0.27	g	59623.33	18.11	0.08
g	59625.22	18.09	0.1	g	59628.2	17.58	0.06	g	59630.42	17.21	0.05
g	59637.37	16.93	0.05	g	59638.41	16.93	0.04	g	59638.44	16.94	0.04
g	59639.32	16.95	0.04	g	59639.35	16.95	0.04	g	59639.38	16.99	0.05
g	59640.36	16.97	0.03	g	59641.34	16.96	0.03	g	59671.43	18.08	0.05
g	59671.43	18.07	0.06	g	59671.47	18.06	0.06	g	59672.17	18.09	0.05
g	59672.31	18.16	0.05	g	59673.4	18.28	0.08	g	59673.32	18.18	0.06
g	59674.38	18.14	0.06	g	59674.38	18.24	0.07	g	59675.16	18.16	0.07
g	59675.38	18.16	0.07	g	59676.32	18.28	0.1	g	59676.32	18.26	0.09
g	59676.39	18.33	0.1	g	59677.24	18.36	0.07	g	59677.32	18.3	0.07
g	59678.18	18.34	0.09	g	59678.35	18.34	0.08	g	59678.35	18.36	0.06
g	59679.16	18.35	0.06	g	59679.28	18.41	0.07	g	59682.22	18.43	0.1
g	59684.28	18.62	0.13	g	59671.43	18.04	0.07	g	59689.28	18.74	0.13
g	59693.23	18.86	0.09	g	59671.43	18.05	0.05	g	59671.47	18.01	0.06
g	59672.17	18.06	0.05	g	59672.31	18.14	0.05	g	59673.32	18.13	0.06
g	59673.4	18.23	0.08	g	59697.26	19.04	0.09	g	59699.24	19.04	0.1
g	59701.31	18.96	0.1	g	59701.35	19.14	0.15	g	59711.22	19.4	0.19
g	59713.32	19.48	0.25	g	59715.22	19.29	0.13	g	59722.3	19.34	0.15
g	59724.33	19.53	0.15	g	59730.21	19.35	0.1	g	59732.19	19.61	0.17
g	59734.2	19.61	0.17	g	59736.26	19.58	0.21	g	59749.24	19.86	0.26

band	MJD	Mag	Δ Mag	band	MJD	Mag	Δ Mag	band	MJD	Mag	Δ Mag
g	59755.27	19.96	0.22	r	59623.37	18.55	0.1	r	59625.29	18.51	0.08
r	59628.42	17.92	0.07	r	59637.32	17.35	0.03	r	59638.48	17.34	0.05
r	59638.5	17.37	0.05	r	59639.3	17.39	0.04	r	59639.24	17.4	0.05
r	59639.47	17.34	0.05	r	59640.39	17.42	0.04	r	59640.41	17.42	0.04
r	59641.29	17.25	0.04	r	59641.31	17.41	0.03	r	59641.37	17.46	0.04
r	59671.36	18.39	0.07	r	59673.3	18.49	0.06	r	59674.46	18.57	0.08
r	59674.46	18.46	0.09	r	59674.46	18.47	0.09	r	59677.16	18.54	0.08
r	59676.36	18.67	0.12	r	59676.36	18.61	0.09	r	59677.37	18.65	0.08
r	59679.22	18.8	0.08	r	59679.24	18.8	0.07	r	59680.24	18.68	0.1
r	59682.32	18.86	0.13	r	59682.33	19.06	0.12	r	59684.34	19.1	0.14
r	59685.26	19.21	0.15	r	59671.36	18.41	0.07	r	59673.3	18.51	0.06
r	59707.24	19.54	0.18	r	59709.2	19.36	0.11	i	59627.4	18.36	0.13
i	59636.39	17.62	0.06	i	59639.37	17.51	0.07				

Table B.2: AT2022dbl - OUV photometry. Filters: ASAS-SN (Sg), ATLAS (o and c), Swift-UVOT (u, w1, w2, m2) and ZTF (g, r and i).

AT2022dsb - OUV photometry

band	MJD	Mag	Δ Mag	band	MJD	Mag	Δ Mag	band	MJD	Mag	Δ Mag
Sg	59635.23	17.06	0.15	Sg	59636.24	17.55	0.18	Sg	59637.51	17.72	0.16
Sg	59639.04	17.6	0.14	Sg	59639.58	17.52	0.09	Sg	59640.04	17.67	0.16
Sg	59641.44	17.04	0.12	Sg	59642.58	17.8	0.14	Sg	59644.38	17.44	0.12
Sg	59646.41	17.18	0.13	Sg	59646.98	17.49	0.16	Sg	59647.38	17.39	0.12

band	MJD	Mag	Δ Mag	band	MJD	Mag	Δ Mag	band	MJD	Mag	Δ Mag
Sg	59649.55	17.48	0.1	Sg	59708.31	18.11	0.22	Sg	59712.23	15.66	0.2
Sg	60064.0	17.14	0.11	c	59645.82	17.88	0.14	c	59672.74	18.56	0.1
o	59629.09	18.49	0.13	o	59630.09	18.16	0.12	o	59637.08	17.81	0.05
o	59644.07	18.17	0.1	o	59647.07	17.9	0.09	o	59648.07	17.88	0.06
o	59653.06	17.94	0.07	o	59654.06	18.3	0.11	o	59655.06	18.33	0.12
o	59656.06	18.23	0.15	o	59657.05	18.34	0.19	o	59658.05	18.47	0.28
o	59663.05	18.79	0.25	o	59666.04	18.56	0.15	o	59674.03	19.37	0.24
o	59677.03	19.09	0.22	o	59678.03	19.38	0.25	o	59680.02	19.92	0.33
o	59682.02	19.37	0.36	o	59694.01	18.61	0.17	o	59697.0	19.59	0.29
o	59702.0	19.63	0.34	o	59703.99	19.65	0.24	o	59705.99	19.67	0.31
o	59708.99	19.26	0.29	o	59724.97	19.74	0.25	o	59726.96	19.82	0.34
o	59731.96	19.76	0.33	o	59735.95	19.77	0.29	o	59780.89	19.49	0.25
o	59815.85	17.16	0.04	o	59818.84	19.48	0.32	o	59831.83	18.96	0.29
w1	59643.11	14.64	0.08	w1	59649.77	14.78	0.09	w1	59656.15	15.49	0.14
w1	59663.97	15.9	0.21	w1	59668.13	16.44	0.4	w1	59673.81	16.41	0.25
w2	59643.12	13.86	0.05	w2	59649.77	13.96	0.06	w2	59656.16	14.99	0.1
w2	59668.13	15.25	0.16	w2	59673.81	15.88	0.22	w2	59677.32	16.02	0.36
w2	59683.21	16.43	0.32	w2	59701.43	16.36	0.34	m2	59643.12	14.03	0.06
m2	59649.78	14.0	0.07	m2	59656.16	14.76	0.1	m2	59668.13	15.16	0.27
m2	59704.75	16.3	0.33	g	59670.48	19.22	0.11	g	59673.42	19.21	0.18
g	59675.46	19.2	0.13	r	59670.46	19.09	0.12	r	59673.48	19.05	0.15

Table B.3: AT2022dsb - OUV photometry. Filters: ASAS-SN (Sg), ATLAS (o and c), Swift-UVOT (u, w1, w2, m2) and ZTF (g, r and i).

AT2023clx - OUV photometry

band	MJD	Mag	Δ Mag	band	MJD	Mag	Δ Mag	band	MJD	Mag	Δ Mag
Sg	59921.42	16.95	0.22	Sg	59991.24	16.99	0.08	Sg	59993.24	16.73	0.08
Sg	59997.22	16.49	0.07	Sg	60000.02	16.42	0.06	Sg	60001.23	16.74	0.07
Sg	60002.37	16.86	0.09	Sg	60002.86	16.64	0.06	Sg	60003.13	16.63	0.07
Sg	60003.2	16.58	0.06	Sg	60003.86	16.73	0.06	Sg	60004.11	16.76	0.08
Sg	60005.24	16.96	0.1	Sg	60005.85	16.84	0.08	Sg	60006.21	17.16	0.18
Sg	60007.33	17.07	0.11	Sg	60008.26	16.56	0.1	Sg	60012.85	16.69	0.1
Sg	60013.82	17.23	0.12	Sg	60014.82	17.42	0.12	Sg	60015.07	17.61	0.17
Sg	60015.83	17.51	0.1	Sg	60016.07	17.37	0.12	Sg	60016.83	17.42	0.1
Sg	60017.07	17.97	0.2	Sg	60017.1	17.26	0.11	Sg	60017.88	17.57	0.11
Sg	60019.13	17.32	0.1	Sg	60019.33	17.04	0.1	Sg	60019.9	17.73	0.13
Sg	60020.84	17.59	0.11	Sg	60021.1	17.36	0.13	Sg	60021.13	17.66	0.13
Sg	60021.5	17.18	0.09	Sg	60021.84	18.21	0.19	Sg	60022.13	17.77	0.12
Sg	60022.44	16.99	0.1	Sg	60022.82	17.91	0.12	Sg	60023.15	17.68	0.14
Sg	60023.33	17.93	0.2	Sg	60024.07	17.48	0.1	Sg	60024.13	17.3	0.1
Sg	60024.41	17.96	0.16	Sg	60024.8	17.85	0.1	Sg	60025.15	17.91	0.2
Sg	60026.18	17.35	0.1	Sg	60027.1	18.01	0.14	Sg	60027.31	17.39	0.08
Sg	60028.1	17.61	0.11	Sg	60028.18	17.96	0.17	Sg	60028.35	17.94	0.12
Sg	60029.05	17.9	0.13	Sg	60029.15	17.65	0.16	Sg	60029.19	17.84	0.11
Sg	60029.37	17.7	0.09	Sg	60030.05	17.63	0.14	Sg	60030.08	17.7	0.15
Sg	60030.16	18.1	0.2	Sg	60030.34	17.44	0.09	Sg	60030.78	18.19	0.14
Sg	60031.34	17.88	0.12	Sg	60031.84	17.98	0.14	Sg	60032.07	18.34	0.18
Sg	60034.77	17.34	0.12	Sg	60041.11	16.85	0.16	Sg	60043.74	18.24	0.2

band	MJD	Mag	Δ Mag	band	MJD	Mag	Δ Mag	band	MJD	Mag	Δ Mag
Sg	60044.74	18.24	0.2	Sg	60045.14	18.18	0.14	Sg	60046.09	17.88	0.18
Sg	60046.12	17.93	0.11	Sg	60047.16	17.92	0.12	Sg	60048.17	17.62	0.11
Sg	60049.11	18.19	0.14	Sg	60049.33	18.2	0.14	Sg	60050.26	18.05	0.15
Sg	60051.2	17.96	0.13	Sg	60056.31	17.63	0.12	Sg	60058.1	17.91	0.16
Sg	60058.28	18.52	0.2	Sg	60059.14	18.39	0.15	Sg	60059.81	18.14	0.19
Sg	60060.18	18.27	0.16	Sg	60061.18	18.3	0.22	Sg	60082.33	18.59	0.2
c	59993.44	16.53	0.02	c	59997.42	16.35	0.03	c	59998.41	16.17	0.01
c	60001.39	16.35	0.02	c	60002.39	16.34	0.02	c	60005.37	16.54	0.02
c	60021.29	17.06	0.06	c	60033.23	17.62	0.04	c	60047.15	17.85	0.23
c	60049.14	18.19	0.06	c	60050.14	18.08	0.07	c	60051.13	18.19	0.07
c	60055.11	18.47	0.08	c	60056.11	18.35	0.09	c	60057.1	18.44	0.08
c	60078.99	18.78	0.14	c	60082.96	18.87	0.13	c	60104.85	19.19	0.17
c	60106.84	19.21	0.18	c	60107.83	19.42	0.25	c	60110.82	19.68	0.32
c	60112.81	19.23	0.18	c	60113.8	19.05	0.17	c	60114.8	19.47	0.24
c	60115.79	19.98	0.35	c	60116.79	18.88	0.13	o	59987.54	19.3	0.26
o	59989.54	18.23	0.1	o	59990.54	17.94	0.07	o	60002.54	16.49	0.03
o	60003.54	16.67	0.15	o	60006.54	16.66	0.05	o	60007.54	16.62	0.06
o	60013.53	17.01	0.08	o	60014.53	16.99	0.06	o	60015.53	17.01	0.04
o	60016.53	17.02	0.04	o	60017.53	17.11	0.04	o	60018.53	17.31	0.08
o	60019.53	17.17	0.03	o	60020.53	16.94	0.16	o	60021.53	17.37	0.04
o	60022.53	17.33	0.04	o	60024.53	17.5	0.05	o	60025.53	17.64	0.06
o	60026.53	17.79	0.11	o	60028.53	17.55	0.05	o	60029.53	17.63	0.05
o	60030.53	17.59	0.05	o	60033.53	17.68	0.06	o	60034.53	17.73	0.08
o	60040.53	16.85	0.15	o	60041.53	17.67	0.11	o	60042.53	18.01	0.11
o	60044.53	17.8	0.09	o	60045.53	17.93	0.1	o	60062.52	18.77	0.16

band	MJD	Mag	Δ Mag	band	MJD	Mag	Δ Mag	band	MJD	Mag	Δ Mag
o	60072.52	19.01	0.29	o	60074.52	19.29	0.36	o	60085.52	19.18	0.17
o	60089.52	18.64	0.12	o	60091.52	19.01	0.24	o	60101.51	17.24	0.16
o	60125.51	18.98	0.3	o	60139.5	18.89	0.18	u	60002.78	15.33	0.09
u	60008.5	15.83	0.2	u	60012.64	15.99	0.18	u	60020.62	15.84	0.19
u	60023.24	16.27	0.23	u	60025.88	16.38	0.24	u	60026.11	16.5	0.24
u	60030.52	16.5	0.25	u	60034.98	16.48	0.3	u	60040.84	16.68	0.25
u	60040.58	17.02	0.38	u	60043.65	16.68	0.27	u	60046.39	17.11	0.51
u	60061.18	17.2	0.54	u	60067.56	17.1	0.37	u	60082.38	17.44	0.47
w1	60002.78	15.15	0.09	w1	60008.5	15.68	0.17	w1	60012.64	15.68	0.14
w1	60020.62	16.1	0.22	w1	60023.24	16.18	0.21	w1	60025.88	16.57	0.28
w1	60026.11	16.57	0.25	w1	60030.52	16.66	0.29	w1	60034.98	16.78	0.38
w1	60040.84	16.88	0.3	w1	60040.58	17.18	0.44	w1	60043.64	17.2	0.42
w1	60072.29	17.2	0.53	w2	60002.78	15.29	0.08	w2	60008.5	15.94	0.18
w2	60012.64	16.33	0.2	w2	60020.62	16.61	0.29	w2	60023.24	16.72	0.28
w2	60025.88	16.71	0.27	w2	60026.11	16.57	0.22	w2	60030.52	16.76	0.27
w2	60040.84	17.1	0.32	w2	60040.58	17.14	0.37	w2	60043.65	17.23	0.38
w2	60046.4	17.36	0.53	w2	60067.56	17.63	0.52	m2	60002.76	14.88	0.07
m2	60008.5	15.3	0.11	m2	60012.65	15.78	0.15	m2	60020.63	16.02	0.25
m2	60023.24	16.23	0.23	m2	60026.12	16.3	0.21	m2	60030.53	16.56	0.27
m2	60040.85	16.72	0.26	m2	60040.59	16.98	0.36	m2	60043.65	16.77	0.29
m2	60046.4	16.79	0.39	m2	60067.57	17.44	0.51	m2	60072.3	17.05	0.47
g	60016.21	17.08	0.08	g	60020.22	17.23	0.06	g	60031.29	17.65	0.07
g	60031.29	17.63	0.14	g	60036.32	17.87	0.1	g	60043.29	17.99	0.15
g	60043.33	18.15	0.09	g	60045.32	18.05	0.09	g	60045.32	18.17	0.06
g	60050.18	18.29	0.08	g	60050.18	18.26	0.08	g	60052.27	18.41	0.08

band	MJD	Mag	Δ Mag	band	MJD	Mag	Δ Mag	band	MJD	Mag	Δ Mag
g	60052.27	18.2	0.1	g	60054.26	18.36	0.14	g	60054.26	18.47	0.08
g	60056.21	18.62	0.13	g	60056.21	18.7	0.1	g	60058.3	18.51	0.13
g	60058.3	18.53	0.07	g	60060.25	18.65	0.08	g	60062.21	18.39	0.14
g	60062.26	18.74	0.1	g	60073.34	18.74	0.15	g	60077.26	18.96	0.12
g	60077.29	18.68	0.16	g	60080.24	18.63	0.13	g	60080.24	18.97	0.1
g	60084.25	18.93	0.08	g	60086.31	19.13	0.14	g	60086.31	19.01	0.14
g	60088.28	19.04	0.17	g	60088.28	19.25	0.13	g	60115.24	19.77	0.2
r	59992.36	16.9	0.12	r	60016.35	17.0	0.09	r	60031.3	17.42	0.11
r	60058.21	18.39	0.18	i	60016.36	17.17	0.2	i	60016.36	17.26	0.21
i	60032.2	17.76	0.1	i	60032.2	17.67	0.13				

Table B.4: AT2023clx - OUV photometry. Filters: ASAS-SN (Sg), ATLAS (o and c), Swift-UVOT (u, w1, w2, m2) and ZTF (g, r and i).

Bibliography

- Aartsen, M. G., Abraham, K., Ackermann, M., Adams, J., Aguilar, J. A., Ahlers, M., Ahrens, M., Altmann, D., Anderson, T., Anseau, I., Anton, G., Archinger, M., Argüelles, C., Arlen, T. C., Auffenberg, J., Bai, X., Barwick, S. W., Baum, V., Bay, R., ... Zoll, M. (2016). An All-Sky Search for Three Flavors of Neutrinos from Gamma-Ray Bursts with the IceCube Neutrino Observatory. *The Astrophysical Journal*, 824(2), 115. <https://doi.org/10.3847/0004-637x/824/2/115> (cit. on p. 33).
- Aartsen, M. G., Ackermann, M., Adams, J., Aguilar, J. A., Ahlers, M., Ahrens, M., Alispach, C., Andeen, K., Anderson, T., Anseau, I., Anton, G., Argüelles, C., Auffenberg, J., Axani, S., Backes, P., Bagherpour, H., Bai, X., V., A. B., Barbano, A., ... Zöcklein, M. (2020). Characteristics of the diffuse astrophysical electron and tau neutrino flux with six years of IceCube high energy cascade data. *Physical Review Letters*, 125(12), 121104. <https://doi.org/10.1103/PhysRevLett.125.121104> (cit. on p. 99).
- Abbott, B. P., Abbott, R., Abbott, T. D., Acernese, F., Ackley, K., Adams, C., Adams, T., Addesso, P., Adhikari, R. X., Adya, V. B., Affeldt, C., Afrough, M., Agarwal, B., Agathos, M., Agatsuma, K., Aggarwal, N., Aguiar, O. D., Aiello, L., Ain, A., ... Zweizig, J. (2017). GW170817: Observation of Gravitational Waves from a Binary Neutron Star Inspiral. *Physical Review Letters*, 119(16). <https://doi.org/10.1103/physrevlett.119.161101> (cit. on p. 31).
- Abdalla, H., et al. (2021). Revealing X-ray and gamma ray temporal and spectral similarities in the GRB 190829A afterglow. *Science*, 372(6546), 1081–1085. <https://doi.org/10.1126/science.abe8560> (cit. on pp. 3, 32, 33).
- Abdalla, H. E., Adam, R., Aharonian, F., Benkhali, F. A., Angüner, E. O., Arakawa, M., Arcaro, C., Armand, C., Ashkar, H., Backes, M., Martins, V. B., Barnard, M., Becherini, Y., Berge, D., Bernloehr, K., Bissaldi, E., Blackwell, R., Boettcher, M., Boisson, C., ... Roberts, O. J. (2019). A very-high-energy component deep in the gamma-ray burst afterglow. *Nature : the international weekly journal of science*, 575(7783), 464–+. <https://doi.org/10.1038/s41586-019-1743-9> (cit. on pp. 3, 32).
- Abdollahi, S., Acero, F., Ackermann, M., Ajello, M., Atwood, W. B., Axelsson, M., Baldini, L., Ballet, J., Barbiellini, G., Bastieri, D., Becerra Gonzalez, J., Bellazzini, R., Berretta, A., Bissaldi, E., Blandford, R. D., Bloom, E. D., Bonino, R., Bottacini, E., Brandt, T. J., ... Zaharijas, G. (2020). Fermi Large Area Telescope Fourth Source Catalog. *Astrophys. J. Suppl. Ser.*, 247(1), Article 33, 33. <https://doi.org/10.3847/1538-4365/ab6bcb> (cit. on pp. 2, 198).

- Abeyssekara, A. U., Archer, A., Benbow, W., Bird, R., Brose, R., Buchovecky, M., Bugaev, V., Connolly, M. P., Cui, W., Errando, M., Falcone, A., Feng, Q., Finley, J. P., Flinders, A., Fortson, L., Furniss, A., Gillanders, G. H., Hütten, M., Hanna, D., ... Beloborodov, A. (2018). A Strong Limit on the Very-high-energy Emission from GRB 150323A. *The Astrophysical Journal*, 857(1), 33. <https://doi.org/10.3847/1538-4357/aab371> (cit. on p. 132).
- Abraham, J., et al. (2008). Observation of the Suppression of the Flux of Cosmic Rays above 4×10^{19} eV. *Physical Review Letters*, 101(6). <https://doi.org/10.1103/physrevlett.101.061101> (cit. on p. 2).
- Acciari, V. A., et al. (2019a). Teraelectronvolt emission from the γ -ray burst GRB 190114C. *Nature*, 575(7783), 455–458. <https://doi.org/10.1038/s41586-019-1750-x> (cit. on pp. 3, 32).
- Acciari, V. A., Aliu, E., Arlen, T., Aune, T., Bautista, M., Beilicke, M., Benbow, W., Böttcher, M., Boltuch, D., Bradbury, S. M., Buckley, J. H., Bugaev, V., Byrum, K., Cannon, A., Cesarini, A., Chow, Y. C., Ciupik, L., Cogan, P., Cui, W., ... Terndrup, D. M. (2009). Discovery of very high energy gamma rays from PKS 1424+240 and multiwavelength constraints on its redshift. *The Astrophysical Journal*, 708(2), L100–L106. <https://doi.org/10.1088/2041-8205/708/2/l100> (cit. on pp. 84, 85).
- Acciari, V. A., Ansoldi, S., Antonelli, L. A., Arbet Engels, A., Arcaro, C., Baack, D., Babić, A., Banerjee, B., Bangale, P., Barres de Almeida, U., Barrio, J. A., Becerra González, J., Bednarek, W., Bellizzi, L., Bernardini, E., Berti, A., Besenrieder, J., Bhattacharyya, W., Bigongiari, C., ... Walker, R. C. (2020). Monitoring of the radio galaxy M87 during a low-emission state from 2012 to 2015 with MAGIC. *Mon. Not. R. Astron. Soc.*, 492, 5354–5365. <https://doi.org/10.1093/mnras/staa014> (cit. on p. 86).
- Acciari, V. A., Ansoldi, S., Antonelli, L. A., Arbet Engels, A., Artero, M., Asano, K., Baack, D., Babić, A., Baquero, A., Barres de Almeida, U., Barrio, J. A., Batković, I., Becerra González, J., Bednarek, W., Bellizzi, L., Bernardini, E., Bernardos, M., Berti, A., Besenrieder, J., ... Valisa, P. (2022). Proton acceleration in thermonuclear nova explosions revealed by gamma rays. *Nature Astronomy*, 6(6), 689–697. <https://doi.org/10.1038/s41550-022-01640-z> (cit. on pp. 3, 21).
- Acciari, V. A., Ansoldi, S., Antonelli, L. A., Arbet Engels, A., Baack, D., Babić, A., Banerjee, B., Barres de Almeida, U., Barrio, J. A., Becerra González, J., Bednarek, W., Bellizzi, L., Bernardini, E., Berti, A., Besenrieder, J., Bhattacharyya, W., Bigongiari, C., Biland, A., Blanch, O., ... Zarić, D. (2019b). Measurement of the extragalactic background light using MAGIC and Fermi-LAT gamma-ray observations of blazars up to $z = 1$. *Mon. Not. R. Astron. Soc.*, 486(3), 4233–4251. <https://doi.org/10.1093/mnras/stz943> (cit. on p. 12).
- Acciari, V. A., Arlen, T., Aune, T., Beilicke, M., Benbow, W., Böttcher, M., Boltuch, D., Bradbury, S. M., Buckley, J. H., Bugaev, V., Cannon, A., Cesarini, A., Ciupik, L., Cui, W., Dickherber, R., Duke, C., Errando, M., Falcone, A., Finley, J. P., ... Hayashida, M. (2011). Spectral Energy Distribution of Markarian 501: Quiescent State vs. Extreme Outburst. *The Astrophysical Journal*, 729(1), 2. <https://doi.org/10.1088/0004-637X/729/1/2> (cit. on p. 148).

- Acharyya, A., Adams, C. B., Bangale, P., Benbow, W., Buckley, J. H., Capasso, M., Dwarkadas, V. V., Errando, M., Falcone, A., Feng, Q., Finley, J. P., Foote, G. M., Fortson, L., Furniss, A., Gallagher, G., Gent, A., Hanlon, W. F., Hervet, O., Holder, J., ... Vurm, I. (2023). VERITAS and Fermi-LAT constraints on the Gamma-ray Emission from Superluminous Supernovae SN2015bn and SN2017egm. *The Astrophysical Journal*, 945(1), 30. <https://doi.org/10.3847/1538-4357/acb7e6> (cit. on p. 138).
- Achterberg, A., Gallant, Y. A., Kirk, J. G., & Guthmann, A. W. (2001). Particle acceleration by ultrarelativistic shocks: theory and simulations. *Mon. Not. R. Astron. Soc.*, 328(2), 393–408. <https://doi.org/10.1046/j.1365-8711.2001.04851.x> (cit. on p. 16).
- Actis, M., Agnetta, G., Aharonian, F., Akhperjanian, A., Aleksić, J., Aliu, E., Allan, D., Allekotte, I., Antico, F., Antonelli, L. A., Antoranz, P., Aravantinos, A., Arlen, T., Araldi, H., Artmann, S., Asano, K., Asorey, H., Bähr, J., Bais, A., ... Zychowski, P. (2011). Design concepts for the Cherenkov Telescope Array CTA: an advanced facility for ground-based high-energy gamma-ray astronomy. *Experimental Astronomy*, 32(3), 193–316. <https://doi.org/10.1007/s10686-011-9247-0> (cit. on p. 41).
- Adams, C. B., Benbow, W., Brill, A., Buckley, J. H., Christiansen, J. L., Falcone, A., Feng, Q., Finley, J. P., Foote, G. M., Fortson, L., Furniss, A., Giuri, C., Hanna, D., Hassan, T., Hervet, O., Holder, J., Hona, B., Humensky, T. B., Jin, W., ... Williamson, T. J. (2022). The throughput calibration of the VERITAS telescopes. *Astronomy amp; Astrophysics*, 658, A83. <https://doi.org/10.1051/0004-6361/202142275> (cit. on pp. 40, 42, 44, 45, 61, 80, 81, 127).
- Aghanim, N., Akrami, Y., Ashdown, M., Aumont, J., Baccigalupi, C., Ballardini, M., Banday, A. J., Barreiro, R. B., Bartolo, N., Basak, S., Battye, R., Benabed, K., Bernard, J.-P., Bersanelli, M., Bielewicz, P., Bock, J. J., Bond, J. R., Borrill, J., Bouchet, F. R., ... Zonca, A. (2020). Planck 2018 results: VI. Cosmological parameters. *Astronomy amp; Astrophysics*, 641, A6. <https://doi.org/10.1051/0004-6361/201833910> (cit. on p. 104).
- Aharonian, F., Ait Benkhali, F., Angüner, E. O., Ashkar, H., Backes, M., Baghmany, V., Barbosa Martins, V., Batzofin, R., Becherini, Y., Berge, D., Bernlöhr, K., Bi, B., Böttcher, M., Boisson, C., Bolmont, J., de Bony de Lavergne, M., Breuhaus, M., Brose, R., Brun, F., ... Żywucka, N. (2022). Time-resolved hadronic particle acceleration in the recurrent nova RS Ophiuchi. *Science*, 376(6588), 77–80. <https://doi.org/10.1126/science.abn0567> (cit. on pp. 3, 21).
- Aharonian, F., Ait Benkhali, F., Arcaro, C., Aschersleben, J., Backes, M., Barbosa Martins, V., Batzofin, R., Becherini, Y., Berge, D., Bernlöhr, K., Bi, B., Böttcher, M., Boisson, C., Bolmont, J., Borowska, J., Bradascio, F., Breuhaus, M., Brose, R., Brun, F., ... Żywucka, N. (2023). Constraining the cosmic-ray pressure in the inner Virgo Cluster using H.E.S.S. observations of M 87. *Astronomy & Astrophysics*, 675, A138. <https://doi.org/10.1051/0004-6361/202346056> (cit. on p. 86).
- Aharonian, F., Akhperjanian, A. G., Aye, K.-M., Bazer-Bachi, A. R., Beilicke, M., Benbow, W., Berge, D., Berghaus, P., Bernlöhr, K., Bolz, O., Boisson, C., Borgmeier, C., Breitling, F., Brown, A. M., Bussons Gordo, J., Chadwick, P. M., Chitnis, V. R., Chounet, L.-M., Cornils, R., ... Wagner, S. J. (2005). H.E.S.S. observations of PKS 2155-304. *Astronomy*

- & *Astrophysics*, 430(3), 865–875. <https://doi.org/10.1051/0004-6361:20041853> (cit. on p. 67).
- Aharonian, F., Akhperjanian, A. G., Bazer-Bachi, A. R., Beilicke, M., Benbow, W., Berge, D., Bernlöhr, K., Boisson, C., Bolz, O., Borrel, V., Braun, I., Breitling, F., Brown, A. M., Bühler, R., Büsching, I., Carrigan, S., Chadwick, P. M., Chounet, L.-M., Cornils, R., ... Ward, M. (2006). Observations of the Crab nebula with H.E.S.S. *Astronomy and Astrophysics*, 457(3), 899–915. <https://doi.org/10.1051/0004-6361:20065351> (cit. on pp. 80, 127).
- Aharonian, F., Benkhali, F. A., Aschersleben, J., Ashkar, H., Backes, M., Baktash, A., Martins, V. B., Batzofin, R., Becherini, Y., Berge, D., Bernlöhr, K., Bi, B., Böttcher, M., Boisson, C., Bolmont, J., de Bony de Lavergne, M., Borowska, J., Bouyahiaoui, M., Bradascio, F., ... Żywucka, N. (2023). H.E.S.S. Follow-up Observations of GRB 221009A. *Astrophys. J. Lett.*, 946(1), L27. <https://doi.org/10.3847/2041-8213/acc405> (cit. on pp. 133, 135).
- Aharonian, F., Hofmann, W., Konopelko, A. K., & Völk, H. J. (1997). The potential of the ground based arrays of imaging atmospheric Cherenkov telescopes. II. Gamma ray flux sensitivities. *Astroparticle Physics*, 6(3-4), 369–377. [https://doi.org/10.1016/S0927-6505\(96\)00070-9](https://doi.org/10.1016/S0927-6505(96)00070-9) (cit. on p. 55).
- Aharonian, F. (2004). *Very high energy cosmic gamma radiation: a crucial window on the extreme Universe*. <https://doi.org/10.1142/4657> (cit. on pp. 2, 7, 9–11, 13, 17–19, 67, 120).
- Ahnen, M. L., Ansoldi, S., Antonelli, L. A., Arcaro, C., Babić, A., Banerjee, B., Bangale, P., Barresde Almeida, U., Barrio, J. A., BecerraGonzález, J., Bednarek, W., Bernardini, E., Berti, A., Bhattacharyya, W., Blanch, O., Bonnoli, G., Carosi, R., Carosi, A., Chatterjee, A., ... Baring, M. G. (2018). Extreme HBL behavior of Markarian 501 during 2012. *Astronomy and Astrophysics*, 620, A181. <https://doi.org/10.1051/0004-6361/201833704> (cit. on p. 148).
- Ajello, M., Atwood, W. B., Axelsson, M., Bagagli, R., Bagni, M., Baldini, L., Bastieri, D., Bellardi, F., Bellazzini, R., Bissaldi, E., Bloom, E. D., Bonino, R., Bregeon, J., Brez, A., Bruel, P., Buehler, R., Buson, S., Cameron, R. A., Caraveo, P. A., ... Zaharijas, G. (2021). Fermi Large Area Telescope Performance after 10 Years of Operation. *The Astrophysical Journal Supplement Series*, 256(1), 12. <https://doi.org/10.3847/1538-4365/ac0ceb> (cit. on pp. 2, 6).
- Alameddine, J.-M. (2023). The particle-shower simulation code CORSIKA 8. *Proceedings of 38th International Cosmic Ray Conference - PoS(ICRC2023)*, 310. <https://doi.org/10.22323/1.444.0310> (cit. on pp. 53, 75).
- Aleksić, J., Ansoldi, S., Antonelli, L., Antoranz, P., Babic, A., Bangale, P., Barrio, J., Becerra González, J., Bednarek, W., Bernardini, E., Biasuzzi, B., Biland, A., Blanch, O., Bonnefoy, S., Bonnoli, G., Borracci, F., Bretz, T., Carmona, E., Carosi, A., ... Meyer, M. (2015). Measurement of the Crab Nebula spectrum over three decades in energy with the MAGIC telescopes. *Journal of High Energy Astrophysics*, 5–6, 30–38. <https://doi.org/10.1016/j.jheap.2015.01.002> (cit. on pp. 80, 127).

- Alexander, K. D., Berger, E., Guillochon, J., Zauderer, B. A., & Williams, P. K. G. (2016). Discovery of an Outflow from Radio Observations of the Tidal Disruption Event ASASSN-14li. *Astrophys. J. Lett.*, 819(2), Article L25, L25. <https://doi.org/10.3847/2041-8205/819/2/L25> (cit. on p. 26).
- Alexander, K. D., van Velzen, S., Horesh, A., & Zauderer, B. A. (2020). Radio Properties of Tidal Disruption Events. *Space Science Reviews*, 216(5), 81. <https://doi.org/10.1007/s11214-020-00702-w> (cit. on pp. 26, 103).
- Aliu, E., Archer, A., Aune, T., Barnacka, A., Behera, B., Beilicke, M., Benbow, W., Berger, K., Bird, R., Buckley, J. H., Bugaev, V., Byrum, K., Cardenzana, J. V., Cerruti, M., Chen, X., Ciupik, L., Connolly, M. P., Cui, W., Dickinson, H. J., ... Zitzer, B. (2015). VERITAS Observations of the BL Lac Object PG 1553+113. *The Astrophysical Journal*, 799, 7. <https://doi.org/10.1088/0004-637X/799/1/7> (cit. on p. 86).
- Aliu, E., Arlen, T., Aune, T., Beilicke, M., Benbow, W., Böttcher, M., Bouvier, A., Bradbury, S. M., Buckley, J. H., Bugaev, V., Cannon, A., Cesarini, A., Ciupik, L., Collins-Hughes, E., Connolly, M. P., Cui, W., Dickherber, R., Errando, M., Falcone, A., ... Williams, D. A. (2011). VERITAS Observations of the Unusual Extragalactic Transient Swift J164449.3+573451. *The Astrophysical Journal*, 738, L30. <https://doi.org/10.1088/2041-8205/738/2/L30> (cit. on pp. 100, 121, 122).
- Aliu, E., Aune, T., Barnacka, A., Beilicke, M., Benbow, W., Berger, K., Biteau, J., Buckley, J. H., Bugaev, V., Byrum, K., Cardenzana, J. V., Cerruti, M., Chen, X., Ciupik, L., Connaughton, V., Cui, W., Dickinson, H. J., Eisch, J. D., Errando, M., ... Zhu, S. (2014). Constraints on Very High Energy Emission from GRB 130427A. *The Astrophysical Journal*, 795(1), L3. <https://doi.org/10.1088/2041-8205/795/1/L3> (cit. on p. 132).
- Andreoni, I., Coughlin, M. W., Perley, D. A., Yao, Y., Lu, W., Cenko, S. B., Kumar, H., Anand, S., Ho, A. Y. Q., Kasliwal, M. M., Postigo, A. d. U., Sagues-Carracedo, A., Schulze, S., Kann, D. A., Kulkarni, S. R., Sollerman, J., Tanvir, N., Rest, A., Izzo, L., ... Zhang, J. (2022). A Very Luminous Jet from the Disruption of a Star by a Massive Black Hole. *Nature*, 612(7940), 430–434. <https://doi.org/10.1038/s41586-022-05465-8> (cit. on p. 100).
- Angelini, L., Cenko, S. B., Kennea, J. A., Siegel, M. H., & Barthelmy, S. D. (2024). The Neil Gehrels Swift Observatory. In *Handbook of X-ray and Gamma-ray Astrophysics* (pp. 1423–1454). Springer Nature Singapore. https://doi.org/10.1007/978-981-19-6960-7_155 (cit. on p. 104).
- Arbet-Engels, A., Baack, D., Balbo, M., Biland, A., Bretz, T., Buss, J., Dorner, D., Eisenberger, L., Elsaesser, D., Hildebrand, D., Iotov, R., Kalenski, A., Mannheim, K., Mitchell, A., Neise, D., Noethe, M., Paravac, A., Rhode, W., Schleicher, B., ... Walter, R. (2021). Long-term multi-band photometric monitoring of Mrk 501. *Astronomy & Astrophysics*, 655, A93. <https://doi.org/10.1051/0004-6361/202141886> (cit. on p. 148).

- Archambault, S., Archer, A., Benbow, W., Bird, R., Bourbeau, E., Bouvier, A., Buchovecky, M., Bugaev, V., Cardenzana, J., Cerruti, M., Ciupik, L., Connolly, M., Cui, W., Daniel, M., Errando, M., Falcone, A., Feng, Q., Finley, J., Fleischhack, H., ... Zitzer, B. (2017). Gamma-ray observations under bright moonlight with VERITAS. *Astroparticle Physics*, *91*, 34–43. <https://doi.org/10.1016/j.astropartphys.2017.03.001> (cit. on pp. 46, 126, 127, 131).
- Archambault, S., Aune, T., Behera, B., Beilicke, M., Benbow, W., Berger, K., Bird, R., Biteau, J., Bugaev, V., Byrum, K., Cardenzana, J. V., Cerruti, M., Chen, X., Ciupik, L., Connolly, M. P., Cui, W., Dumm, J., Errando, M., Falcone, A., ... Fermi LAT Collaboration. (2014). Deep Broadband Observations of the Distant Gamma-Ray Blazar PKS 1424+240. *Astrophys. J. Lett.*, *785*(1), Article L16, L16. <https://doi.org/10.1088/2041-8205/785/1/L16> (cit. on pp. 84, 85).
- Auchettl, K., Guillochon, J., & Ramirez-Ruiz, E. (2017). New Physical Insights about Tidal Disruption Events from a Comprehensive Observational Inventory at X-Ray Wavelengths. *Astrophys. J.*, *838*(2), Article 149, 149. <https://doi.org/10.3847/1538-4357/aa633b> (cit. on p. 22).
- Aydi, E., Sokolovsky, K. V., Chomiuk, L., Steinberg, E., Li, K. L., Vurm, I., Metzger, B. D., Strader, J., Mukai, K., Pejcha, O., Shen, K. J., Wade, G. A., Kuschnig, R., Moffat, A. F. J., Pablo, H., Pigulski, A., Popowicz, A., Weiss, W., Zwintz, K., ... Sokoloski, J. L. (2020). Direct evidence for shock-powered optical emission in a nova. (Cit. on pp. 20, 21, 35, 118).
- Barrau, A., Bazer-Bachi, R., Beyer, E., Cabot, H., Cerutti, M., Chounet, L., Debiais, G., Degrange, B., Delchini, H., Denance, J., Descotes, G., Dezalay, J., Djannati-Ataï, A., Dumora, D., Espigat, P., Fabre, B., Fleury, P., Fontaine, G., George, R., ... Vrana, J. (1998). The CAT imaging telescope for very-high-energy gamma-ray astronomy. *Nuclear Instruments and Methods in Physics Research Section A: Accelerators, Spectrometers, Detectors and Associated Equipment*, *416*(2–3), 278–292. [https://doi.org/10.1016/s0168-9002\(98\)00749-9](https://doi.org/10.1016/s0168-9002(98)00749-9) (cit. on p. 6).
- Bell, A. R. (1978). The acceleration of cosmic rays in shock fronts – I. *Mon. Not. R. Astron. Soc.*, *182*(2), 147–156. <https://doi.org/10.1093/mnras/182.2.147> (cit. on p. 13).
- Bell, A. R. (1987). The non-linear self-regulation of cosmic ray acceleration at shocks. *Mon. Not. R. Astron. Soc.*, *225*, 615–626. <https://doi.org/10.1093/mnras/225.3.615> (cit. on p. 16).
- Bell, A. R., & Lucek, S. G. (2001). Cosmic ray acceleration to very high energy through the non-linear amplification by cosmic rays of the seed magnetic field. *Mon. Not. R. Astron. Soc.*, *321*(3), 433–438. <https://doi.org/10.1046/j.1365-8711.2001.04063.x> (cit. on p. 35).
- Bellm, E. C., Kulkarni, S. R., Graham, M. J., Dekany, R., Smith, R. M., Riddle, R., Masci, F. J., Helou, G., Prince, T. A., Adams, S. M., Barbarino, C., Barlow, T., Bauer, J., Beck, R., Belicki, J., Biswas, R., Blagorodnova, N., Bodewits, D., Bolin, B., ... Zolkower, J. (2018). The Zwicky Transient Facility: System Overview, Performance, and First Results. *Publications of the Astronomical Society of the Pacific*, *131*(995), 018002. <https://doi.org/10.1088/1538-3873/aaecbe> (cit. on pp. 3, 102, 194).

- Beloborodov, A. M., & Mészáros, P. (2017). Photospheric Emission of Gamma-Ray Bursts. *Space Science Reviews*, 207(1–4), 87–110. <https://doi.org/10.1007/s11214-017-0348-6> (cit. on p. 31).
- Benbow, W. (2015). Highlights from the VERITAS AGN Observation Program. *34th International Cosmic Ray Conference (ICRC2015)*, 34, Article 821, 821. <https://doi.org/10.22323/1.236.0821> (cit. on pp. 85, 86).
- Beniamini, P., Giannios, D., & Metzger, B. D. (2017). Constraints on millisecond magnetars as the engines of prompt emission in gamma-ray bursts. *Mon. Not. Roy. Astron. Soc.*, 472(3), 3058–3073. <https://doi.org/10.1093/mnras/stx2095> (cit. on p. 31).
- Berge, D., Funk, S., & Hinton, J. (2007). Background modelling in very-high-energy γ -ray astronomy. *Astronomy and Astrophysics*, 466(3), 1219–1229. <https://doi.org/10.1051/0004-6361:20066674> (cit. on pp. 57, 58, 78, 148).
- Bethe, H., & Heitler, W. (1934). On the Stopping of Fast Particles and on the Creation of Positive Electrons. *Proceedings of the Royal Society of London Series A*, 146(856), 83–112. <https://doi.org/10.1098/rspa.1934.0140> (cit. on p. 8).
- Biehl, D., Boncioli, D., Lunardini, C., & Winter, W. (2018). Tidally disrupted stars as a possible origin of both cosmic rays and neutrinos at the highest energies. *Scientific Reports*, 8(1). <https://doi.org/10.1038/s41598-018-29022-4> (cit. on p. 27).
- Biskamp, D. (1996). Magnetic Reconnection in Plasmas. *Astrophys. Space Sci.*, 242(1-2), 165–207. <https://doi.org/10.1007/BF00645113> (cit. on p. 16).
- Blandford, R. D., & Ostriker, J. P. (1978). Particle acceleration by astrophysical shocks. *Astrophys. J. Lett.*, 221, L29–L32. <https://doi.org/10.1086/182658> (cit. on p. 13).
- Blandford, R., Meier, D., & Readhead, A. (2019). Relativistic jets from active galactic nuclei. *Annual Review of Astronomy and Astrophysics*, 57(1), 467–509. <https://doi.org/10.1146/annurev-astro-081817-051948> (cit. on p. 23).
- Blasi, P. (2002). A semi-analytical approach to non-linear shock acceleration. *Astroparticle Physics*, 16(4), 429–439. [https://doi.org/10.1016/s0927-6505\(01\)00127-x](https://doi.org/10.1016/s0927-6505(01)00127-x) (cit. on p. 16).
- Bloom, J. S., Giannios, D., Metzger, B. D., Cenko, S. B., Perley, D. A., Butler, N. R., Tanvir, N. R., Levan, A. J., O’Brien, P. T., Strubbe, L. E., De Colle, F., Ramirez-Ruiz, E., Lee, W. H., Nayakshin, S., Quataert, E., King, A. R., Cucchiara, A., Guillochon, J., Bower, G. C., ... van der Horst, A. J. (2011). A Possible Relativistic Jetted Outburst from a Massive Black Hole Fed by a Tidally Disrupted Star. *Science*, 333(6039), 203. <https://doi.org/10.1126/science.1207150> (cit. on p. 24).
- Bond, I. H., Hillas, A. M., & Bradbury, S. M. (2003). An island method of image cleaning for near threshold events from atmospheric Cherenkov telescopes. *Astropart. Phys.*, 20, 311–321. [https://doi.org/10.1016/S0927-6505\(03\)00193-2](https://doi.org/10.1016/S0927-6505(03)00193-2) (cit. on p. 49).
- Bose, D., Chitnis, V. R., Majumdar, P., & Shukla, A. (2022). Galactic and extragalactic sources of very high energy gamma rays. *European Physical Journal Special Topics*, 231(1), 27–66. <https://doi.org/10.1140/epjs/s11734-022-00434-8> (cit. on p. 2).
- Bradley Cenko, S., Krimm, H. A., Horesh, A., Rau, A., Frail, D. A., Kennea, J. A., Levan, A. J., Holland, S. T., Butler, N. R., Quimby, R. M., Bloom, J. S., Filippenko, A. V., Gal-Yam,

- A., Greiner, J., Kulkarni, S. R., Ofek, E. O., Olivares E., F., Schady, P., Silverman, J. M., ... Xu, D. (2012). Swift J2058.4+0516: Discovery of a Possible Second Relativistic Tidal Disruption Flare? *The Astrophysical Journal*, 753(1), 77. <https://doi.org/10.1088/0004-637x/753/1/77> (cit. on p. 24).
- Brough, S., Collins, C., Demarco, R., Ferguson, H. C., Galaz, G., Holwerda, B., Martinez-Lombilla, C., Mihos, C., & Montes, M. (2020). The Vera Rubin Observatory Legacy Survey of Space and Time and the Low Surface Brightness Universe. *arXiv e-prints*, Article arXiv:2001.11067, arXiv:2001.11067. <https://doi.org/10.48550/arXiv.2001.11067> (cit. on p. 124).
- Brown, G. C., Levan, A. J., Stanway, E. R., Tanvir, N. R., Cenko, S. B., Berger, E., Chornock, R., & Cucchiaria, A. (2015). Swift J1112.2–8238: a candidate relativistic tidal disruption flare. *Mon. Not. R. Astron. Soc.*, 452(4), 4297–4306. <https://doi.org/10.1093/mnras/stv1520> (cit. on p. 24).
- Bruel, P., Burnett, T. H., Digel, S. W., Johannesson, G., Omodei, N., & Wood, M. (2018). Fermi-LAT improved Pass~8 event selection. *8th International Fermi Symposium: Celebrating 10 Year of Fermi* (cit. on p. 197).
- Burrows, D. N., Kennea, J. A., Ghisellini, G., Mangano, V., Zhang, B., Page, K. L., Eracleous, M., Romano, P., Sakamoto, T., Falcone, A. D., Osborne, J. P., Campana, S., Beardmore, A. P., Breeveld, A. A., Chester, M. M., Corbet, R., Covino, S., Cummings, J. R., D'Avanzo, P., ... Gehrels, N. (2011). Relativistic jet activity from the tidal disruption of a star by a massive black hole. *Nature*, 476(7361), 421–424. <https://doi.org/10.1038/nature10374> (cit. on p. 24).
- Burrows, D. N., Hill, J. E., Nousek, J. A., Kennea, J. A., Wells, A., Osborne, J. P., Abbey, A. F., Beardmore, A., Mukerjee, K., Short, A. D. T., Chincarini, G., Campana, S., Citterio, O., Moretti, A., Pagani, C., Tagliaferri, G., Giommi, P., Capalbi, M., Tamburelli, F., ... Hartner, G. D. (2005a). The Swift X-ray Telescope. *Space Science Reviews*, 120(3-4), 165–195. <https://doi.org/10.1007/s11214-005-5097-2> (cit. on p. 23).
- Burrows, D. N., Hill, J. E., Nousek, J. A., Kennea, J. A., Wells, A., Osborne, J. P., Abbey, A. F., Beardmore, A., Mukerjee, K., Short, A. D. T., Chincarini, G., Campana, S., Citterio, O., Moretti, A., Pagani, C., Tagliaferri, G., Giommi, P., Capalbi, M., Tamburelli, F., ... Hartner, G. D. (2005b). The Swift X-ray Telescope. *Space Science Reviews*, 120(3-4), 165–195. <https://doi.org/10.1007/s11214-005-5097-2> (cit. on pp. 100, 195).
- Cahillane, C., & Mansell, G. (2022). Review of the Advanced LIGO Gravitational Wave Observatories Leading to Observing Run Four. *Galaxies*, 10(1), 36. <https://doi.org/10.3390/galaxies10010036> (cit. on p. 2).
- Cao, Z., della Volpe, D., Liu, S., Editors, : Bi, X., Chen, Y., D'Ettorre Piazzoli, B., Feng, L., Jia, H., Li, Z., Ma, X., Wang, X., Zhang, X., Referees, E., : Qie, X., Hu, H., Referees, I., ... Zuo, X. (2019). The Large High Altitude Air Shower Observatory (LHAASO) Science Book (2021 Edition). *arXiv e-prints*, Article arXiv:1905.02773, arXiv:1905.02773. <https://doi.org/10.48550/arXiv.1905.02773> (cit. on p. 132).

- Caraveo, P. (2020). The golden age of high-energy gamma-ray astronomy: the Cherenkov Telescope Array in the multimessenger era. *La Rivista del Nuovo Cimento*, 43. <https://doi.org/10.1007/s40766-020-00006-3> (cit. on p. 61).
- Chantell, M., Akerlof, C. W., Buckley, J., Carter-Lewis, D. A., Cawley, M. F., Connaughton, V., Fegan, D. J., Fleury, P., Gaidos, J., Hillas, A. M., Lamb, R. C., Pare, E., Rose, H. J., Rovero, A. C., Sarazin, X., Sembroski, G., Schubnell, M. S., Urban, M., Weekes, T. C., & Wilson, C. (1995). Gamma-Ray Observations in Moonlight with the Whipple Atmospheric Cherenkov Hybrid Camera. *International Cosmic Ray Conference*, 2, 544 (cit. on p. 67).
- Charalampopoulos, P., Kotak, R., Wevers, T., Leloudas, G., Kravtsov, T., Ramsden, P., Reynolds, T. M., Aamer, A., Anderson, J. P., Arcavi, I., Cai, Y.-Z., Chen, T.-W., Dennefeld, M., Galbany, L., Gromadzki, M., Gutiérrez, C. P., Ihanec, N., Kangas, T., Kankare, E., ... Young, D. R. (2024, January). The fast transient AT 2023clx in the nearby LINER galaxy NGC 3799, as a tidal disruption event of a very low-mass star. <https://doi.org/10.48550/arXiv.2401.11773> (cit. on p. 106).
- Chen, C., & Shen, R.-F. (2022). Radiative Diffusion in a Time-dependent Outflow: a Model for Fast Blue Optical Transients. *Research in Astronomy and Astrophysics*, 22(3), 035017. <https://doi.org/10.1088/1674-4527/ac488a> (cit. on p. 34).
- Chen, X., Gómez-Vargas, G. A., & Guillochon, J. (2016). The γ -ray afterglows of tidal disruption events. *Mon. Not. R. Astron. Soc.*, 458(3), 3314–3323. <https://doi.org/10.1093/mnras/stw437> (cit. on p. 28).
- Chen, Y.-P., Zaw, I., Farrar, G. R., & Elgamal, S. (2022). A Uniformly Selected, Southern-sky 6dF, Optical AGN Catalog. *The Astrophysical Journal Supplement Series*, 258(2), 29. <https://doi.org/10.3847/1538-4365/ac4157> (cit. on p. 105).
- Cherenkov, P. A. (1934). Visible emission of clean liquids by action of gamma radiation. *Doklady Akademii Nauk SSSR*, 2, 451 (cit. on p. 17).
- Cheung, C. C., Johnson, T. J., Jean, P., Kerr, M., Page, K. L., Osborne, J. P., Beardmore, A. P., Sokolovsky, K. V., Teyssier, F., Ciprini, S., Martí-Devesa, G., Mereu, I., Razzaque, S., Wood, K. S., Shore, S. N., Korotkiy, S., Levina, A., & Blumenzweig, A. (2022). Fermi LAT Gamma-ray Detection of the Recurrent Nova RS Ophiuchi during its 2021 Outburst. *The Astrophysical Journal*, 935(1), 44. <https://doi.org/10.3847/1538-4357/ac7eb7> (cit. on p. 21).
- Cogan, P. (2007). VEGAS, the VERITAS Gamma-ray Analysis Suite. (Cit. on p. 49).
- Cooray, A. (2016, March). Extragalactic background light: Measurements and applications. <https://doi.org/10.1098/rsos.150555> (cit. on p. 12).
- Cristofari, P. (2021). The Hunt for Pevatrons: The Case of Supernova Remnants. *Universe*, 7(9). <https://doi.org/10.3390/universe7090324> (cit. on p. 35).
- Cucchiara, A., Levan, A. J., Fox, D. B., Tanvir, N. R., Ukwatta, T. N., Berger, E., Krühler, T., Yoldaş, A. K., Wu, X. F., Toma, K., Greiner, J., E. Olivares, F., Rowlinson, A., Amati, L., Sakamoto, T., Roth, K., Stephens, A., Fritz, A., Fynbo, J. P. U., ... D'Avanzo, P. (2011). A Photometric Redshift of $z \sim 9.4$ for GRB 090429B. *The Astrophysical Journal*, 736(1), 7. <https://doi.org/10.1088/0004-637x/736/1/7> (cit. on p. 32).

- Dai, L., McKinney, J. C., Roth, N., Ramirez-Ruiz, E., & Miller, M. C. (2018). A Unified Model for Tidal Disruption Events. *The Astrophysical Journal*, 859(2), L20. <https://doi.org/10.3847/2041-8213/aab429> (cit. on pp. 27, 28, 113).
- Dai, Z., Daigne, F., & Mészáros, P. (2017). The Theory of Gamma-Ray Bursts. *Space Sci. Rev.*, 212(1-2), 409–427. <https://doi.org/10.1007/s11214-017-0423-z> (cit. on p. 30).
- Daniel, M. (2007). The veritas standard data analysis. *Proceedings of the 30th International Cosmic Ray Conference, ICRC 2007*, 3, 1325 (cit. on pp. 47, 49).
- Davies, J. M., & Cotton, E. S. (1957). Design of the Quartermaster Solar Furnace. *Solar Energy*, 1(2), 16–22. [https://doi.org/10.1016/0038-092X\(57\)90116-0](https://doi.org/10.1016/0038-092X(57)90116-0) (cit. on p. 40).
- De Colle, F., & Lu, W. (2020a). Jets from Tidal Disruption Events. *New Astronomy Reviews*, 89, 101538. <https://doi.org/10.1016/j.newar.2020.101538> (cit. on pp. 24, 27).
- De Colle, F., & Lu, W. (2020b). Jets from Tidal Disruption Events. *New Astronomy Reviews*, 89, 101538. <https://doi.org/10.1016/j.newar.2020.101538> (cit. on pp. 24, 25, 27).
- de Jager, O. C., Harding, A. K., Michelson, P. F., Nel, H. I., Nolan, P. L., Sreekumar, P., & Thompson, D. J. (1996). Gamma-Ray Observations of the Crab Nebula: A Study of the Synchro-Compton Spectrum. *Astrophys. J.*, 457, 253. <https://doi.org/10.1086/176726> (cit. on p. 32).
- de Naurois, M. (2006, July). Analysis methods for Atmospheric Cerenkov Telescopes. (Cit. on p. 52).
- de Naurois, M. (2018). H.E.S.S. upper limits on VHE gamma emission from AT2018cow. <https://www.astronomerstelegram.org/?read=11956> (cit. on p. 138).
- Derishev, E., & Piran, T. (2019). The Physical Conditions of the Afterglow Implied by MAGIC's Sub-TeV Observations of GRB 190114C. *Astrophys. J. Lett.*, 880(2), Article L27, L27. <https://doi.org/10.3847/2041-8213/ab2d8a> (cit. on pp. 33, 132).
- Di Francesco, J., Chalmers, D., Denman, N., Fissel, L., Friesen, R., Gaensler, B., Hlavacek-Larrondo, J., Kirk, H., Matthews, B., O'Dea, C., Robishaw, T., Rosolowsky, E., Rupen, M., Sadavoy, S., Sa-Harb, S., Sivakoff, G., Tahani, M., van der Marel, N., White, J., & Wilson, C. (2019). The Next Generation Very Large Array. *Canadian Long Range Plan for Astronomy and Astrophysics White Papers, 2020*, Article 32, 32. <https://doi.org/10.5281/zenodo.3765763> (cit. on p. 124).
- Di Sciascio, G. (2016). The Ihaaso experiment: From gamma-ray astronomy to cosmic rays [Proceedings of the 9th Cosmic Ray International Seminar]. <https://doi.org/10.1016/j.nuclphysbps.2016.10.024> (cit. on p. 132).
- Dicke, R. H., Peebles, P. J. E., Roll, P. G., & Wilkinson, D. T. (1965). Cosmic Black-Body Radiation. *Astrophys. J.*, 142, 414–419. <https://doi.org/10.1086/148306> (cit. on p. 2).
- Diehl, R. (2001). Gamma-ray production and absorption processes. In V. Schönfelder (Ed.), *The universe in gamma rays* (pp. 9–25). Springer Berlin Heidelberg. https://doi.org/10.1007/978-3-662-04593-0_2 (cit. on p. 8).
- Donley, J. L., Brandt, W. N., Eracleous, M. C., & Boller, T. (2002). Large-amplitude X-ray outbursts from galactic nuclei: A Systematic survey using ROSAT archival data. *Astron. J.*, 124, 1308. <https://doi.org/10.1086/342280> (cit. on pp. 27, 147).

- Dorigo Jones, J., Johnson, S. D., Muzahid, S., Charlton, J., Chen, H. .-, Narayanan, A., Sameer, Schaye, J., & Wijers, N. A. (2022). Improving blazar redshift constraints with the edge of the Ly α forest: 1ES 1553+113 and implications for observations of the WHIM. *Mon. Not. R. Astron. Soc.*, *509*, 4330–4343 (cit. on p. 148).
- Drenkhahn, G., & Spruit, H. C. (2002). Efficient acceleration and radiation in Poynting flux powered GRB outflows. *Astronomy amp; Astrophysics*, *391*(3), 1141–1153. <https://doi.org/10.1051/0004-6361:20020839> (cit. on p. 31).
- Durrer, R. (2015). The cosmic microwave background: the history of its experimental investigation and its significance for cosmology. *Classical and Quantum Gravity*, *32*(12), 124007. <https://doi.org/10.1088/0264-9381/32/12/124007> (cit. on p. 2).
- Egberts, K., Hoischen, C., Steppa, C., Fülling, M., Neise, D., de Ona Wilhelmi, E., & Oya, I. (2022, August). The transients handler system for the cherenkov telescope array observatory. In C. R. Benn, R. L. Seaman, & D. S. Adler (Eds.), *Observatory operations: Strategies, processes, and systems ix*. SPIE. <https://doi.org/10.1117/12.2629372> (cit. on p. 147).
- Evans, P. A., Beardmore, A. P., Page, K. L., Osborne, J. P., O’Brien, P. T., Willingale, R., Starling, R. L. C., Burrows, D. N., Godet, O., Vetere, L., Racusin, J., Goad, M. R., Wiersema, K., Angelini, L., Capalbi, M., Chincarini, G., Gehrels, N., Kennea, J. A., Margutti, R., ... Tanvir, N. (2009). Methods and results of an automatic analysis of a complete sample of Swift-XRT observations of GRBs. *Mon. Not. R. Astron. Soc.*, *397*(3), 1177–1201. <https://doi.org/10.1111/j.1365-2966.2009.14913.x> (cit. on p. 195).
- Evans, P. A., Beardmore, A. P., Page, K. L., Tyler, L. G., Osborne, J. P., Goad, M. R., O’Brien, P. T., Vetere, L., Racusin, J., Morris, D., Burrows, D. N., Capalbi, M., Perri, M., Gehrels, N., & Romano, P. (2007). An online repository of Swift/XRT light curves of γ -ray bursts. *Astron. Astrophys.*, *469*(1), 379–385. <https://doi.org/10.1051/0004-6361:20077530> (cit. on p. 195).
- Evans, P. A., Willingale, R., Osborne, J. P., O’Brien, P. T., Page, K. L., Markwardt, C. B., Barthelmy, S. D., Beardmore, A. P., Burrows, D. N., Pagani, C., Starling, R. L. C., Gehrels, N., & Romano, P. (2010). TheSwift Burst Analyser: I. BAT and XRT spectral and flux evolution of gamma ray bursts. *Astronomy and Astrophysics*, *519*, A102. <https://doi.org/10.1051/0004-6361/201014819> (cit. on p. 24).
- Evoli, C. (2020). The cosmic-ray energy spectrum. <https://doi.org/10.5281/zenodo.4396125> (cit. on p. 1).
- Fang, K., Metzger, B. D., Vurm, I., Aydi, E., & Chomiuk, L. (2020). High-energy Neutrinos and Gamma Rays from Nonrelativistic Shock-powered Transients. *The Astrophysical Journal*, *904*(1), 4. <https://doi.org/10.3847/1538-4357/abbc6e> (cit. on pp. 16, 21, 30, 36–38, 99, 101).
- Fegan, D. J. (1997). Gamma/hadron separation at TeV energies. *J. Phys. G*, *23*, 1013–1060. <https://doi.org/10.1088/0954-3899/23/9/004> (cit. on p. 55).
- Fermi, E. (1949). On the Origin of the Cosmic Radiation. *Phys. Rev.*, *75*, 1169–1174. <https://doi.org/10.1103/PhysRev.75.1169> (cit. on p. 13).

- Flesch, E. W. (2023). The Million Quasars (Milliquas) Catalogue, v8. *The Open Journal of Astrophysics*, 6, 49. <https://doi.org/10.21105/astro.2308.01505> (cit. on p. 106).
- Fox, O. D., & Smith, N. (2019). Signatures of circumstellar interaction in the unusual transient AT 2018cow. *Mon. Not. R. Astron. Soc.*, 488(3), 3772–3782. <https://doi.org/10.1093/mnras/stz1925> (cit. on p. 35).
- Franceschini, A., & Rodighiero, G. (2017). The Extragalactic Background Light Revisited and the Cosmic Photon-Photon Opacity. *Astronomy & Astrophysics*, 603, A34. <https://doi.org/10.1051/0004-6361/201629684> (cit. on pp. 12, 100, 135, 199).
- Frank, J., & Rees, M. J. (1976). Effects of Massive Central Black Holes on Dense Stellar Systems. *Monthly Notices of the Royal Astronomical Society*, 176(3), 633–647. <https://doi.org/10.1093/mnras/176.3.633> (cit. on p. 21).
- Funk, S. (2014). Indirect detection of dark matter with γ rays. *Proceedings of the National Academy of Sciences*, 112(40), 12264–12271. <https://doi.org/10.1073/pnas.1308728111> (cit. on p. 7).
- Funk, S. (2015). Ground- and Space-Based Gamma-Ray Astronomy. *Annual Review of Nuclear and Particle Science*, 65, 245–277. <https://doi.org/10.1146/annurev-nucl-102014-022036> (cit. on pp. 6, 8).
- Gabici, S., Evoli, C., Gaggero, D., Lipari, P., Mertsch, P., Orlando, E., Strong, A., & Vittino, A. (2019). The origin of Galactic cosmic rays: Challenges to the standard paradigm. *International Journal of Modern Physics D*, 28(15), 1930022. <https://doi.org/10.1142/s0218271819300222> (cit. on p. 2).
- Gaisser, T. K. (2006). The Cosmic-ray Spectrum: from the knee to the ankle. *Journal of Physics Conference Series*, 47, 15–20. <https://doi.org/10.1088/1742-6596/47/1/002> (cit. on p. 1).
- Gallant, Y. A., & Achterberg, A. (1999). Ultra-high-energy cosmic ray acceleration by relativistic blast waves. *Mon. Not. R. Astron. Soc.*, 305(1), L6–L10. <https://doi.org/10.1046/j.1365-8711.1999.02566.x> (cit. on p. 16).
- Gao, S., Fedynitch, A., Winter, W., & Pohl, M. (2018). Modelling the coincident observation of a high-energy neutrino and a bright blazar flare. *Nature Astronomy*, 3(1), 88–92. <https://doi.org/10.1038/s41550-018-0610-1> (cit. on p. 11).
- Garczarczyk, M. (2011). The major atmospheric gamma-ray imaging Cherenkov telescope (R. Forty, G. Hallewell, W. Hofmann, E. Nappi, & B. Ratcliff, Eds.). *Nucl. Instrum. Meth. A*, 639, 33–36. <https://doi.org/10.1016/j.nima.2010.09.020> (cit. on p. 7).
- Gezari, S., et al. (2008). UV/Optical Detections of Candidate Tidal Disruption Events by GALEX and CFHTLS. *Astrophys. J.*, 676, 944. <https://doi.org/10.1086/529008> (cit. on pp. 27, 147).
- Gezari, S. (2021). Tidal Disruption Events. *Annual Review of Astronomy and Astrophysics*, 59(1), 21–58. <https://doi.org/10.1146/annurev-astro-111720-030029> (cit. on p. 3).
- Gezari, S., Heckman, T., Cenko, S. B., Eracleous, M., Forster, K., Gonçalves, T. S., Martin, D. C., Morrissey, P., Neff, S. G., Seibert, M., Schiminovich, D., & Wyder, T. K. (2009). Luminous Thermal Flares from Quiescent Supermassive Black Holes. *The Astrophysical Journal*, 698(2), 1367–1379. <https://doi.org/10.1088/0004-637X/698/2/1367> (cit. on p. 112).

- Goodwin, A., Anderson, G., Miller-Jones, J., Liu, Z., Malayi, A., & Rau, A. (2022, March). ATCA Radio Detection of the TDE AT2022dsb. (Cit. on p. 106).
- Grainge, K., Alexander, P., Battye, R., Birkinshaw, M., Blain, A., Bremer, M., Bridle, S., Brown, M., Davis, R., Dickinson, C., Edge, A., Efstathiou, G., Fender, R., Hardcastle, M., Hatchell, J., Hobson, M., Jarvis, M., Maughan, B., McHardy, I., ... Schammel, M. (2012, August). Future Science Prospects for AMI. <https://doi.org/10.48550/arXiv.1208.1966> (cit. on p. 106).
- Greisen, K. (1966). End to the Cosmic-Ray Spectrum? *Phys. Rev. Lett.*, *16*, 748–750. <https://doi.org/10.1103/PhysRevLett.16.748> (cit. on p. 2).
- Grieder, P. (2010). *Extensive Air Showers* (Vol. 1+2). Springer-Verlag Berlin Heidelberg. (Cit. on pp. 17, 19).
- Guépin, C., Kotera, K., Barausse, E., Fang, K., & Murase, K. (2018). Ultra-High Energy Cosmic Rays and Neutrinos from Tidal Disruptions by Massive Black Holes. *Astron. Astrophys.*, *616*, A179. <https://doi.org/10.1051/0004-6361/201732392> (cit. on p. 27).
- Gunn, J. E., Siegmund, W. A., & et al, E. J. M. (2006). The 2.5 m Telescope of the Sloan Digital Sky Survey. *The Astronomical Journal*, *131*(4), 2332–2359. <https://doi.org/10.1086/500975> (cit. on p. 103).
- Halzen, F., & Klein, S. R. (2010). Invited Review Article: IceCube: An instrument for neutrino astronomy. *Review of Scientific Instruments*, *81*(8). <https://doi.org/10.1063/1.3480478> (cit. on p. 2).
- Hammerstein, E., van Velzen, S., Gezari, S., Cenko, S. B., Yao, Y., Ward, C., Frederick, S., Villanueva, N., Somalwar, J. J., Graham, M. J., Kulkarni, S. R., Stern, D., Andreoni, I., Bellm, E. C., Dekany, R., Dhawan, S., Drake, A. J., Fremling, C., Gatkine, P., ... Yan, L. (2022). The Final Season Reimagined: 30 Tidal Disruption Events from the ZTF-I Survey. *The Astrophysical Journal*, *942*(1), 9. <https://doi.org/10.3847/1538-4357/aca283> (cit. on p. 22).
- Hanna, D., McCann, A., McCutcheon, M., & Nikkinen, L. (2010). An LED-based Flasher System for VERITAS. *Nucl. Instrum. Meth. A*, *612*, 278–287. <https://doi.org/10.1016/j.nima.2009.10.107> (cit. on p. 43).
- Hanna, D., & Mukherjee, R. (2024). The Very Energetic Radiation Imaging Telescope Array System (VERITAS). In *Handbook of X-ray and Gamma-ray Astrophysics* (pp. 2703–2743). Springer Nature Singapore. https://doi.org/10.1007/978-981-19-6960-7_68 (cit. on p. 41).
- Hays, E. (2007). VERITAS Data Acquisition. *Proceedings of the 30th International Cosmic Ray Conference, ICRC 2007*, *3*, 1543–1546 (cit. on pp. 41, 42).
- Heinze, A. N., Tonry, J. L., Denneau, L., Flewelling, H., Stalder, B., Rest, A., Smith, K. W., Smartt, S. J., & Weiland, H. (2018). A First Catalog of Variable Stars Measured by the Asteroid Terrestrial-impact Last Alert System (ATLAS). *The Astronomical Journal*, *156*(5), 241. <https://doi.org/10.3847/1538-3881/aae47f> (cit. on p. 102).
- Hillas, A. M. (1985). Cerenkov Light Images of EAS Produced by Primary Gamma Rays and by Nuclei. *19th International Cosmic Ray Conference (ICRC19)*, *Volume 3*, *3*, 445 (cit. on p. 52).

- Hillas, A. M. (1996). Differences between gamma-ray and hadronic showers. *Space Science Reviews*, 75, 17–30. <https://doi.org/10.1007/BF00195021> (cit. on p. 17).
- Hillas, A. M. (2013). Evolution of ground-based gamma-ray astronomy from the early days to the Cherenkov Telescope Arrays. *Astroparticle Physics*, 43, 19–43. <https://doi.org/10.1016/j.astropartphys.2012.06.002> (cit. on p. 6).
- Hinton, J. (2004). The status of the H.E.S.S. project. *New Astronomy Reviews*, 48(5–6), 331–337. <https://doi.org/10.1016/j.newar.2003.12.004> (cit. on p. 7).
- Ho, A. Y. Q., Perley, D. A., Gal-Yam, A., Lunnan, R., Sollerman, J., Schulze, S., Das, K. K., Dobie, D., Yao, Y., Fremling, C., Adams, S., Anand, S., Andreoni, I., Bellm, E. C., Bruch, R. J., Burdge, K. B., Castro-Tirado, A. J., Dahiwalé, A., De, K., ... Winters, J. M. (2023). A Search for Extragalactic Fast Blue Optical Transients in ZTF and the Rate of AT2018cow-like Transients. *The Astrophysical Journal*, 949(2), 120. <https://doi.org/10.3847/1538-4357/acc533> (cit. on pp. 34, 146).
- Ho, A. Y. Q., Perley, D. A., Kulkarni, S. R., Dong, D. Z. J., De, K., Chandra, P., Andreoni, I., Bellm, E. C., Burdge, K. B., Coughlin, M., Dekany, R., Feeney, M., Frederiks, D. D., Fremling, C., Golkhou, V. Z., Graham, M. J., Hale, D., Helou, G., Horesh, A., ... Svinkin, D. S. (2020). The Koala: A Fast Blue Optical Transient with Luminous Radio Emission from a Starburst Dwarf Galaxy at $z = 0.27$. *The Astrophysical Journal*, 895(1), 49. <https://doi.org/10.3847/1538-4357/ab8bcf> (cit. on pp. 35, 138).
- Hofmann, W., Jung, I., Konopelko, A., Krawczynski, H., Lampeitl, H., & Pühlhofer, G. (1999). Comparison of techniques to reconstruct the gamma-ray showers from multiple stereoscopic Cherenkov images. *Astropart. Phys.*, 122, 135–143. [https://doi.org/10.1016/S0927-6505\(99\)00084-5](https://doi.org/10.1016/S0927-6505(99)00084-5) (cit. on p. 53).
- Hofmann, W., & Zanin, R. (2024). The cherenkov telescope array (C. Bambi & A. Santangelo, Eds.). https://doi.org/10.1007/978-981-19-6960-7_70 (cit. on p. 37).
- Holder, J. (2005). Exploiting VERITAS timing information. *29th International Cosmic Ray Conference, ICRC 2005*, 5 (cit. on pp. 49–51).
- Holder, J., Acciari, V. A., Aliu, E., Arlen, T., Beilicke, M., Benbow, W., Bradbury, S. M., Buckley, J. H., Bugaev, V., Butt, Y., Byrum, K. L., Cannon, A., Celik, O., Cesarini, A., Ciupik, L., Chow, Y. C. K., Cogan, P., Colin, P., Cui, W., ... Rieger, F. (2008). Status of the VERITAS Observatory. *AIP Conference Proceedings*. <https://doi.org/10.1063/1.3076760> (cit. on p. 39).
- Holder, J., Atkins, R., Badran, H., Blaylock, G., Bradbury, S., Buckley, J., Byrum, K., Carter-Lewis, D., Celik, O., Chow, Y., Cogan, P., Cui, W., Daniel, M., de la Calle Perez, I., Dowdall, C., Dowkontt, P., Duke, C., Falcone, A., Fegan, S., ... Wagner, R. (2006). The first VERITAS telescope. *Astroparticle Physics*, 25(6), 391–401. <https://doi.org/10.1016/j.astropartphys.2006.04.002> (cit. on pp. 3, 7, 39, 40, 44).
- Holder, J. (2015). Atmospheric cherenkov gamma-ray telescopes. <https://doi.org/10.48550/arXiv.1510.05675> (cit. on p. 6).

- Huang, Y., Hu, S., Chen, S., Zha, M., Liu, C., Yao, Z., & Cao, Z. (2022). LHAASO observed GRB 221009A with more than 5000 VHE photons up to around 18 TeV. *GRB Coordinates Network*, 32677, 1 (cit. on p. 132).
- Hümmer, S., Rieger, M., Spanier, F., & Winter, W. (2010). Simplified models for photohadronic interactions in cosmic accelerators. *The Astrophysical Journal*, 721(1), 630–652. <https://doi.org/10.1088/0004-637x/721/1/630> (cit. on p. 36).
- Hütten, M. (2017). *Prospects for galactic dark matter searches with the cherenkov telescope array (cta)* [Doctoral dissertation, Humboldt-Universität zu Berlin, Mathematisch-Naturwissenschaftliche Fakultät]. <https://doi.org/http://dx.doi.org/10.18452/17766> (cit. on pp. 17, 18).
- Inserra, C. (2019). Observational properties of extreme supernovae. *Nature Astronomy*, 3(8), 697–705. <https://doi.org/10.1038/s41550-019-0854-4> (cit. on p. 34).
- Kelner, S. R., & Aharonian, F. (2008). Energy spectra of gamma rays, electrons, and neutrinos produced at interactions of relativistic protons with low energy radiation. *Physical Review D*, 78(3). <https://doi.org/10.1103/physrevd.78.034013> (cit. on p. 11).
- Khangulyan, D., Taylor, A. M., & Aharonian, F. (2023). The Formation of Hard Very High Energy Spectra from Gamma-ray Burst Afterglows via Two-zone Synchrotron Self-Compton Emission. *The Astrophysical Journal*, 947(2), 87. <https://doi.org/10.3847/1538-4357/acc24e> (cit. on p. 33).
- Kherlakian, M. (2023). Application of the optimised next neighbour image cleaning method to the VERITAS array. *Proceedings of 38th International Cosmic Ray Conference - PoS(ICRC2023)*. <https://doi.org/10.22323/1.444.0588> (cit. on p. 65).
- Kieda, D. B. (2013). The Gamma Ray Detection sensitivity of the upgraded VERITAS Observatory. (Cit. on p. 40).
- Kildea, J., Atkins, R. W., Badran, H. M., Blaylock, G., Bond, I. H., Bradbury, S. M., Buckley, J. H., Carter-Lewis, D. A., Celik, O., Chow, Y. C. K., Cui, W., Cogan, P., Daniel, M. K., de la Calle Perez, I., Dowdall, C., Duke, C., Falcone, A. D., Fegan, D. J., Fegan, S. J., ... White, R. J. (2007). The Whipple Observatory 10 m gamma-ray telescope, 1997–2006. *Astroparticle Physics*, 28(2), 182–195. <https://doi.org/10.1016/j.astropartphys.2007.05.004> (cit. on p. 2).
- Klinger, M., Rudolph, A., Rodrigues, X., Yuan, C., de Clairfontaine, G. F., Fedynitch, A., Winter, W., Pohl, M., & Gao, S. (2023). Am³: An open-source tool for time-dependent lepto-hadronic modeling of astrophysical sources. (Cit. on p. 115).
- Klose, S., Schmidl, S., Kann, D. A., Nicuesa Guelbenzu, A., Schulze, S., Greiner, J., Olivares E., F., Krühler, T., Schady, P., Afonso, P. M. J., Filgas, R., Fynbo, J. P. U., Rau, A., Rossi, A., Takats, K., Tanga, M., Updike, A. C., & Varela, K. (2019). Four GRB-Supernovae at Redshifts between 0.4 and 0.8. *Astronomy and Astrophysics*, 622, A138. <https://doi.org/10.1051/0004-6361/201832728> (cit. on p. 31).
- Kobayashi, S., Piran, T., & Sari, R. (1997). Can Internal Shocks Produce the Variability in Gamma-Ray Bursts? *The Astrophysical Journal*, 490(1), 92–98. <https://doi.org/10.1086/512791> (cit. on p. 30).

- Kochanek, C. S., Shappee, B. J., Stanek, K. Z., Holoiien, T. W. .-, Thompson, T. A., Prieto, J. L., Dong, S., Shields, J. V., Will, D., Britt, C., Perzanowski, D., & Pojmański, G. (2017). The All-Sky Automated Survey for Supernovae (ASAS-SN) Light Curve Server v1.0. *Publications of the Astronomical Society of the Pacific*, 129, 104502. <https://doi.org/10.1088/1538-3873/aa80d9> (cit. on pp. 22, 102, 194).
- Komossa, S., & Bade, N. (1999). The giant X-ray outbursts in NGC 5905 and IC 3599: Follow-up observations and outburst scenarios. *Astron. Astrophys.*, 343, 775–787. <https://doi.org/10.48550/arXiv.astro-ph/9901141> (cit. on p. 22).
- Kouveliotou, C., Meegan, C. A., Fishman, G. J., Bhyat, N. P., Briggs, M. S., Koshat, T. M., Paciesas, W. S., & Pendleton, G. N. (1993). Identification of two classes of gamma-ray bursts. *Astrophys. J. Lett.*, 413, L101–104. <https://doi.org/10.1086/186969> (cit. on p. 31).
- Krause, M., Pueschel, E., & Maier, G. (2017). Improved γ /hadron separation for the detection of faint gamma-ray sources using boosted decision trees. *Astroparticle Physics*, 89, 1–9. <https://doi.org/10.1016/j.astropartphys.2017.01.004> (cit. on pp. 57, 79, 152).
- Krawczynski, H., Carter-Lewis, D. A., Duke, C., Holder, J., Maier, G., Le Bohec, S., & Sembroski, G. (2006). Gamma-Hadron Separation Methods for the VERITAS Array of Four Imaging Atmospheric Cherenkov Telescopes. *Astropart. Phys.*, 25, 380–390. <https://doi.org/10.1016/j.astropartphys.2006.03.011> (cit. on p. 55).
- Krolik, J., Piran, T., Svirski, G., & Cheng, R. M. (2016). ASASSN-14li: A Model Tidal Disruption Event. *The Astrophysical Journal*, 827(2), 127. <https://doi.org/10.3847/0004-637x/827/2/127> (cit. on p. 26).
- Lacy, M., Baum, S. A., Chandler, C. J., Chatterjee, S., Clarke, T. E., Deustua, S., English, J., Farnes, J., Gaensler, B. M., Gugliucci, N., Hallinan, G., Kent, B. R., Kimball, A., Law, C. J., Lazio, T. J. W., Marvil, J., Mao, S. A., Medlin, D., Mooley, K., ... Yoon, I. (2020). The Karl G. Jansky Very Large Array Sky Survey (VLASS). Science case and survey design. *Publications of the Astronomical Society of the Pacific*, 132(1009), 035001. <https://doi.org/10.1088/1538-3873/ab63eb> (cit. on pp. 25, 105).
- Lagage, P. O., & Cesarsky, C. J. (1983). The maximum energy of cosmic rays accelerated by supernova shocks. *Astron. Astrophys.*, 125, 249–257 (cit. on p. 16).
- Leinert, C., Bowyer, S., Haikala, L. K., Hanner, M. S., Hauser, M. G., Lévassieur-Regourd, A. .-, Mann, I., Mattila, K., Reach, W. T., Schlosser, W., Staude, H. J., Toller, G. N., Weiland, J. L., Weinberg, J. L., & Witt, A. N. (1998). The 1997 reference of diffuse night sky brightness. *Astron. Astrophys. Suppl.*, 127, 1–99. <https://doi.org/10.1051/aas:1998105> (cit. on p. 47).
- Lemoine-Goumard, M. (2015). Ground-based gamma-ray astronomy. *34th International Cosmic Ray Conference (ICRC2015)*, 34, Article 12, 12. <https://doi.org/10.22323/1.236.0012> (cit. on p. 6).
- Leroy, C., & Rancoita, P.-G. (2016). *Principles of Radiation Interaction in Matter and Detection* (4th ed.). World Scientific Publishing Co. <https://doi.org/10.1142/9167> (cit. on p. 18).

- Lesage, S., Veres, P., Briggs, M. S., Goldstein, A., Kocevski, D., Burns, E., Wilson-Hodge, C. A., Bhat, P. N., Huppenkothen, D., Fryer, C. L., Hamburg, R., Racusin, J., Bissaldi, E., Cleveland, W. H., Dalessi, S., Fletcher, C., Giles, M. M., Hristov, B. A., Hui, C. M., ... Zaharijas, G. (2023). Fermi-GBM Discovery of GRB 221009A: An Extraordinarily Bright GRB from Onset to Afterglow. *The Astrophysical Journal Letters*, 952(2), L42. <https://doi.org/10.3847/2041-8213/ace5b4> (cit. on p. 125).
- Levan, A. J., Tanvir, N. R., Starling, R. L. C., Wiersema, K., Page, K. L., Perley, D. A., Schulze, S., Wynn, G. A., Chornock, R., Hjorth, J., Cenko, S. B., Fruchter, A. S., O'Brien, P. T., Brown, G. C., Tunnicliffe, R. L., Malesani, D., Jakobsson, P., Watson, D., Berger, E., ... Zauderer, B. A. (2013). A new population of ultra-long duration gamma-ray bursts. *The Astrophysical Journal*, 781(1), 13. <https://doi.org/10.1088/0004-637x/781/1/13> (cit. on p. 24).
- Li, K.-L., Metzger, B. D., Chomiuk, L., Vurm, I., Strader, J., Finzell, T., Beloborodov, A. M., Nelson, T., Shappee, B. J., Kochanek, C. S., Prieto, J. L., Kafka, S., Holoiien, T. W.-S., Thompson, T. A., Luckas, P. J., & Itoh, H. (2017). A nova outburst powered by shocks. *Nature Astronomy*, 1(10), 697–702. <https://doi.org/10.1038/s41550-017-0222-1> (cit. on pp. 20, 118).
- Li, T. P., & Ma, Y. Q. (1983, September). Analysis methods for results in gamma-ray astronomy. <https://doi.org/10.1086/161295> (cit. on p. 58).
- Lin, L., Liang, E., & Zhang, S. (2010). GRB 090423: Marking the death of a massive star at $z=8.2$. *Science China Physics, Mechanics, and Astronomy*, 53(1), 64–68. <https://doi.org/10.1007/s11433-010-0027-z> (cit. on p. 32).
- Liu, B., & Qiao, E. (2022). Accretion around black holes: The geometry and spectra. <https://doi.org/https://doi.org/10.1016/j.isci.2021.103544> (cit. on p. 7).
- Loeb, A., & Ulmer, A. (1997). Optical Appearance of the Debris of a Star Disrupted by a Massive Black Hole. *Astrophys. J.*, 489(2), 573–578. <https://doi.org/10.1086/304814> (cit. on p. 112).
- Longair, M. S. (2011). *High Energy Astrophysics* (3rd ed.). Cambridge University Press. (Cit. on pp. 7–9, 14–16).
- Lu, W., & Bonnerot, C. (2020). Self-intersection of the fallback stream in tidal disruption events. *Mon. Not. R. Astron. Soc.*, 492(1), 686–707. <https://doi.org/10.1093/mnras/stz3405> (cit. on p. 26).
- Lyutikov, M. (2022). On the nature of fast blue optical transients. *Mon. Not. R. Astron. Soc.*, 515(2), 2293–2304. <https://doi.org/10.1093/mnras/stac1717> (cit. on pp. 3, 34).
- Magorrian, J., & Tremaine, S. (1999). Rates of tidal disruption of stars by massive central black holes. *Mon. Not. Roy. Astron. Soc.*, 309, 447. <https://doi.org/10.1046/j.1365-8711.1999.02853.x> (cit. on pp. 27, 147).
- Maier, G. (2005). Monte Carlo Studies of the first VERITAS telescope. (Cit. on p. 48).
- Maier, G., & Holder, J. (2017, August). Eventdisplay: An Analysis and Reconstruction Package for Ground-based Gamma-ray Astronomy. <https://doi.org/10.48550/arXiv.1708.04048> (cit. on pp. 49, 70, 134, 199).

- Maier, G., & Knapp, J. (2007). Cosmic-Ray Events as Background in Imaging Atmospheric Cherenkov Telescopes. *Astropart. Phys.*, 28, 72–81. <https://doi.org/10.1016/j.astropartphys.2007.04.009> (cit. on p. 54).
- Malik, Z., Sahayanathan, S., Shah, Z., Iqbal, N., Manzoor, A., & Bhatt, N. (2022). Model-independent redshift estimation of BL Lac objects through very-high-energy observations. *Mon. Not. R. Astron. Soc.*, 511(1), 994–1003. <https://doi.org/10.1093/mnras/stab3173> (cit. on p. 84).
- Malyali, A., Rau, A., Bonnerot, C., Goodwin, A. J., Liu, Z., Anderson, G. E., Brink, J., Buckley, D. A. H., Merloni, A., Miller-Jones, J. C. A., Grotova, I., & Kawka, A. (2023, September). Transient fading X-ray emission detected during the optical rise of a tidal disruption event. (Cit. on pp. 105, 106, 196).
- Mangano, V., Burrows, D. N., Sbarufatti, B., & Cannizzo, J. K. (2016). The Definitive X-Ray Light Curve of Swift J164449.3+573451. *Astrophys. J.*, 817(2), Article 103, 103. <https://doi.org/10.3847/0004-637X/817/2/103> (cit. on p. 24).
- Matsumoto, T., & Piran, T. (2021). Limits on mass outflow from optical tidal disruption events. *Mon. Not. R. Astron. Soc.*, 502(3), 3385–3393. <https://doi.org/10.1093/mnras/stab240> (cit. on p. 21).
- Mattila, S., Pérez-Torres, M., Efstathiou, A., Mimica, P., Fraser, M., Kankare, E., Alberdi, A., Aloy, M. Á., Heikkilä, T., Jonker, P. G., Lundqvist, P., Martí-Vidal, I., Meikle, W. P. S., Romero-Cañizales, C., Smartt, S. J., Tsygankov, S., Varenus, E., Alonso-Herrero, A., Bondi, M., ... Östlin, G. (2018). A dust-enshrouded tidal disruption event with a resolved radio jet in a galaxy merger. *Science*, 361(6401), 482–485. <https://doi.org/10.1126/science.aao4669> (cit. on p. 26).
- McCann, A., Hanna, D., Kildea, J., & McCutcheon, M. (2010). A new mirror alignment system for the VERITAS telescopes. *Astroparticle Physics*, 32(6), 325–329. <https://doi.org/10.1016/j.astropartphys.2009.10.001> (cit. on pp. 40, 44).
- Meagher, K. (2015). Six years of VERITAS observations of the Crab Nebula. 34, 792. <https://doi.org/10.22323/1.236.0792> (cit. on pp. 80, 107, 127–130).
- Megias Homar, G., Meyers, J. M., & Kahn, S. M. (2023). Prompt Detection of Fast Optical Bursts with the Vera C. Rubin Observatory. *The Astrophysical Journal*, 950(1), 21. <https://doi.org/10.3847/1538-4357/acb93> (cit. on p. 142).
- Merloni, A., Lamer, G., Liu, T., Ramos-Ceja, M. E., Brunner, H., Bulbul, E., Dennerl, K., Doroshenko, V., Freyberg, M. J., Friedrich, S., Gatuzz, E., Georgakakis, A., Haberl, F., Igo, Z., Kreykenbohm, I., Liu, A., Maitra, C., Malyali, A., Mayer, M. G. F., ... Zheng, X. (2024). The SRG/eROSITA all-sky survey: First X-ray catalogues and data release of the western Galactic hemisphere. *Astronomy & Astrophysics*, 682, A34. <https://doi.org/10.1051/0004-6361/202347165> (cit. on p. 105).
- Meszáros, P., & Rees, M. J. (1993). Relativistic Fireballs and Their Impact on External Matter: Models for Cosmological Gamma-Ray Bursts. *Astrophys. J.*, 405, 278. <https://doi.org/10.1086/172360> (cit. on p. 31).

- Meszáros, P., & Rees, M. J. (1997). Optical and Long-Wavelength Afterglow from Gamma-Ray Bursts. *The Astrophysical Journal*, 476(1), 232–237. <https://doi.org/10.1086/303625> (cit. on p. 31).
- Miceli, D., & Nava, L. (2022). Gamma-Ray Bursts Afterglow Physics and the VHE Domain. *Galaxies*, 10(3), 66. <https://doi.org/10.3390/galaxies10030066> (cit. on pp. 30, 32).
- Mohan, P., An, T., & Yang, J. (2020). The Nearby Luminous Transient AT2018cow: A Magnetar Formed in a Subrelativistically Expanding Nonjetted Explosion. *Astrophys. J. Lett.*, 888(2), Article L24, L24. <https://doi.org/10.3847/2041-8213/ab64d1> (cit. on p. 35).
- Mou, G., & Wang, W. (2021). Years delayed gamma-ray and radio afterglows originated from TDE wind–torus interactions. *Mon. Not. R. Astron. Soc.*, 507(2), 1684–1698. <https://doi.org/10.1093/mnras/stab2261> (cit. on p. 28).
- Murase, K., Kimura, S. S., Zhang, B. T., Oikonomou, F., & Petropoulou, M. (2020). High-energy Neutrino and Gamma-Ray Emission from Tidal Disruption Events. *The Astrophysical Journal*, 902(2), 108. <https://doi.org/10.3847/1538-4357/abb3c0> (cit. on pp. 29, 30, 99).
- Nagai, T., McKay, R., Sleege, G., & Petry, D. (2007). Focal Plane Instrumentation of VERITAS. (Cit. on pp. 40, 41).
- Nasa High Energy Astrophysics Science Archive Research Center (Heasarc). (2014). HEASoft: Unified Release of FTOOLS and XANADU. *Astrophysics Source Code Library* (cit. on p. 195).
- Nicholl, M. (2018). SuperBol: A User-friendly Python Routine for Bolometric Light Curves. *Research Notes of the American Astronomical Society*, 2(4), Article 230, 230. <https://doi.org/10.3847/2515-5172/aaf799> (cit. on pp. 113, 200).
- Noda, K., & Parsons, R. D. (2022). Gamma-Ray Bursts at TeV Energies: Observational Status. *Galaxies*, 10(1), 7. <https://doi.org/10.3390/galaxies10010007> (cit. on p. 33).
- Oke, J. B. (1974). Absolute Spectral Energy Distributions for White Dwarfs. *Astrophys. J. Suppl. Ser.*, 27, 21. <https://doi.org/10.1086/190287> (cit. on p. 104).
- Otte, A. N., Gebremedhin, L., Kaplan, K., & Long, D. (2011). The Upgrade of VERITAS with High Efficiency Photomultipliers. *32nd International Cosmic Ray Conference*, 9, 247. <https://doi.org/10.7529/ICRC2011/V09/1305> (cit. on pp. 40, 51).
- Pareschi, G., Spiga, D., & Pellicciari, C. (2021, April). X-ray Telescopes Based on Wolter-I Optics. In *The WSPC Handbook of Astronomical Instrumentation* (pp. 3–31). WORLD SCIENTIFIC. https://doi.org/10.1142/9789811203800_0001 (cit. on p. 195).
- Parizot, E. (2014). Cosmic Ray Origin: Lessons from Ultra-High-Energy Cosmic Rays and the Galactic/Extragalactic Transition. *Nuclear Physics B - Proceedings Supplements*, 256–257, 197–212. <https://doi.org/10.1016/j.nuclphysbps.2014.10.023> (cit. on p. 2).
- Parsons, R. D., Gajdus, M., & Murach, T. (2015, September). H.E.S.S. II Data Analysis with IMPACT. (Cit. on p. 67).
- Pasham, D. R., Lucchini, M., Laskar, T., Gompertz, B. P., Srivastav, S., Nicholl, M., Smartt, S. J., Miller-Jones, J. C. A., Alexander, K. D., Fender, R., Smith, G. P., Fulton, M. D., Dewangan, G., Gendreau, K., Coughlin, E. R., Rhodes, L., Horesh, A., van Velzen, S., Sfaradi, I., ...

- Yang, S. (2022). The Birth of a Relativistic Jet Following the Disruption of a Star by a Cosmological Black Hole. *Nature Astronomy*, 7(1), 88–104. <https://doi.org/10.1038/s41550-022-01820-x> (cit. on pp. 24, 100).
- Peng, F.-K., Tang, Q.-W., & Wang, X.-Y. (2016). Search for High-energy Gamma-ray Emission from Tidal Disruption Events with the Fermi Large Area Telescope. *The Astrophysical Journal*, 825(1), 47. <https://doi.org/10.3847/0004-637x/825/1/47> (cit. on p. 100).
- Penzias, A. A., & Wilson, R. W. (1965). A Measurement of Excess Antenna Temperature at 4080 Mc/s. *Astrophys. J.*, 142, 419–421. <https://doi.org/10.1086/148307> (cit. on p. 2).
- Perkins, J. S., & Maier, G. (2010, March). VERITAS Telescope 1 Relocation: Details and Improvements. (Cit. on p. 39).
- Pescalli, A., Ghirlanda, G., Salafia, O. S., Ghisellini, G., Nappo, F., & Salvaterra, R. (2015). Luminosity function and jet structure of Gamma-Ray Burst. *Mon. Not. R. Astron. Soc.*, 447(2), 1911–1921. <https://doi.org/10.1093/mnras/stu2482> (cit. on p. 24).
- Pierro, F. D. (2023). Status of the Large-Sized Telescope of the Cherenkov Telescope Array. *Journal of Physics: Conference Series*, 2429(1), 012020. <https://doi.org/10.1088/1742-6596/2429/1/012020> (cit. on p. 62).
- Pillera, R., Bissaldi, E., Omodei, N., La Mura, G., Longo, F., & Fermi-LAT team. (2022). GRB 221009A: Fermi-LAT refined analysis. *GRB Coordinates Network*, 32658, 1 (cit. on p. 125).
- Piran, T. (1999). Gamma-ray bursts and the fireball model. *Phys. Rep.*, 314(6), 575–667. [https://doi.org/10.1016/S0370-1573\(98\)00127-6](https://doi.org/10.1016/S0370-1573(98)00127-6) (cit. on p. 30).
- Piran, T., Svirski, G., Krolik, J., Cheng, R. M., & Shiokawa, H. (2015). Disk Formation Versus Disk Accretion - What Powers Tidal Disruption Events? *The Astrophysical Journal*, 806(2), 164. <https://doi.org/10.1088/0004-637X/806/2/164> (cit. on p. 112).
- Prokoph, H. (2013). *Observations and modeling of the active galactic nucleus B2 1215+30 together with performance studies of the ground-based gamma-ray observatories VERITAS and CTA* [Doctoral dissertation, Humboldt-Universität zu Berlin, Mathematisch-Naturwissenschaftliche Fakultät I]. <https://doi.org/10.18452/16844> (cit. on pp. 50, 54).
- Racusin, J. L., Oates, S. R., Schady, P., Burrows, D. N., de Pasquale, M., Donato, D., Gehrels, N., Koch, S., McEnery, J., Piran, T., Roming, P., Sakamoto, T., Swenson, C., Troja, E., Vasileiou, V., Virgili, F., Wanderman, D., & Zhang, B. (2011). Fermi and Swift Gamma-ray Burst Afterglow Population Studies. *Astrophys. J.*, 738(2), Article 138, 138. <https://doi.org/10.1088/0004-637X/738/2/138> (cit. on p. 30).
- Razzaque, S., Mészáros, P., & Waxman, E. (2003). Neutrino tomography of gamma ray bursts and massive stellar collapses. *Physical Review D*, 68(8). <https://doi.org/10.1103/physrevd.68.083001> (cit. on p. 120).
- Rees, M. J., & Meszaros, P. (1994). Unsteady outflow models for cosmological gamma-ray bursts. *The Astrophysical Journal*, 430, L93. <https://doi.org/10.1086/187446> (cit. on p. 30).
- Rees, M. J. (1988). Tidal disruption of stars by black holes of $10^6 - 10^8$ solar masses in nearby galaxies. *Nature*, 333, 523–528. <https://doi.org/10.1038/333523a0> (cit. on pp. 21, 22).
- Reusch, S., Stein, R., Kowalski, M., van Velzen, S., Franckowiak, A., Lunardini, C., Murase, K., Winter, W., Miller-Jones, J. C. A., Kasliwal, M. M., Gilfanov, M., Garrappa, S., Paliya,

- V. S., Ahumada, T., Anand, S., Barbarino, C., Bellm, E. C., Brinell, V., Buson, S., ... Zimmerman, E. (2022). Candidate Tidal Disruption Event AT2019fdr Coincident with a High-Energy Neutrino. *Physical Review Letters*, 128(22), 221101. <https://doi.org/10.1103/PhysRevLett.128.221101> (cit. on pp. 3, 27, 99, 112).
- Ribeiro, D. (2023). The VERITAS gamma-ray burst follow-up program. *The Sixteenth Marcel Grossmann Meeting*, 3017–3029. https://doi.org/10.1142/9789811269776_0244 (cit. on pp. 131, 132, 146).
- Rigault, M. (2018, August). *ztfquery*, a python tool to access ZTF data. Zenodo. <https://doi.org/10.5281/zenodo.1345222> (cit. on p. 194).
- Roache, E., Irvin, R., Perkins, J., Harris, K., Falcone, A., Finley, J., & Weekes, T. (2008). Mirror facets for the veritas telescopes. *Proceedings of the 30th International Cosmic Ray Conference, ICRC 2007*, 3 (cit. on p. 40).
- Rolke, W. A., & Lopez, A. M. (2001). Confidence Intervals and Upper Bounds for Small Signals in the Presence of Background Noise. *Nuclear Instruments and Methods in Physics Research Section A: Accelerators, Spectrometers, Detectors and Associated Equipment*, 458(3), 745–758. [https://doi.org/10.1016/S0168-9002\(00\)00935-9](https://doi.org/10.1016/S0168-9002(00)00935-9) (cit. on pp. 62, 135, 199).
- Roming, P. W. A., Kennedy, T. E., Mason, K. O., Nousek, J. A., Ahr, L., Bingham, R. E., Broos, P. S., Carter, M. J., Hancock, B. K., Huckle, H. E., Hunsberger, S. D., Kawakami, H., Killough, R., Koch, T. S., McLelland, M. K., Smith, K., Smith, P. J., Soto, J. C., Boyd, P. T., ... Stock, J. (2005). The Swift Ultra-Violet/Optical Telescope. *Space Science Reviews*, 120(3-4), 95–142. <https://doi.org/10.1007/s11214-005-5095-4> (cit. on pp. 32, 195).
- Roth, N., Rossi, E. M., Krolik, J. H., Piran, T., Mockler, B., & Kasen, D. (2020). Radiative Emission Mechanisms of Tidal Disruption Events. *Space Science Reviews*, 216(7), 114. <https://doi.org/10.1007/s11214-020-00735-1> (cit. on pp. 23, 112).
- Russell, D. M., Miller-Jones, J. C. A., Maccarone, T. J., Yang, Y. J., Fender, R. P., & Lewis, F. (2011). Testing the jet quenching paradigm with an ultradeep observation of a steadily soft state black hole. *Astrophys. J. Lett.*, 739, L19. <https://doi.org/10.1088/2041-8205/739/1/L19> (cit. on p. 24).
- Sari, R., & Piran, T. (1997). Variability in Gamma-Ray Bursts: A Clue. *The Astrophysical Journal*, 485(1), 270–273. <https://doi.org/10.1086/304428> (cit. on p. 30).
- Sari, R., Piran, T., & Narayan, R. (1998). Spectra and light curves of gamma-ray burst afterglows. *Astrophys. J. Lett.*, 497, L17. <https://doi.org/10.1086/311269> (cit. on p. 32).
- Saxton, C. J., Soria, R., Wu, K., & Kuin, N. P. M. (2012). Long-term X-ray variability of Swift J1644+57. *Mon. Not. R. Astron. Soc.*, 422(2), 1625–1639. <https://doi.org/10.1111/j.1365-2966.2012.20739.x> (cit. on p. 24).
- Saxton, R., Komossa, S., Auchettl, K., & Jonker, P. G. (2021, February). Correction to: X-ray properties of tdes. <https://doi.org/10.1007/s11214-020-00759-7> (cit. on pp. 23, 105).
- Schartel, N., González-Riestra, R., Kretschmar, P., Kirsch, M., Rodríguez-Pascual, P., Rosen, S., Santos-Lleó, M., Smith, M., Stuhlinger, M., & Verdugo-Rodrigo, E. (2022). XMM-Newton. https://doi.org/10.1007/978-981-16-4544-0_41-1 (cit. on p. 105).

- Schönfelder, V. (2004). Imaging principles and techniques in space-borne gamma-ray astronomy. *Nuclear Instruments and Methods in Physics Research A*, 525(1-2), 98–106. <https://doi.org/10.1016/j.nima.2004.03.029> (cit. on p. 5).
- Schure, K. M., & Bell, A. R. (2013). Cosmic ray acceleration in young supernova remnants. *Mon. Not. R. Astron. Soc.*, 435(2), 1174–1185. <https://doi.org/10.1093/mnras/stt1371> (cit. on p. 35).
- Schussler, F. (2019). The transient program of the cherenkov telescope array. *Proceedings of 36th International Cosmic Ray Conference — PoS(ICRC2019)*. <https://api.semanticscholar.org/CorpusID:197431023> (cit. on p. 37).
- Sfaradi, I., Horesh, A., Bright, J., Fender, R., Rhodes, L., Green, D., & Titterton, D. (2023, February). *A possible AMI-LA radio detection of the Tidal Disruption Event AT 2023clx*. <https://www.astronomerstelegam.org/?read=15918> (cit. on pp. 106, 196).
- Sfaradi, I., Horesh, A., & Fender, R. (2022a, March). *A possible VLA radio detection of the Tidal Disruption Event AT 2022dbl*. <https://www.astronomerstelegam.org/?read=15258> (cit. on p. 196).
- Sfaradi, I., Horesh, A., & Fender, R. (2022b, March). *Erratum: Flux density uncertainties for AT2022dbl in ATel 15258*. <https://www.astronomerstelegam.org/?read=15258> (cit. on p. 196).
- Shappee, B. J., Prieto, J. L., Grupe, D., Kochanek, C. S., Stanek, K. Z., De Rosa, G., Mathur, S., Zu, Y., Peterson, B. M., Pogge, R. W., Komossa, S., Im, M., Jencson, J., Holoi, T. W. .-. , Basu, U., Beacom, J. F., Szczygiel, D. M., Brimacombe, J., Adams, S., ... Yoon, Y. (2014). The Man behind the Curtain: X-Rays Drive the UV through NIR Variability in the 2013 Active Galactic Nucleus Outburst in NGC 2617. *Astrophys. J.*, 788(1), Article 48, 48. <https://doi.org/10.1088/0004-637X/788/1/48> (cit. on pp. 22, 102).
- Shayduk, M., Hengstebeck, T., Kalekin, O., Pavel, N. A., & Schweizer, T. (2005). A New Image Cleaning Method for the MAGIC Telescope. *29th International Cosmic Ray Conference (ICRC29), Volume 5, 5*, 223 (cit. on pp. 67, 68).
- Shayduk, M. (2013). Optimized Next-Neighbor Image Cleaning Method for Cherenkov Telescopes. (Cit. on pp. 3, 65, 68–70).
- Shingles, L., Smith, K. W., Young, D. R., Smartt, S. J., Tonry, J., Denneau, L., Heinze, A., Weiland, H., Flewelling, H., Stalder, B., Clocchiatti, A., Förster, F., Pignata, G., Rest, A., Anderson, J., Stubbs, C., & Erasmus, N. (2021). Release of the ATLAS Forced Photometry server for public use. *Transient Name Server AstroNote*, 7, 1–7 (cit. on p. 195).
- Skole, C. (2016). *Search for Extremely Short Transient Gamma-Ray Sources with the VERITAS Observatory* [Doctoral dissertation, Mathematisch-Naturwissenschaftlichen Fakultät, Humboldt-Universität zu Berlin]. (Cit. on p. 57).
- Smith, K. W., Smartt, S. J., Young, D. R., Tonry, J. L., Denneau, L., Flewelling, H., Heinze, A. N., Weiland, H. J., Stalder, B., Rest, A., Stubbs, C. W., Anderson, J. P., Chen, T. .-. , Clark, P., Do, A., Förster, F., Fulton, M., Gillanders, J., McBrien, O. R., ... Wright, D. E. (2020). Design and Operation of the ATLAS Transient Science Server. *Publ. Astron. Soc. Pac.*,

- 132(1014), Article 085002, 085002. <https://doi.org/10.1088/1538-3873/ab936e> (cit. on p. 102).
- Smith, N. (2017). Interacting Supernovae: Types II_n and Ibn. In *Handbook of supernovae* (p. 403). https://doi.org/10.1007/978-3-319-21846-5_38 (cit. on p. 33).
- Socrates, A. (2012). Swift J1644+57: An Ultra-Luminous X-ray Event. *Astrophys. J. Lett.*, 756, L1. <https://doi.org/10.1088/2041-8205/756/1/L1> (cit. on p. 24).
- Spruit, H. C., Daigne, F., & Drenkhahn, G. (2001). Large scale magnetic fields and their dissipation in GRB fireballs. *Astronomy and Astrophysics*, 369(2), 694–705. <https://doi.org/10.1051/0004-6361:20010131> (cit. on p. 31).
- Stecker, F. W. (1971). *Cosmic gamma rays* (Vol. 249). (Cit. on p. 10).
- Stein, R., & IceCube Collaboration. (2019). Search for Neutrinos from Populations of Optical Transients. *Proceedings of 36th International Cosmic Ray Conference — PoS(ICRC2019)*, 1016. <https://doi.org/10.22323/1.358.1016> (cit. on pp. 27, 100).
- Stein, R., van Velzen, S., Kowalski, M., Franckowiak, A., Gezari, S., Miller-Jones, J. C. A., Frederick, S., Sfaradi, I., Bietenholz, M. F., Horesh, A., Fender, R., Garrappa, S., Ahumada, T., Andreoni, I., Belicki, J., Bellm, E. C., Böttcher, M., Brinnet, V., Burruss, R., ... Yao, Y. (2021). A Tidal Disruption Event Coincident with a High-Energy Neutrino. *Nature Astronomy*, 5(5), 510–518. <https://doi.org/10.1038/s41550-020-01295-8> (cit. on pp. 3, 27, 99, 100).
- Strotjohann, N. L., Ofek, E. O., Gal-Yam, A., Bruch, R., Schulze, S., Shaviv, N., Sollerman, J., Filippenko, A. V., Yaron, O., Fremling, C., Nordin, J., Kool, E. C., Perley, D. A., Ho, A. Y. Q., Yang, Y., Yao, Y., Soumagnac, M. T., Graham, M. L., Barbarino, C., ... Zhuang, Z. (2021). Bright, Months-long Stellar Outbursts Announce the Explosion of Interaction-powered Supernovae. *The Astrophysical Journal*, 907(2), 99. <https://doi.org/10.3847/1538-4357/abd032> (cit. on p. 34).
- Tavani, M., Cavaliere, A., Munar-Adrover, P., & Argan, A. (2018). The Blazar PG 1553+113 as a Binary System of Supermassive Black Holes. *The Astrophysical Journal*, 854(1), 11. <https://doi.org/10.3847/1538-4357/aaa3f4> (cit. on p. 86).
- Tchekhovskoy, A., Metzger, B. D., Giannios, D., & Kelley, L. Z. (2014). Swift J1644+57 gone MAD: the case for dynamically important magnetic flux threading the black hole in a jetted tidal disruption event. *Mon. Not. R. Astron. Soc.*, 437(3), 2744–2760. <https://doi.org/10.1093/mnras/stt2085> (cit. on p. 24).
- Teboul, O., & Metzger, B. D. (2023). A Unified Theory of Jetted Tidal Disruption Events: From Promptly Escaping Relativistic to Delayed Transrelativistic Jets. *The Astrophysical Journal Letters*, 957(1), L9. <https://doi.org/10.3847/2041-8213/ad0037> (cit. on pp. 27, 100, 147).
- The HEGRA Collaboration. (1997). First results on the performance of the HEGRA IACT array. [https://doi.org/10.1016/S0927-6505\(97\)00031-5](https://doi.org/10.1016/S0927-6505(97)00031-5) (cit. on pp. 6, 67).
- The LHAASO Collaboration. (2021). Peta-electron volt gamma-ray emission from the Crab Nebula. *Science*, 373(6553), 425–430. <https://doi.org/10.1126/science.abg5137> (cit. on p. 8).

- The LHAASO Collaboration. (2023). Very high-energy gamma-ray emission beyond 10 TeV from GRB 221009A. *Science Advances*, 9(46), eadj2778. <https://doi.org/10.1126/sciadv.adj2778> (cit. on pp. 132, 133).
- Thompson, D. J. (2008). Gamma ray astrophysics: the EGRET results. *Reports on Progress in Physics*, 71(11), 116901. <https://doi.org/10.1088/0034-4885/71/11/116901> (cit. on p. 5).
- Tonry, J. L., Denneau, L., Heinze, A. N., Stalder, B., Smith, K. W., Smartt, S. J., Stubbs, C. W., Weiland, H. J., & Rest, A. (2018). ATLAS: A High-cadence All-sky Survey System. *Publ. Astron. Soc. Pac.*, 130(988), 064505. <https://doi.org/10.1088/1538-3873/aabadf> (cit. on p. 102).
- Truemper, J. (1982). The ROSAT mission. *Advances in Space Research*, 2(4), 241–249. [https://doi.org/10.1016/0273-1177\(82\)90070-9](https://doi.org/10.1016/0273-1177(82)90070-9) (cit. on p. 22).
- Tucker, M. A., Hinkle, J., Angus, C. R., Auchettl, K., Hoogendam, W. B., Shappee, B., Kochanek, C. S., Ashall, C., de Boer, T., Chambers, K. C., Desai, D. D., Do, A., Fulton, M. D., Gao, H., Herman, J., Huber, M., Lidman, C., Lin, C.-C., Lowe, T. B., ... Wainscoat, R. J. (2024). The Extremely Metal-Poor SN 2023ufx: A Local Analog to High-Redshift Type II Supernovae. (Cit. on pp. 140, 142).
- Usov, V. V. (1992). Millisecond pulsars with extremely strong magnetic fields as a cosmological source of γ -ray bursts. *Nature*, 357(6378), 472–474. <https://doi.org/10.1038/357472a0> (cit. on p. 31).
- van Velzen, S., Gezari, S., Cenko, S. B., Kara, E., Miller-Jones, J. C., Hung, T., Bright, J., Roth, N., Blagorodnova, N., Huppenkothen, D., Yan, L., Ofek, E., Sollerman, J., Frederick, S., Ward, C., Graham, M. J., Fender, R., Kasliwal, M. M., Canella, C., ... Tachibana, Y. (2019). The first tidal disruption flare in ZTF: From photometric selection to multi-wavelength characterization. *The Astrophysical Journal*, 872(2), 198. <https://doi.org/10.3847/1538-4357/aafe0c> (cit. on p. 112).
- van Velzen, S., Gezari, S., Hammerstein, E., Roth, N., Frederick, S., Ward, C., Hung, T., Cenko, S. B., Stein, R., Perley, D. A., Taggart, K., Sollerman, J., Andreoni, I., Bellm, E. C., Brinnel, V., De, K., Dekany, R., Feeney, M., Foley, R. J., ... Soumagnac, M. T. (2021). Seventeen Tidal Disruption Events from the First Half of ZTF Survey Observations: Entering a New Era of Population Studies. *The Astrophysical Journal*, 908(1), 4. <https://doi.org/10.3847/1538-4357/abc258> (cit. on pp. 23, 112, 113, 116, 123).
- van Velzen, S., Pasham, D. R., Komossa, S., Yan, L., & Kara, E. A. (2021). Reverberation in Tidal Disruption Events: Dust Echoes, Coronal Emission Lines, Multi-wavelength Cross-correlations, and QPOs. *Space Science Reviews*, 217(5), 63. <https://doi.org/10.1007/s11214-021-00835-6> (cit. on p. 112).
- van Velzen, S., Stein, R., Gilfanov, M., Kowalski, M., Hayasaki, K., Reusch, S., Yao, Y., Garrappa, S., Franckowiak, A., Gezari, S., Nordin, J., Fremling, C., Sharma, Y., Yan, L., Kool, E. C., Stern, D., Veres, P. M., Sollerman, J., Medvedev, P., ... Rusholme, B. (2024). Establishing accretion flares from supermassive black holes as a source of high-energy neutrinos. *Monthly Notices of the Royal Astronomical Society*, 529(3), 2559–2576. <https://doi.org/10.1093/mnras/stae610> (cit. on p. 27).

- Veres, P., Bhat, P. N., Briggs, M. S., Cleveland, W. H., Hamburg, R., Hui, C. M., Mailyan, B., Preece, R. D., Roberts, O. J., von Kienlin, A., Wilson-Hodge, C. A., Kocevski, D., Arimoto, M., Tak, D., Asano, K., Axelsson, M., Barbiellini, G., Bissaldi, E., Dirirsa, F. F., ... Young, D. R. (2019). Observation of inverse Compton emission from a long γ -ray burst. *Nature*, 575(7783), 459–463. <https://doi.org/10.1038/s41586-019-1754-6> (cit. on p. 33).
- Vurm, I., & Metzger, B. D. (2018). High-energy Emission from Nonrelativistic Radiative Shocks: Application to Gamma-Ray Novae. *Astrophys. J.*, 852(1), Article 62, 62. <https://doi.org/10.3847/1538-4357/aa9c4a> (cit. on p. 21).
- Wang, X.-Y., Liu, R.-Y., Zhang, H.-M., Xi, S.-Q., & Zhang, B. (2019). Synchrotron Self-Compton Emission from External Shocks as the Origin of the Sub-TeV Emission in GRB 180720B and GRB 190114C. *The Astrophysical Journal*, 884(2), 117. <https://doi.org/10.3847/1538-4357/ab426c> (cit. on p. 33).
- Weinstein, A. (2007). The VERITAS trigger system. *Proceedings of the 30th International Cosmic Ray Conference, ICRC 2007*, 3 (cit. on p. 42).
- Weisskopf, M. C. (2012). Chandra X-ray optics. *Optical Engineering*, 51(1), 011013. <https://doi.org/10.1117/1.oe.51.1.011013> (cit. on p. 25).
- Weltman, A., Bull, P., Camera, S., Kelley, K., Padmanabhan, H., Pritchard, J., Raccanelli, A., Riemer-Sørensen, S., Shao, L., Andrianomena, S., Athanassoula, E., Bacon, D., Barkana, R., Bertone, G., Böhm, C., Bonvin, C., Bosma, A., Brüggén, M., Burigana, C., ... Gaensler, B. M. (2020). Fundamental physics with the Square Kilometre Array. *Publications of the Astronomical Society of Australia*, 37. <https://doi.org/10.1017/pasa.2019.42> (cit. on p. 124).
- Wilhelm, A. (2021). *Stochastic re-acceleration of particles in supernova remnants* [Doctoral dissertation, Universität Potsdam]. <https://doi.org/10.25932/publishup-51291> (cit. on p. 15).
- Williams, M. A., Kennea, J. A., Dichiara, S., Kobayashi, K., Iwakiri, W. B., Beardmore, A. P., Evans, P. A., Heinz, S., Lien, A., Oates, S. R., Negoro, H., Cenko, S. B., Buisson, D. J. K., Hartmann, D. H., Jaisawal, G. K., Kuin, N. P. M., Lesage, S., Page, K. L., Parsotan, T., ... Ziaeeepour, H. (2023). GRB 221009A: Discovery of an Exceptionally Rare Nearby and Energetic Gamma-Ray Burst. *The Astrophysical Journal Letters*, 946(1), L24. <https://doi.org/10.3847/2041-8213/acbcd1> (cit. on p. 125).
- Wilson, E. B., & Hilferty, M. M. (1931). The Distribution of Chi-Square. *Proceedings of the National Academy of Sciences of the United States of America*, 17(12), 684–688 (cit. on p. 198).
- Winston, R. (1974). Principles of solar concentrators of a novel design. *Solar Energy*, 16, 89–95. [https://doi.org/10.1016/0038-092X\(74\)90004-8](https://doi.org/10.1016/0038-092X(74)90004-8) (cit. on p. 40).
- Winter, W., & Lunardini, C. (2023). Interpretation of the Observed Neutrino Emission from Three Tidal Disruption Events. *The Astrophysical Journal*, 948(1), 42. <https://doi.org/10.3847/1538-4357/acbe9e> (cit. on pp. 27, 29, 112, 120).
- Wood, M., Caputo, R., Charles, E., Mauro, M. D., Magill, J., & Perkins, J. (2017). Fermipy: An open-source Python package for analysis of Fermi-LAT Data. (Cit. on p. 198).

- Woosley, S. E. (1993). Gamma-ray bursts from stellar mass accretion disks around black holes. *Astrophys. J.*, *405*, 273. <https://doi.org/10.1086/172359> (cit. on p. 31).
- Xiang, D., Wang, X., Lin, W., Mo, J., Lin, H., Burke, J., Hiramatsu, D., Hosseinzadeh, G., Howell, D. A., McCully, C., Valenti, S., Vinkó, J., Wheeler, J. C., Ehgamberdiev, S. A., Mirzaqulov, D., Bódi, A., Bognár, Z., Cseh, B., Hanyecz, O., ... Li, W. (2021). The Peculiar Transient AT2018cow: A Possible Origin of a Type Ibn/IIIn Supernova. *Astrophys. J.*, *910*(1), Article 42, 42. <https://doi.org/10.3847/1538-4357/abdeba> (cit. on p. 35).
- Yang, J., & Wang, J. (2010). Redshifts of Distant Blazars Limited by Fermi and VHE Gamma-Ray Observations. *Publ. Astron. Soc. Jpn.*, *62*, L23–L26. <https://doi.org/10.1093/pasj/62.4.L23> (cit. on p. 84).
- Yao, Y., Lu, W., Harrison, F., Kulkarni, S. R., Gezari, S., Guolo, M., Cenko, S. B., & Ho, A. Y. Q. (2024). The On-axis Jetted Tidal Disruption Event AT2022cmc: X-ray Observations and Broadband Spectral Modeling. (Cit. on pp. 24, 100).
- Yaron, O., Perley, D. A., Gal-Yam, A., Groh, J. H., Horesh, A., Ofek, E. O., Kulkarni, S. R., Sollerman, J., Fransson, C., Rubin, A., Szabo, P., Sapir, N., Taddia, F., Cenko, S. B., Valenti, S., Arcavi, I., Howell, D. A., Kasliwal, M. M., Vreeswijk, P. M., ... Soumagnac, M. T. (2017). Confined dense circumstellar material surrounding a regular type II supernova. *Nature Physics*, *13*(5), 510–517. <https://doi.org/10.1038/nphys4025> (cit. on p. 35).
- Yu, Y.-W., Li, S.-Z., & Dai, Z.-G. (2015). Rapidly Evolving and Luminous Transients Driven by Newly Born Neutron Stars. *Astrophys. J. Lett.*, *806*(1), L6. <https://doi.org/10.1088/2041-8205/806/1/L6> (cit. on p. 34).
- Yuan, C., & Winter, W. (2023). Electromagnetic Cascade Emission from Neutrino-Coincident Tidal Disruption Events. *The Astrophysical Journal*, *956*(1), 30. <https://doi.org/10.3847/1538-4357/acf615> (cit. on pp. 27, 112, 120).
- Zatsepin, G. T., & Kuzmin, V. A. (1966). Upper Limit of the Spectrum of Cosmic Rays. *Soviet Journal of Experimental and Theoretical Physics Letters*, *4*, 78 (cit. on p. 2).
- Zauderer, B. A., Berger, E., Margutti, R., Pooley, G. G., Sari, R., Soderberg, A. M., Brunthaler, A., & Bietenholz, M. F. (2013). Radio monitoring of the Tidal Disruption Event SWIFT J164449.3+573451. II. The relativistic jet shuts off and a transition to forward shock X-ray/Radio emission. *The Astrophysical Journal*, *767*(2), 152. <https://doi.org/10.1088/0004-637x/767/2/152> (cit. on p. 24).
- Zauderer, B. A., Berger, E., Soderberg, A. M., Loeb, A., Narayan, R., Frail, D. A., Petitpas, G. R., Brunthaler, A., Chornock, R., Carpenter, J. M., Pooley, G. G., Mooley, K., Kulkarni, S. R., Margutti, R., Fox, D. B., Nakar, E., Patel, N. A., Volgenau, N. H., Culverhouse, T. L., ... Hull, C. L. H. (2011). Birth of a relativistic outflow in the unusual γ -ray transient Swift J164449.3+573451. *Nature*, *476*(7361), 425–428. <https://doi.org/10.1038/nature10366> (cit. on p. 25).
- Zhu, J., Jiang, N., Wang, T., Huang, S., Lin, Z., Wang, Y., & Wang, J.-G. (2023). AT 2023clx: The Faintest and Closest Optical Tidal Disruption Event Discovered in Nearby Star-forming Galaxy NGC 3799. *The Astrophysical Journal Letters*, *952*(2), L35. <https://doi.org/10.3847/2041-8213/ace625> (cit. on p. 106).

- Zitzer, B. (2013). The VERITAS Upgraded Telescope-Level Trigger Systems: Technical Details and Performance Characterization. *33rd International Cosmic Ray Conference*, 1138 (cit. on p. [42](#)).

Acronyms

AGN	active galactic nucleus (<i>p. 2</i>)
ASAS-SN	All Sky Automated Survey for SuperNovae (<i>p. 22</i>)
ATLAS	Asteroid Terrestrial-impact Last Alert System (<i>p. 102</i>)
BDT	boosted decision tree (<i>p. 54</i>)
C. L.	Confidence Level (<i>p. 63</i>)
CAT	Cherenkov Array at Themis (<i>p. 6</i>)
CFD	constant fraction discriminator (<i>p. 42</i>)
CMB	cosmic microwave background (<i>p. 2</i>)
CNM	circumnuclear medium (<i>p. 21</i>)
CSM	circumstellar medium (<i>p. 33</i>)
CTAO	Cherenkov Telescope Array Observatory (<i>p. 28</i>)
DAQ	data acquisition system (<i>p. 41</i>)
DR	dark run (<i>p. 102</i>)
DSA	diffusive shock acceleration (<i>p. 2</i>)
EAS	extensive air showers (<i>p. 3</i>)
EBL	extragalactic background light (<i>p. 12</i>)
EGRET	Energetic Gamma Ray Experiment Telescope (<i>p. 5</i>)
FADC	flash analog-to-digital converter (<i>p. 41</i>)
FBOT	fast blue optical transient (<i>pp. i, ii, 3</i>)
Fermi-GBM	Gamma-ray Burst Monitor of the Fermi Gamma-ray Space Telescope (<i>pp. i, ii, 32</i>)
Fermi-LAT	Large Area Telescope of the Fermi Gamma-ray Space Telescope (<i>pp. i, ii, 2</i>)
FoV	Field of View (<i>p. 3</i>)
GCN	Gamma-ray Coordination Network (<i>p. 32</i>)
GRB	gamma-ray burst (<i>p. 3</i>)
GZK	Greisen–Zatsepin–Kuzmin (<i>p. 2</i>)
H.E.S.S.	High Energy Stereoscopic System (<i>p. 7</i>)

HBL	high-frequency peaked BL Lac object (<i>p. 84</i>)
HE	high-energy; $100 \text{ MeV} < E < 100 \text{ GeV}$ (<i>p. 7</i>)
HEGRA	High-Energy-Gamma-Ray Astronomy (<i>p. 6</i>)
HV	high voltage (<i>p. 41</i>)
IACT	imaging atmospheric Cherenkov telescope (<i>pp. i, ii, 3</i>)
IC	inverse Compton (<i>p. 7</i>)
IPR	individual pixel rate (<i>p. 70</i>)
IRF	instrument response function (<i>p. 43</i>)
ISM	interstellar medium (<i>p. 16</i>)
KN	Klein–Nishina (<i>p. 9</i>)
LIGO	Laser Interferometer Gravitational-wave Observatory (<i>p. 2</i>)
LST	Large-sized telescope of the CTAO (<i>p. 68</i>)
MAGIC	Major Atmospheric Gamma Imaging Cherenkov Telescopes (<i>p. 7</i>)
MC	Monte Carlo (<i>p. 4</i>)
MSCL	mean scaled length (<i>p. 55</i>)
MSCW	mean scaled width (<i>p. 55</i>)
NSB	night sky background (<i>pp. i, ii, 4</i>)
ONN	Optimised Next Neighbor (<i>pp. i, ii, 4</i>)
OUV	optical and ultra-violet (<i>p. 23</i>)
PeV	petaelectronvolt (<i>pp. i, ii, 1</i>)
PMT	photomultiplier tube (<i>p. 39</i>)
PSF	point spread function (<i>p. 40</i>)
PWN	pulsar wind nebula (<i>p. 2</i>)
RedHV	reduced High Voltage (<i>p. 89</i>)
RoI	Region of Interest (<i>p. 57</i>)
SED	spectral energy distribution (<i>p. 33</i>)
SLSN	Superluminous supernova (<i>p. 34</i>)
SMBH	super-massive black hole (<i>p. 21</i>)
SN	Supernova (<i>p. 20</i>)
SNR	supernova remnant (<i>p. 1</i>)
SSC	synchrotron self-Compton (<i>p. 9</i>)

Swift-BAT	Swift Burst Alert Telescope (<i>p. 24</i>)
Swift-UVOT	Swift UltraViolet/Optical Telescope (<i>p. 32</i>)
Swift-XRT	Swift X-ray telescope (<i>p. 23</i>)
TDE	tidal disruption event (<i>pp. i, ii, 3</i>)
ToO	target of opportunity (<i>pp. i, ii, 3</i>)
UHECRs	ultra-high-energy cosmic rays; $E > 10^{17}$ eV (<i>p. 2</i>)
UL	upper limit (<i>p. i</i>)
UV	ultra-violet (<i>p. 11</i>)
UVF	ultra violet filter (<i>pp. i, ii, 4</i>)
VERITAS	Very Energetic Radiation Imaging Telescope Array System (<i>pp. i, ii, 3, 4</i>)
VHE	very-high-energy; $100 \text{ GeV} < E < 100 \text{ TeV}$ (<i>pp. i, ii, 2</i>)
WIMP	weakly interacting massive particle (<i>p. 7</i>)
ZTF	Zwicky Transient Facility (<i>p. 3</i>)

Acknowledgements

I would like to thank Dr. Gernot Maier for his supervision and guidance throughout these years. I have learned immensely from our discussions, and his insights have greatly enhanced my understanding of what it means to be a researcher. His thorough review of this manuscript and constructive criticism have been invaluable in improving my scientific journey. I also would like to thank Prof. Dr. David Berge for his official supervision through the Humboldt University. I have also learned a lot from his intriguing questions, especially during the Gamma meetings.

I would like to thank my former supervisors: Prof. Dr. Vitor de Souza, Prof. Dr. Aion Viana and Prof. Dr. Manuela Vecchi, for their encouragement and for introducing me to the field of astrophysics.

I am very grateful to Dr. D. Parsons, Dr. M. Tsirou, Dr. O. Gueta, Dr. T. Kleiner and Dr. V. Barbosa for taking the time to proofread parts of this thesis and providing extremely valuable suggestions. All your comments were essential for this thesis to be completed. Special acknowledgements to Victor, who had the patience to provide comments on almost every chapter of this document, has helped with the submission process and for all the discussions and his friendship. I thank Dr. C. Yuan for the help with AM3 and discussions, script and results contributions and corrections in the gamma-ray annihilation study for TDEs.

I am thankful to the Gamma group at DESY and to the VERITAS Collaboration for providing a motivating environment. Thanks also to D. Ribeiro, B. Humensky, Q. Feng, B. Metzger and S. Wong for their contributions to the TDEs and FBOTs TAC proposals. I appreciate all the discussions with Dr. E. Poeschel, Prof. Dr. K. Ragan, Dr. S. Patel, Dr. D. Tak, Dr. R. Prado, Dr. O. Gueta, Dr. A. Sarkar, Tobias, Pedro, Konstantin, and Chiara. Thanks to the Multimessenger School for giving me the opportunity to participate in several academic courses, present my work in many meetings, and meet several other students from my field.

I am thankful to my family for their support and encouragement. I am also thankful for the good times with my friends, the old and the new from Berlin. Thank you, Gon, for your support and for making this period more meaningful.

Selbständigkeitserklärung

Ich erkläre, dass ich die Dissertation selbständig und nur unter Verwendung der von mir gemäß § 7 Abs. 3 der Promotionsordnung der Mathematisch-Naturwissenschaftlichen Fakultät, veröffentlicht im Amtlichen Mitteilungsblatt der Humboldt-Universität zu Berlin Nr. 42/2018 am 11.07.2018 angegebenen Hilfsmittel angefertigt habe.

Berlin, April 15, 2025.

Maria Kherlakian